ENGINEERING EXPERIMENT STATION
COLLEGE OF ENGINEERING

CONVECTIVE HEAT AND MASS TRANSFER IN COMPACT REGENERATIVE DEHUMIDIFIERS

by

ERIC VAN DEN BULCK

DOCTOR OF PHILOSOPHY
(Mechanical Engineering)

University of Wisconsin

1987

CONVECTIVE HEAT AND MASS TRANSFER IN COMPACT REGENERATIVE DEHUMIDIFIERS

by

ERIC VAN DEN BULCK

A thesis submitted in partial fulfillment of the
requirements for the degree of

DOCTOR OF PHILOSOPHY
(Mechanical Engineering)

at the

UNIVERSITY OF WISCONSIN-MADISON

1987

A dissertation entitled

CONVECTIVE HEAT AND MASS TRANSFER IN COMPACT REGENERATIVE DEHUMIDIFIERS

submitted to the Graduate School of the
University of Wisconsin-Madison in partial fulfillment of
the requirements for the degree of Doctor of Philosophy

by

Eric Van den Bulck

Degree to be awarded: December 19____ May 19____ August 19 87

Approved by Dissertation Readers:

John W Mitchell
Major Professor

May 11, 1987
Date of Examination

S. A. Klein

Patrick V. Farrell

Dean, Graduate School

ABSTRACT

This work presents an analytical investigation of the equilibrium sorption capacity of water vapor on regular density silica gel, and an analytical and experimental study of the dynamic sorption process during laminar flow of humid air through a compact dehumidifier matrix.

Regular density silica gel is identified as the candidate desiccant for regenerative dehumidification of humid air operating at low regeneration temperatures and high process humidities. The literature on the equilibrium sorption uptake of water vapor by R.D. silica gel is reviewed in this work, and a large number of experimental sorption data is collected from various technical reports. The Dubinin-Polanyi sorption theory for microporous adsorbents is discussed and applied to the retrieved sorption data. A graphical presentation of the experimental data establishes the characteristic curve for the sorption of water vapor on silica gel. The Dubinin-Astakhov correlation is used to represent the equilibrium sorption isotherm and values for the characteristic sorption energies are determined by curve fitting with the experimental data. An accurate, generalized isotherm equation for the sorption of water vapor on regular density silica gel is presented in the first part of this work.

The second part of this work presents an analytical and experimental investigation of the transient heat and mass transfer in laminar flow of humid air over a silica gel surface. Experimental results are presented for the transient response of a parallel-plate dehumidifier matrix in single-blow type experiments, in which the test matrix is conditioned at specified initial conditions, and the air stream is subjected to a near step change in inlet conditions. The air stream outlet conditions, i.e., temperature and humidity, as functions of time form the experimental data which are subject of the presented analysis.

These dynamic response curves are prepared for input to a 3-part analysis which computes, respectively: the distributions of the air-side Nusselt and Sherwood numbers with the flow length as independent variable; the distributions with time of the desiccant-side dimensionless heat-conduction and mass-diffusion coefficients; and the combined distributions of the overall heat and mass transfer coefficients. A simplified technique is presented to compute the overall Lewis number from the dynamic response curves. The results of this analysis can be used for the theoretical modeling of the performance of periodic-flow type heat and mass exchangers.

ACKNOWLEDGEMENTS

This work would not be complete without the proper acknowledgement of the support which I received from many people during the production of this thesis. First of all, I wish to dedicate this thesis to my parents to thank them for the thirty years of continuous support, encouragement and trust.

I also wish to express my utmost gratitude to my wife, Mary. Her contribution to this work includes far more than her assistance in the technical production of this manuscript, including some of the more artistic drawings. Her assistance in performing the experiments proved to be that extra effort which established the quality of the experimental data. I have appreciated her overall engagement in my work, and I have continuously relied on her support and patience to accomplish what needed to be done.

Special thanks go to my family and parents in-law, which have provided my wife and me with all their moral support during our graduate student lives.

I wish to thank my advisors, Professors John Mitchell and Sandy Klein, for their continuous support during my entire graduate studies. Maybe it was my fortune that John became department chairman about at the time I started my PhD studies.

The research we were involved in often served as an escape from his growing frustration with administrative duties, a catharsis which even sharpened his eagerness and enthusiasm to study and discuss the strategy in overcoming the many problems which we encountered in our search. His profound knowledge of the thermal sciences was indispensable in shaping the final outcome of this work.

Sandy always seemed to be engaged in a quadrillion simultaneous projects, illustrating his capacity to generate innovative ideas and research tools. I was fortunate that we shared at least a few common interests and I have learned from his many philosophies. Certainly, I could have finished this research with a 64K computer instead of a Cray, even using BASIC instead of FORTRAN, it just would have taken me a little bit longer. It probably would have taken me a lot longer without Sandy's advice and experience.

I must acknowledge the patience of Professor Jack Duffie, and apologize for the many times in which I considered myself to be too busy to produce a half-page monthly progress report. I have learned something about myself during my stay with the Solar Lab, and I will have to work at that.

I have learned a lot about computers during my stay here, and I must thank Professor Bill Beckman for providing me with

the opportunities to work with a variety of different systems and software.

The many discussions I had with my student-colleague Ken Schultz, an expert in desiccant systems, have helped me in refining the scope of my work. It was fun having him and our fellow PhD students, Jim Braun and John Seem, around to discuss the ups and downs of graduate student live. I wish them all lots of success in their post-university careers.

Their are also a number of friends which I have to acknowledge in this proceeding. Frienships come and go in this dynamic community where leaving Madison means moving a thousand miles, at least, and sometimes even crossing an ocean. I would like to especially mention my good friend Jeff Hoerning, whose friendship has made my stay in Madison far more enjoyable.

The experimental work in this thesis was performed at the Solar Energy Research Institute in Golden, Colorado, in a joint research program made possible by Professor Mitchell and Mr. Terry Penney. I would like to thank Dr. Ahmad Pesaran for providing the experimental facilities and technical support which enabled the experiments. During my stay at SERI, I was fortunate to work with Dr. Ian Maclaine-cross. His broad experience in experimental work, which he willingly shared with me, have helped me in the planning of the experiments.

This project was funded by the Solar Heating and Cooling Research Branch, Office of Conservation and Solar Applications, U.S. Department of Energy.

TABLE OF CONTENTS

Table of Contents (continued)

Table of Contents (continued)

Table of Contents (continued)

Table of Contents (continued)

LIST OF FIGURES

List of Figures (continued)

List of Figures (continued)

LIST OF TABLES

List of Tables (continued)

NOMENCLATURE

a_i	thermodynamic coefficients for wave speeds, Eq.(2.14)
A	adsorption potential, Eq. (3.1), or transfer area of a flow passage
A_c	free flow area of a flow passage
b	height of a flow passage
c_p	fluid thermal capacitance
C_m	matrix thermal capacitance
D_{aw}	mass diffusivity of water vapor in air
D_h	hydraulic diameter of flow passage
D_K	Knudsen diffusion coefficient in solids
D_S	surface diffusion coefficient in solids
E_o	characteristic energy of adsorption
f	friction factor of a flow passage
F	Riemann invariant for equilibrium equations, Eq.(2.18), or distribution function defined by Eq. (5.41)
h	heat transfer coefficient
h_m	mass transfer coefficient
i_f	specific enthalpy of fluid stream
i_w	specific enthalpy of water vapor
I_d	specific enthalpy of wet desiccant
I_m	specific enthalpy of matrix
I_W	specific enthalpy of adsorbed water
k	thermal conductivity
K	loss coefficients for pressure drop across flow passage
L	length of flow passage

nomenclature (continued)

m_f process air mass flow rate

M_d mass of dry desiccant

M_f fluid mass entrained in flow passages

P vapor pressure, or total pressure

P_o saturation vapor pressure

P_v vapor pressure

Q_{st} isosteric heat of adsorption

R gas constant

S shock wave speeds

t temperature

t_d dewpoint temperature or desiccant temperature

t_m matrix temperature

U average fluid velocity of a flow passage

w_d humidity ratio of air in equilibrium with desiccant

w_f humidity ratio of air stream

W width of flow passage

W_o uptake capacity of dry desiccant

W_d water load per unit mass of dry desiccant

y transverse flow coordinate

z flow coordinate, Eq. (2.3) or (5.64)

vector quantities

$\boldsymbol{e}$ total energy flux

$\boldsymbol{j}$ diffusion mass flux of a species

nomenclature (continued)

$\boldsymbol{m}$	total mass flux of a species
$\boldsymbol{q}$	energy flux by conduction

Dimensionless Groups

Le_o	overall Lewis number
NTU	Number of Transfer Units
Nu	Nusselt number
Re	Reynolds number
Sh	Sherwood number

greek symbols

ε_p	particle porosity
Γ	mass capacitance rate ratio for a regenerator
λ	expansion wave speeds
μ	dynamic viscosity of fluid
ν	kinematic viscosity of fluid
θ	time variable
θ^*	dimensionless breakthrough time
τ	dimensionless time, Eq. (2.3) or (5.68)
T	rotation period of a regenerative dehumidifier
ρ	fluid density
ρ_s	solid density
ω	water vapor mass fraction in air stream

nomenclature (continued)

superscripts

$\dot{}$	rate
$^+$	dimensionless variable based upon characteristic value

subscripts

$_a$	air
$_d$	desiccant
$_e$	effective
$_f$	fluid or air stream
$_i$	1 or 2: index for first or second wave
$_j$	1 or 2: index for period of a regenerator
$_m$	matrix
$_o$	reference or overall
$_p$	particle
$_s$	solid or silica
$_w$	water (vapor)
$_W$	adsorbed water

units

kgDA	kg dry air
kgDD	kg dry desiccant

CHAPTER 1

INTRODUCTION

Research and development of the use of low-grade thermal energy for heating, cooling and air-conditioning has been evolving ever since its thermodynamic foundations were established by Carnot (1824) and his contemporary scientists. Heat pumps, heat transformers, chillers, air-conditioners, and various other devices driven by thermal energy have been developed for residential and industrial applications, using established absorption and adsorption technologies. Low-temperature energy sources are provided by solar energy, industrial waste heat, or direct gas-fired furnaces. A class within this assortment of devices are the desiccant air-conditioning systems. These systems utilize the latent energy exchange associated with the adsorption or absorption of water vapor in a solid or liquid desiccant, for the cooling or heating of a working fluid.

An overview of current research efforts on the design and installation of desiccant systems has been published recently by Chinery and Penney (1987). Desiccant air-conditioning systems can be classified according to their working medium, either solid or liquid desiccants; their working cycle, either open or closed cycles; and their general structure, either

single or hybrid systems. Liquid desiccants such as LiCl- or LiBr-water solutions are used in adiabatic or cooled absorbers which can be operated continuously in a counter-flow, cross-flow or parallel-flow arrangement. Because of their nature, solid desiccants such as silica gel and molecular sieve are invariably used in regenerative-type adsorbers or dehumidifiers which operate in cyclic or batch mode. Closed-cycle solid desiccant systems are generally used for refrigeration purposes (e.g., Guilleminot et al., 1980; Sizmann et al., 1981; Khelifa et al., 1983; Sakoda and Suzuki, 1984; Chang and Roux, 1985), whereas open-cycle solid desiccant systems are used more for air-conditioning purposes (e.g., Collier et al., 1982; Jurinak et al., 1984b; Maclaine-cross, 1985).

Penney and Maclaine-cross (1985) presented a detailed overview of the current status of research in open-cycle solid desiccant air conditioning systems, and identified three general areas in which research could improve their performance: the use of new desiccant materials with improved thermo-physical and adsorption properties; the use of compact dehumidifiers with enhanced heat and mass transfer characteristics; and the use of advanced cycle configurations with increased performance coefficients.

Summary of Contents

This work is part of a continuing research program conducted at the Solar Energy Laboratory of the University of Wisconsin-Madison, related to the design and application of open-cycle, solid desiccant air-conditioning systems, and is funded by the U.S. Department of Energy. It is a fundamental study of the heat and mass transfer characteristics of compact, regenerative dehumidifier designs, including experimental work which has been conducted in cooperation with the Solar Energy Research Institute.

Chapter 2 reviews the mathematical theory for modeling regenerative dehumidifiers. The basic assumptions and governing model equations are listed and an overview of various solution methods is presented. The equilibrium theory of adiabatic dehumidifiers is discussed in detail and the necessary tools and concepts to understand the remainder of this work are explained. Unexplored research areas in the design theory for regenerative dehumidifiers are identified, and the objectives and contents of this thesis are presented in relationship to these areas.

Chapter 3 discusses the physical phenomena of adsorption. The microporous adsorbents are identified as the candidate desiccants for regenerative dehumidification, and the literature on the sorption of water vapor on silica gel is reviewed. The phenomena of hysteresis and its relevance to dehumidifier

operation are discussed. Experimental sorption equilibrium data are retrieved from the literature and a generalized isotherm expression is developed based upon the Dubinin-Polanyi theory of micropore filling.

Chapter 4 describes the single-blow facility which was used for collecting the experimental data analyzed in this work. This test facility is located at the Solar Energy Reseach Institute and was made available to the author for collecting experimental data. The first section in this chapter contains a general description of the test apparatus and procedures, and is sufficient for a general understanding of the nature of the single-blow experiments. The remainder of the chapter lists the details of the measurement and control instrumentation.

Chapter 5 contains the report and analysis of the single-blow experiments. A complete literature review of the analysis methods for single blow experiments is presented and a specific analysis method is adapted. The transient distributions of the heat and mass transfer coefficients for flow of humid air through a compact desiccant matrix are described and the overall Lewis number for use in dehumidifier modeling is determined.

Chapter 6 compiles the results of the analysis into practical design principles for compact dehumidifiers. An

experimental method for characterizing the exchange performance of compact dehumidifiers is presented.

Chapter 7 presents the contributions of this work to the general area of forced convection heat and mass transfer in laminar flow, and to the literature on solid desiccant dehumidification in particular. Recommendations for future research on regenerative dehumidifiers are formulated.

CHAPTER 2

THEORY OF ADIABATIC REGENERATIVE DEHUMIDIFIERS

This chapter describes the status of current research in the formulation and verification of adiabatic, regenerative dehumidifier models. The first section reviews the standard mathematical model for performance prediction of solid desiccant adiabatic dehumidifiers. Conservation and transfer rate equations are derived from overall mass and energy balances in accordance with a predefined set of constraints and simplifying assumptions. The dynamic operation of desiccant dehumidifiers is rather complicated, involving multi-dimensional, transient heat and mass transfer with a desiccant with nonlinear properties, and consequently there are a number of crucial assumptions which drastically reduce the computational effort in solving the model equations. Some of these assumptions have been accepted without theoretical or experimental justification and a discussion of unresolved issues formulated as research objectives is provided at the end of this chapter.

The second part of this chapter reviews some common tools for solving the model equations. In particular the equilibrium theory of adiabatic dehumidifiers provides physical insight into the dynamics of the exchanger. The formation of transfer zones propagating through the test matrix at characteristic speeds can be explained with the equilibrium theory. Concepts

such as wave speeds and intermediate equilibrium states are defined and discussed in light of the analysis of experimental data which is presented in Chapter 5 of this thesis.

The dehumidifier theory reviewed in this chapter draws on the extensive work published by researchers in Australia (Maclaine-cross and Banks, 1972; Close and Banks, 1972; Close, 1983; Banks, 1985a; - 1985b) and researchers from the Solar Energy Laboratory of the University of Wisconsin-Madison (Jurinak, 1982; Jurinak and Banks, 1982; Van den Bulck, Mitchell and Klein, 1985a; - 1985b).

2.1 Mathematical Model for Adiabatic Dehumidifiers

The mathematical model for predicting the dynamic performance of adiabatic, solid desiccant dehumidifiers is based upon the formulation of mass and energy conservation equations for the air stream and the desiccant matrix. These conservation equations are supported by mechanistic expressions for the overall heat and mass transfer rates. Assumptions are formulated to limit the number of variables and dimensions in the model equation.

2.1.1 Description of Dehumidifier Matrix Geometries

The geometry and capacitance of regenerative desiccant matrices must be described at the level of the simulation model to define the appropriate parameters which appear in the governing equations. The nomenclature and coordinate system for a rotary regenerator are illustrated in Figure 2.1. The desiccant matrix is arranged as a cylindrical wheel with a length in the flow direction L and a total mass of dry desiccant M_d.

Two air streams flow in counter-flow through the rotating dehumidifier. The process air stream, indicated by subscript $j = 1$, has a low temperature and high relative humidity, while the regeneration air stream, indicated by $j = 2$, has a high temperature and low relative humididdity. The inlet face of the wheel for a given period is indicated by subscript $l = 1$, while the corresponding exit face is indicated by $l = 2$. Both indices are used to describe the various state properties of the alternate air stream: the temperature $t_{j,l}$, the humidity ratio $w_{j,l}$, and the specific enthalpy $i_{j,l}$. Dry air mass flow rates are symbolized by $\dot{m}_j$, and the mass of air entrained within the porous matrix is M_j.

The additional subscripts d, f, and m are used to distinguish between, respectively, the desiccant, fluid stream and matrix properties. Upper case characters W_d and I_m symbolize the desiccant water content and matrix specific enthalpy.

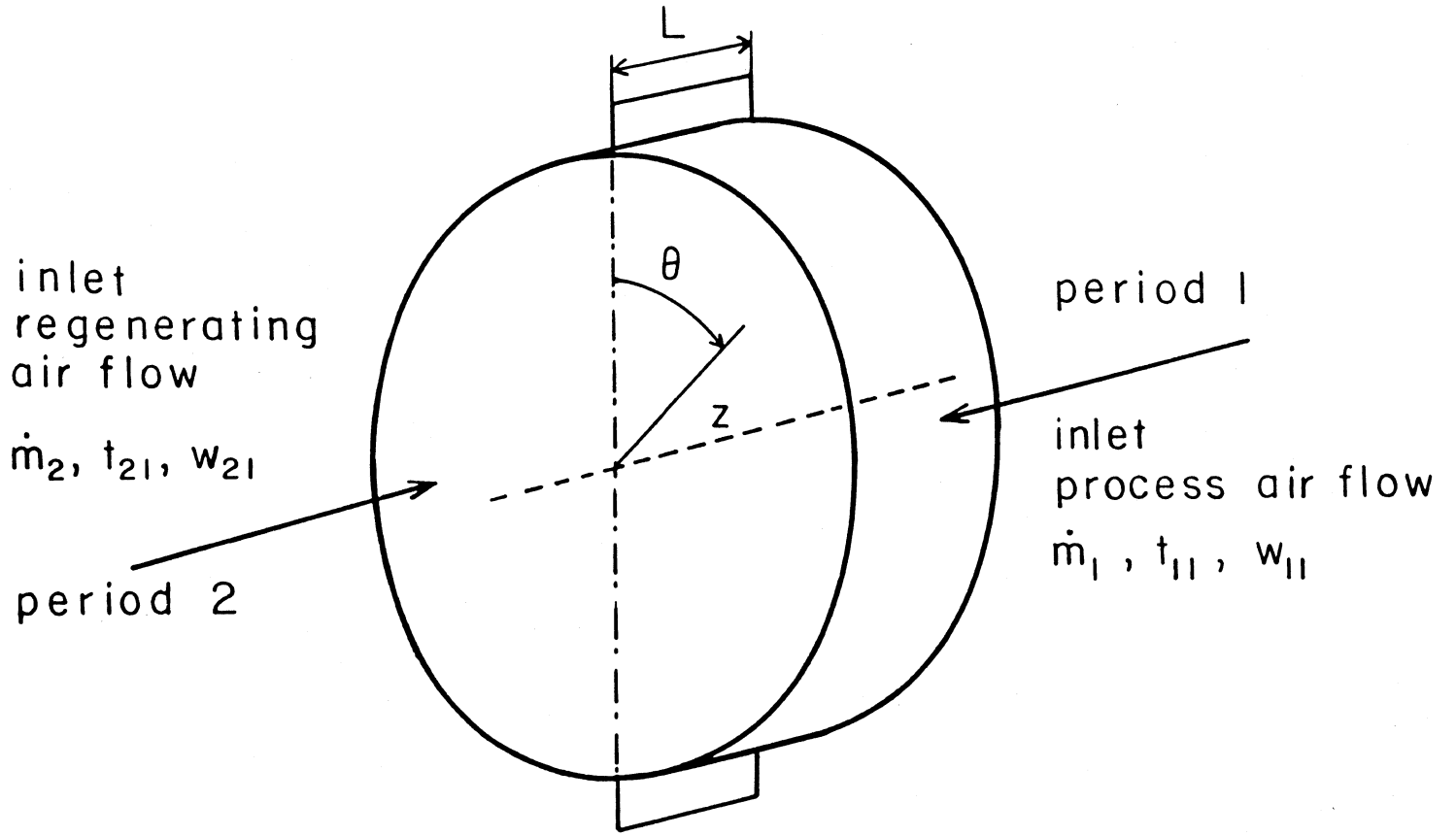

Figure 2.1 Nomenclature and coordinate system for a regenerative dehumidifier.

For each period, the axial coordinate x is defined as positive in the flow direction, while the rotary position of a matrix element is measured by the time coordinate θ. The duration of period j is T_j and the time for a complete wheel rotation is T. The dwell time of each flow rate within the matrix is θ_j.

The desiccant matrix adsorbs the water vapor from the process air stream. Because of the adiabatic nature of the sorption process, there is a considerable temperature increase of the process air stream. The wet desiccant then rotates into the regeneration period where it is dried by the hot regeneration air stream. The desiccant and air temperature decrease during the desorption period. The geometry illustrated in Fig. 2.1 shows only one of the configurations which have been proposed for regenerative operation. Other arrangements are the rotating cylindrical drum with radial flow of the fluid, and the stationary two-matrix configuration with periodic switching of two parallel fluid streams. The dehumidifier matrix can be operated adiabatically or approximately isothermally by cross-cooling. The internal core geometry of the matrix can be that of a packed bed or a compact heat transfer surface.

2.1.2 Constraints and Assumptions

Existing models for regenerative dehumidifiers which describe the exchange of heat and mass between a humid air stream and a regenerative desiccant matrix are based upon the following conventional assumptions.

1. The state properties of the air stream are constant in time and spatially uniform at the inlet face of the exchanger matrix for each period.

2. There is no mixing or carry-over of the process and regeneration air streams.

3. The pressure drop across the desiccant matrix is small compared to the absolute pressure, and the effect of varying pressure on the properties of the air stream and desiccant can be neglected.

4. There is no flux coupling between the transport of water vapor by mass diffusion and the transport of energy by heat conduction.

5. The temporary distributions of the fluid and matrix state properties are uniform in the *radial* direction.

6. *Angular* diffusion fluxes of heat and mass due to tangential gradients of matrix and air state properties can be neglected.

7. *Axial* heat conduction and mass diffusion in the flow direction can be neglected in both the air stream and the desiccant material.

8. The exchanger matrix is modeled as being of parallel passage form, consisting of a *homogeneous solid with constant matrix characteristics and porosity,* through which an air-water vapor mixture flows with constant velocity.

9. The heat and mass transfer processes between the air stream and the desiccant matrix can be described by *overall transfer coefficients,* which are *constant with time and position* in the flow direction.

Assumptions 1 through 4 are generally acceptable, and do not influence the fundamental nature of the modeling equations. Assumptions 5 and 6 reduce the level of the model from transient, 3-dimensional to transient, 1-dimensional with time and position in the flow direction being the independent variables. Assumption 7 changes the character of the differential equations from parabolic to hyperbolic, thereby causing a major reduction in computational effort for a numerical solution of the model equations. Assumptions 8 and 9 are the crucial assumptions in modeling regenerative dehumidifiers and discussed after the model equations have been established.

2.1.3 Model Formulation

With the assumptions listed above, the overall conservation and transfer rate equations for each period j can be written as follows where the subscript j has been omitted:

1. water vapor conservation

$$\dot{m}_f \frac{\partial w_f}{\partial x} + \frac{M_f}{L}\frac{\partial w_f}{\partial \theta} + \frac{M_d}{L}\frac{\partial W_d}{\partial \theta} = 0$$

2. energy conservation

$$\dot{m}_f \frac{\partial i_f}{\partial x} + \frac{M_f}{L}\frac{\partial i_f}{\partial \theta} + \frac{M_d}{L}\frac{\partial I_m}{\partial \theta} = 0 \qquad (2.1)$$

3. rate of water vapor mass transfer

$$\frac{M_d}{L}\frac{\partial W_d}{\partial \theta} = h_m \frac{A}{L}(w_f - w_d)$$

4. rate of thermal energy transfer

$$\frac{M_d}{L}\frac{\partial I_m}{\partial \theta} = h \frac{A}{L}(t_f - t_m) + h_m \frac{A}{L}(w_f - w_d)\, i_w$$

In these equations, written with respect to a coordinate system fixed to the wheel, w_d is the local humidity ratio of air in equilibrium with the desiccant at temperature t_m and adsorbed amount W_d. A is the total transfer area of the regenerator. The transfer rate expressions define the overall transfer coefficients h and h_m based upon A.

The capacitance rate ratios Γ_1 and Γ_2 are defined as the ratio of the matrix- to fluid mass capacity rate,

$$\Gamma_j = \frac{M_d}{T \dot{m}_{f,j}} \tag{2.2}$$

and the following dimensionless coordinates are defined;

for position in the flow direction:

$$z = \frac{x}{L}; \qquad \text{where} \quad 0 \le z \le 1$$

and for time and period j:

$$\tau = \frac{\theta}{T_j}\frac{1}{\Gamma_j}; \qquad \text{where} \quad 0 \le \tau \le \frac{1}{\Gamma_j} \tag{2.3}$$

The conservation and transfer rate equations for the rotary dehumidifier can be written in terms of these dimensionless coordinates:

1. water vapor conservation

$$\frac{\partial w_f}{\partial z} + \frac{M_f}{M_d}\frac{\partial w_f}{\partial \tau} + \frac{\partial W_d}{\partial \tau} = 0$$

2. energy conservation

$$\frac{\partial i_f}{\partial z} + \frac{M_f}{M_d}\frac{\partial i_f}{\partial \tau} + \frac{\partial I_m}{\partial \tau} = 0 \qquad (2.4)$$

3. rate of water vapor mass transfer

$$\frac{\partial W_d}{\partial \tau} = NTU_{w,j}\,(w_f - w_d)$$

4. rate of thermal energy transfer

$$\frac{\partial I_m}{\partial \tau} = \mathrm{NTU}_{t,j}\frac{\partial i_f}{\partial t_f}\,(t_f - t_m) + \mathrm{NTU}_{w,j}\,(w_f - w_d)\,i_w$$

where the parameters $NTU_{w,j}$ and $NTU_{t,j}$ are the *Number of Transfer Units* for period j, and for mass and heat transfer, respectively:

$$NTU_w = \frac{h_w A}{\dot{m}_f}$$

and

$$NTU_t = \frac{h A}{\dot{m}_j c_{p,f}} \qquad (2.5)$$

The number of parameters in Eqs. (2.4) is further reduced by one with the introduction of an overall effective Lewis number;

$$\frac{NTU_{t,1}}{NTU_{w,1}} = \frac{NTU_{t,2}}{NTU_{w,2}} = Le_o. \tag{2.6}$$

This effective Lewis number should not be confused with the Lewis number conventionally defined as the ratio of thermal to mass diffusivity of a fluid, which is 0.85 for air-water vapor mixtures at standard conditions. The overall Lewis number determines the relative ratio of the overall resistances to mass and heat transfer. $Le_o > 0.85$ indicates that the mass transfer rate is small compared to the heat transfer rate, and that the diffusion resistance for water vapor inside the desiccant particles is larger than in the air stream.

Equations (2.4) are coupled through the thermodynamic property relationships for the desiccant-air-water vapor mixture:

$$\begin{aligned} w_d &= w_d(W_d, t_m) \\ i_f &= i_f(t_f, w_f) \\ I_m &= I_m(t_m, W_d) \end{aligned} \tag{2.7}$$

The system of equations (2.4) needs a set of boundary conditions, formed by the inlet states of the air streams:

at $z = 0$,

$$w_f = w_{j,1} \qquad t_f = t_{j,1} \qquad \text{for } 0 \le \tau \le \frac{1}{\Gamma_j};\quad j = 1,\ 2. \tag{2.8}$$

The initial conditions for Eqs. (2.4) are formed by the periodic matching of the matrix state properties at the turnover between the two periods:

at $\tau_1 = 0$,

$$\lim_{\tau_1 \to 0^+} W_d = \lim_{\tau_2 \to (1/\Gamma_2)^-} W_d \qquad \lim_{\tau_1 \to 0^+} t_m = \lim_{\tau_2 \to (1/\Gamma_2)^-} t_m \qquad \text{for } 0 \le z \le 1 \tag{2.9}$$

at $\tau_2 = 0$,

$$\lim_{\tau_2 \to 0^+} W_d = \lim_{\tau_1 \to (1/\Gamma_1)^-} W_d \qquad \lim_{\tau_2 \to 0^+} t_m = \lim_{\tau_1 \to (1/\Gamma_1)^-} t_m \qquad \text{for } 0 \le z \le 1$$

Equations (2.4, 2.7-9) form a closed set of equations which are correct within the assumptions listed above. These equations can only be solved numerically, requiring a large computational effort. Typical CPU times of 1 to 3 minutes on mainframe computers restrict the use of this technique to single case studies. Simulation of entire systems in which the dehumidifier is only one component among many others requires a component model with CPU times less than 1 s.

Simple solution methods developed by Banks and his coworkers (1985a, 1985b), Van den Bulck et al. (1985a, 1985b) and

Epstein et al. (1985), are obtained from the equilibrium theory for regenerative heat and mass exchangers. This theory is reviewed next.

2.2 Equilibrium Theory for Adiabatic Dehumidifiers

The equilibrium theory assumes that at all times and positions within the matrix, there exists complete thermodynamic equilibrium, i.e., thermal and vapor pressure equilibrium, between the desiccant and the air stream:

$$t_f = t_m$$
$$w_f = w_d \tag{2.10}$$

The overall transfer coefficients are infinite for this situation. Based upon this assumption, the system of equations (2.4) reduces to a set of two coupled conservation equations:

$$\frac{\partial w_f}{\partial z} + \frac{M_f}{M_d}\frac{\partial w_f}{\partial \tau} + \frac{\partial W_d}{\partial \tau} = 0$$
$$\frac{\partial i_f}{\partial z} + \frac{M_f}{M_d}\frac{\partial i_f}{\partial \tau} + \frac{\partial I_m}{\partial \tau} = 0 \tag{2.11}$$

A complete and detailed description of systems of equations of this type, known as *hyperbolic systems of conservation laws*, is given by P. Lax in a *SIAM* monogram (1972). There exist two

type of solutions for Eqs. (2.11): the genuine or differentiable solutions and the generalized or integral solutions.

GENUINE SOLUTIONS

The genuine solutions for Eqs. (2.11) are obtained by the classic method of characteristics for hyperbolic systems. The conservation equations are expressed in terms of their Riemann invariants, denoted by F_1 and F_2:

$$\lambda_1 \frac{\partial F_1}{\partial z} + \frac{\partial F_1}{\partial \tau} = 0$$

$$\lambda_2 \frac{\partial F_2}{\partial z} + \frac{\partial F_2}{\partial \tau} = 0 \qquad (2.12)$$

where λ_1 and λ_2 are the wave speeds in dimensionless coordinates. They can be computed as the roots of the following quadratic equation, referred to as the *equation of the direction of the characteristics*:

$$a_2 a_4 \lambda + (a_2 \lambda - 1)(a_5 \lambda - a_3) = 0 \qquad (2.13)$$

where the functions a_i are state property functions defined by:

$$a_1 = \left.\frac{\partial W_d}{\partial t_f}\right)_{w_f}$$

$$a_2 = \left.\frac{\partial W_d}{\partial w_f}\right)_{t_f}$$

$$a_3 = \frac{\partial i_f}{\partial t_f}\Big)_{w_f} \tag{2.14}$$

$$a_4 = \frac{\partial i_f}{\partial w_f}\Big)_{t_f} - \frac{\partial I_m}{\partial W_d}\Big)_{t_m}$$

$$a_5 = \frac{\partial I_m}{\partial t_m}\Big)_{W_d}$$

where it is assumed for matters of illustration that $M_f/M_d = 0$, i.e., the storage capacity of the air is neglected with respect to that of the matrix. The wave speeds are always positive, real numbers (Lax, 1972) and are sorted as:

$$\lambda_1 > \lambda_2 > 0 \tag{2.15}$$

For silica gel, λ_1 ranges from 1 to 5, and is about 10-100 times larger than λ_2. The *characteristics* of the hyperbolic system of equations are defined by the two ordinary differential equations:

$$\frac{dz}{d\tau} = \lambda_i; \quad i = 1,2. \tag{2.16}$$

Along the characteristics, the state properties of the fluid stream satisfy the equations

$$\begin{aligned} &a_3\,(a_2\,\lambda_i - 1)\,dt_f + a_4\,a_2\,\lambda_i\,dw_f = 0; \\ &a_1\,a_3\,dt_f - (a_5\lambda_i - a_3)\,a_2\,dw_f = 0; \end{aligned} \qquad i=1,2 \tag{2.17}$$

Integration of expression (2.17) along the characteristic (2.16) yields

$$dF_i = 0; \quad i = 1,2 \tag{2.18}$$

The functions F_i are the Riemann invariants of the system of conservation laws (2.11), and are in the dehumidifier literature sometimes referred to as the F-potentials (Banks, 1985a-b)

Equation (2.18) along with Eq. (2.16) is equivalent with Eqs. (2.11) and (2.12). These equations illustrate the nature of the dynamic character of the exchange processes which occur within regenerative dehumidifiers. The F_i-invariant is constant along the λ_i characteristic. Thus, values of constant F_i propagate through the matrix in the direction of the fluid flow at speed λ_i, and this phenomena may be interpreted as a state property wave moving with speed λ_i. This wave speed is a local speed and depends only upon the local state properties at the point of interest. The F_1 wave, which is the fast wave, is referred to as the heat transfer wave, because this wave is similar in nature to the single wave which occurs in heat exchanger matrices. Similarly, the F_2 wave is the slow mass transfer wave because this wave is analogous to the single wave which occurs in isothermal mass exchanger matrices. Heat and mass transfer occurs only within the boundaries set by the leading and trailing edges of the waves, and therefore the F_1- and F_2 waves are also referred to as the heat transfer zone and the mass transfer zone, respectively. For silica gel the two

waves are always completely separated, with the F_1 wave preceding the F_2 wave. The leading edge of the F_1 wave has the properties of the initial state of the matrix. The trailing edge of the F_2 wave has the properties of the inlet state of the air stream. The state in between the trailing edge of the first wave and the leading edge of the second wave is a well-defined state with constant properties. This intermediate state has the F_2 value of the initial state of the matrix and the F_1 value of the inlet state of the air stream. The properties of this state are completely determined by the thermodynamic properties (2.7), and the properties of the fluid-inlet and matrix-initial state.

The waves that are described by Eqs. (2.12) are rarefaction waves, that is, they can only exist if and only if they are continuously expanding while they propagate through the desiccant matrix (Lax, 1972; Van den Bulck, Mitchell and Klein, 1985a). For dehumidifiers, this requires that a dry desiccant is processed by a humid air stream. However, there exists an alternate solution for the conservation equations (2.11) for the case when a wet desiccant is regenerated by a hot air stream.

GENERALIZED SOLUTIONS

The generalized solutions to Eqs. (2.11) are obtained by the mathematical theory of shock waves. This method assumes

that the waves propagating through the matrix are discontinuous waves. Shock waves are formed naturally by rarefaction waves for which the leading edge of the waves has a lower wave speed than the trailing edge of that same wave. The shock-wave method expresses the conservation equations (2.11) in the form of integral jump expressions, for $M_f/M_d = 0$:

$$\frac{\Delta w_f}{\Delta z} + \frac{\Delta W_d}{\Delta \tau} = 0$$

$$\frac{\Delta i_f}{\Delta z} + \frac{\Delta I_m}{\Delta \tau} = 0 \qquad (2.19)$$

where Δ must be interpreted as the integral across a discontinuity. These jump equations can be rewritten as

$$\frac{\Delta i_f}{\Delta I_m} = \frac{\Delta w_f}{\Delta W_d} = \frac{\Delta z}{\Delta \tau} = S \qquad (2.20)$$

where S denotes the shock wave speed. Because there are two quantities conserved, i.e., water-vapor mass and energy, Equation (2.20) has two distinct solutions which are obtained from

$$\frac{(w_{f,int} - w_{f,11})}{(W_{d,int} - W_{d,11})} = \frac{(i_{f,int} - i_{f,11})}{(I_{m,int} - I_{m,11})} = S_1$$

$$\frac{(w_{f,21} - w_{f,int})}{(W_{d,21} - W_{d,int})} = \frac{(i_{f,21} - i_{f,int})}{(I_{m,21} - I_{m,int})} = S_2 \qquad (2.21)$$

The index 11 refers to the initial matrix state, and 21 refers to the air stream inlet conditions. The subscript *int* refers to the intermediate state in between the two waves. Equations (2.21) can be used to compute the intermediate state properties and the two wave speeds, and reveal the nature of the intermediate state properties. These properties are defined by finite integral equations, and depend only upon the integral form of the state property functions (2.7). Thus, the intermediate state properties are not sensitive to numerical inaccuracies in the functional representation for the state property relationships.

The shock wave speeds S_i are related to the rarefaction wave speeds λ_i through the *generalized entropy condition* (Lax, 1972):

$$\begin{aligned} \lambda_{1,11} < S_1 < \lambda_{1,int} \\ \lambda_{2,int} < S_2 < \lambda_{2,21} \end{aligned} \tag{2.22}$$

These conditions were first established for compressible flow, where they formulate that the fluid crossing the shock wave zone suffers an increase in entropy (Lax, 1972). Van den Bulck, Klein and Mitchell (1985c) showed theoretically that Eq. (2.22) is an alternative formulation of the second law of thermodynamics applied to the specific case of adiabatic heat and mass transfer in flow through porous media. Equations (2.22) indicate that the shock wave speeds have the same nature

as the rare-faction wave speeds, λ_i. These latter speeds are determined by the functions a_i, which are differentials of the state property functions. Hence, the wave speeds are very sensitive to the numerical accuracy of the functional representation for the state property relationships (2.7), and in particular of the curve fit for the adsorption isotherm. Typically, polynomial curve fits give high accuracy in the integral properties, yet low accuracy in the differentials.

The effect of finite transfer coefficients is to smear the waves. The rare-faction waves tend to expand even more when the transfer rates are reduced, whereas the shock waves become continuous property distributions with a constant pattern (Ruthven, 1984).

Concepts such as intermediate state, shock wave vs. rare-faction wave, heat and mass transfer zones, and wave speeds are common in the literature on adsorption processes, and are employed throughout the remainder of this volume.

2.3 Unresolved Issues and Thesis Objectives

Numerical solutions for the model equations (2.1) were developed by Maclaine-cross (1974), Pla-Barby et al. (1978), Holmberg (1979), and Barlow (1981). These schemes use conventional finite difference techniques which lead to relatively

slow computer codes. More advanced finite element schemes for thermal regenerators have been developed (Baclic, 1985) and offer the potential of a significant reduction in computational effort for the same numerical accuracy.

Numerical schemes are generally used to verify the accuracy of simplified solution techniques. Matriprakasam and Lavan (1980) presented a simplified solution of the model equations based upon linearization of the equations and Laplace transforms. Maclaine-cross and Banks (1972) and Banks (1985a-b) use the concept of the *F*-potentials to relate the performance of rotary dehumidifiers to that of rotary heat exchangers by analogy. Epstein et al. (1985) use the solutions of the integral shock wave equations to evaluate dehumidifier performance. Van den Bulck et al. (1985a-b) developed an *effectiveness-NTU* theory for rotary dehumidifiers. The ideal rotary dehumidifier is modeled exactly by the equilibrium theory, and empirical effectiveness curves are established by comparison with numerical solutions.

The underlying key to all these models is the set of assumptions formulated above. The validity of some of these assumptions has been investigated theoretically and experimentally. Brandemuehl (1982) and Brandemuehl and Banks (1984) studied the effect of time-varying or nonuniform inlet conditions on the performance of rotary heat and mass exchangers, and concluded that, for high effectiveness regenerators, non-

uniformities in inlet conditions have little effect on the steady-state regenerator performance. Banks (1982, 1984) has numerically investigated the effect of fluid carryover on the performance of regenerative heat exchangers. Whereas correction schemes can be applied for fast rotating heat exchangers, the effect of carryover on dehumidifier performance is negligible because of their low rotation speed. Experiments on prototype dehumidifier matrices (Rousseau, 1980) have indicated that the pressure drop is less than 1% of the total pressure, and the effect on property evaluation is negligible. The effect of axial or longitudinal heat conduction in the matrix has been studied in great detail for thermal regenerators, and correction schemes have been developed (Shah, 1981). For desiccant dehumidifiers, this effect has not been studied; however, axial conduction may be small if the matrix is constructed with thin carriers to which individual desiccant particles adhere to.

Assumption 8 lumps the dehumidifier matrix into a single, homogeneous capacitance. The validity of this assumption has not yet been investigated for regenerators. Structural parts which form the skeleton of the exchanger cause a nonuniform distribution of the thermal capacitance of the matrix, while these parts do not affect the total moisture capacitance. A two-capacitance model would incorporate an additional transfer

rate expression and an additional unknown temperature. The computational effort would then increase by about 25%; however, the model would require an additional unknown transfer rate coefficient which may prove difficult to estimate.

Assumption 8 also makes the desiccant temperature t_d equal to the matrix temperature t_m. If there exist distributed capacitances within the exchanger, these temperatures may differ significantly, and errors in the performance evaluation may occur. Because the distribution of the capacitances is determined by the construction and geometry of the dehumidifier, the validity of assumption 8 can only be investigated by experiments on an actual prototype dehumidifier. Such investigation is currently performed by K. Schultz (1987) in his PhD work at the Solar Energy Laboratory. The effect of nonuniform capacitance distributions is briefly discussed in Chapters 5 and 6 of this thesis.

Assumption 9 makes the transfer coefficients empirical input parameters to the dehumidifier model, rather than computing the transfer rates from general transport or diffusion type equations. This assumption reduces the number of dimensions in the model equations by 1, and of all assumptions 1-9 reduces the computational effort the most.

Effectiveness charts for rotary dehumidifiers have been published by Ingram and Vliet (1982), and Van den Bulck et al.

(1985b). The *effectiveness-NTU* curves are similar to those of counter-flow heat exchangers, and show the reduction in regenerator performance due to finite transfer coefficients. Because of the dynamic character of the regenerator, the transfer coefficients depend on time and position within the matrix. Furthermore, they are dependent upon thermo-physical properties such as thermal and mass diffusivities which may be strong functions of temperature and water mass fraction. Hence, the transfer coefficients may not be constant parameters, and the effect of their nonuniform distribution on the performance evaluation of the dehumidifier needs to be determined. Such investigation with a detailed literature review is presented in Chapter 5 of this PhD work based upon an analysis of original experimental data.

The ansatz of overall transfer coefficients in the dehumidifier model leads to the concept of an overall Lewis number, Eq. (2.6). Jurinak (1982; Jurinak and Mitchell, 1982) investigated in great detail the effect of the Lewis number and concluded that the existence of a diffusion resistance within the desiccant has a profound effect on the performance of desiccant dehumidifiers. A regenerator with $Le_o = 4$ needs twice the volume of a $Le_o = 1$ regenerator for the same performance, and thus the fan power to force the air streams through the regenerator also doubles. This increase in parasitic power can make the difference between a competitive and a non-competitive

device (Jurinak, 1982), and an accurate estimate of the overall Le_o is recommended for system performance evaluation. Various efforts to determine this number have been reported in the technical literature and are reviewed in Chapter 5. The analysis presented in that chapter determines the Lewis number for the investigated dehumidifier matrix.

Jurinak (1982; Jurinak and Mitchell, 1982) also studied the effect of the isotherm correlation on the dehumidifier performance, and concluded that "hysteresis in the adsorption isotherm has a very pronounced adverse effect on the performance of the dehumidifier." Hysteresis has been reported for the silica gels which are used in regenerative dehumidifiers (Mikhail and Shebl, 1970b), and the issue of hysteresis with a detailed literature review is presented in the next chapter.

CHAPTER 3

SORPTION EQUILIBRIUM PROPERTIES OF REGULAR DENSITY SILICA GEL

The performance of solid desiccant, regenerative dehumidifiers is determined in part by the thermo-physical equilibrium properties of the desiccant. These properties include the physical adsorption isotherm for water vapor, the isosteric heat of adsorption, and the thermal capacity of the dry solid desiccant. To model regenerative dehumidifiers, correlations are needed which describe the water uptake by the desiccant as a function of the water vapor pressure and temperature. For adiabatic dehumidifiers, the heat of adsorption determines the drying capacity of the desiccant for a specified regeneration temperature. Thermodynamic equilibrium constraints establish a relationship between the heat of adsorption and the derivative of the sorption isotherm correlation with respect to temperature. Dynamic time constants of the dehumidifier are determined by the derivative of the isotherm with respect to the water vapor pressure. Thus, for an accurate simulation of desiccant dehumidifiers, a correlation for the sorption isotherm is needed which has accuracy in predicting the water uptake by the desiccant as well as the derivative thereof with respect to temperature and water vapor pressure. A curve fit of experimental data with an empirical functional form for the

isotherm may not have the required accuracy for the derivatives. Rather a functional form is desired which includes some of the physics of the adsorption process.

This chapter presents a generalized isotherm equation for the physical adsorption of water vapor by regular density silica gel. The functional form is the Dubinin-Polanyi isotherm for microporous adsorbents. This form is derived from physical principles underlying the sorption process, and has been applied successfully sorbents and adsorptive gases. A literature review of proposed correlations for the uptake of water by silica gel is presented. Experimental data are collected from the respective publications, and are correlated with the Dubinin-Polanyi isotherm.

First, the general theory of physical adsorption is reviewed. The classification of the adsorbents based upon the shape of the sorption isotherm as accepted by the *International Union of Pure and Applied Chemistry* is presented and the microporous adsorbents as favorable adsorbents for regenerative dehumidification are identified. The Dubinin-Polanyi sorption theory for microporous adsorbents is discussed.

3.1 Physical Adsorption

This section reviews the general principles of physical adsorption which have been established and reported in the technical literature.

3.1.1 Description of Physical Adsorption

The physical phenomena involved with the adsorption of gases on solids have been well established, and there are a numerous amount of technical papers and several reference handbooks which cover the subject in great detail (e.g., Barrer, 1978; Gregg and Sing, 1982; Ruthven, 1984). The study of physical adsorption includes molecular-kinetic theories for the equilibrium of the gaseous and adsorbed phase and the surface layer of the adsorbent. Physical adsorption theories also focus on the statistical and classical thermodynamic aspects of the sorption processes, including the heat of adsorption, entropy and heat capacity of the sorbent-sorbate system. The dynamics of sorption processes is governed by the diffusion in porous adsorbents, and various theoretical and mechanistic models for the transport processes have been developed. A useful monogram has been published by the International Union of Pure and Applied Chemistry (Sing, 1982), which provides the exact definitions and nomenclature for

reporting physical sorption data. The (ad)sorptive is the adsorbable gas, the (ad)sorbent is the adsorbing solid and the adsorbed phase is the (ad)sorbate. The following description and discussion is based on the cited literature references.

Physical adsorption is a natural phenomena which occurs whenever a gas or liquid is in contact with a solid. Molecules of the gaseous or liquid phase attach to or detach from the surface of the solid in a dynamic transfer-exchange process. The adsorbed molecules accumulate on the surface and form an interfacial layer which has properties similar to those of the liquid or condensed phase of the adsorptive. Physical adsorption is generally distinguished from chemisorption. In the first process, attraction between the individual molecules of the adsorbate and the adsorbent surface is the result of weak, intermolecular forces and the sorption is reversible. In the latter process, the individual molecules react chemically with each other and the formation of the resulting complexes is irreversible. The main feature of chemisorption is its high heat of sorption which is similar to the heat of chemical reaction. For the physical adsorption of gases by solids, the heat of sorption is of the same magnitude as the heat of condensation.

Adsorption is the result of various physical forces between the sorbate and sorbent molecules. These forces always include dispersion forces, which are attractive forces, and

short-range repulsion forces. These intermolecular forces are called the *van der Waals* forces which, in the case of pure substances, produce the phase change from gas to liquid. If the solid and gas molecules are polar, or if the solid has an ionic structure such as zeolites, additional strong intermolecular forces arise. The work produced by these combined forces is the heat of sorption. In the presence of electrostatic forces, the heat of sorption is increased significantly.

Adsorption is a surface phenomena in which the adsorbate molecules do not penetrate into the volume of the adsorbent. When the adsorbed molecules diffuse into the lattice of the solid, the process is referred to as absorption. To adsorb a large amount of sorptive per unit mass or volume, adsorbents are either porous solids or porous compacts of powders. Adsorbents are characterized by the specific, internal surface area, expressed as area/mass (m^2/kg), which is typically many orders of magnitude larger than the external particle surface area. Adsorbents are conventionally classified in three categories according to the average diameter of the internal pores. Macroporous adsorbents have pores with diameters or widths exceeding ± 500 A°, microporous adsorbents have pores with diameters less than about 20 A°, and adsorbents with pores of intermediate sizes are called mesoporous adsorbents. These three adsorbent types have distinct sorption characteristics, and are studied and modeled separately.

3.1.2 Sorption Isotherm Classification

The adsorption isotherm expresses the relationship between the amount of adsorbed species and the equilibrium vapor pressure of the gas for a specified constant temperature. The isotherm is a property of the chemistry of the solid and gas materials, and of the internal pore structure of the adsorbent. The *International Union of Pure and Applied Chemistry* (Sing, 1982) has accepted a classification of adsorption isotherms into 6 types. Representative shapes for the alternate isotherm types are shown in Fig. 3.1.

Type ***I*** isotherms are characteristic for microporous adsorbents. These adsorbents exhibit a maximum sorptive uptake which is determined by the filling of the internal pore volume, rather than the coverage of the internal surface area. Vapor molecules within the pores are continuously subjected to an intermolecular force field generated by the surrounding surfaces. The adsorption-desorption loop is reversible. Physico-chemical theories for the type I sorption process include the Langmuir isotherm expression and the Dubinin-Radushkevitch plot based upon the Polanyi theory for adsorption. Molecular sieve zeolites (Barrer, 1978), various types of charcoal, including activated carbon (Gregg and Sing, 1982), and the xerogels of silica, including microporous or

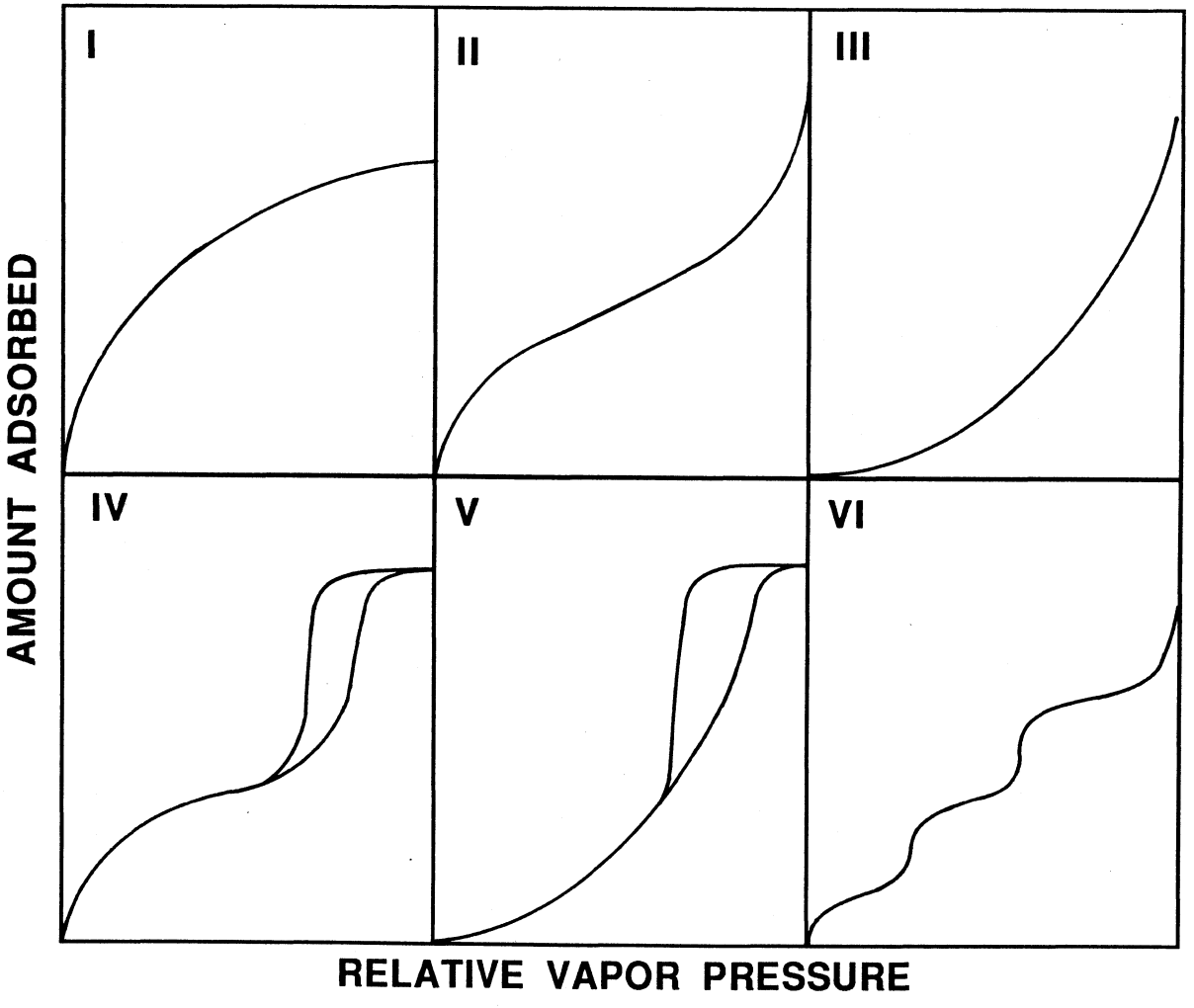

Figure 3.1 Classification of physisorption-isotherm types accepted by the International Union of Pure and Applied Chemistry, (Sing, 1982).

regular density silica gel (Iler, 1979), are typical examples of this very important class of adsorbents.

Type ***II*** is representative for non-porous surfaces, macroporous adsorbents and some compacted powders. These sorbents produce the unrestricted coverage of a monolayer of sorbate molecules and subsequently the construction of molecular multilayers on the surface of the sorbent. The vapor molecules are subjected only to the force field of the adsorbing surface, and consequently the physical sorption process is less complicated than the type I isotherms. The B.E.T. theory, named after its developers Brunauer, Emmett and Teller, to predict sorption uptake is accepted as the *de facto* standard for this type of physisorption and provides a standard technique for computing the specific surface area of the sorbent. Examples of this type II isotherm are graphitized carbon and the compact powders of silica and alumina.

Type ***III*** isotherms are found with nonporous or macroporous solids for which the intermolecular forces between the sorbate and the sorbent are weak compared to the sorbate-sorbate molecular forces. Frequently, either the gas and/or the solid has an organic nature. The sorption of selected alcohols on various plastics, of water vapor on Lexan, various polymers and graphitized carbon, and of benzene on treated samples of silica aerogels produce isotherms of type III.

Adsorption theories and isotherm expressions are not well established for this type of sorbents.

Type ***IV*** isotherms are characterized by the typical hysteresis loop, and are common for many mesoporous adsorbents. The intermolecular forces are of the same nature as the type I and type II isotherms. Adsorption hysteresis occurs when the ad- and desorption differ from each other. The hysteresis is traditionally explained by the occurrence of capillary condensation taking place within ink-bottle type pores. However, new and more fundamental theories for hysteresis have recently been proposed and these theories are reviewed later in this section. The challenge encountered by the hysteresis theories is to establish the relationship between the pore size distribution of the adsorbent and the sorption isotherm. The *Kelvin* equation is the starting point for most theories. A prime example of a type IV isotherm is given by the adsorption of water vapor on mesoporous or low-density silica gel.

Type ***V*** isotherms are similar in nature to the type III isotherm, except that the sorbents are typically mesoporous or microporous. Mesoporous solids show hysteresis. This type of sorption process involves often organic vapors, e.g., the sorption of benzene on calcium sulphate, of pentane, benzene, hexane and carbon tetrachloride on mesoporous silica, and of water on heat-treated mesoporous silica gel. Theories to compute the specific surface area from experimental sorption

equilibrium data or to predict the sorption uptake as a function of the vapor pressure and temperature are less established.

Type ***VI*** isotherms illustrate the stepwise adsorption in multilayers on a non-porous surface or a macroporous sorbent, and is similar in nature to the type II isotherm. Each step represents the coverage of a subsequent monolayer. This type of adsorption is rather rare, e.g., the adsorption of argon or krypton on graphitized carbon at cryogenic temperatures.

Adsorption Hysteresis

Hysteresis is traditionally explained by the theory of capillary condensation within the individual pores. The pores may be cylindrical or have the shape of an ink bottle. (de Boer, 1958). Different pore size distributions or different pore geometries produce different hysteresis loops. Two theories exist which approach the physics of the hysteresis phenomena from different sides.

The independent domain theory has been proposed by Everett and his coworkers (Everett and Whitton, 1952; Everett and Smith, 1954; Everett, 1954a; Everett, 1954b; Enderby, 1955; Everett, 1958; Everett and Haynes, 1972). This theory assumes that each pore domain behaves as though it were interacting with the vapor as an isolated pore. Interconnections with adjacent pores do not influence the adsorption or

desorption of the individual pores. Hysteresis is caused by capillary condensation which is studied for a model pore, e.g., cylindrical pores or voids between spherical particles in a random packing. The functional behavior of the system is characterized by the sum of the independent sorption functions of the individual pores.

The interconnectivity theory has been proposed by Mason (Mason, 1971; Mason, 1972; Mason, 1982; Mason, 1983; Enderby, 1956; Mason and Yadav, 1983). The interconnectivity theory studies the hysteresis produced by an assembly of pores. For a pore to empty during desorption, vapor has to leave it and this requires a pathway available to the vapor. A large pore might be connected to surrounding small pores in such a way that it cannot empty until an adjacent smaller pore empties. This phenomena is the pore blocking effect, and can produce hysteresis. In the interconnectivity theory, individual pore sorption does not show hysteresis.

The network theory for adsorption hysteresis links the interconnectivity theory and the independent domain theory. Each domain is capable of producing hysteresis through capillary condensation, and the assembly of pores can produce hysteresis through pore blocking. This theory is still in development.

The phenomena of hysteresis is not restricted to physisorption processes. For example, hysteresis is also

occurring in organic tissues and determines the important hygroscopic behavior of food products which is related to food preservation (Ngoddy and Bakker-Arkema, 1970; *ibid.*, 1975). The occurrence of hysteresis has also been linked to human memory recording and biological rhythms (Neumann, 1973).

3.1.3 Favorable Adsorbents for Regenerative Dehumidification

Adsorption columns are used for the selective removal by adsorption of a specific component from a gas stream flowing through the column. Regenerative adsorption columns operate in cyclic batch mode. At the start of each sorption process, the adsorbent particles contain a low amount of the species to be removed. The variation with time of the concentration of this adsorbable species in the gas stream at the exit of the column determines the performance of the adsorber. This performance increases if the average species concentration in the outlet gas stream decreases for any operating time, and given initial conditions of the bed and inlet concentration of the gas stream. The shape of the equilibrium sorption isotherm determines the distribution of the concentration profile in time, and thus has a major effect on the performance of adsorption columns.

Ruthven (1984) classifies the equilibrium isotherms of adsorbents for use in regenerative adsorption columns in three

categories according to their effect on the column performance: linear, favorable and unfavorable isotherm shapes. Figure 3.2 illustrates representative curves for these three isotherm shapes. Unfavorable and linear isotherms produce concentration profiles which are rarefaction waves, i.e., waves that are broadening continuously as they propagate through the column. However, the concentration profiles reach the steady, constant pattern of a shock wave if the isotherm has a favorable shape. The dispersive behavior of unfavorable or linear isotherms results in a higher time-average outlet concentration of the adsorbable species than for the case in which the concentration profile has a constant pattern. The type I, type II and type IV isotherms in Fig. 3.1 have favorable shapes for use in adsorption columns. However, type II isotherms are given by nonporous solids which generally have a too low specific sorption uptake to enable compact adsorption beds. For desorption columns in which the gas stream is enriched by a desorbable species, the classification is reversed, and type III and type V are favorable.

Grolmes and Epstein (1985) discuss the negative effect of wave broadening associated with unfavorable isotherms on the performance of regenerative dehumidifiers. Jurinak and Mitchell (1982) studied in more detail the effect of the isotherm shape on the performance of regenerative dehumidifiers. Their report indicates that the type III and type V

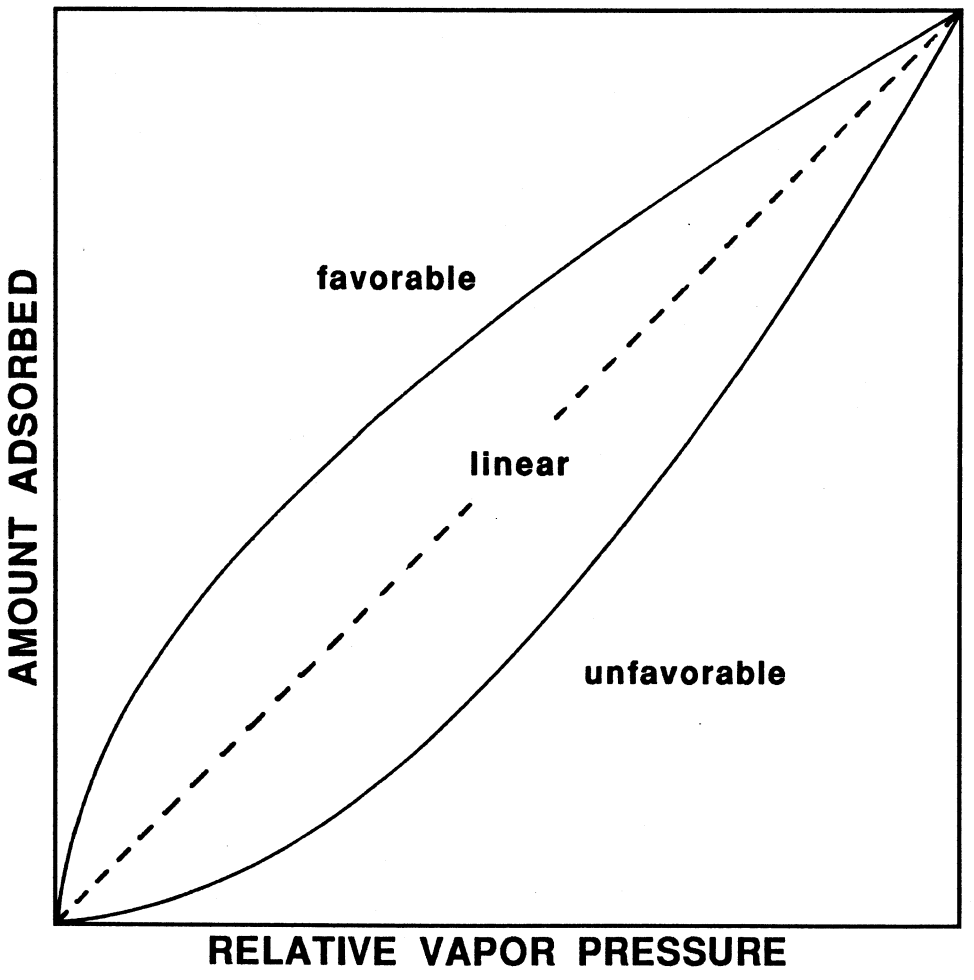

Figure 3.2 Classification of favorable, linear and unfavorable sorption isotherms for dynamic operation of adiabatic adsorption columns, (Ruthven, 1984). For desorption, the classification is reversed.

isotherms are unfavorable for regenerative dehumidification. Type I and type II isotherms have favorable shapes, although type I performs consistently about 5% better than type II. The use of a type I desiccant also yields the most compact dehumidifier with dimensions about half of dehumidifiers using other types. Although the shape of type IV isotherms may be favorable, the hysteresis associated with this type results in a significant decrease of about 15 to 30% in regenerator effectiveness.

The literature reported here is consistent and conclusive with respect to the optimum shape of the sorption isotherm of solid desiccant for use in regenerative dehumidifiers. Microporous solid adsorbents have the favorable type I isotherm shape, and are recommended. Regular density silica gel, molecular sieves Na-A or 4A and Na-X or 13X, activated alumina, activated bauxite, and activated carbon are the candidate solid desiccants for regenerative dehumidification. Recent research is focusing on regular density silica gel as the prime candidate for use in rotary dehumidifiers with relative low regeneration temperatures and high process humidities.

However, anhydrous lithium chloride and activated calcium sulfate have a tremendous capacity for water uptake, about 2 times that of regular density silica gel per unit mass before going into solution, and about 8 times in liquid solution, and thus their use yields very compact dehumidifiers. The dis-

continuities in their isotherms produce constant pattern or favorable concentration profiles. Furthermore, regenerator matrices can be impregnated with these salts with relative ease whereas the industrial manufacturing of solid desiccant matrices is challenging. These considerations have established the wide use of salts in commercial dehumidifiers today. The disadvantage with salts is that, during operation, the liquid salt solution may drip due to gravity and this causes a non-uniform distribution of the desiccant mass which may have a pronounced negative effect on the dehumidifier performance.

3.1.4 Dubinin-Polanyi Equilibrium Theory for Microporous Adsorbents

The adsorption potential theory was originally proposed by Polanyi (1932). In this key paper, Polanyi discusses the nature of the various forces of adsorption: the electrostatic forces, the valence forces and the dispersion forces. The common feature of these forces is that they are potential forces unlike the surface-tension forces associated with capillary condensation. Using gas-kinetic theories of Boltzmann, Polanyi arrives at a theoretical relationship between the average potential energy of the adsorbed molecules and the adsorbed amount expressed in the form:

$$A = RT\,ln(\frac{P}{P_o}) = const., \text{ for } W_d = const. \qquad (3.1)$$

where A is called the adsorption potential. The physical nature of the adsorption potential can be readily understood by expressing the adsorbed amount in terms of A with a generic function,

$$W_d = fn(A). \qquad (3.2)$$

The differential heat of adsorption is given by the Clausius-Clapeyron equation:

$$Q_{st} = - RT^2 \frac{\partial lnP}{\partial T}\Big)_{W_d}, \qquad (3.3)$$

and using the definition expression for A, Eq. (3.1), and the Polanyi assumption Eq. (3.2), it can be shown that

$$Q_{st} = \Delta I_{fg} + A \qquad (3.4)$$

where ΔI_{fg} is the latent heat of condensation of the pure liquid. The adsorption potential is thus the difference in free energy between the adsorbed phase and the saturated liquid phase of the adsorptive at the same temperature, and is a true thermodynamic property, characteristic for the physical state of the adsorbate layer.

Equation (3.2) states that the mass of the adsorbed phase is directly related to the adsorption potential, and the func-

tional relationship is independent of the temperature. This relationship is called the *characteristic curve*. The main advantage of expressing the sorption isotherm in terms of A is that experimental sorption equilibrium data need only be collected at one temperature and a discrete set of vapor pressures. The relation provides a function for interpolation for intermediate vapor pressures or extrapolation for different temperatures. However, the application of the Polanyi theory is restricted to those systems for which the existence of a temperature-independent characteristic curve has been verified experimentally. The Polanyi theory has been applied successfully for correlating adsorption equilibrium data for activated carbons and zeolites or molecular sieves.

Dubinin (1972, 1975) examined experimental sorption equilibrium data for many systems, and showed that the characteristic curve can often be approximated by a Weibull expression,

$$W_d = W_o \exp(- (A/E_o)^n) . \qquad (3.5)$$

where W_o is the total micropore volume, and E_o is the characteristic energy of adsorption. For most microporous systems, the parameter n = 2 is recommended in which case Eq. (3.5) is referred to as the Dubinin-Radushkevich expression. Stoeckli (1977) commented on the application of this latter form and

showed experimentally that Eq. (3.5) with n = 2 applies only to homogeneous systems of pores, i.e., pores with equal dimensions. A heterogeneous pore system can be approximately visualized as the superposition of independent homogeneous microporous substructures. Often a two-sited D-R expression is used to represent the alternate sorption in the smaller ultramicropores and the larger supermicropores, respectively:

$$W_d = W_{o,1} \exp(-(A/E_{o,1})^2) + W_{o,2} \exp(-(A/E_{o,2})^2). \quad (3.6)$$

This expression, presumably established by Dubinin and Polstyanov (Dubinin, 1975), and sometimes also referred to as the Dubinin-Astakhov equation, is used to correlate the experimental equilibrium sorption data of water vapor on regular density silica gel in the following discussion.

3.2 Generalized Sorption Isotherm Correlation for Water Vapor and Regular Density Silica Gel

3.2.1 Literature Review

A literature survey on the sorption properties of silica gel yielded a large number of publications of which the majority reported on the hysteresis phenomena associated with the sorption by low-density silica gel of nitrogen and water vapor. Nine technical papers reporting experimental sorption

Table 3.1 Test parameters for published experimental sorption equilibrium data for R.D. silica gel and water vapor

SOURCE	SILICA GEL	EXPERIMENTAL RANGE P/P_o	T (°C)	# POINTS
Ahlberg	Davison	0 - 1.00	8 - 40	35
Taylor	Davison	0 - 0.73	24 - 232	87
Hubard	Davison	0 - 1.00	4 - 93	84
Mikhail et.al.	Davison GR-03	0 - 1.00	35	48
Jury et.al.	Davison GR-01	0 - 0.67	28 - 93	74
Kester et.al.	Davison GR-05	0 - 0.54	26 - 121	10
Rosas	Davison PA-40	0 - 0.90	25 - 40	19
Pendleton et.al.	Unilever G200	0 - 0.83	25	24
Fraioli	Davison GR-40	0 - 1.00	20	18

equilibrium data for water vapor and regular density silica gel were found (Ahlberg, 1939; Taylor, 1945; Hubard, 1954; Mikhail and Shebl, 1970a; - 1970b; - 1972; Jury and Edwards, 1971; Kester and Lunde, 1973; Lunde and Kester, 1975; Pashley, 1980; Pendleton and Zettlemoyer, 1984; Fraioli, 1984). Representative test parameters for each of the published experiments are listed in Table 3.1.

Ahlberg's data (1939) are among the first experimental sorption equilibrium data for water vapor on commercial silica gel. The accuracy of the reported data may be questionable, probably due to the dynamic character of the measurement techniques. The reported data indicate a maximum water uptake of 0.43 kg-water/kg-dry-silica, whereas all experimental data

obtained on later dates show a maximum water uptake of about 0.36 kg/kg. The only other source which shows an uptake capacity of 0.43 kg/kg is the technical product literature from Davison (1981), a major manufacturer of commercial silica gel. Ahlberg's data are not included in the analysis presented in the next section.

Taylor (1945) determined the static sorption equilibrium isotherm for water vapor on an unspecified type R.D. silica gel. Data were collected in the absence of air, although selected experiments were repeated in the presence of air, and no differences were observed. Kester and Lunde (1973) commented on Taylor's experiments that the reported data may be in error due to experimental inaccuracies for $T \geq 60°C$. The larger error for higher temperatures was expected by Taylor and verified by Kester and Lunde by comparison with new and more accurate data. For the present analysis, Taylor's data are used for $T \leq 60°C$ which gives 19 experimental data points. Taylor states explicitly that his experiments could not detect the presence of hysteresis.

Hubard (1954) presented an update of Taylor's data and added original experimental sorption data at intermediate temperatures. The data are presented in graphical form, and for this analysis 84 data points read from the graphs in Hubard's publication are retrieved. Brandemuehl (1982) analyzed the data from Hubard and correlated the isotherm data

with the assumption that the differential heat of adsorption is independent of the temperature. The resulting isotherm is almost linear, and has been used in the extensive work of Jurinak et. al. (1982a, 1982b, 1984a, 1984b) and Van den Bulck et. al. (1985a, 1985b, 1986, 1987).

Mikhail and Shebl (1970b) studied the adsorption of water vapor on Grade 03 Davison silica gel. Before sorption measurements were taken, the samples were heated at three different temperatures, *viz.*, 120, 140 and 1000 °C. Whereas the 1000 °C sample yielded a type III reversible isotherm, the lower temperature samples showed considerable hysteresis. The maximum water uptake measured at saturation pressure was 0.49 kg/kg, which is substantially higher than the values obtained by the other researchers. Furthermore, the samples retained water after the adsorption-desorption cycle, which indicates that the surface of the gel had changed during the exposure of fresh silica to water vapor. Infrared experiments by Mikhail and Shebl (1970c) confirmed this hypothesis. Their measurements were performed on fresh samples after being thermally treated. Only the first sorption-desorption data are presented and it was not shown whether the hysteresis was reproducible. Rao (1941) showed that the initial adsorption-desorption hysteresis after heat treatment of R.D. silica gel disappears after a few sorption cycles. The data published by Mikhail and Shebl (1970b) are useless for the equilibrium

sorption isotherm of water vapor on silica gel, and are not considered in this study. Jurinak (1982) misinterpreted the data from Mikhail and Shebl (1970b) and concluded that hysteresis may exist for regular density silica gel. This discussion proves otherwise.

Jury and Edwards (1971) published a detailed set of experimental data for the equilibrium isotherm of water vapor on Grade 01 Davison silica gel. These authors showed experimentally the existence of a characteristic curve for this sorption pair. The experimental data were curve-fitted with a two-sited Langmuir expression with good accuracy. The full set of 74 data points is used in this study.

Kester and Lunde (1973) and Lunde and Kester (1975) analyzed Taylor's data and also presented a limited set of original data at intermediate temperatures. Their equilibrium model assumed chemisorption for the first layer and physi-sorption for the subsequent layers. All sorption stages were characterized by an equilibrium constant and an enthalpy of reaction. Temperature effects were included with the *van't Hoff* relationship. The parameters were fitted to the experimental data, and a good overall curve fit was obtained. All the data points of Kester and Lunde are used in this study.

Pashley (1980) investigated experimental data on the formation by adsorption of thin liquid water films on hydroxylated silica and quartz plates at constant temperatures.

Pashley showed that the film thickness is a unique function of the disjoining pressure, which is in turn proportional to the adsorption potential.

Rosas (1980) presented experimental equilibrium sorption data on Davison PA40 silica gel. The data were correlated with the B.E.T isotherm correlation for multilayer adsorption, which is strictly valid only for type II isotherms, and a close agreement was nevertheless reported.

Pendleton and Zettlemoyer (1984) studied the adsorption of benzene, methanol, 2-propanol and water on a microporous silica. The experimental data were curve fitted with the two-sited Dubinin-Astakhov equation (3.6) with close agreement for all adsorptives. Unfortunately, the silica gel in their study had a maximum water uptake of only 0.20 kg/kg, which indicates that the properties of that gel are considerably different than the R.D. silica gel that is commonly used as desiccant. Seven of the reported data points with $P/P_o \leq 0.1$, representing the filling of the ultramicropores, are retrieved for this study.

Fraioli (1984) reported a set of carefully equilibrated, experimental sorption data. No correlation or analysis was presented, and his full data set is included in this study. This author acknowledges the release by Dr. A. Frailoi of his original experimental data.

Table 3.2 Summary of the parameters of the Dubinin-Astakov sorption isotherm equation

SOURCE	#	$E_{o,1}$ J/mole	$E_{o,2}$ J/mole	W_{o1} kg-water/kg-dry-silica	$W_{o,2}$ kg-water/kg-dry-silica	W_o kg-water/kg-dry-silica	RMSx1000
Taylor	18	7310	2980	0.117	0.228	0.335	7.4
Jury et.al.	74	8550	3120	0.107	0.264	0.371	3.5
Kester et.al.	10	9880	3570	0.067	0.288	0.355	1.0
Pendelton et.al.	7	9750		0.085			2.5
Fraoli	18	8670	3060	0.117	0.228	0.351	6.9
Combined	128	8590	3140	0.106	0.242	0.348	7.1
Hubard	84	7840	2600	0.109	0.246	0.355	11
Rosas	19	7050	2140	0.152	0.202	0.354	13
Pendelton et.al.	7	9750		0.085			2.6
Combined	110	7740	2500	0.117	0.237	0.354	11

3.2.2 A Generalized Sorption Isotherm Equation

The experimental data retrieved from the literature are analyzed with the two-sited Dubinin-Astakhov equation (3.6). First, the parameters $W_{o,1}$, $E_{o,1}$, $W_{o,2}$, and $E_{o,2}$ are determined for each individual data set using a least square curve fit of the experimental data within that set. Because the functional form of the isotherm equation has a high degree of flexibility, the curve fit procedure indicates that, for equal RMS value of the error, there exist an interdependence among the 4 curve fit parameters. One of the parameters may vary over a wide range, while the other three parameters are then well determined for a

minimum RMS error. This dependency is illustrated in Fig. 3.3. The characteristic adsorption energies, $E_{o,1}$ and $E_{o,2}$ are plotted as functions of $W_{o,1}$ and $W_{o,2}$, respectively. There exists also a relationship between $W_{o,1}$ and $W_{o,2}$ which is established by the equation for maximum water uptake,

$$W_o = W_{o,1} + W_{o,2} \tag{3.7}$$

The maximum uptake capacity is well determined by the discrete experimental data, and is constant.

The discrete data points in Fig. 3.3 illustrate the curve fit results for each of the alternate data sets. The continuous curves show the relationships between the various parameters for the same accuracy of the curve fit. The results in Fig. 3.3 indicate that there exists little variance between the alternate results for the $E_{o,1}$ vs. $W_{o,1}$ parameters. However, the results for the $E_{o,2}$ vs. $W_{o,2}$ indicate that there exists two groups of data, each characterized by a different interdependency between the parameters. The experimental data from Taylor (1945), Jury and Edwards (1971), Kester and Lunde (1973), and Fraoli (1984) belong to a group which has a consistently higher $E_{o,2}$ than a second group, formed by the data from Hubard (1954) and Rojas (1980). The selected data from Pendleton and Zettlemoyer (1984) give values only for $W_{o,1}$ and $E_{o,1}$, and belong to both groups.

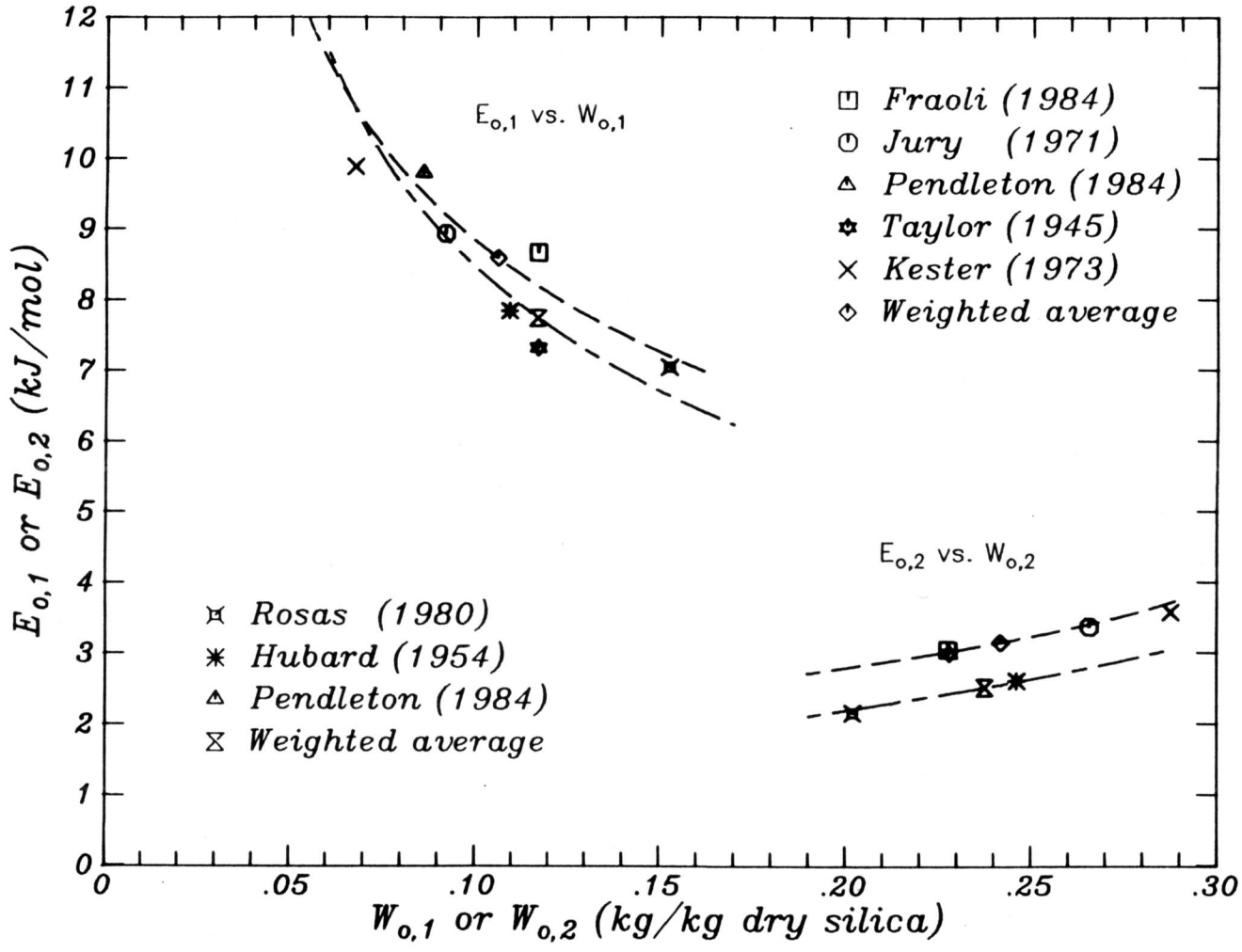

Figure 3.3 Dependency among the parameters of the Dubinin-Astakhov sorption isotherm equation.

In a second step, the experimental data of the alternate sets within the same group are combined and curve fitted with the two-sited Dubinin-Astakhov equation (3.6). Figures 3.4a and 3.4b show the characteristic curves for the adsorption of water vapor on R.D. silica gel in comparison with the experimental data points for both groups, respectively. The parameters which give the best curve fit are listed in Table 3.2. The scatter of the experimental data about the curve fits is about 0.0071 kg/kg for the group with high $E_{o,2}$ and about 0.011 kg/kg for the group with low $E_{o,2}$. The maximum water uptake is, respectively, 0.348 kg/kg and 0.354 kg/kg for both groups. The sorption isotherms for both groups of data are shown in Figures 3.5a and 3.5b in comparison with selected experimental data. Figure 3.6 compares the isotherms with the isotherm correlation developed by Brandemuehl (1982). Although the Brandemuehl isotherm seems to agree with the low $E_{o,2}$ isotherm, it misses the curvatures at the low and high vapor pressures. These curvatures determine the speed with which the transfer zones propagate through a desiccant matrix, and are therefore important for predicting the performance of regenerative dehumidifiers.

Finally, the isotherm expression with the low $E_{o,2}$ is used in a model for analyzing experimental, dynamic sorption data of water vapor on R.D. silica gel, which are presented in the next chapters of this work. There, it is shown that this isotherm

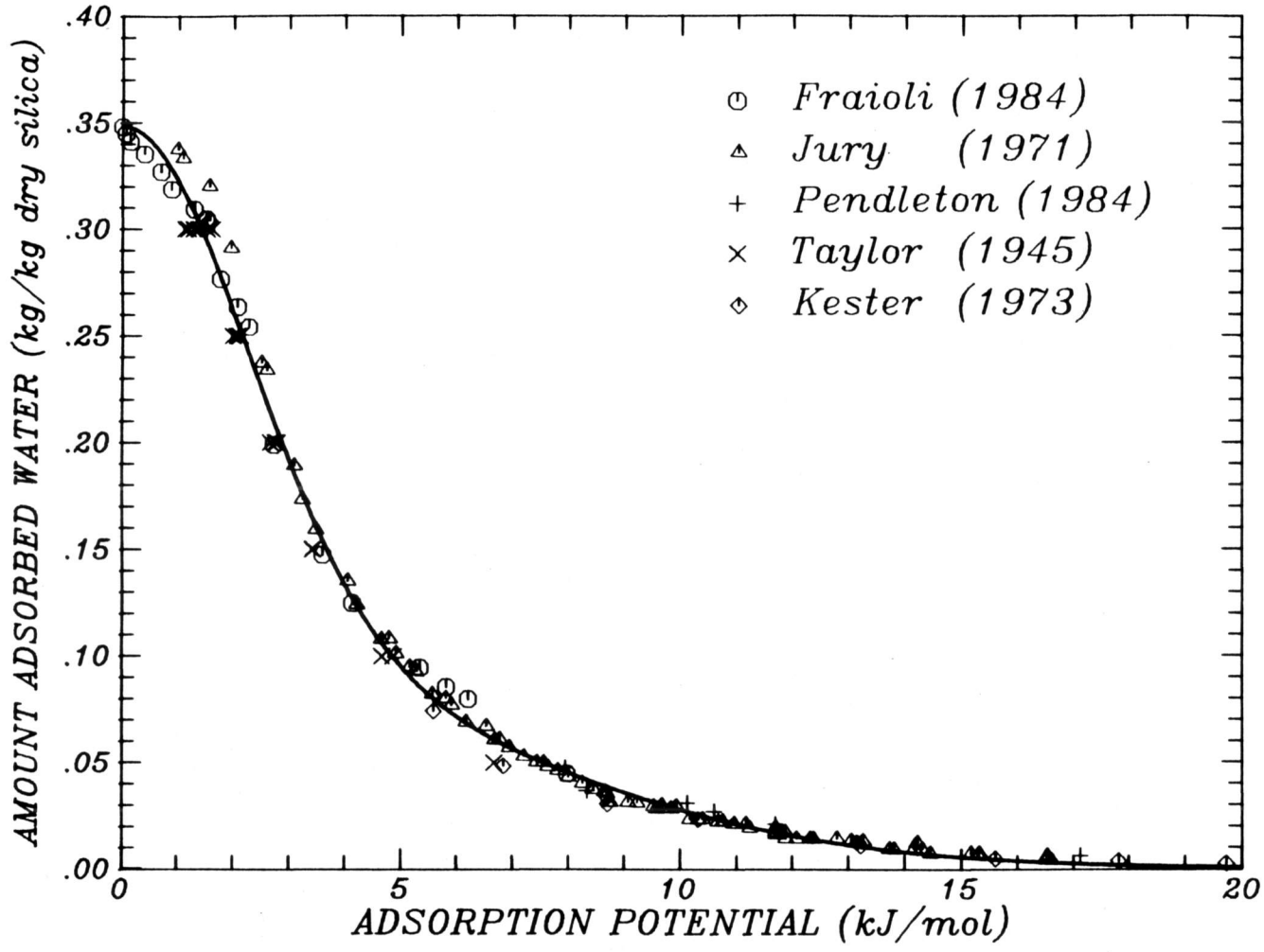

Figure 3.4a Characteristic curve for the adsorption of water vapor on regular density silica gel in comparison with selected experimental data, high $E_{0,2}$.

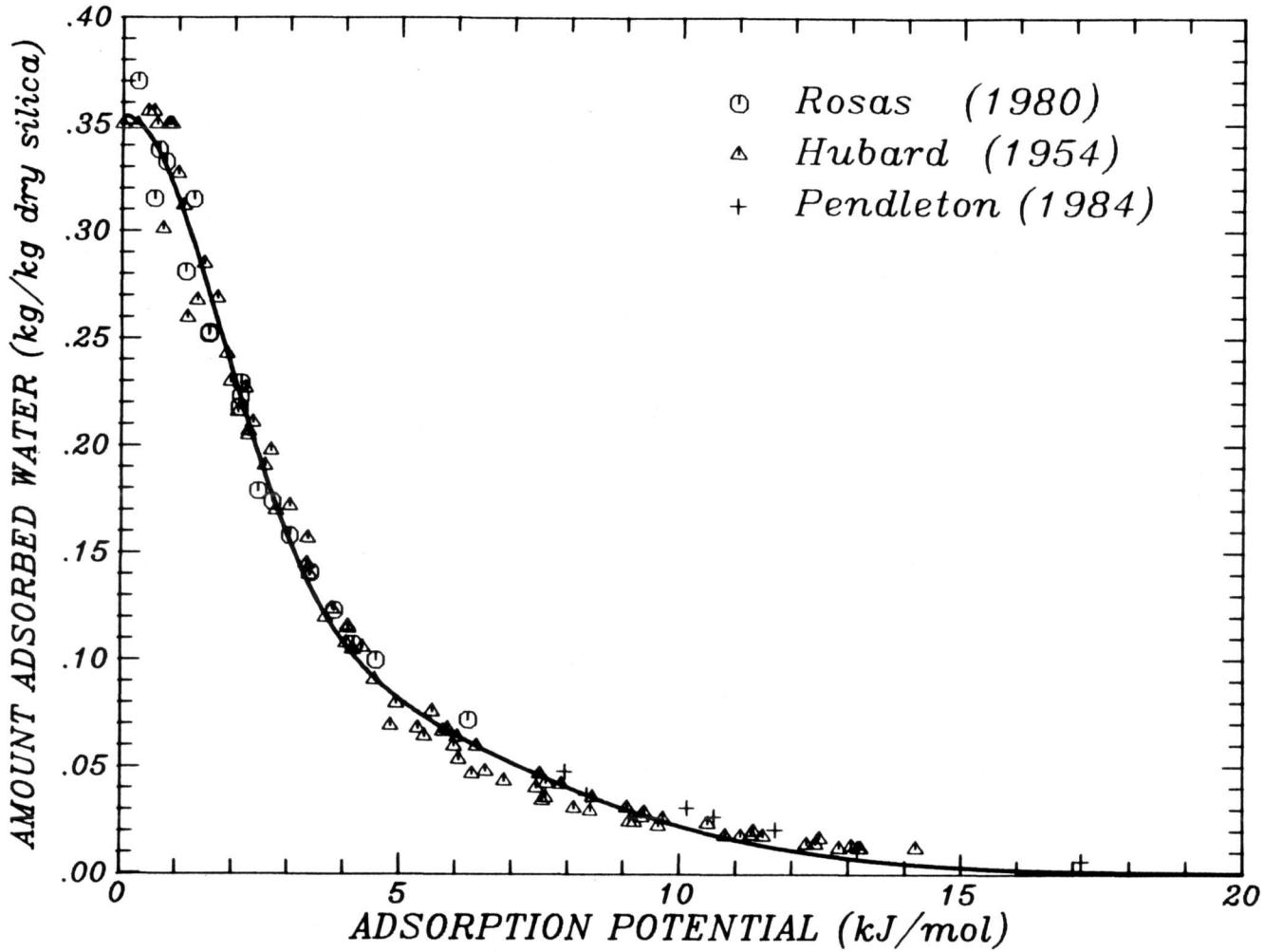

Figure 3.4b Characteristic curve for the adsorption of water vapor on regular density silica gel in comparison with selected experimental data, low $E_{0,2}$.

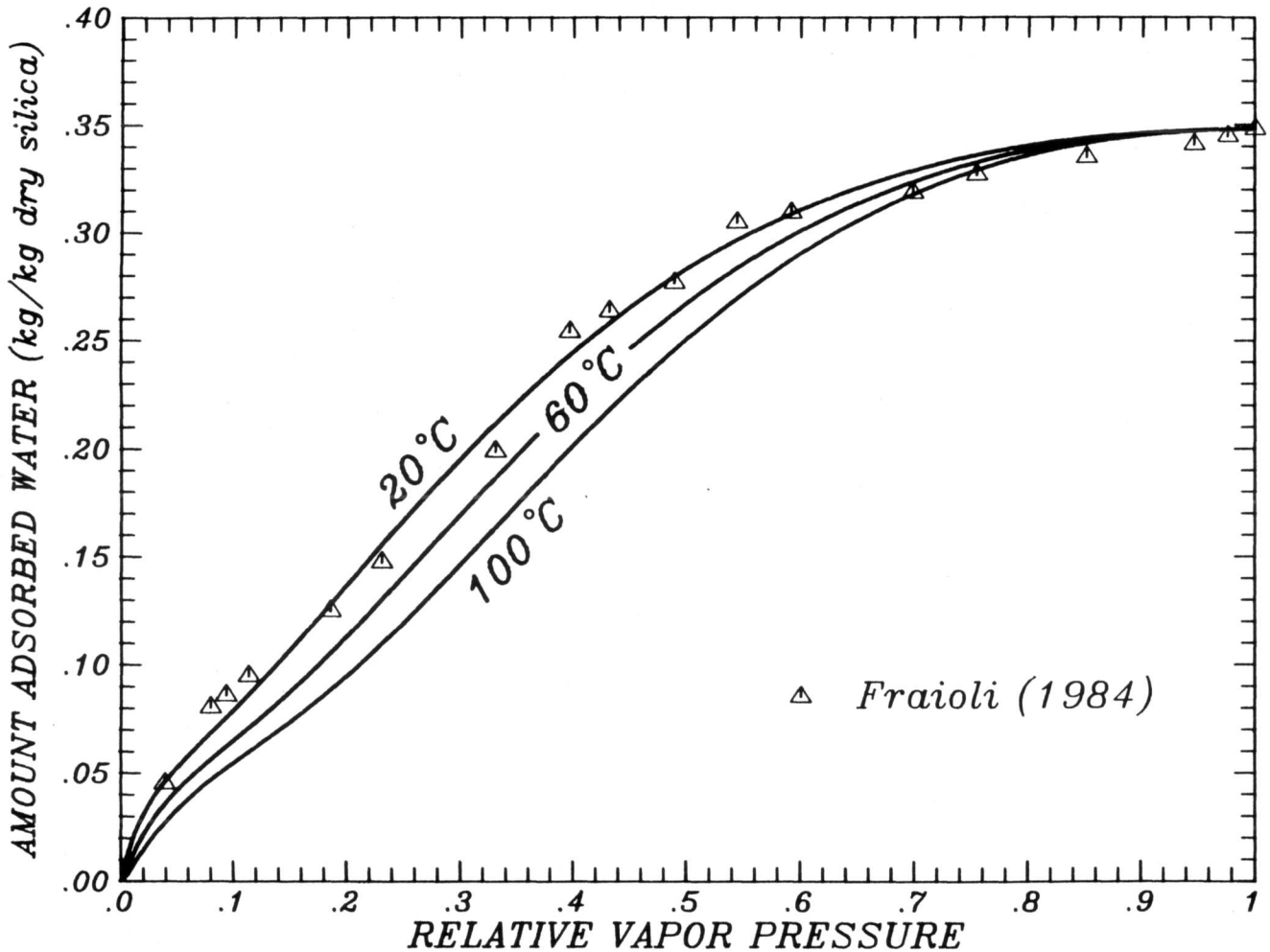

Figure 3.5a Sorption isotherm for the adsorption of water vapor on regular density silica gel in comparison with selected experimental data, high $E_{0,2}$.

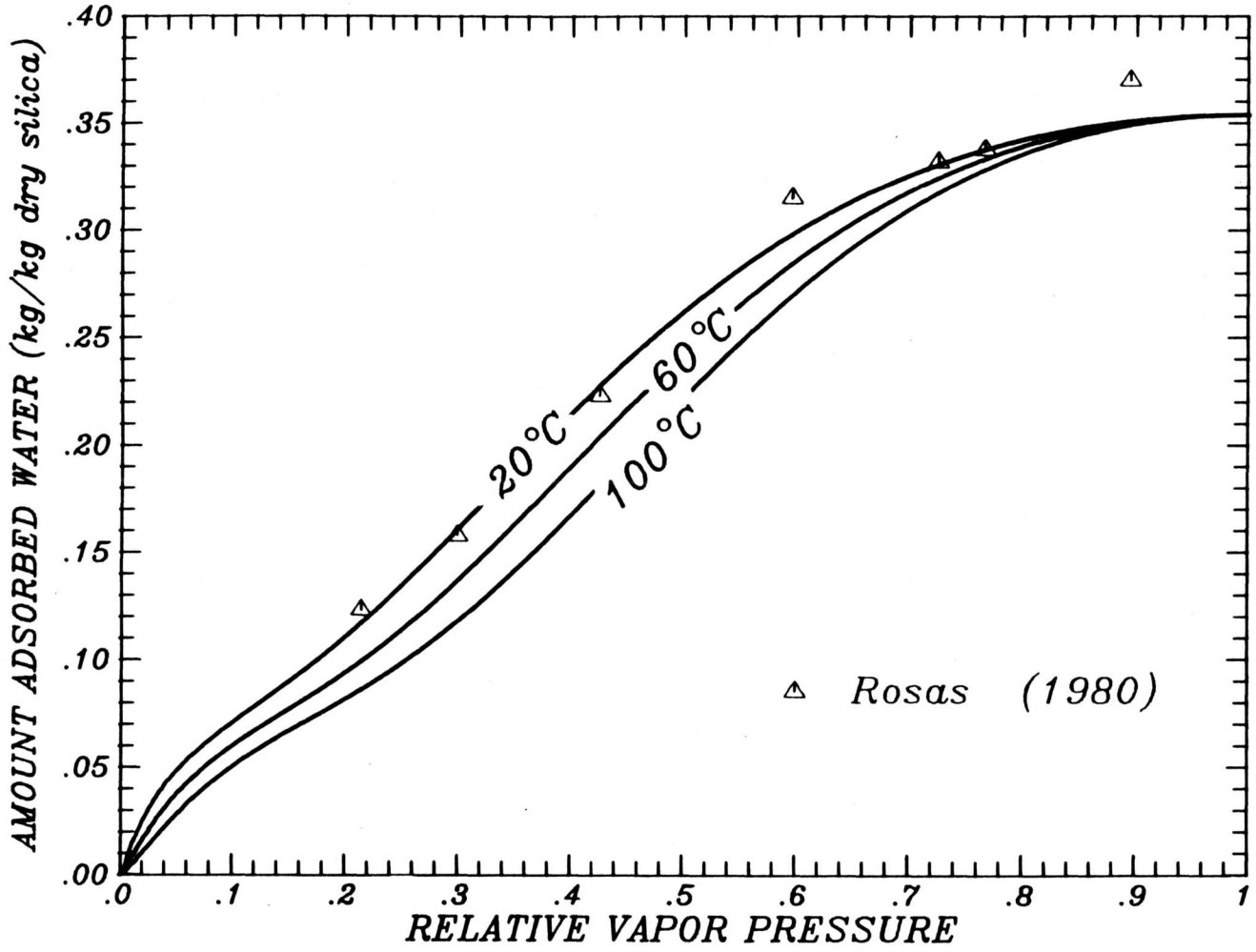

Figure 3.5b Sorption isotherm for the adsorption of water vapor on regular density silica gel in comparison with selected experimental data, low $E_{0,2}$.

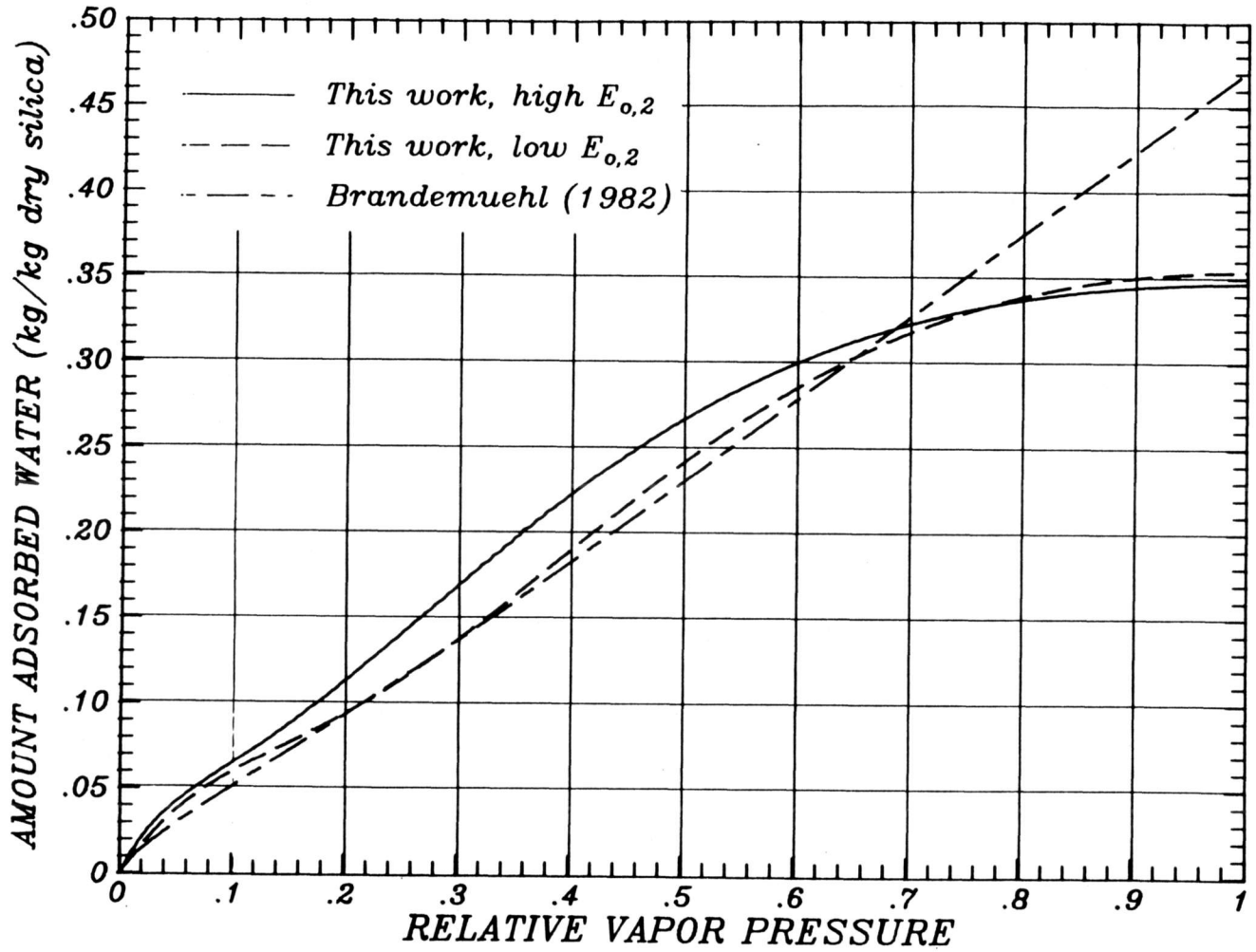

Figure 3.6 Comparison of various isotherm correlations.

gives a close agreement between selected experimental and predicted results, and the accuracy of the established isotherm expression is experimentally verified. The next chapter gives a detailed description of the experimental apparatus used to obtain the experimental data presented in this work.

CONCLUSION

1. The literature review of the sorption of water vapor on regular density silica gel indicates that the uptake is reversible, i.e., there is no hysteresis. This experimental finding is an accordance with established theories for microporous adsorbents, and hysteresis effects should not be present in the microporous desiccants which are the candidate desiccants for use in regenerative dehumidification.

2. The isotherm expression given by Eq. (3.6) with the values listed in Table 3.2 is an accurate correlation of various independent sets of experimental data, and is straightforward to use.

3. The correlation is cast in a functional form that is provided by the physico-chemical theories of adsorption. Other desiccants, such as molecular sieves and aluminum oxide can be correlated using the same functional form. Hence, a generic,

ideal dehumidifier model can be developed which has as input the 4 parameters which appear in the isotherm expression, and which can give a fast prediction of dehumidifier performance for various desiccants.

CHAPTER 4

EXPERIMENTAL APPARATUS AND PROCEDURES

The experiments which are the object of this study relate to the transient exchange of momentum, heat and mass in laminar flow of humid air through parallel plates with desiccant surfaces. Ghezelayagh and Gidaspow (1982), Biswas, Kim and Mills (1984), Clark, Mills and Buchberg (181), Allander (1953) and Pesaran and Zangrando (1985) describe apparatuses and desiccant matrices which facilitate this type of experiments. The experimental procedure involves a common sequence of operations. Air is passed through a desiccant matrix at fixed inlet conditions. Initial conditions for the matrix are established when the desiccant is in equilibrium with the air stream. A step change in the air inlet conditions is then introduced and the air outlet state is recorded with time. This response of the air stream outlet state forms the experimental data that characterize the exchange performance of the test matrix and that are the subject of the discussion presented in the next chapter.

This chapter describes the experimental apparatus which was used for the experiments reported in this work. The test matrix and test section are described separately. The instrumentation for measurement and control of the air state

properties is described and the errors involved with the measurements are discussed. The test procedures are listed in detail.

4.1 Description of Test Loop Configuration

The test loop configuration is that of a single-blow test facility, used for transient heat and mass transfer experiments. The purpose of the test loop is to provide a humid air stream with controlled state properties and mass flow rate, to facilitate the use of this air stream to pass it through a test matrix, and to introduce a step change in the air stream inlet properties. A perspective view of the test loop is shown in Fig. 4.1. The test loop is an assembly of various sections each accomplishing a dedicated task to control or measure a selected state property of the air stream. The major sections which can be identified in Fig. 4.1 are respectively the intake section, the heating and humidification section, the blower, the orifice plate with accompanying duct, the bypass loop, the test section and the exhaust. The test loop is completed with a data acquisition system and a control system. During operation, the test loop is continuously monitored by a facility operator.

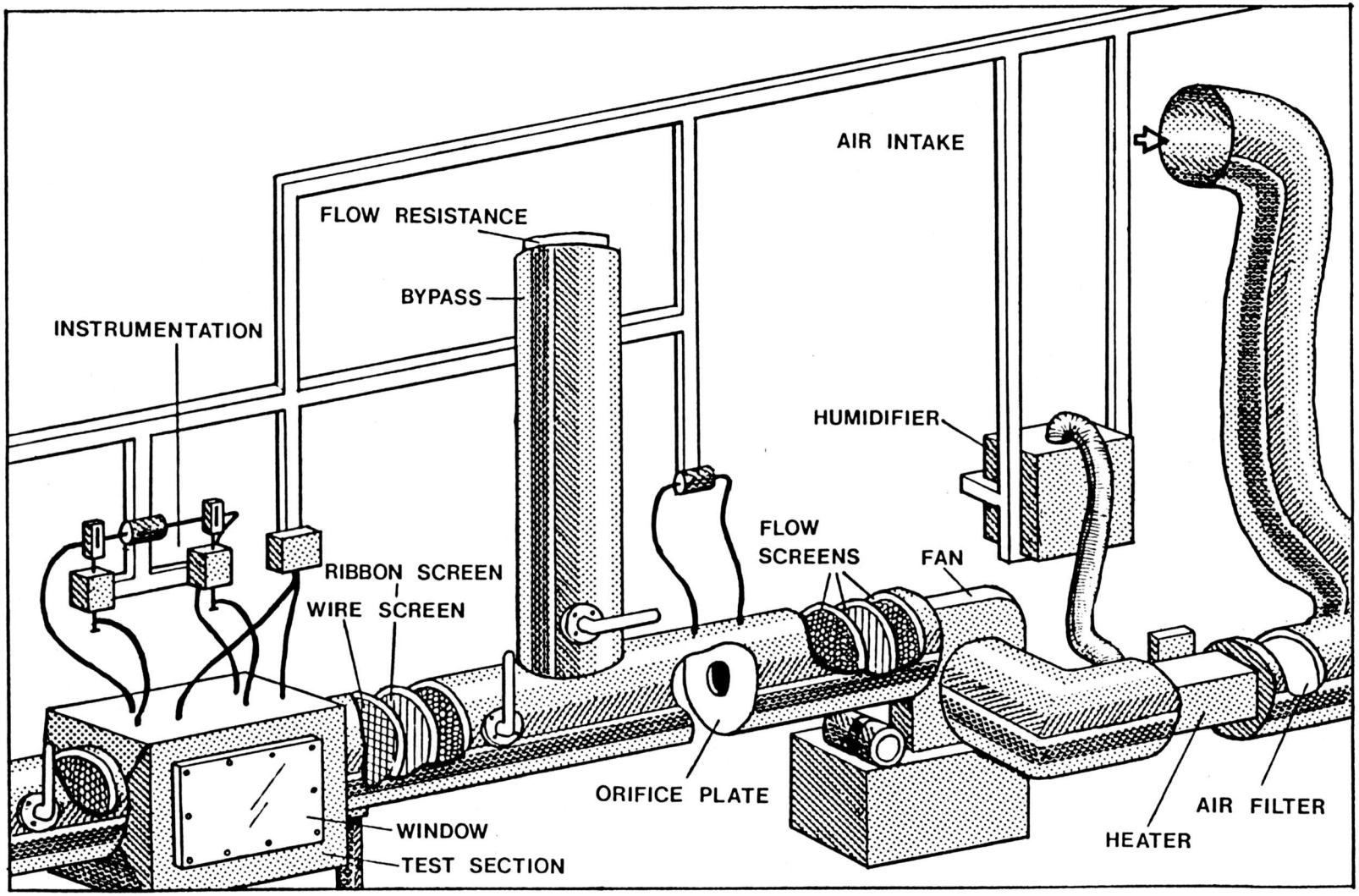

Figure 4.1 Perspective rendering of the experimental test facility.

Indoor air is drawn into the air intake duct mounted 3 m above floor level. The air is passed through a cloth filter to remove most of the dust and all of the larger particles within the air stream. The air then enters the heating section of the test loop at room temperature, typically 20°C. An electric, finned, tubular duct heater is used to heat the air stream. The power supply to the heater is automatically adjusted by the control system to provide a controlled process air temperature at the entrance of the test matrix located further downstream. Leaving the heating section at an elevated temperature, the air enters the humidification section. At this location, the pressure of the air within the duct is below atmospheric pressure and saturated steam is sucked from an atmospheric boiler through a steam injection tube into the duct and mixed with the air stream. Electrical energy is supplied to the boiler heaters and is automatically adjusted by the control system to provide a controlled humidification of the air.

The fan is located downstream of the heater and humidifier. It is a centrifugal blower driven by an electric motor through a belt. A honeycomb screen, a flow screen and a second honeycomb screen are mounted in series in the exhaust of the fan to provide a uniform velocity profile across the duct and minimize the flow swirl. Manual control of the motor speed by the operator produces a defined mass flow rate of the air stream at the exhaust of the fan. To measure the flow rate, an

orifice plate is mounted in a duct with circular cross section downstream of the fan and screens. The pressure drop across the orifice plate is measured through pressure taps mounted on the duct at each side of the orifice plate.

The duct then splits into the bypass and the process loop. Manually operated butterfly valves on each of these two loops direct the air stream into either one of these loops. During bypass operation, the test section inlet valve is closed and the bypass valve is open. The air flows in the bypass duct and is exhausted into the laboratory room. An adjustable flow resistance mounted in the bypass exhaust accommodates equal flow rates in process and bypass for a given blower rotational speed. State properties of the bypass flow, temperature and humidity, are measured by a thermocouple and dewpoint hygrometer mounted in the bypass air stream.

When the bypass valve is closed and the test section inlet and exit valves are open, the process air flows through a honeycomb screen, a ribbon screen and a wire screen designed to straighten the flow, make the velocity profile across the duct uniform and reduce the turbulence level of the air stream. After passing through the flow screens, the air enters the test section. The test matrix is mounted into the test section and seals at the edges force the process air stream to pass through the test matrix. Temperature, humidity and pressure sensors are provided at the entrance and exit faces of the test matrix.

A black painted honeycomb screen is mounted downstream of the matrix and serves as a radiation shield for the temperature sensors. The process air flows through the test section exit valve and is exhausted into the laboratory room. When the test section inlet and exit valves are closed, the matrix is isolated from the room environment and the state properties of the test matrix can thus be preserved.

Temperature, humidity and pressure are measured at various locations throughout the test loop and the sensor outputs are automatically sampled by the data acquisition system. The information is transferred to a separate control system which establishes defined state properties of the air stream in process or bypass. The operator monitors the data acquisition and control systems, and positions the various flow valves within the loop.

The test loop facility is located at the Field Testing Laboratory Building of the Solar Energy Research Institute in Denver, Colorado. The facility was designed and build under supervision of Dr. A.A. Pesaran, and made available for use to the author. The experiments which are reported in this work were done on this test loop which is described in detail in the subsequent sections of this chapter.

4.1.1 The Test Section

The test section of the experimental facility contains the test matrix and the necessary instrumentation for measuring the air state properties at the inlet and outlet of the matrix. This section is designed such that a cubical matrix with standard dimensions fits into the test section with small clearance. In addition, the test section also contains a number of screens which serve to clean up the flow pattern. A cross-sectional view of the test section is shown in Figure 4.2. The test section is a rectangular duct, measuring 0.173 by 0.166 m and is made of 0.85 mm thick galvanized steel plate. The total flow length of the test section is 0.785 m. Square flanges are welded on both sides of the duct over a length of 0.710 m. Two 9.5 mm thick rectangular Lexan plates, measuring 0.212 by 0.710 m, are bolted against each flange. These transparent windows can thus be removed and provide easy access to the inside of the test section for positioning the matrix. They also allow visualization of the internal flow by use of smoke.

Figure 4.3 presents a longitudinal section of the test section illustrating the relative position of the matrix, screens and instrumentation sensors within the test section. When entering the test section, the air flows first through a flow straightening screen. This screen is a standard hexagonal

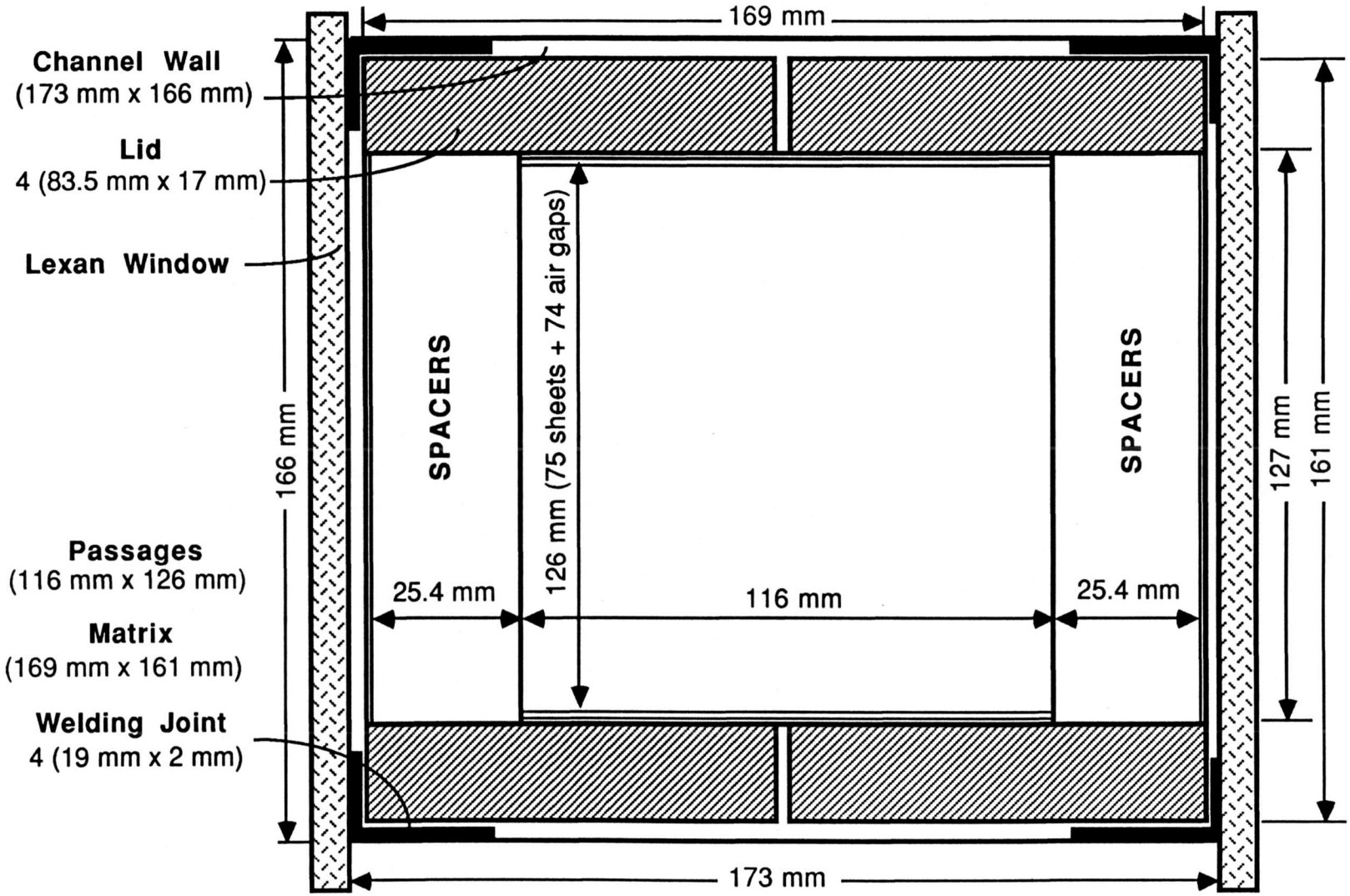

Figure 4.2 Cross section of test matrix positioned within the test section.

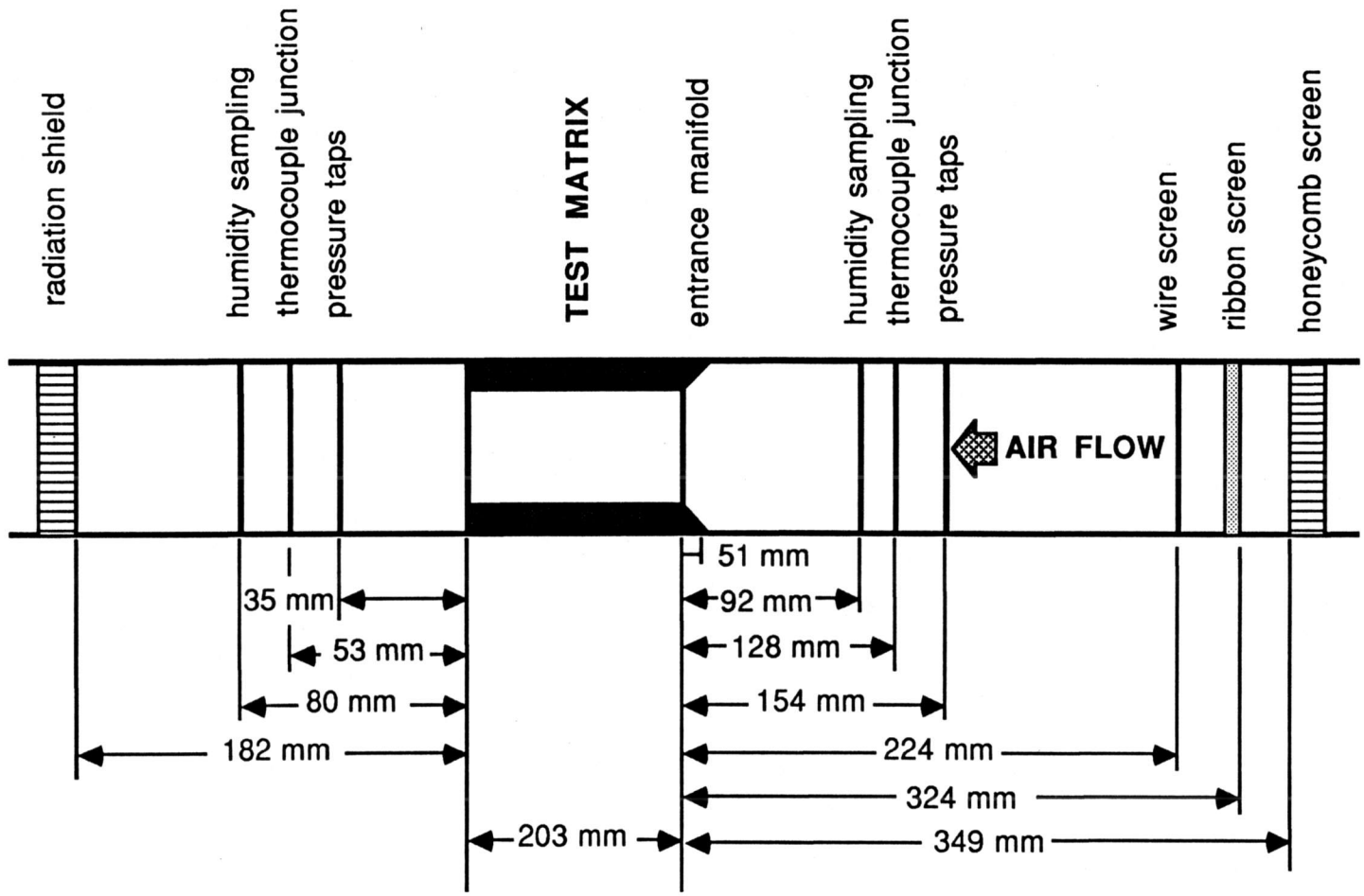

Figure 4.3 Longitudinal view of the test section.

honeycomb screen made of commercial grade aluminum. The flow length is 25.4 mm and the cell size is 6.35 mm. This screen is designed following the manufacturer's recommendations (Hexcel, 1973) to yield a pressure drop of one velocity head at nominal flow conditions. The honeycomb screen removes the flow swirl and the large scale turbulence and vortices. The air then flows through a combination of a ribbon screen and a wire screen. Both screens were designed by Maclaine-cross (1985) following Hart et. al. (1980). The ribbon screen is a 0.6 mm thick aluminum plate with 25 square apertures measuring 25 by 25 mm. The spacing between the centers of the apertures is 32 mm. The wire screen is a standard aluminum insect screen with wire thickness of 0.25 mm and wire spacing of 1.6 mm. A theoretical analysis by Maclaine-cross (1985) shows that the combination of these two screens produce a flow with low level, homogeneous turbulence and uniform velocity profile across the duct.

After passing through the flow screens, the air stream enters the first measuring station at which the inlet air state properties are measured. The station includes a set of 4 thermocouples, 8 air sampling holes for humidity measurements and 4 pressure taps. The configuration of the thermocouples and the temperature measurements are discusses in Sect. 4.2.2. The arrangement of the sampling holes and the humidity measurements are discussed in Sect. 4.2.3. The location of the

pressure taps and pressure measurements are discussed in Sect. 4.2.4.

An entrance manifold is installed in front of the matrix inlet face to provide a smooth transition for the air flow from the larger cross-sectional area of the duct to the smaller frontal area of the test matrix. This manifold is made of polystyrene insulating material covered by an aluminum film. This combination has a small thermal capacitance. Seals between the inner walls of the duct and the outer edges of the frontal side of the matrix force the air to flow through the parallel plates of the test matrix. Because of the uniform velocity profile upstream, the air flow is assumed to be uniformly distributed between the alternate passages of the matrix. The dwell time of the air in the matrix for a typical mass flow rate, 0.02 kg/s, is about 0.1 s. During this time, heat and mass are exchanged between the air stream and the desiccant within the matrix. Care is taken to avoid the presence of any hygroscopic material within the test section except for the desiccant.

Figure 4.3 illustrates the location of the exit measuring station relative to the test matrix. Pressure taps, thermocouple junctions and air sampling tubes are provided to measure the air stream outlet properties. The position of the individual sensors within the plane of measurement is identical to the position of the corresponding sensors in the inlet

measuring station, except for the air sampling points as discussed in following sections. Finally the air passes through a radiation shield before leaving the test section. This shield is a black painted honeycomb with dimensions equal to those of the flow straightener at the inlet of the test section, and provides a radiation barrier between the exit thermocouples and the colder exhaust section.

4.1.2 The Test Matrix

The test matrix is a metal frame consisting of solid lids at the top and bottom which are connected at both sides through three solid rods. This construction forms a sturdy, open structure which can hold a variable number of flexible desiccant sheets in a parallel-plate type configuration. A single desiccant sheet is formed by a thin polyester film coated on both sides with an acrylic adhesive. This tape is the double-coated film, model ARclad 5190, manufactured by Adhesives Research, Inc. The polyester carrier is 25.4 μm thick. The total thickness of the carrier with acrylic adhesive is 76.2 μm. A tight packing of small silica gel particles covers both surfaces of the adhesive-carrier tape. The desiccant sprinkled on the tape is crushed, regular density silica gel, Grade 11, from W.P. Grace and is sieved through a 50 mesh and retained on

an 80 mesh sieve. The screen sizes for these sieves are 177 and 297 μm, respectively. The desiccant sheets measure 169 by 203 mm, and the average thickness of a desiccant sheet is 613 μm. Figure 4.4 shows a cross section of a single desiccant sheet and illustrates the nomenclature.

The individual desiccant sheets are sandwiched between four aluminum shims or spacers, two on each side of the sheets. These shims measure 25.4 by 203 mm and are 794 μm thick. The desiccant sheets with shims are stacked on top of each other and are held in place by the rods of the frame which run through three circular apertures in the shims and sheets. The lids form the top and bottom of the stack. The supporting frame allows to compress the stacking of the sheets. The top and bottom lids are split, enabling the two shim-sides of the sheets to be pulled apart. A number of highly uniform parallel plate passages are thus created. The spacing in between the sheets is determined by the thickness of the shims.

The complete core and surface geometry of the test matrix is given in Table 5.1. The dimensions were either measured with vernier calipers, supplied by the manufacturer, or obtained from the pressure drop analysis discussed in the next chapter. The test matrix was designed and built by Dr. A. Pesaran and Mr. J. Dolan of the Solar Energy Research Institute.

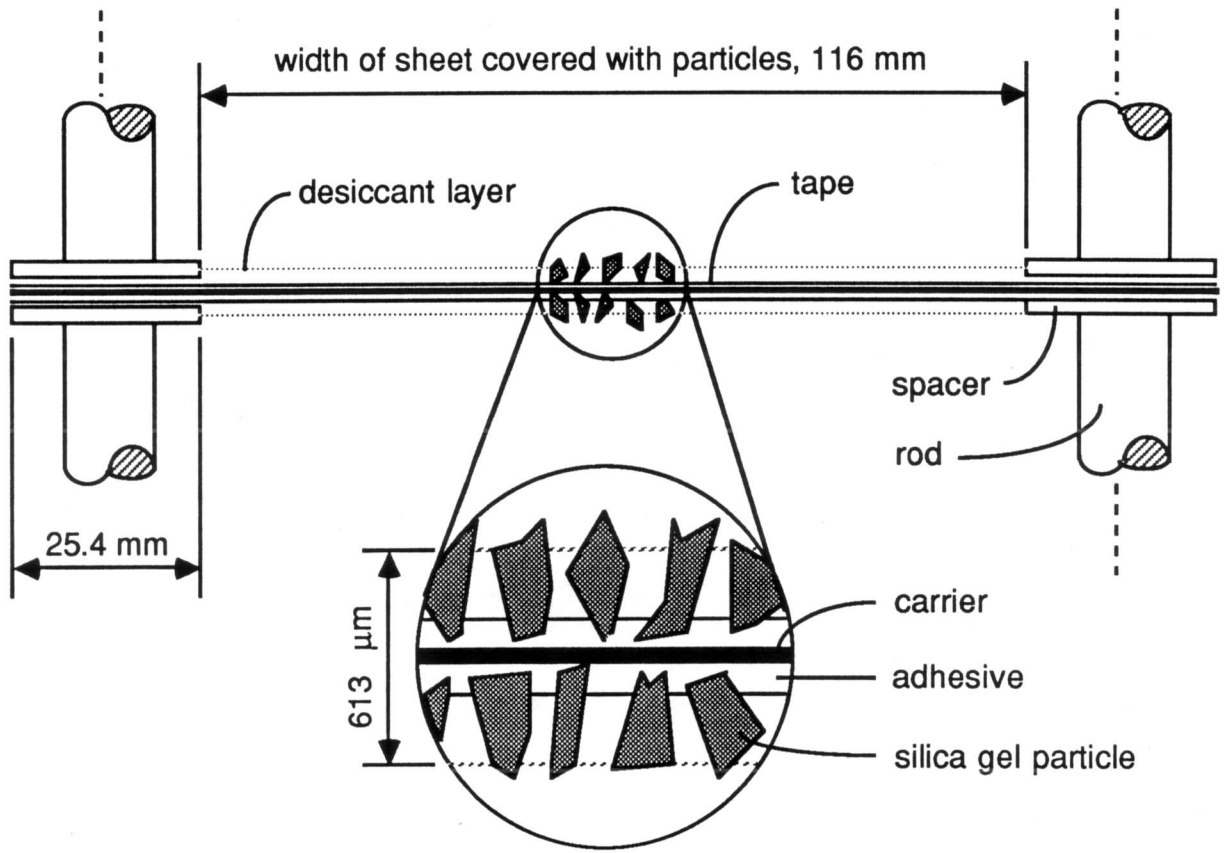

Figure 4.4 Schematic cross section of a desiccant sheet.

4.2 Instrumentation and Measurements

The measurement of the experimental variables during a test is completely automated. During a data acquisition scan, ten independent measurements are taken. These measurements include the reading of the real time from an electronic clock, four temperature measurements, two dewpoint temperature measurements and three pressure measurements. The measurement of the experimental variables, except for the elapsed time, is done by individual, active and passive sensors which produce a voltage output related to the magnitude of the physical property being measured. Thus the data analysis consists of two sequential parts: data collection and data conversion. The following section describes the data acquisition. Data conversion for temperature, humidity and pressure measurements is discussed in subsequent sections.

4.2.1 Description of Data Acquisition System

Figure 4.5 shows the schematic configuration of the data acquisition hardware. The acquisition system consists of a scanner, a digital voltmeter and a computer serving as the system controller. Nine transducers measure the air inlet- and outlet dry bulb- and dewpoint temperatures, the bypass and

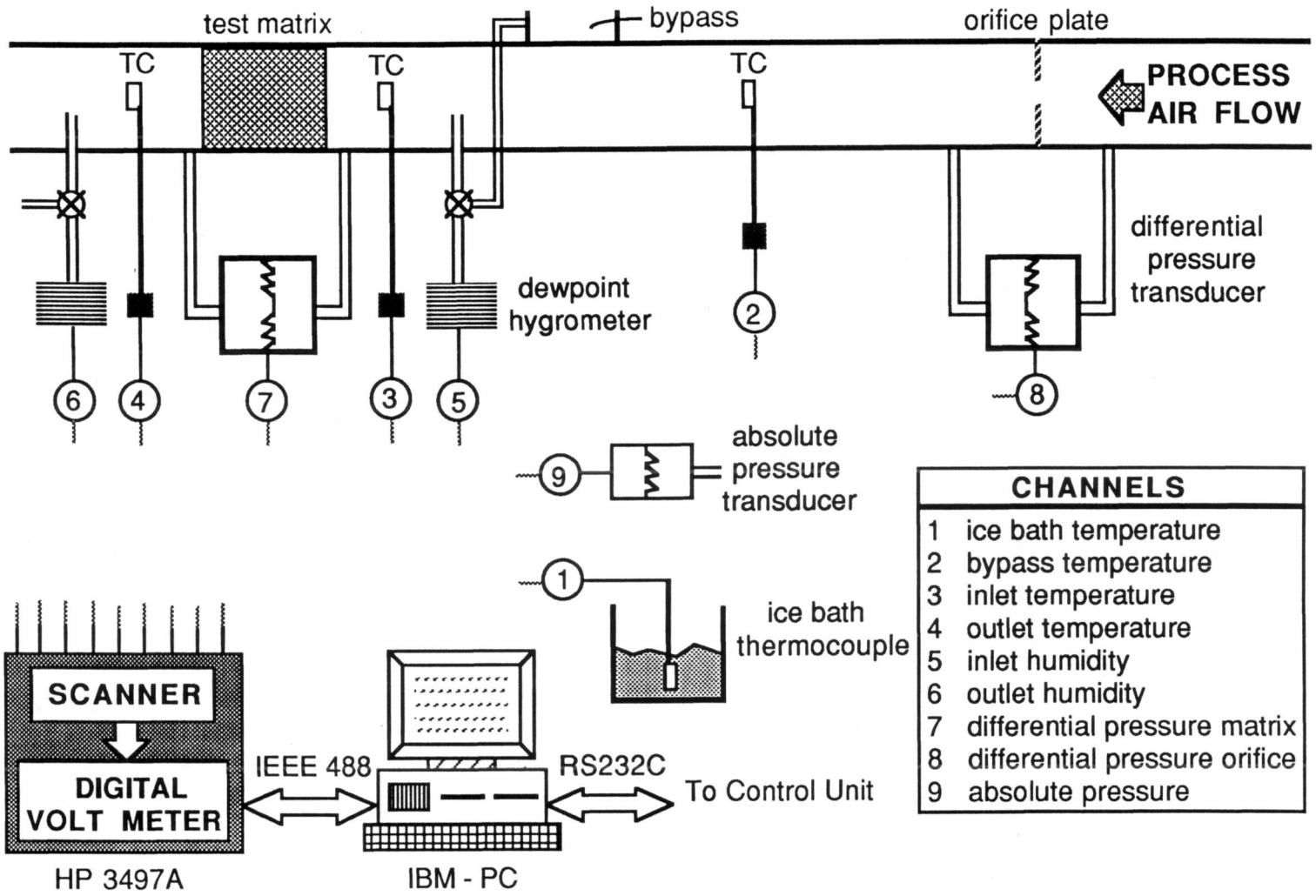

Figure 4.5 Schematic configuration of the data acquisition system

reference temperatures, the pressure drops across the test matrix and orifice plate, and the ambient pressure. The outputs of these transducers are wired to the terminal input connector of an electronic scanner.

The computer is an IBM PC, serial # 058052 55150, equipped with a GPIB-PC board from National Instruments and a multifunction Quadboard from Quadram Corporation. The GPIB-PC board provides the computer with an IEEE-488 Instrumentation Interface which forms the data link between the computer and the digital voltmeter. The multifunction board is equipped with a crystal driven clock/calendar, a RS-232C asynchronous communication port and 256 KB of RAM memory which can be allocated to a virtual disk. This port forms the communication link between the computer and the control system described in section 4.3.

The second hardware unit of the data acquisition system is a Data Acquisition/Control Unit, model 3497A, serial # 2011A00118, from Hewlett Packard. This unit is equipped with a standard IEEE-488 interface bus and device options 001 and 020. Option 020 is a Low Thermal Relay Assembly With Thermocouple Compensation unit. This relay card switches the high, low and guard signals on each of twenty input channels to the mainframe common analog bus by means of reed actuated relays. The thermal offset of each relay is less than 2 μV and the maximum switching rate is 475 per second per relay. The output of the

common signal bus is wired to the input terminals of a $5^1/_2$ Digit Digital Voltmeter installed as Option 001. The resolution of the voltmeter is 1 μV and the uncertainty of the measurement is ± 0.007% of the reading. This voltmeter was calibrated by the manufacturer to be within these specifications.

Channel selection and triggering of the voltmeter is done by the HP3497A on command by the IBM PC at regular time intervals. During each scan, the nine channels are alternately selected and the voltage of the corresponding sensor is measured and stored in the voltmeter's internal memory. At the end of each scan, the measured data are transferred to the computer through the IEEE 488 interface bus. This task is supervised by the data acquisition software executed by the computer. The software is a modular program performing various sequential tasks and was written in Pascal by this author. A complete listing of the program is given by Pesaran, Maclaine-cross and Van den Bulck (1986). Interrupts are generated at a regular time interval, typically 1 s, by a software procedure using the computer's internal clock. The resolution of the interrupt interval is ± 25 ms. On each interrupt, a series of commands are send to the 3497A which in return passes the 9 measured voltages to the PC. These voltages, completed with the reading of the real time clock, form a raw data record which is stacked sequentially in internal memory. This raw

data record is also converted to a physical data record that contains the magnitude of the measured experimental variables expressed in SI units. Selected state variables are displayed on the monitor of the computer to provide the operator with real time measurements of the ongoing experiments. Concurrently, another set of selected measurements are sent to the control unit through the computer's serial port. The control unit controls the process air inlet temperature and humidity about user supplied setpoints.

On command of the operator, the data acquisition software retrieves the accumulated raw data and stores it onto a diskette in ASCII format.

4.2.2 Measurement of Process Air Temperature

The temperature of the air stream is measured by an arrangement of copper/constantan ANSI type T thermocouples. Each thermocouple is made of NN-T-30 duplex insulated thermocouple wire manufactured by Omega Engineering. Nylon insulation is extruded over each metal wire and an overall nylon jacket is applied over the two conductors. The diameter of the copper and constantan wires is 0.254 mm.

Each individual thermocouple junction is configured following a design by I.L. Maclaine-cross (1985). The con-

figuration of the junctions is shown in Fig. 4.6. To balance the conduction heat losses from the junction through both wires, the ratio of the lengths of the copper and constantan wires is the square root of the ratio of the thermal conductivities of both metals. With the small wire diameter, the air flow perpendicular to the bare wire section produces high convective heat transfer coefficients. Before each series of experiments, the bare wire section was cleaned with alcohol to decrease the emissivity and consequently the radiative heat transfer coefficients. The error in temperature due to conduction and radiation heat losses may be calculated using a conventional engineering analysis (Eckert and Drake, 1972). For this particular geometry, a surrounding wall temperature of 20°C, air velocities ranging from 0.5 to 1.8 m/s, and air temperatures ranging from 20 to 80 C, the radiative heat transfer coefficients ranges from 0.23 to 0.53 $W/m^2 \cdot K$ for the bare wire sections and from 15 to 17 $W/m^2 \cdot K$ for the insulated wire sections. The convective heat transfer coefficients range from 200 to 280 $W/m^2 \cdot K$ for the perpendicular bare wires, from 21 to 33 $W/m^2 \cdot K$ for the parallel bare wires and from 207 to 315 $W/m^2 \cdot K$ for the insulated wires. The radiative coefficients are estimated using an emissivity ranging from 0.03 to 0.07 for the copper and constantan. The relative temperature error E,

$$E = \frac{t_a - t_c}{t_a - t_w}, \tag{4.1}$$

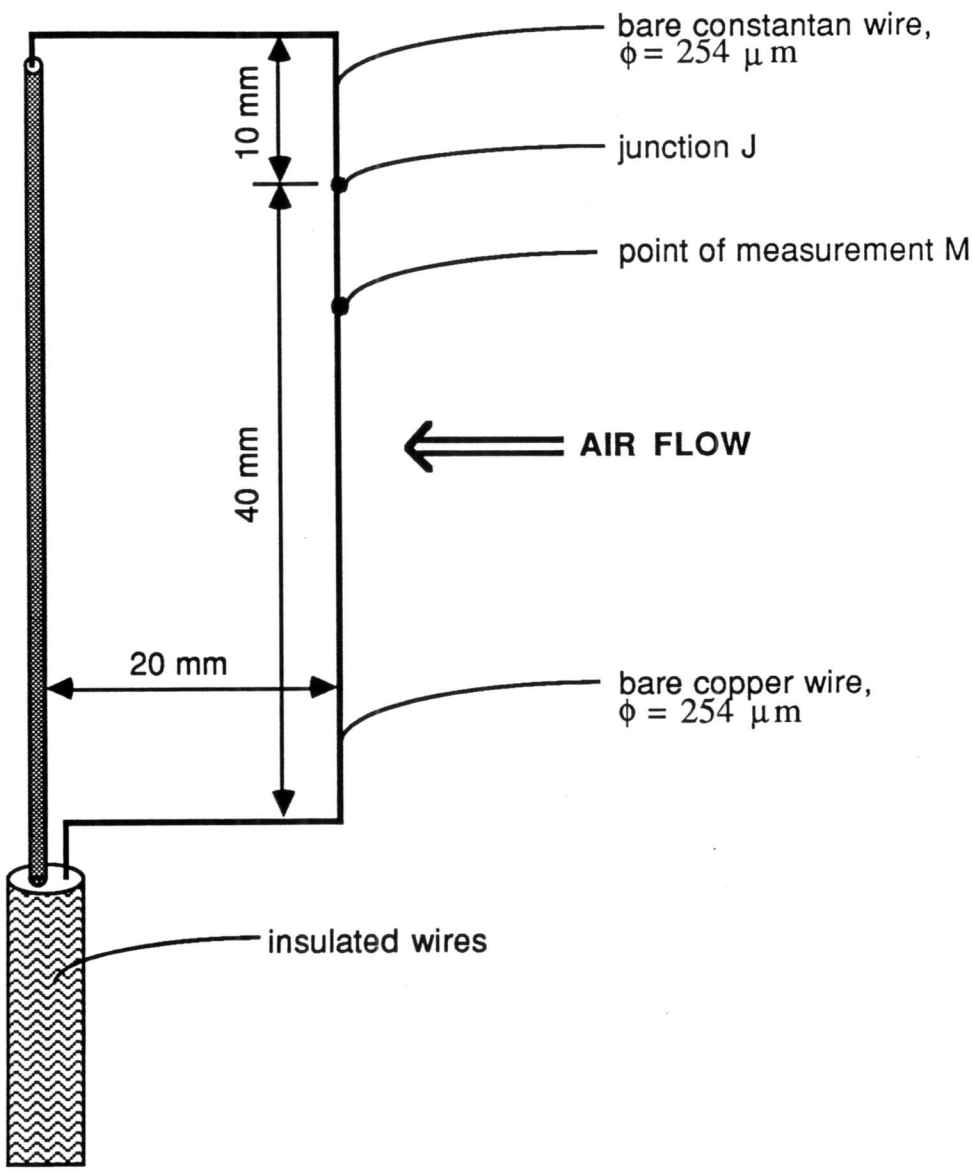

Figure 4.6 Schematic configuration of a thermocouple.

where t_a, t_w and t_c are the temperatures of, respectively, the air, wall and thermocouple junction, ranges from 0.0011 to 0.0033 for combined radiation and conduction, and from 0.0008 to 0.0026 for radiation only. This analysis shows that for the conditions of the experiments reported in this work, the difference between the air temperature and junction temperature is less than 0.2°C. If the air temperature profile is not uniform along the thermocouple wire, the junction temperature will approximate the air temperature at a position away from the junction along the copper wire. For a linear temperature profile and for the conditions of this study, the distance between the junction and the virtual point of measurement ranges from 6.7 to 7.4 mm. This virtual point of temperature measurement is indicated by point M in Fig. 4.6.

The time constant of the thermocouples for transient air temperature measurements may be estimated using a lumped capacitance model. For the thermocouple configuration of Fig. 4.6, the time constant is less than 1 s and thus negligible for this study.

The bypass temperature is measured using a single thermocouple placed in the center of the duct in front of the T connection where the main duct splits into the bypass loop and the process loop. The matrix inlet and outlet thermocouples are measured by four thermocouples arranged geometrically in a Saint Andrew's cross in a plane perpendicular to the air flow.

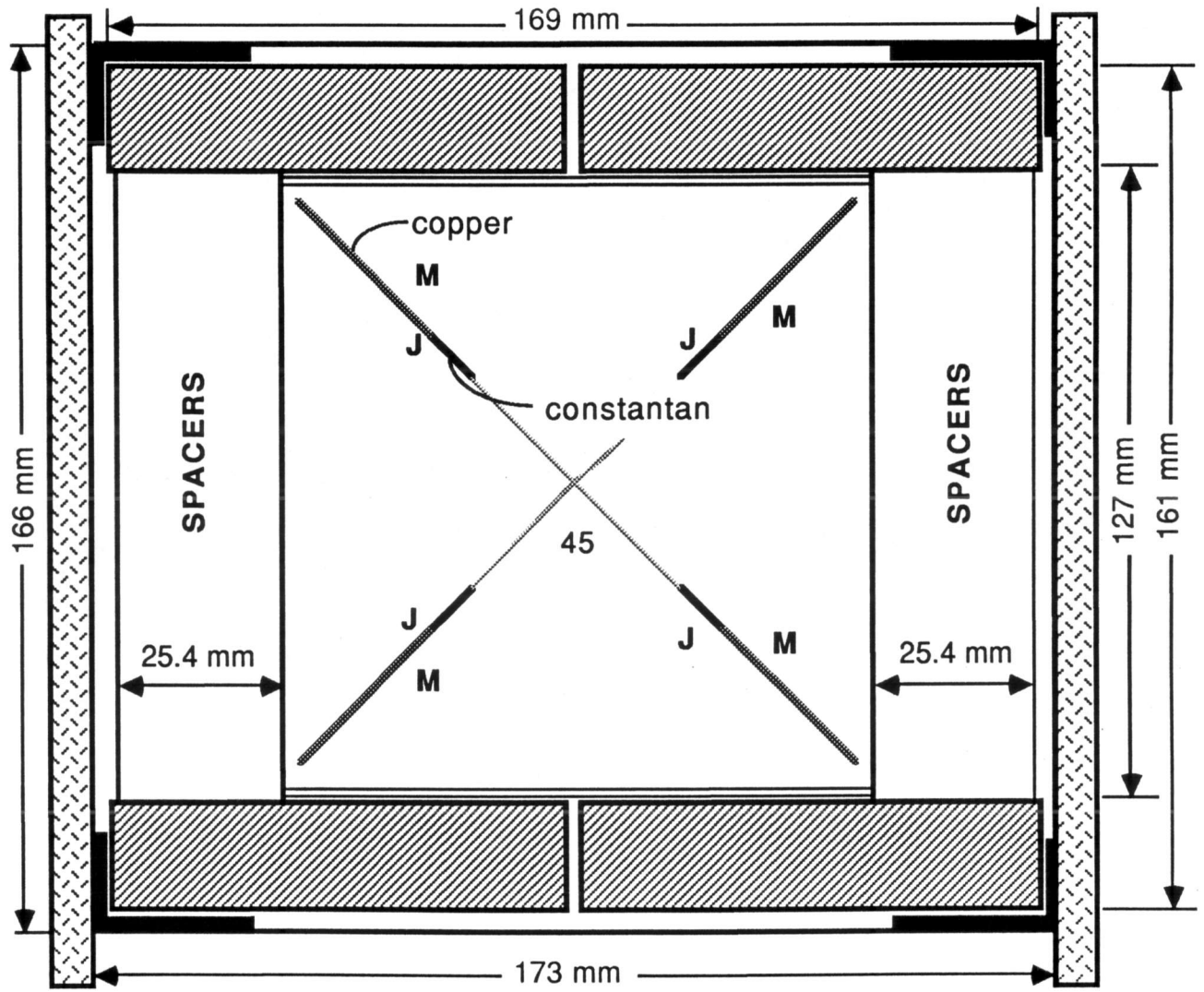

Figure 4.7 Location of thermocouples junctions at inlet and outlet face of the test matrix.

Figure 4.7 shows the position of the junctions in the plane of measurement relative to the window of the test matrix face. The thermocouples are wired in series, with every alternate junction maintained at a common room temperature in an aluminum box. The total *emf* of the thermocouples is divided by four to give an average *emf* corresponding to the temperature difference between the two sets of junctions. The common junction at room temperature is further electrically wired to a reference junction. The sum of the emf produced by the reference junction and the average emf of the air thermocouples corresponds to the true average air temperature. The reference junction is made of the same thermocouple wire as the measuring junctions and inserted into a 0.2 m long glass tube closed at one side and sealed at the side where the thermocouple wire enters the tube. This tube is inserted in an ice-water mixture of deionized water with a melting point of 0 ± 0.01°C. The voltages of the reference junction and the air junctions are measured with the digital voltmeter with an accuracy of ± 1 μV. This voltage measurement in combination with the averaging introduces a negligible error in temperature measurements.

The conversion of the measured *emf* to the actual temperature is done using a polynomial expression for the emf as a function of the temperature as proposed by the NBS monograph 125 (Benedict, 1984). This conversion is exact for the temperature range of 0 to 400°C. Combined, the total error

in local temperature measurement is less than ± 0.2°C for the configuration and conditions reported in this study.

4.2.3 Measurement of Process Air Humidity

The humidity of the process air stream is measured indirectly at three different locations within the experimental facility with two individual dewpoint hygrometers. A small suction pump draws sampling air from within the duct of the experimental loop to the hygrometer sensors through a series of sampling lines. The sampling air flow rate is about 8×10^{-6} m^3/s at standard conditions for each dewpoint hygrometer. The sampling lines inside the air duct are made of 6.35 mm stainless steel. This tubing is connected to the sensor located outside of the duct with 6.35 mm plastic Impolene lines. Connections between the various lines are made with Swagelok connectors and checked for absence of flow leaks. One sampling point is located in the bypass duct behind the bypass valve at the center of the duct. There are also two sets of 8 sampling points within the test section, measuring, respectively, the inlet and outlet humidity of the test matrix. They are located in two planes perpendicular to the air flow before and behind the test matrix. Figure 4.3 indicates the position of the measurement planes relative to the entrance and exit

faces of the test matrix. The sampling points are distributed within each plane such as to obtain an air sample averaged over the flow area of the process air stream. Figure 4.8 indicates the position of the suction holes at the inlet and outlet of the test matrix. The sampling lines of the inlet humidity and the humidity of the air stream in bypass are connected by a two-way valve to the same dewpoint hygrometer. The other hygrometer samples either the outlet humidity or the room air humidity also by means of a two-way valve.

Each dewpoint hygrometer device consists of a dewpoint sensor and an indicator unit. The indicator unit is the System 1100DP Dewpoint Hygrometer with serial number 10616 for the inlet-bypass and 10593 for the outlet-room air humidity. The dewpoint sensors are Type 1111D with serial numbers 10617 and 10594, respectively. The devices are manufactured by General Eastern. The dewpoint sensors are "thermo-electrically cooled, automatically controlled, condensation hygrometers". In these sensors, air is passed over a condensate detection mirror. Water vapor condenses on the mirror surface as it is cooled on the back side with a thermo-electric cooler. The condensate layer thickness is measured by a light-emitting diode and photodetector combination. The photodetector signal serves as the input to a controller, housed in the indicator unit. This controller monitors the cooling rate of the thermo-electric cooler to control the condensate thickness about a standard

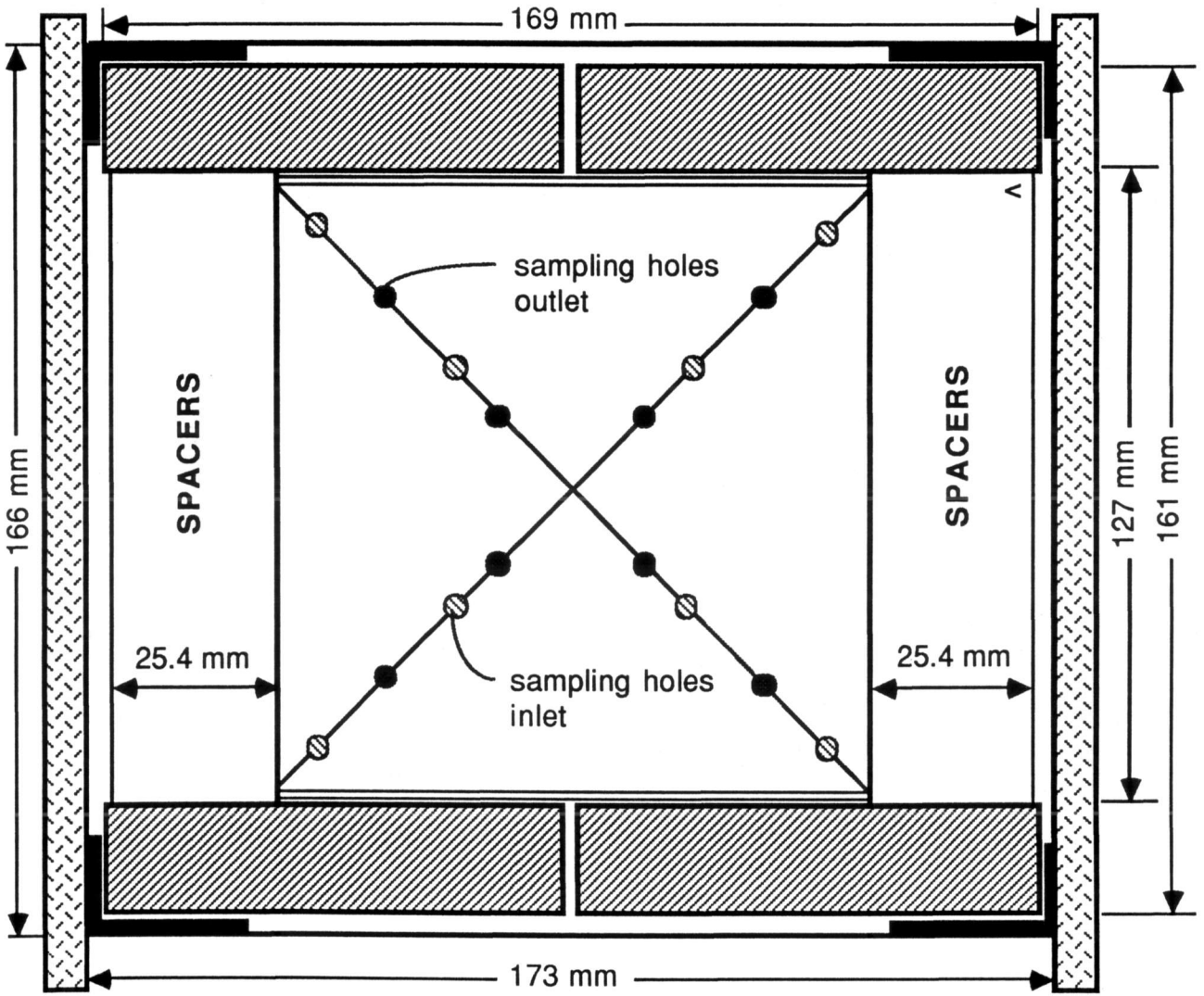

Figure 4.8 Location of humidity sampling points.

thickness. The temperature of the mirror surface is the dewpoint temperature of the air sample and is measured directly by a precision platinum resistance thermometer. The indicator unit contains the necessary power supplies and control circuits for operating the sensor, the network for the platinum resistance thermometer, a digital display, and the output ports for interfacing with external measuring systems.

The conversion of the dewpoint temperature to the absolute humidity is based upon conventional psychrometric correlations. Let t_d be the measured dewpoint temperature and P the absolute pressure of the sampled air. The partial vapor pressure of the water vapor within the air sample, P_v, is obtained from the dewpoint temperature,

$$P_v = 1.004\, P_s(t_d), \tag{4.2}$$

where $P_s(t_d)$ represents the saturation pressure of pure water vapor at the saturation temperature t_d. The functional expression for the saturation pressure as a function of the saturation temperature for pure water vapor is taken from the polynomial correlation recommended by ASHRAE (1980). The numerical factor appearing in Eq. (4.2) is the partial fugacity coefficient of water vapor in humid air at 0.85×10^5 Pa and temperatures ranging from 20 to 80°C. This factor is recommended by ASHRAE to take account of nonideal gas behavior. The

humidity ratio of the sampled air, w_f, is then given by the 'law of partial pressures' for a perfect gas mixture,

$$w_f = 0.62198 \frac{P_v}{(P - P_v)} . \qquad (4.3)$$

The manufacturer's specification lists an accuracy of ± 0.4°C for the absolute dewpoint temperature over the entire operating range with a resolution of 0.1±C. The outlet signal is a voltage ranging between -5 and +5 Vdc for a dewpoint temperature of -50 to +50°C. The output characteristic is 0.1 V/°C and is linear. The maximum rate of response of the hygrometer is 2 °C/s typical in both directions.

Conventional applications of the condensation hygrometer are the measurement of steady state dewpoint temperatures ranging from the ambient temperature to 40°C below the ambient temperature. For the experiments reported in this work, however, the outlet humidity changes with time and the transient behavior of the hygrometers must also be considered. In addition, the time delay between the moment the air stream passes by the sampling point and the moment the measurement is transferred to the data acquisition system needs to be determined.

Steady State Dewpoint Temperature Measurements

It was not possible for the author to calibrate the dewpoint hygrometers for steady state measurements during his stay at SERI because there was no standard calibration equipment for these devices available. However, a few checks with regard to the absolute accuracy of the dewpoint measurement were made and these are discussed below.

Two experiments were performed in which the dewpoint temperature of an ice bath is measured by both hygrometers with a 4 month period in between both experiments. The ice bath is a mixture of demineralized crushed ice and water, with a dewpoint of 0 ± 0.01°C. A sampling air stream flows through a copper coil submerged in the ice bath and the hygrometer sensor in a closed loop set-up as recommended by the manufacturer. After steady state is reached the dewpoint hygrometer output signals are recorded with the data acquisition system for a period of 5 minutes at a rate of 1 reading every 10 seconds. The data are then converted using the manufacturer's conversion formula. The statistical description of the experimental data for both hygrometers and experiments is given in Table 4.1. The standard deviation about the mean value is about 0.03°C and is due to noise on the hygrometer output signal. The readings in Table 4.2 are consistent with the accuracy claim of the hygrometers, ± 0.4 C.

Table 4.1 Statistical description of the hygrometer ice-bath experiments

Exp.	Number of Data Points	Hygrometer Recording, t_d (°C)			
		Inlet		Outlet	
		mean	st. dev.	mean	st. dev.
1	30	-0.25	0.04	0.06	0.02
2	30	-0.32	0.02	0.10	0.03

A further check on the consistency and accuracy of both hygrometers is made using a specific analysis of the experimental data of the dynamic sorption tests which are described in the next chapter. Each adsorption and desorption test includes two phases in which the air stream is passed through the desiccant matrix and during which there exists thermodynamic equilibrium between the air stream and the desiccant. For these phases, the end of the initializing period and the end of the actual sorption experiment, the humidity of the air stream measured at the inlet of the matrix should be equal to the humidity measured at the outlet of the test matrix. Let Δt_d be the difference between the measured inlet and outlet dewpoint temperature,

$$\Delta t_d = t_{d,in} - t_{d,out}. \tag{4.4}$$

Table 4.2 gives the statistical description of Δt_d for all adsorption and desorption experiments and for both equilibrium

Table 4.2 Statistical description of the difference in dewpoint hygrometer readings for equal dewpoint temperatures, based upon 88 experimental data points

Phase	Number of Data Points	Δt_d, Adsorption mean	Adsorption st. dev.	Desorption mean	Desorption st. dev.
Initializing	88	0.09	0.08	0.02	0.06
Sorption Test	88	0.11	0.04	-0.05	0.06

phases. There are 44 dewpoint temperature readings for both phases and hygrometers, ranging from 4 to 30°C. Based on all 88 experimental datapoints, the mean value of Δt_d is 0.04 ± 0.18°C. This comparison of the measurement accuracy of the dewpoint hygrometers substantiates the accuracy claim of the hygrometers. Furthermore, because the hygrometers are identical, it is accepted for the analysis that the absolute uncertainty of the dewpoint temperature measurements is ± 0.4°C, and that the uncertainty of the difference between the measurements of the inlet and outlet hygrometers is ± 0.2°C.

The error in absolute humidity due to errors in the measurement of the dewpoint temperature and ambient pressure can be estimated with a conventional error analysis and is 1.5% for humidity differences and 2.8% for absolute humidity measurements.

Transient Dewpoint Temperature Measurements

The performance of the hygrometers for measuring transient dewpoint temperatures is studied based on the transient response of the hygrometers for a step change in the dewpoint temperature of the sampled air. The response characteristic of each of the hygrometers is obtained from a set of specific experiments in which two air streams are prepared at different dewpoint conditions, and the hygrometer output is recorded for an abrupt switch of the sampling flow between the two air streams. One air stream is conditioned at a dewpoint temperature of 0 ± 0.01°C. A first set of experiments consists of a series of 5 repeated experiments in which the response of the inlet-bypass hygrometer is determined for a 10°C step in dewpoint temperature. The second set has 3 repeated experiments showing the outlet hygrometer response for a 15°C step in dewpoint temperature. Both sets of experiments show complete repeatability of the transient response of the hygrometers.

Figure 4.9 shows the dewpoint temperature response of the hygrometers as a function of time for a step change in the inlet dewpoint temperature. The response curves in Fig. 4.9 are the average of all experiments within each set. An analysis of these experimental results based on the operation principle of the hygrometers described by the manufacturer leads to the following conclusions.

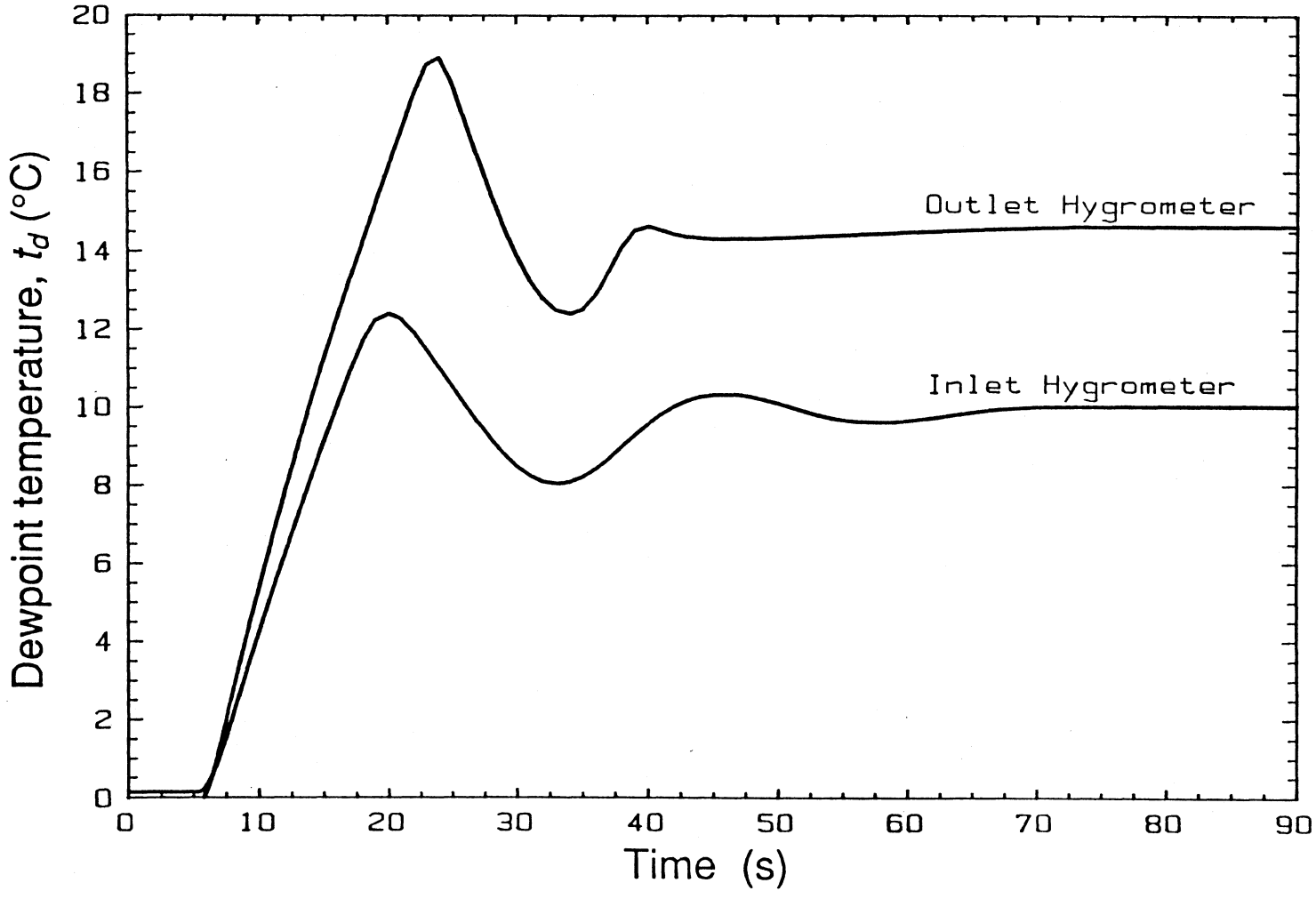

Figure 4.9 Transient response of the dewpoint hygrometers.

1. There are two modes of operation in which the hygrometer responds as a first order system. For a large difference between the mirror temperature and the air dewpoint temperature, the cooling rate supplied the the mirror is either zero, for a negative difference, or maximum for a positive difference. In both cases, the cooling rate is constant and the mirror temperature approaches quasi-exponentially a steady state temperature.

2. There is one mode of operation in which the hygrometer response is of second order. The cooling rate supplied to the mirror is controlled by a feedback system to maintain the mirror temperature about the actual dewpoint temperature. The time constant and pulsation period are strongly dependent on the flow rate of the sampled air stream. If the sample flow rate is too large, the hygrometer is unstable and the mirror temperature oscillates about the dewpoint temperature.

3. All three modes of operation can appear sequentially during a single transient response of the hygrometers.

4. The responses of the hygrometers are nonlinear with respect to time and inlet conditions.

The response curves shown in Fig. 4.9 can be numerically differentiated with respect to time to obtain the transfer function of the hygrometer devices. However these transfer functions are a sequence of several individual transfer functions, one for each operation mode. Because the initial conditions for the second and following modes do not satisfy the general constraints of zero initial conditions, the transfer functions for each of these modes obtained from the differentiation are not true transfer functions. In addition, the concept of transfer functions is not applicable due to the nonlinearity of the hygrometers. An analysis of the transient experiments shows that the response functions can not be

described as the solution of a zero initial value problem associated with either a seventh order linear ordinary differential equation or a general second order nonlinear ordinary differential equation. The transfer functions obtained from the numerical differentiation can not reproduce the input signals by either the inverse of a Fast Fourier Transform or an iterative solution of the inverse convolution integral using a quadrature of a tenth order series of orthogonal Legendre polynomials.

The results of this analysis show that the hygrometers are not suited for the measurement of transient dewpoint temperatures with rates of change larger than about 1°C/s. The response characteristic of the hygrometers does interfere with the measurement and it is not possible to retrieve the input signal from the hygrometer output with standard analytical techniques. In this study, no correction is applied to the measured dewpoint temperature to account for the dynamic behavior of the hygrometers.

Time Delay

The time delay associated with the hygrometer measurements is the time lapse between the moment the sample gas passes by the sample entry point and the moment the hygrometer indicates the dewpoint temperature of the gas sample. Because time delays are relevant for transient

measurements only, the time delay is the sum of the flow time in the sampling tube and the time delay of the hygrometer response. The time delay of the hygrometer response can be obtained from the transient hygrometer experiments discussed in the previous paragraph. These experiments indicate the presence of a small time constant in the response curve which results in an apparent time delay of about 1 ± 0.1 s.

The flow time of the air in the sampling tubes is obtained from a series of specifically designed experiments. In these experiments, a water jet is sprayed on an ensemble of a sample entry point and a dry bulb thermocouple. The thermocouple records the exact moment the water vapor hits the sample entry point. The change of slope of the hygrometer output signal indicates the exact moment the air enters the hygrometer sensor. The analysis of a series of 5 experiments for each hygrometer indicates a flow lag of about 5 ± 0.2 s. The total time delay is therefore estimated at about 6 s.

4.2.4 Measurement of Pressure

Two differential pressure gauges are installed to measure the pressure drop across the orifice plate and the test matrix. An absolute pressure gauge continuously monitors the ambient room pressure. The pressure gauges are electronic units con-

sisting of a pressure transducer and associated measuring circuits. They produce an analog voltage signal as a measure of the differential or absolute pressure.

Differential Pressure Measurements

Two 6.7 mm ID Tygon R-3603 plastic tubes connect the pressure ports of each differential transducer to a set of pressure sampling tubes. Each tubing interconnects four individual pressure tappings with 6.35 mm ID stainless steel or Impolene 44-pp-1/4 plastic tubes by means of Swagelok fittings. The pressure tappings are located on both sides of the orifice plate and test matrix, and aligned on square angles in each plane of measurement. The tappings are circular with a diameter of 1.6 mm and a minimum length of 5 mm. Burrs and wire edges at the inner edge of the point of break-through through the duct walls are eliminated. The axes of the tappings are perpendicular to the axial axis of the flow channel.

The differential pressure transducers are MKS Baratron Pressure Gauges type 221AD-00010A with serial numbers 32866-1A, -1B, and manufactured by MKS Instruments. According to the product data literature, the range of the transducers is 0 to 133.32 Pa and the output signal ranges from 0 to 10 Vdc. The transducer characteristic is linear. A differential pressure across the transducer ports is measured by measuring the

deflection of an Inconel diaphragm. The differential changes of the capacitances of two electrodes placed at different locations on the diaphragm surface provides an indication of the degree of deflection. Solid state electronics are housed in a separate indicator and perform the linear conversion from pressure difference to voltage output. The accuracy of the transducer-indicator as claimed by the manufacturer's specifications is 0.5% of the reading including nonlinearity, nonrepeatability and hysteresis, and an additional 0.2% for temperature effects. The zero offset due to temperature effects gives an absolute error of 0.07 Pa.

To check the accuracy of the differential pressure transducers, both transducers were calibrated with a Dwyer Microtector. This Microtector is a Hook Gage type Manometer, manufactured by Dwyer Instruments, Inc. The height of a water column is measured with a vernier micrometer with an accuracy and repeatability of 2.5 μm or 0.05 Pa. During the calibration experiments, the electronic transducers and Microtector are carefully adjusted to zero offset. A differential pressure is generated using a U-shaped glass tube open on one side and connected to the input ports of both pressure gauges on the other side. The open side is filled with water to an adjustable height to establish a calibration point. For each transducer, the experimental calibration points are analyzed with a linear regression procedure. The results of this analysis are shown

in Tables 4.3 and 4.4. The analysis shows that the voltage output of the transducers can be linearly correlated with the measured pressure difference across the ports of the transducers. The experimental calibration points are randomly distributed about the regression curves for both transducers. The accuracy of the regression is about 0.2% and is due to the effects of nonlinearity and non-repeatability. For the analysis of the experimental data, the maximum bound for the relative error is increased to 0.5% to include the additional effects of hysteresis and temperature.

Table 4.3 Statistical description of the calibration results of the pressure transducer across the test matrix

Number of Calibration Points: 70

Range: 0 - 400 Pa

Calibration Curve

$\Delta P = 132.819\, V$

Accuracy of Calibration

absolute error < 0.26 Pa (σ = 0.11 Pa)

relative error < 0.18 % (σ = 0.08%)*

* for $V > 0.12$ Volt or $\Delta P > 16$ Pa

Accepted accuracy for analysis

relative error < ± 0.5%

Table 4.4 Statistical description of the calibration results of the pressure transducer across the orifice plate

Number of Calibration Points: 113

Range: 0 - 500 Pa

Calibration Curve

$\Delta P = 132.366\, V$

Accuracy of Calibration

absolute error < 0.27 Pa (σ = 0.12 Pa)

relative error < 0.23% (σ = 0.10%) *

* for V > 0.10 Volt or ΔP > 13 Pa

Accepted accuracy for analysis

relative error < ± 0.5%

Absolute Pressure Measurements

The absolute pressure is measured by an MKS Baratron Pressure Gauge, type 220A, manufactured by MKS Instruments, Inc. This pressure gauge is a self contained unit with the transducer and associated solid state circuits mounted in a single casing. According to the manufacturer's specifications, the range of the transducer is 0 to 13.32×10^5 Pa and the output signal ranges between 0 and 10 Vdc. The transducer characteristic is linear. The absolute pressure is measured against a 'zero' reference pressure by measuring the deflection of an Inconel diaphragm by means of two capacity type electrodes.

The product data literature gives a maximum bound for the relative error of 0.15% for nonlinearity, non-repeatability and hysteresis, and 0.2% for temperature effects.

The accuracy of the absolute pressure gauge is checked against the readings of a Fortin type mercurial barometer, model 469 NOVA Economy, manufactured by Princo Instruments, Inc. This barometer is mounted in the laboratory room and senses the same ambient pressure as the pressure transducer. The accuracy of the barometer reading is 13 Pa according to the specifications. The final barometer readings used in the calibration analysis are the average of three readings and are corrected for temperature and gravity effects. The transducer readings are the average of 300 readings for 14 calibration points, and 3600 readings for 39 calibration points at a rate of 1 voltage reading per second. The range of the experimental calibration points is between 0.81 and 0.835×10^5 Pa. The experimental results are analyzed with a linear regression procedure and the results are given in Table 4.5. The analysis shows that the ambient pressure can be correlated as a linear function of the transducer voltage output with a non-zero offset. There is a random distribution of the experimental points about the regression curve. The accuracy of the regression is 0.68 % and includes deviations due to hysteresis, nonlinearity, non-repeatability, and temperature effects. For the analysis of the experimental data reported in the rest of

Table 4.5 Statistical description of the calibration results of the absolute pressure transducer

Number of Calibration Points: 53

Range: 0.81 to 0.835×10^5 Pa

Calibration Curve

$$P_a = 133322\,V + 1409.$$

Accuracy of Calibration

absolute error < 560 Pa (σ = 242 Pa)

relative error < 0.68 % (σ = 0.30%)

Accepted accuracy for analysis

relative error < ± 0.7%

this work, an uncertainty in the measurement of the absolute pressure of 0.7% is accepted.

4.2.5 Measurement of Process Air Mass Flow Rate

The measurement of the air flow rate is done by means of an orifice plate inserted in a circular cross-section conduit. This measurement follows the standard ISO 5167, "Measurement of fluid flow by means of orifice plates, nozzles and venturi tubes inserted in circular cross-section conduits running full," (1980). The conduit is a standard 20 gauge circular

duct with internal diameter of 0.152 m and is made of galvanized iron. The duct runs between the blower and the bypass T section. The length of the duct upstream of the orifice plate is 1.84 m and downstream is 1.12 m. The downstream section is about 7.4 times the diameter of the duct thereby exceeding the "zero additional uncertainty" value of 5 as recommended by the ISO standard. The upstream section, however, is about 12 times the diameter which is in between the minimum required straight length and the recommended value for zero additional uncertainty. Following the ISO standard, a ± 0.5% additional uncertainty should be added to the flow coefficient to account for the effect of this installation condition.

To reduce the effect of the blower impellers, three flow straighteners are mounted in the outlet of the blower. A 1.5 mm perforated steel plate with circular holes of 4.8 mm spaced 6.4 mm center-to-center is located between two aluminum honeycomb screens each with 25.4 mm thickness and 6.4 mm cell size. The spacing between the two screens is about 50 mm. The pressure loss across these three screens is estimated at about 3.6 times the velocity head. It is assumed that these screens reduce the swirl flow angle and make the velocity profile at the exit of the screens sufficiently uniform to comply with the ISO standard. It is further assumed that the circularity of the pipe is within +/- 0.3%, that the orifice plate is mounted

perpendicular to the center line of the pipe, and that the orifice plate is centered in the pipe. These assumptions bring the installation of the orifice plate within the specifications required by the ISO standard. It is also assumed that the geometries of the pressure tappings conform with those of the standard. The pressure tappings are cylindrical with a diameter of 1.6 mm and a length to diameter ratio of larger than 8. There are four upstream and four downstream pressure tappings positioned at right angles on the duct circumference. The spacing of the upstream and downstream pressure tappings is equal to, respectively, 1 and 1/2 times the duct diameter within the limits allowed by the standard.

According to the ISO standard, the mass flow rate through the orifice plate is given as a corrected form of Bernouilli's equation,

$$\dot{m}_f = C\ E\ \varepsilon\ (\pi/4)\ \beta^2\ D^2\ \sqrt{(2\rho\Delta P)}, \tag{4.5}$$

where ρ is the upstream density, ΔP is the measured pressure drop across the orifice plate, D is the duct diameter and β is the orifice to duct diameter ratio. E is the theoretical velocity of approach factor, defined as

$$E = \sqrt{(1-\beta^4)}. \tag{4.6}$$

C is the discharge coefficient. For orifice plates with D and $D/2$ pressure tappings, C is given by the empirical Stolz equation (ISO 5167, 1980),

$$C = 0.5959 + 0.0312\beta^{2.1} - 0.1840\beta^{8} - 0.0337(0.47)\beta^{3}. + 0.0029\beta^{2.5}(10^{6}/Re_{D})^{0.75} + 0.039\beta^{4}/(1-\beta^{4}). \quad (4.7)$$

Re_D is the Reynolds number based upon the duct diameter and the upstream air properties. This correlation has an estimated uncertainty of 1.1% for the installation conditions of the experimental facility. ε is the expansion factor. For air flow through an orifice plate, ε is given by the empirical formula:

$$\varepsilon = 1 - (0.41 + 0.35\beta^{4})\frac{\Delta P}{1.4P}. \quad (4.8)$$

This formula has a claimed accuracy of about 0.01% for the conditions of the experiments performed for this work. Inserting Eqs. (4.6-4.8) into (4.5) gives an implicit relationship between the process air mass flow rate and the pressure drop across the orifice plate with the upstream air state properties as parameters. This resulting equation can be solved iteratively by Newton's method.

The uncertainty of the computed mass flow rate results from the uncertainty of the measurements, the random fluctuations of the measured variables about their mean values due

to the blower performance, and the uncertainty of the flow coefficient correlations. An analytical method for computing the error in flow rate measurements is published in the standard ISO 5168, "Measurement of fluid flow. Estimation of uncertainty of a flow rate measurement," (1978). Applying this standard to the conditions of this experimental work yields a total uncertainty for the mass flow rate computation of about 1.5% with a random component of about 0.7%.

The discussion of the pressure drop experiments presented in the following chapter shows that a small mass flow leak developed between the orifice plate and the test matrix during the course of the experimental work. This leak requires that an additional correction should be applied to Eq. (4.5). The corrected mass flow rate equation is

$$\dot{m}_f = \dot{m}_{orifice} - 1.636\text{x}10^{-5}\sqrt{(2\rho\Delta P)}, \qquad (4.9)$$

where ρ is the density at the inlet face of the test matrix and ΔP is the pressure drop across the matrix. This correction adds a 1% uncertainty to the computation of the mass flow rate, increasing it to ± 2.5%.

To check the accuracy of the mass flow rate measurement and computation, two specific pressure drop experiments were performed. These tests involved the pressure drop measurement across the test matrix as a function of the process air mass flow rate through the matrix at fixed air state properties.

Both experiments used the same matrix. However, they employed two orifice plates with orifice diameter ratios β of 0.2 and 0.3. Using cubic spline interpolation, the mass flow rates for both experiments can be computed from the experimental data using Eqs. (4.5-4.9) for a common pressure drop across the test matrix. Table 4.6 shows the experimental results of the two pressure drop tests. The computed mass flow rates based on the experimental measurements for a common pressure drop differ an average of 0.3%. The data scatter is well within the error limits as predicted by the error analysis. Table 4.7 substantiates the analysis presented in this section and also demonstrates the accuracy of the procedure which converts the experimental data into the mass flow rate.

Table 4.6 Experimental mass flow rates for different orifice plates as a function of the pressure drop across the matrix

PRESSURE DROP (Pa)	MASS FLOW RATE (kg/s)		DIFFERENCE (%)
	β		
	0.3	0.2	
28.7	0.00579	0.00579	-0.019
39.0	0.00782	0.00775	0.888
49.0	0.00973	0.00967	0.649
59.7	0.01170	0.01170	-0.011
70.7	0.01369	0.01370	-0.039
82.4	0.01572	0.01571	0.026
93.7	0.01766	0.01761	0.265
105.6	0.01963	0.01960	0.167
118.0	0.02166	0.02154	0.582
		average difference:	0.28%

4.3 Instrumentation and Controls

In the original experimental facility, control of the process air temperature and humidity was dedicated to separate conventional, industrial controllers (Pesaran, 1985). However, these controllers were not able to meet the requirements for the control of these variables with respect to accuracy and stability about the setpoint. Part of the problems associated with the controllers could be contributed to the small capacity of the experimental facility. This is further discussed in Sections 4.3.2 and 4.3.3. Because of these control problems, more advanced control was required and the experimental facility was modified by the author. An integrated automatic control system was designed and built to control both process air temperature and humidity. A manual control system was installed for control of the process air mass flow rate.

4.3.1 Description of Control System

In the modified experimental facility, a microcomputer is assigned complete automatic control of both process air temperature and humidity. The microcomputer is a HP Series 9800 System 45 Desktop Computer, model 9845A, serial number 1742A01458, manufactured by Hewlett Packard. This control

computer has 64 kB of RAM memory and is equipped with a RS-232C serial I/O interface, model HP 98036A, and an IEEE standard 488-1975 Instrumentation Interface bus, model HP 98034A. In addition to this desktop computer, the hardware of the control system further includes a Data Acquisition/Control Unit, model HP 3497A, serial number 2011A04915, manufactured by Hewlett Packard. This unit is equipped with a dual output 0 - 20 mA current digital-to-analog converter, model HP 44430A. The resolution of these programmable current sources is 5 μA which is also their accuracy.

Figure 4.10 illustrates the hardware configuration of the control system. Data communication between the control computer and the data acquisition computer is established through the serial interface at a baud rate of 2400. Each second the control computer receives a 33 ASCII character data string from the data acquisition computer. This data string contains the setpoints for process air temperature and humidity, and the real time values of measured process air inlet and outlet temperature and humidity, bypass temperature, and process air mass flow rate. The data string ends with a synchronization character. The control computer is linked with the control unit through the IEEE 488 interface. Every 5 seconds, two 4 digit integer numbers are sent to the control unit which in turn sets the current output of each of the D/A converters in proportion to the magnitude of the numbers. The

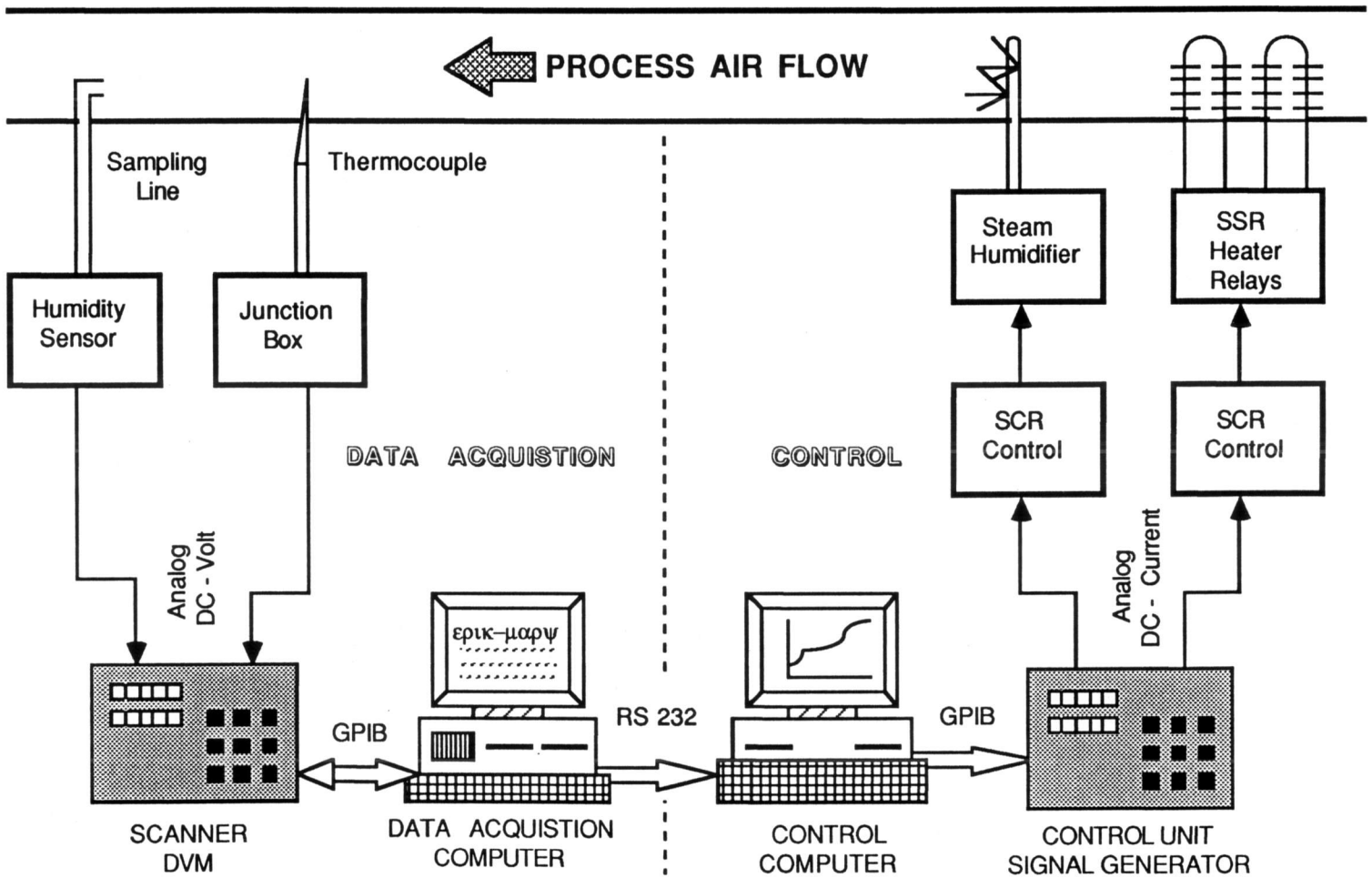

Figure 4.10 Schematic configuration of the control system and instrumentation.

analog DC current outputs of the converters are wired to the terminal input ports of the individual controllers for temperature and humidity.

The software for the control system was written in BASIC by this author. In sequential order, the software receives and decodes the data string from the data acquisition system, computes the settings for the controller signals for process temperature and humidity, and sends these settings to the control unit. A detailed description of the control software algorithms for temperature and humidity is provided in section 4.4.2 and 4.4.3. A listing of the program is given by Pesaran, Mclaine-cross and Van den Bulck (1986). The control computer also displays process temperature and humidity in graphical form and the controller status in tabular form.

The control system further consists of a separate controller for the process air mass flow rate. This control is manual and performed by the facility operator. A complete description is given in section 4.3.4.

4.3.2 Control of Process Air Temperature

To set the process air temperature to any desired value ranging from room temperature to 90 °C, and maintaining that temperature about the setpoint within the limits of accuracy of

the temperature measurements, ± 0.2°C, is a prerequisite for versatile operation of the single blow experimental facility. In the original experimental facility, temperature control was achieved by wiring the bypass thermocouple directly to the input terminal of a conventional solid state temperature controller (Pesaran, 1985). This controller provided regular proportional control with integral action. However, three problems were identified with this arrangement.

1. The quality of the sorption experiments is determined by the sharpness of the step change in inlet temperature when the flow is switched from bypass to process. The controller maintains the upstream air temperature at a constant value and the response of the actual inlet temperature is exponential rather than square, due to the thermal capacity of the intermediate duct and valve.

2. The continuity of consecutive experiments is determined by the transient response of the controller-duct system to a step change in temperature setpoint. The integral action of the controller, which cannot be disabled, causes a typical overshoot of the duct temperature. Because the heater is located at the entrance of the duct and the thermal capacitance of the insulated duct is large, the total time to reach steady state is too long to provide continuity of the experiments. In addition, the optimal controller gain varies in proportion with process air mass flow rate which itself can vary in a ratio range of 1 to 4. Hence, favorable response can only be achieved at one selected flow rate. At different flow rates, the controller gain is either too low or too high, and the overall response time increases substantially.

3. The temperature controller provides its own thermocouple reference junction and voltage-to-temperature conversion. Due to the inaccuracy of this conversion, the temperature computed by the controller differs from the actual temperature by a few degrees and, depending on the room temperature, the actual setpoint differs from the hardware controller setpoint by the same amount.

The quality of the experimental data could be significantly improved by eliminating these three problems. The experimental facility was modified as described below.

A controlled, analog 0-20 mA current signal, generated by the control system, is wired to the thermocouple input of a conventional, industrial temperature controller. A shunt resistance of 1 Ω ± 1% is mounted in parallel to the connected thermocouple wires. A controlled input voltage is thereby generated simulating the input signal of a regular thermocouple. The programmable voltage ranges from 0 to 20 mV with a resolution and accuracy of ± 5 μV. In terms of temperatures, these numbers correspond to a simulated temperature of 28 to larger than 100 °C with a resolution and accuracy of ± 0.1 °C.

The temperature Controller is a Solid State Temperature Controller, model 1622, serial number 8412, manufactured by Omega Engineering, Inc. The controller is equipped with options OT-9523-9440C-9456-9457-9460-04B. It is a fully adjustable, time proportioning controller featuring proportional control with integral and derivative action. An error signal is generated within the controller derived from the hardware temperature setting on the front panel of the controller and the sensor input signal. Based on this error signal, a time-proportioning switching signal, 0 to 15 Vdc, is

generated at the output terminal of the controller. This digital output signal carries a controlled proportion of On/Off time that is supplied to a Solid State Relay, model SSR-240D45, manufactured by Omega Engineering, Inc. This relay in turn switches the power to a Fin Tubular Duct Heater, type DHA15BLOA100MX, manufactured by Wellman Thermal Systems, Inc. The heater is a 4.1 kW, 208 Vac, 19.7 A, single phase, insulated heater, arranged in 2 rows of each 3 U-shaped, finned heating elements. These rows are mounted horizontally and the air flow is perpendicular to the elements.

In this arrangement, the temperature controller with relay operates as a conventional SCR controller for the heater. The temperature setpoint on the controller front panel is set at 40°C, independent of the actual process temperature setpoint that is established by the software of the control system and varies in the range from 20 to 100 °C. The controller base cycle-time of the time proportioning action is set at 2 s. The proportional band of the controller is set at 3, the reset time for the integral action is set at 1000 s, and the derivative time for the rate action is set at 0 s. These hardware controller settings are constant for all experiments. The temperature controller then generates a time proportioning switching signal for the heater relay proportional to the difference between the temperature setpoint on the controller front panel, 40 °C, and the temperature simulated by the analog

current signal and generated by the control system software. Unfortunately the reset time of 1000 s, which is the maximum setting of the controller, is not large enough to turn the integral action completely off.

Actual control of the process temperature is transferred via the analog current signal to the control system. The analog current signal is generated in proportion to a four digit integer computed by the temperature control software. This software provides complete automatic and manual control of the process air temperature. In the manual mode, the operator can select any power level of the heater, ranging from zero to full power. In the automatic mode, three control strategies are offered: proportional, proportional-derivative and proportional-integral control. The operator can select any one of these three automatic control modes. Selection of a particular option is executed by pressing the appropriate function key on the keyboard of the control computer. In general, proportional-derivative action is selected to stabilize the process temperature at a level slightly below the setpoint, and proportional-integral action is selected to eliminate the offset error in steady state operation. A frequency control analysis of the closed-loop system {heater - air stream - temperature - measurement - control system} shows that the overall controller gain should be proportional to the process air mass flow rate. In the controller software, this is

accomplished by a single program statement. For a mass flow rate of 0.02 kg/s, the software controller bandwidth is 2.5. The derivative time for the rate action is 80 s and the reset time for the integral action is 500 s. Both times are constant and do not vary with the flow rate. These three software controller settings were obtained experimentally by the conventional method of Ziegler and Nichols for optimum controller settings.

The controller software also provides two additional features. One feature is the "freeze" option in which the temperature control signal is frozen at its current level. A second special feature is the "switch" action. When hitting the function key assigned to this action, the temperature control software switches instantaneously from controlling the bypass temperature about the software setpoint to controlling the matrix inlet temperature about the value which this temperature has at the moment the function key is pressed. The purpose of the "switch" action is to freeze the matrix inlet temperature at its momentary value. To be successful, it is necessary that the controller is operating in the P-I mode and that the error integral for the bypass temperature is fully established to eliminate the steady state offset error. The error integral retains that offset value during switching.

Proper use of the temperature control software by the facility operator can improve the quality of the experimental data.

1. The response of the matrix inlet temperature to the switching of the air flow from bypass to process can be changed from exponential to quasi-square by hitting the control-switch function key at the right time. Timing by the operator is critical to achieve rapid stabilizing of that temperature.

2. To ensure continuity of the experiments, it is imperative that the settling time of the air temperature for a step change in setpoint be less than 1 hour. Minimum bypass time is guaranteed when automatic temperature control is used in the sequential order from proportional-derivative to proportional to proportional-integral in the fashion described above. The operator changes the control options at the proper time. Proper timing is critical to avoid temperature overshooting. Minimum bypass time also occurs when the air flow rate is maximum. The time response of the insulated duct is that of a system with large time delay and a small time constant for low flow rates and with no time delay and large time constant for high flow rates. The latter is recommended because the total response time is shorter and the duct temperature is more uniform.

3. The software temperature setting corresponds to the physical temperature setpoint within the accuracy of the temperature measurements.

This control system when used properly provides fast response times for transient control. In steady state operation the temperature which is controlled, either the bypass or the inlet temperature, fluctuates about the software setpoint within ± 0.1 °C. These random fluctuations are within the accuracy of the temperature measurements, ± 0.2 °C.

4.3.3 Control of Process Air Humidity

To study the effect of the inlet conditions on the performance of any desiccant matrix with the single blow experimental facility, control of the process air humidity is necessary. The range for the humidity setpoint should be continuous from room air humidity, typically 0.005 kg/kg, to 0.035 kg/kg. The actual process humidity in steady state should approximate the setpoint within the accuracy of the humidity measurements.

In the original experimental facility, the process humidity was controlled with a conventional control system (Pesaran, 1985). This control system incorporated a humidistat with resistance-type relative humidity sensor and discrete set of setpoints for the relative humidity, a solid state electronic proportional controller and a hydraulic valve actuator. These three components were respectively models HS 8201, CP-8102-0-1, and MP-5210-0-0-2, manufactured by Barber Colman Co. The controller received a process signal from the humidistat and controlled the position of a steam valve with the actuator. Dry steam was supplied to the valve by a steam boiler and injected into the air duct through a steam injector. The pressure inside the boiler was kept constant by a separate pressure regulator at 80000 Pa gauge pressure. Two problems were identified with this setup.

1. The quality of the experiments is determined in part by the stability of the process humidity. For a typical experiment, the process humidity fluctuated in a periodic fashion about the setpoint with an amplitude of ± 0.001 kg/kg (Pesaran, 1985). This control performance was unacceptable with respect to the quality standards of the experimental data.

2. The humidity setpoint could not be varied continuously within the operating range of the experimental facility. The discrete set of setpoints limited the versatility of the facility.

Control of the actuator valve was first attempted with the control system described in Section 4.4.1. However, a software algorithm was developed showing even a perfect software controller could not give a humidification performance of the hardware in accordance with the performance criteria, due to the hysteresis in the control characteristic of the flow valve. Therefore, a complete new humidification control system was added to the test facility, and this system is described below.

The hardware of the humidification system incorporates a humidifier, a steam injection tube and a SCR controller. The humidifier is a Vaporstream model "D.I." electric steam humidifier, model VSDI-2, serial number V4691, manufactured by Dri-Steem Humidifier co. This humidifier is constructed as an evaporating chamber with a gasketed cover. The walls of the chamber are stainless steel with heli-arc welded joints and the

volume is 0.027 m^3. Steam is produced through pool boiling of demineralized water. Electric resistance heaters provide the required heat of vaporization. The capacity of these U-shaped, plain immersion heaters is 2 kW at 9.6 A and 208 V. The humidifier is equipped with a low-water cut-off switch, an overflow stand pipe, a float valve for automatic, periodic water make-up, and a manually operated ball valve for draining. The capacity of the humidifier is $8x10^{-4}$ kg/s of dry steam. The humidifier is mounted separate from the air duct by use of a steam hose. The steam flows from the evaporating chamber into the 0.038 m ID steam hose connected to the top cover plate. This steam hose carries the steam to a dispersion tube mounted in the air duct. The dispersion tube is made from 0.038 m ID, type 304 stainless steel and has a tilted 'F' shape. The two dispersion tubes make an angle of 3 deg with a horizontal to provide gravitational condensate removal. Each dispersion tube is fitted with properly spaced orifices along its length. The orifice sizes are graduated to provide uniform steam injection across the duct width.

The humidifier and steam hose are thermally insulated to minimize steam condensation through heat loss. The humidifier is mounted higher than the dispersion tube. The steam hose and water drain pipes are installed in accordance with the manufacturer's recommendation for removing condensate build-up. However, three problems were identified after initial operation

of this humidifier configuration. The humidifier was further modified as follows.

1. The float valve for water make-up operates in a periodic fashion producing inflow of cold water into the evaporating chamber at a regular time interval, typically 5 minutes. This discharge of cold water immediately stops the boiling of the water for about 30 s. Because the volumetric capacitance of the humidification is very small, large variations in steam production result. It was necessary to inhibit the float valve mechanism and provide manual control of the water make-up.

2. During steam dispersion, there is a substantial heat loss from the injection tube and orifices to the passing air stream. This heat loss causes condensation of the steam within the orifices. Because of the small capacity of the humidification system, the diameters of the orifices are small and they retain the condensate drops through capillary action. These water drops grow in size and are periodically discharged into the air stream. It was necessary to remove the orifices and seal off one of the dispersion tubes. The remaining dispersion tube is then simply a circular tube with regularly spaced holes. This configuration gives satisfactory performance.

3. During operation of the modified humidifier, a severe oscillation of the steam flow was observed. The true nature of this oscillation could not be determined, although it was accepted that the oscillations resulted from a thermal instability of the top cover plate causing a periodical, sinusoidal condensation of vapor on that plate. The steam flow oscillations could be significantly dampened by the following two actions.

    a. Putting a heavy steel plate on top of the top cover plate of the evaporating chamber to increase its thermal capacitance.

    b. Providing an air suction line at the connection of the steam hose to the top cover plate. The evaporating chamber then becomes an open chamber operating at a pressure close to ambient pressure. Furthermore, the air suction line acts as a small jet pump actually drawing the steam from the evaporating chamber into the steam hose. Air suction is produced by the pressure difference

between the ambient air and the air stream in the duct at the location of the steam injection tube.

The steam flow oscillations were damped to about 20% of their original amplitude. Even these small amplitudes caused serious problems with the humidity control as is discussed later.

Electrical energy is supplied to the humidifier immersion heaters by a solid state power controller, model H3, manufactured by Solitech. This controller comes with the humidifier and is supplied by Dri-Steem Humidifier Co. The controller employs two heavy duty switching triacs to provide the power circuit control. The logic circuits provide 0 to 100% proportional power control by establishing a basic time interval, 4.9 s, and energizing the heaters for a percentage of each interval. The fraction is proportional to the input signal of an external humidistat. At the beginning of each time interval, the logic circuits analyze the humidistat signal and determine the number of AC cycles.

The humidistat signal is a standard 4 - 20 mA dc current signal generated by the control system. The current intensity is proportional to a four digit number calculated by the humidity control software. Input parameters to the software are the setpoint and measured value of the process humidity, and the process air mass flow rate. The software provides full automatic and manual control of the process air humidity. In

the manual control mode, the operator can select between zero and full power for the immersion heaters. In the automatic control mode, two control options are offered: proportional and proportional-integral control. Selection is made by pressing the assigned function key on the keyboard of the control computer. As for the temperature control, the overall gain factor for humidity control is made proportional to the process flow rate. Optimal controller settings were determined experimentally with the method of Ziegler and Nichols. For a mass flow rate of 0.02 kg/s, the recommended software controller bandwidth is 8.3×10^{-4}. The reset time for the integral action is 60 s. However, the steam flow oscillations described in the previous paragraph have a natural period of 50 to 55 s. The time delay in the humidity control system is established independent of this instability and ranges between 20 to 25 s which is about half of the natural period. This coincidence made it necessary to lower the gain factor by a factor of two. In addition to these standard control options, the software also provides a "freeze" option. When selected, the control signal is frozen at its current level. The error sum for the integral action is retained. This feature is useful when changing the flow from bypass to process. Only one humidity sensor is therefore needed to measure the humidity sequentially in the two separate flows. In steady state operation, the humidity fluctuations are within ± 1%, well within the accuracy of the

measurement, ± 3%.

4.3.4 Control of Process Air Mass Flow Rate

The mass flow rate is an important parameter among those which characterize a particular experiment. Prior to each experiment, the process air flow is prepared in bypass. The proper mass flow rate is set and control signals for temperature and humidity ratio are established. These control signals establish the precise amount of thermal energy and water vapor to the air stream in order to reach the desired setpoints of temperature and humidity ratio. Both control signals change with the process flow rate. When steady state of the air stream is achieved in bypass, flow valves are switched and the air is passed through the matrix. In this operation, the process flow rate changes abruptly because of even slightly different flow resistances in both loops. If this deviation from the setpoint is not eliminated immediately, unsteady inlet temperatures and humidity ratios will result.

These considerations establish the criteria for the mass flow rate controller. There should be a wide range for the setpoint and the flow rate should be continuously adjustable about the setpoint in the range of ± 20% with the accuracy of the measurement of the flow rate, ± 2.5%. In the original experimental apparatus, a discrete set of setpoints for the

flow rate was obtained by means of a 2-speed electric motor in combination with a stepped-cone pulley system (Pesaran, 1985). Flow adjustments were made with a duct damper. However, this configuration did not provide adequate and flexible control of the process air mass flow rate. The experimental facility was modified as described below.

The flow of process air is provided by a belt driven air blower mounted on a common base plate with an electric motor. The blower is a compact GI Fan, size 123, manufactured by the New York Blower co. It is a centrifugal fan in a scroll type housing with radial impeller design and wheel diameter of 0.305 m. The blower capacity is 0.045 kg/s at 2200 RPM and 994 Pa total pressure head. The motor is a variable speed, permanent magnet DC motor with a capacity of 2 kW at 2500 RPM. The armature voltage ranges from 0 to 180 Vdc and is supplied by a solid state motor controller through which 0 - 100% speed control is accomplished. The motor speed is adjusted by a dial on the front panel of the motor controller. The motor and controller come as one unit, model 4Z226A, and is manufactured by Dayton Electric Mfg. co.

Air state properties and pressure drop across the orifice plate downstream of the blower are measured and collected by the data acquisition system. The process air flow rate and the Reynolds number of the flow based on the matrix dimensions are

computed and their real time values are continuously displayed on the monitor of the data acquisition computer. The operator of the test loop reads the values of the mass flow rate and Reynolds number and manually adjusts the fan speed to maintain the process variable about the setpoint for the ongoing experiment. The range for the setpoint is 0 to 0.04 kg/s. Typical fluctuations of the flow rate about the setpoint are within ± 1%.

4.4 Description of Test Procedures

The type of experiments facilitated by the experimental facility are adiabatic, single blow, transient heat and mass transfer experiments, in which an air stream is passed through a test matrix containing a desiccant, and the response of the air-stream outlet state to a step change in the air-stream inlet state is investigated. The initial and final conditions of the air stream and test matrix are steady state conditions in which the test matrix and the air stream are in thermodynamic equilibrium. The matrix is insulated and no heat or mass is exchanged with the surroundings during the experiment. For each test, passing air through the test matrix at fixed inlet conditions for a sufficiently long period establishes the initial conditions of the test matrix. The test

matrix is then isolated to preserve the initial state, while a different set of inlet conditions for the air stream is established in bypass flow. When these inlet conditions reach steady state, the air stream is abruptly diverted and passed through the test matrix with fixed conditions thereby approximating the step change in inlet conditions. If the adsorption potential of the initial state is higher than that of the inlet state, the desiccant adsorbs water vapor from the air stream and the test is called an adsorption test. In the reverse case the test is called a desorption test.

A single blow experiment consists of an adsorption test followed by a desorption test. It was experimentally found that this order of tests improves the quality and repeatability of the experiments. Furthermore, for each test, a predefined set of rules has to be followed in order to ensure repeatability of the experiment. The following set of procedures was established based upon the practical experience obtained from the use of the experimental apparatus. These procedures include the following sequence of operations.

1. Start up the experimental facility; approximate time 45 minutes.
2. Establish the matrix initial conditions for adsorption; approximate time 1 hour.
3. Establish the process air inlet conditions for adsorption; approximate time 1 hour.
4. Perform the adsorption test; approximate time 1 hour.

5. Establish the matrix initial conditions for desorption; approximate time 45 minutes.

6. Establish the process air inlet conditions for desorption; approximate time 1 hour.

7. Perform the desorption test; approximate time 1 hour.

8. Shut down the experimental facility; approximate time 15 minutes.

Each of these operations are briefly described and the major features of the experimental procedure are highlighted. A more detailed description is given elsewhere (Pesaran, MacLaine-cross and Van den Bulck, 1985).

1. **Start up the experimental facility**

This procedure includes checks which have to be performed before each series of experiments.

1.1 The icebath for the thermocouple reference junction is filled with a fresh mixture of crushed demineralized ice and water.

1.2 The pressure transducers measuring the pressure drop across the test matrix and orifice plate are adjusted to zero voltage offset.

1.3 The pressure taps are checked for leakage by running the blower with closed exit valves.

1.4 The humidifier water reservoir is filled with demineralized water.

1.5 The lab room conditions, temperature and barometric pressure are recorded from the Fortin mercury barometer mounted in the laboratory.

1.6 The computer programs for the data acquisition and control systems are started.

2. **Establish the matrix initial conditions for adsorption**

At this stage, the matrix is initialized to a high, uniform temperature in order to adsorb moisture from a humid air stream. The preparation conditions are the actual conditions of the air stream. The actual initial conditions of the test matrix at the beginning of the adsorption test may differ from these preparation conditions due to heat losses from the test matrix.

2.1 The blower is ON, the test section inlet valve and exit valve are open, and the bypass valve is closed. The air stream is passed through the matrix at a moderate flow rate, typically 0.02 kg/s. The dewpoint hygrometers are sampling air from the test section.

2.2 The facility operator starts the initializing software procedures for data acquisition and control. The setpoints for air inlet temperature and humidity are entered into the data acquisition computer.

2.3 The process humidity is manually controlled until the humidifier starts producing steam, and automatically in the P-I mode after that.

2.4 The process temperature is controlled automatically in the P-D mode until the temperature stabilizes at a level slightly below the setpoint, and in the P-I mode from there on.

After the inlet state of the process air stream reaches steady state, the actual initialization starts. To assure complete equilibrium of the matrix, the initialization period is continued for a standard time, 45 to 60 minutes. At the end of this period, the facility operator proceeds with the following actions.

2.5 Using the data acquisition program, 30 measurements of the experimental variables are recorded at a rate of 1 scan per second.

2.6 The bypass valves is opened, and the test section inlet and exit valves are closed. The outlet hygrometer samples the room air. The inlet hygrometer samples the air flowing in the bypass line.

3. **Establish the air inlet conditions for adsorption**

This procedure consists of two phases. In the first phase, the air and duct temperature is decreased to below the setpoint for the air inlet temperature, typically 3 C. In the second phase, the actual air inlet conditions are established.

The first phase is accomplished as follows.

3.1 The computer programs on the data acquisition and control computers are set in the specified option for the bypass flow. Values for the setpoints of the air inlet conditions, temperature and humidity, are entered into the data acquisition computer.

3.2 The blower is set at full speed.

3.3 The air temperature is lowered using all means available, e.g., injecting liquid refrigerant 22 into the air duct, removing the insulation around the blower and putting ice packs on top of it, ...

The first phase is finished when the air temperature measured by the bypass thermocouple is about 3 C below the air inlet temperature. In the second phase, the following actions are taken.

3.4 The air mass flow rate is adjusted manually about the setpoint.

3.5 The air temperature is controlled automatically starting with P and continuing with P-I control.

3.6 The air humidity is brought to the setpoint using P-I automatic control.

When the air properties are stable, this procedure is completed.

4. **Perform the adsorption test**

The air stream is flowing in bypass. The adsorption test is started by the following sequence of procedures.

4.1 The humidity controller is put into the "FREEZE" mode. This deactivates the control. The outlet dewpoint hygrometer is switched from sampling room air to air in the test section. The inlet dewpoint hygrometer is switched from sampling bypass air to sampling air in the test section.

4.2 The dedicated software for this phase of the experiment is started for the data acquisition and control.

4.3 The test section exit valve is opened. The test section inlet valve is opened and, simultaneously, the bypass valve is closed in a fluent, fast motion.

At this moment, the adsorption test has started. Three variables need to be controlled: the air mass flow rate, the air inlet temperature and the inlet humidity. The following actions are taken to control these variables about their setpoints.

4.4 Immediately after switching the flow valves, the air mass flow rate is adjusted with the fan motor speed controller to the setpoint value in bypass.

4.5 The inlet humidity should be continuously monitored by the operator. There is a one minute transition period for the inlet dewpoint hygrometer to stabilize. After one minute, the humidity measured by the hygrometer should be equal to the setpoint humidity in bypass. At that moment, the humidity control software is reactivated and put into the P-I mode.

4.6 After switching the flow valves, the inlet temperature decreases exponentially to a steady state value slightly above the bypass setpoint temperature. The sharpness of the inlet temperature step change is significantly enhanced by selecting the "SWITCH" control mode. By pressing the dedicated function key on the keyboard of the control computer, the temperature control software switches immediately from controlling the upstream bypass temperature about the setpoint to control of the process air inlet temperature about the value this temperature has at the moment the function key is hit. This action in effect freezes the inlet temperature at its current level. Proper timing of this control option for producing a square inlet step change is critical and experience of the operator is necessary. Typically, the function key is hit for the first time a few minutes after the valves have been switched. The key can be hit a second or third time if the inlet temperature overshoots the effective controller setpoint.

These control actions apply to the initial stage of the adsorption test and determine the quality of the experiment. After the inlet temperature and humidity are established at steady state values, the operator continuously monitors the test. He manually adjusts the mass flow rate about the setpoint with the fan motor speed controller. The adsorption test lasts until the process air outlet state reaches steady state. After the test is finished, actions are taken to orderly conclude the test.

4.7 The appropriate software procedures for the data acquisition and control are selected. The recorded measurements are stored on a diskette.

4.8 The test section inlet and exit valves are closed, the bypass valve is opened, and the dewpoint hygrometer valves are switched.

5. **Establish the matrix initial condition for desorption**

For the desorption test, the matrix is initialized at low temperatures to load the desiccant with water. A hot air stream is then passed through the matrix to desorb the water. Often, the initial condition for desorption coincides with the final condition of the previous adsorption test. However, the operator may choose to establish a different initial condition at a slightly lower temperature and humidity. During the time it takes to prepare the air inlet state for desorption, the matrix temperature may change due to residual heat storage within the test section. The air stream in bypass is stabilized and then passed through the matrix. The initializing procedure is analogous to the initializing procedure for adsorption.

6. **Establish the air inlet conditions for desorption**

The air stream flows in bypass and steady state conditions for temperature, humidity and mass flow rate are established. As for the adsorption test, the air temperature is

increased in two stages. This procedure is the same as procedure 3.

7. **Perform the desorption test**

The desorption test is similar to the adsorption test. The procedures described for the latter test can be repeated for this test. The desorption test takes less time to complete than the adsorption test. However, the test time should not be shorter than the standard test time of 1 hour and a few minutes.

8. **Shut down of the experimental facility**

A few safety measures should be taken to safely shut down the experimental facility. After the desorption test, hot air is flowing in bypass. The humidifier, heater and blower need to be stopped manually in this order.

CHAPTER 5

EXPERIMENTAL RESULTS AND DISCUSSION

This work is an analytical and experimental investigation of transient, combined heat and mass transfer in laminar flow of humid air over a desiccant surface. Experimental results are presented for the transient response of a parallel-plate test matrix in single-blow type experiments, in which the test matrix is conditioned at specified initial conditions, and the air stream is subjected to a near step change in inlet conditions. The air stream outlet conditions as functions of time form the experimental data which are subject of the presented analysis.

The first section in this chapter presents a literature review of existing methods for analysis of single blow experiments. These methods accept analytical or numerical models that are based on a specific implementation of the general conservation and transport equations for momentum, energy and mass. One conventional approach is to compare the experimental data with theoretical results from the model, founded on a predefined set of simplifying assumptions. In an alternative approach, the experimental results can be used in intermediate steps of the analysis to verify certain assumptions and to derive specific, quantitative information about the studied process. This latter approach is followed in this work. The

set of experiments is designed such that it fits within the framework of the analysis.

Subsequent parts of the analysis need, respectively, the surface and core geometry of the test matrix, the thermodynamic properties of the fluid and desiccant in general and the equilibrium sorption-isotherm in specific, and the spatial and temporal distributions of the state properties of the fluid stream. For each of these three sub-analyses, a specific set of experiments is designed to yield the required quantitative information.

The first subset of experiments is a set of 4 pressure drop experiments. Results of two of the pressure drop tests are compared to show repeatability of the experiments, two of these tests are compared to verify the accuracy of the flow rate measurement, and two tests are analyzed to determine the surface and core geometry of the test matrix. The discussion and analysis of the pressure drop experiments is presented in the second part of this chapter.

The second series of experiments is a set of 8 dynamic sorption experiments in which the initial state of the desiccant matrix and the inlet state of the air stream are varied in a systematic pattern. The analysis of these experiments involves the computation of the thermodynamic properties of the test matrix: the mass of active desiccant within the matrix, the lumped thermal capacitance of the matrix, and the static

sorption-isotherm type of the desiccant. These sorption experiments are discussed and analyzed in the third part of this chapter.

The third subset of experiments is a set of 15 dynamic sorption experiments in which the process air mass flow rate is varied in a systematic sequence. Each experiment has the same pair of matrix-initial and air-inlet states. The results of these tests directly give the experimental distributions of the air stream state properties, temperature and humidity, as a function of time and position in the flow direction. These distributions are combined with the surface geometry and thermodynamic properties of the test matrix, and are input to a numerical model which computes the distributions of the air-side and desiccant-side heat and mass transfer coefficients. The discussion of this last series of experiments is given in the fourth section of this chapter.

5.1 Analysis Techniques for Single Blow Experiments

The techniques for analyzing experimental data from single blow experiments are well-established. In single blow experiments, a test matrix is conditioned at specified initial conditions and a step change is applied to the inlet conditions of the fluid stream passing through the matrix. The distri-

butions in time of the fluid stream outlet conditions form the experimental data which characterize the heat and/or mass transfer performance of the test matrix. Retrieving quantitative information, i.e., the heat and/or mass transfer coefficients, is the objective of the analysis tools. The approaches vary for thermal regenerators and adsorbers, and are discussed separately.

5.1.1 Single Blow Methods for Heat Transfer

The single blow method is widely used for evaluating the performance of compact heat exchanger geometries (Heggs, 1983). Almost all analysis techniques are based upon the 'porous-matrix' or 'insulated-duct' equations which were first established by Anzelius (1926) in the German technical literature and later by Schumann (1929) in the English technical literature. These equations express the overall energy equation for the adiabatic system air-stream plus matrix and a heat transfer rate equation based upon an overall transfer coefficient, i.e., the transfer rate is proportional to the difference in fluid-mean and matrix-mean temperatures. This model is often referred to as the Schumann, or Anzelius, or Schumann-Anzelius model. A closed form solution in terms of the integral of the modified Bessel function is discussed by Bateman (1944).

There exist two classes of solution methods for single blow experiments: the point matching technique and the curve matching procedure.

Point Matching Solutions

The analytic solution of the insulated duct equations provide the basis of this class of solutions. The principle is to match one parameter derived directly from the experimental data with a theoretical curve showing that parameter as a function of the exchanger *Number of Transfer Units*. These methods include an assumption about the shape of the inlet step change, either square or exponential. The following approaches have been taken.

i) Effectiveness at the point of breakthrough.

The fluid temperature effectiveness at the time of breakthrough of a wave with infinite transfer coefficients is a unique function of the matrix *NTU* (London, Biancardi and Mitchell, 1959). The functional dependency is weak for high *NTU*'s, and this method does therefore not give accurate performance estimates for compact heat exchangers.

ii) Maximum slope matching.

The maximum slope of the fluid temperature response or the time for the maximum slope in proper dimensionless forms are unique functions of the *NTU* (Kays and London, 1984). The

conventional criticism of this method is that the maximum slope is usually not well defined for tabulated experimental data with measurement errors.

iii) Initial rise procedure.

The instantaneous step of the outlet temperature at the dwell time of the fluid stream is a unique, well-defined function of the *NTU* in the range $NTU < 1$. Application of this method is limited to low *NTU* exchangers, e.g., heat exchangers operating at high flow rates.

iv) Area matching - method of moments.

The second central moment of the fluid outlet temperature characterizes the width of the response curve and is a unique function of the *NTU*. Jeffreson (1970) reports a general study of the method of moments for dynamic testing of single-component exchangers. Accurate moments are more difficult to obtain from a step response than from the impulse response, and pulse testing is recommended. Jeffreson discusses the effect of 'tailing' of the outlet response, typically due to the thermal capacity of structural materials, and the decrease in accuracy of the method of moments for step responses with tailing.

v) Area matching - partial integration.

Baclic, Heggs and Abou Ziyan (1986) present a solution of the conventional porous matrix equations by means of Laplace transforms. The integral with time of the dimensionless fluid

enthalpy difference between inlet and outlet from the start of the step input to the breakthrough time of a sharp wave with infinite transfer coefficients is expressed as a function of the exchanger *NTU* in a sort of exchanger-effectiveness curve. Corrections can be applied to account for exponential inputs rather than step inputs, and the method is applicable for a wider range of *NTU* than the conventional methods.

vi) 20-80% time interval

This method uses the time interval between the 20-80% boundaries of the response curve (Heggs, 1983). This method is not well-defined if the response curve tails due to thermal capacitances of the matrix or heat loss.

Point matching methods make assumptions about the nature and shape of the inlet step change. The shape of the breakthrough curve is very sensitive to the shape of the inlet step (Baclic, Heggs and Abou Ziyan, 1986), and the accuracy of these methods is determined by the exactness of the step input and also the measuring accuracy (Heggs, 1983). The point matching solutions are strictly limited to linear systems with constant coefficients, because the solution methods invariably use Laplace transforms to arrive at closed form relationships. Recent trends in single blow experiments include the design of experimental facilities with sophisticated on-line computer control of the fluid-stream inlet properties, and fast-

switching, low capacity heaters at the inlet face of the test exchanger. State of the art facilities reach a step change in inlet temperatures in less than 0.2 s (Rapley and Webb, 1983). For the facility used in this work, this time is about 20 to 40 s depending on the mass flow rate.

Curve Matching Techniques

These methods generally use finite difference solutions of the insulated-duct equations. They are therefore more general than the point matching techniques because they do not make assumptions about the shape of the inlet temperature profile. Curve matching is typically an iterative procedure in which the *NTU* parameter is determined by minimizing the RMS error of the experimental data with model predicted data. This error is a function of the exchanger *NTU* only. Elliot, Rapley and Webb (1986) present a finite difference solution of the insulated duct equations including axial dispersion and axial conduction for arbitrary inlet step changes. Their method illustrates a recent trend toward fast finite-difference algorithms for the solution of the hyperbolic conservation equation without iteration on the parameters in the model and accurate for a wide range of the exchanger *NTU*.

Although the single blow method has been widely used for the study of transient heat transfer, there is still question

about the appropriate boundary conditions for predicting the convective Nusselt numbers for passages in regenerators (Rapley and Webb, 1983). The local wall heat flux has a Gaussian, skewed distribution which is slowly expanding while shifting in the flow direction. This type of transient, nonuniform boundary condition is not included in the standard literature on forced convection heat transfer in laminar flow through ducts (Shah and London, 1978). The effect of this type of boundary condition on the local and average heat transfer coefficients is uncertain.

For thermal regenerators, conduction resistance within the solid is usually neglected because the effect is small; however, axial conduction in the matrix material may be important. In his review of packed bed regenerators, Heggs concludes that convective fluid-to-particle heat transfer coefficients cannot be predicted with high confidence with the single blow method. The complete set of equations incorporating conduction within the solid and the effect thereof has not yet been determined (Heggs, 1983). For regenerative parallel-duct dehumidifiers, the situation is reversed. Axial diffusion is usually negligible, and the diffusion resistance of the desiccant particles may be important.

5.1.2 Single Blow Methods for Isothermal Mass Transfer

The general classification of the various techniques for heat transfer alone can be used for isothermal mass transfer in adsorbers. Eagleton and Bliss (1953) present experimental results for the isothermal drying of air in fixed beds of silica gel. They observed the constant width of the break-through curves, indicating the favorable curvature of the silica gel isotherm. Their model includes an overall transfer rate equation, and a nonlinear isotherm correlation. The mass transfer coefficient is obtained with a method analogous to the method of maximum slope, and indicates an effect of intraparticle diffusion.

Jeffreson (1968, 1972) provides a theoretical discussion of the application of the method of moments and the frequency response technique to the analysis of dynamic, packed beds transferring either heat in thermal regenerators, or mass in cooled adsorbers. The technique can be applied to models that include either intraparticle diffusion resistance or axial dispersion in the fluid stream. For systems with linear isotherms, Jeffreson gives expressions for the first, second and third moment in terms of non-dimensional parameters quantifying, respectively, the equilibrium constant, the external transfer coefficient, and either the particle diffusivity or axial dispersion coefficient. The first absolute

moment describes the position of the response and is related to the equilibrium constant of the system. The second central moment quantifies the width of the response curve, and the third moment describes the distribution skewness. For adsorption columns, the theory is restricted to linear isotherms, implying dilute, binary systems.

Schneider and Smith (1968) experimentally studied the isothermal mass transfer of hydrocarbons on silica gel in a packed bed geometry. Their analysis includes separate conservation equations for the fluid stream and the sorbent particles, and linear expressions for the axial dispersion and rate of sorption. Three dimensionless parameters exist, describing the inter- and intraparticle diffusivity and the sorption rate constant. Schneider and Smith state that the curve matching procedure is unsatisfactory for this model because good agreement between the experimental data and a theoretical response curve can be obtained with more than one set of these three constants. They established expressions for the first absolute moment, and the second and third central moments of the breakthrough curve. These latter two moments yield the axial dispersion coefficient and intra-particle diffusion constants. Schneider and Smith obtain good agreement between the predicted and experimental breakthrough curves and derive values for the effective mass diffusivities of hydrocarbons in silica gel.

Pesaran and Zangrando (1985) report experimental breakthrough curves for the isothermal adsorption of water vapor on silica gel in laminar flow through a parallel plate configuration. Their model describes an overall mass balance and an air-to-desiccant transfer rate with a constant, overall transfer coefficient. The isotherm correlation is nonlinear. When the transfer coefficient is computed from the theoretical Sherwood number for constant wall concentrations, agreement between the experimental and predicted breakthrough curves is unsatisfactory. Further adjustment of the transfer coefficient by curve matching does not improve the agreement. The authors attribute the discrepancy to the presence of intraparticle resistance and an inaccurate isotherm correlation.

Although the matching techniques for heat transfer can be applied for isothermal mass transfer, these methods are restricted to either linear systems, or to models that incorporate only few adjustable parameters. Consequently, the conventional single blow techniques can only be applied to dilute, binary systems, and to models which are limited in their description of the sorption process. Neither one of these restrictions may be applicable to dehumidification systems.

Gidaspow and his coworkers have used a more fundamental approach for single blow experiments which involve mass transfer. Solbrig and Gidaspow (1967) and Kulacki and Gidaspow (1967) discuss experimental results of the combustion of

hydrogen in fully developed, laminar flow of air through parallel plate duct with one catalytic wall of platinized alumina. Their model includes the parabolic mass-diffusion equation for the air flow with a first order rate equation for the combustion of hydrogen at the wall. A Graetz- and Leveque type analysis is applied and the eigenfunctions and eigenvalues are computed. The analytical concentration profile is in good agreement with the experimental results. Their model illustrates the use of a fluid-diffusion equation for systems involving mass transfer. Ghezelayagh and Gidaspow (1982) report experiments on the isothermal adsorption of water vapor in laminar flow of humid air through parallel plates. The walls are made of porous solid Teflon web, 710 μm thick, holding 9 μm regular-density silica particles. The plate spacing is 1.59 mm. Their technique uses experimental data to separate the conservation and rate equations for the air stream from those for the desiccant sheet. The air stream model includes the parabolic diffusion equation. A micro-macro pore sorption model with a linear isotherm is used for the sheets. Boundary conditions for the wall-transport fluxes are obtained directly from the experimental data. A curve matching procedure to arrive at the sheet mass diffusivities yields unrealistically low values. Their study indicates the need to study the position and time dependency of the gas-side and sheet-side transfer coefficients and the effect of the boundary

conditions on the transfer coefficients.

The use of separate conservation and rate equations for the fluid stream and the solid phase is often referred to as the Rosen model (1952, 1954). This model is more fundamental in nature, does not introduce an empirical transfer coefficient; however, it introduces more thermo-physical properties which are often only approximately known. Carter (1960, 1966, 1968) published key papers, reviewing Rosen's and some of the earlier work on analysis techniques.

5.1.3 Single Blow Methods for Simultaneous Heat and Mass Transfer

Standard techniques for analyzing single-blow, adiabatic sorption experiments are less developed. The models describing the transient process invariably include a fair number of adjustable parameters for the transfer rate and equilibrium constants. Various efforts have been reported.

Hougen and Marshall (1947) discuss the adiabatic sorption of water vapor on silica gel in a packed granular bed. Their theoretical analysis includes empirical correlations for the overall, constant heat and mass transfer coefficients which were fitted to the earlier experimental data of Ahlberg (1939). The overall transfer coefficients are about 3.6 times smaller

than the air-side transfer coefficients, and the overall Lewis number is about 1. Chi and Wasan (1970) use these empirical correlations in their numeric model for the adiabatic adsorption of water vapor on silica gel in a packed bed geometry. Overall conservation equations for mass and energy with constant overall heat and mass transfer coefficients are solved numerically. The model includes a nonlinear expression for the isotherm. They conclude a fair agreement between their theoretical curves and experimental breakthrough curves published by Bullock and Threlkeld (1966). Clark, Mills, and Buchberg (1981) report experiments on the adiabatic sorption of water vapor on silica gel-packed beds. Their model includes overall conservation equations, a nonlinear isotherm, and overall heat and mass transfer coefficients for the rate equations. The transfer coefficients are also computed from the Hougen-Marshall correlations. The agreement between theoretical and experimental breakthrough curves is poor and the authors conclude that the discrepancy cannot be explained by experimental errors. They point to the existence of an intraparticle diffusion resistance which is neglected in their model. However, a graphical comparison of experimental and theoretical breakthrough curves also reveals the use of an inaccurate isotherm correlation.

Allander (1953) reports an experimental and analytical study of adiabatic adsorption of water vapor on regular density

silica gel in laminar flow of air through packed beds. His model includes a linear isotherm, overall conservation equations, and overall transfer rate equations with constant transfer coefficients corrected for intraparticle resistance to mass transfer. His experiments indicate negligible intraparticle resistance to heat transfer. The effective, overall Lewis number is 3 for particle diameters of 3.4 mm. The equations are solved with Laplace transforms after applying an interesting coordinate transformation, and the theoretical breakthrough curves are in fair agreement with the experimental curves. The Hougen-Marshall correlations indicate that the overall *NTU*'s for heat and mass transfer are about equal. However, Allander's work showed that the overall heat transfer coefficient is almost the air-side heat transfer coefficient due to the high thermal conductivity of the solid particles; thus the Hougen-Marshall correlations may indicate a Lewis number of 3.6 for silica gel.

Chase, Gidaspow and Peck (1969) analytically studied the adiabatic sorption of water vapor on silica gel from an air stream flowing over a semi-infinite porous medium. The mass and energy transfer rate equations in the air flow include overall, constant transfer coefficients. The porous medium is modeled with one-dimensional diffusion equations for heat and mass. The sorption isotherm is linearized and solutions to the equations are obtained in terms of Green's functions. They

discuss the smoothing effect of finite transfer coefficients on the shape and skewness of the breakthrough curves.

Biswas, Kim and Mills (1984) and Kim, Biswas and Mills (1984) present a theoretical and experimental investigation of the adiabatic sorption of water vapor on regular density silica gel in a parallel plate geometry, similar to the one reported in this work. The walls are Lexan polycarbonate sheets coated with a RTV 162 silicone rubber adhesive and silica gel particles with diameters, respectively, 120 and 250 μm. The plate spacing ranges from 1 to 4 mm. Their model includes overall mass and energy conservation equations for air and desiccant, overall transfer rate equations with constant heat and mass transfer coefficients, and a nonlinear isotherm expression. The agreement between experimental and predicted breakthrough curves is fair. The authors perform a sensitivity study and conclude that several factors can explain the difference, e.g., the mass of desiccant, *NTU*, fluid flow rate, gel-initial water content, and heat of adsorption. They conclude that their model may be too simple, not accounting for solid side resistance.

Pesaran, Maclaine-cross, and Van den Bulck (1986) perform a theoretical analysis of adiabatic single blow experiments, similar to the experiments presented in this work. The model is based upon the method of moments applied to the two characteristic invariants of the overall hyperbolic conservation

equations for infinite transfer coefficients. The model assumes overall, constant heat and mass transfer coefficients, and $Le = 1$. However, analysis of the experimental data yields erroneous heat and mass transfer coefficients due to experimental inaccuracies and the inappropriate assumption of linear equations.

5.1.4 Analysis of Single Blow Experiments

The literature review presented in this chapter indicates the following guidelines for analyzing single blow experiments with simultaneous heat and mass transfer in laminar flow of humid air over silica gel particles in a parallel plate configuration.

1. The geometry of parallel plates has not been studied in as much depth as packed bed configurations. In parallel flow channels, the appropriate boundary conditions for computing the fluid side transfer coefficients for transient, nonuniform distributions of the wall concentration or transport flux are not known. Incorporating a fluid side diffusion equation for energy and mass does not require assumptions about these boundary

conditions, and does not introduce transfer coefficients which may only be approximately known.

2. Intraparticle resistance may have a significant effect on the transfer rates of heat and mass and there is question about what the effect can be. The Rosen model with an additional diffusion equation for the particle seems to give better accuracy than the Schumann model which assumes a constant, overall transfer coefficient.
3. The correlation for the sorption isotherm has a major effect on the shape and position of the breakthrough curve. An accurate correlation should be used for any theoretical analysis.
4. The effects of various parameters such as equilibrium constants, Number of Transfer Units, and diffusivities on the position and shape of the response curve are intermixed. A theoretical model should contain as few as possible adjustable parameters. Alternate, independent fitting procedures should be used to sequentially determine the numerical values for these parameters.

The model used in this work is similar to the method of Ghezelayagh and Gidaspow (1982). The analysis includes separate conservation and diffusion equations for the fluid and particle phases, and is explained in detail in section 4 of this chapter. The equilibrium property parameters appearing in

the model are obtained from an independent fitting procedure applied to a separate set of dynamic, adiabatic sorption experiments. This sub-analysis is discussed in section 5.3. First, however, the adjustable parameters with respect to the geometry of the test matrix are determined from an independent set of pressure drop experiments, presented next.

5.2 Pressure Drop Experiments

The geometry of the flow passages within the test matrix is that of a rectangular channel with a width of 116 mm, a height of 1.1 mm, and a length of 203 mm. The upper and lower walls of the passages are coated on both sides with silica gel particles with highly irregular shape. Particle dimensions range from 0.15 to 0.3 mm. The presence of these particles affects the matrix free flow area and the internal transfer area sheared by the air stream in such a manner that these areas cannot be directly measured or computed. A series of pressure drop experiments is presented and analyzed to indirectly determine the surface and core geometry of the matrix.

A list of the pressure drop experiments is presented in the first part of this section. The experimental data are discussed and analyzed in the second part. The effect of the

irregular wall surface on the flow resistance of the test matrix is investigated. The matrix free flow area and transfer area are determined, and the complete surface and core geometry of the test matrix is listed at the end of this section.

5.2.1 Experimental Results

The pressure drop experiments consist of the measurement of the pressure drop across the test matrix as a function of the process air mass flow rate through the matrix. Room air with no additional heating or humidification is used for the process air stream. Prior to each experiment, process air at steady state conditions is passed through the matrix for a sufficiently long period to establish equilibrium between the desiccant and the air stream. There is no heat or mass transfer during the pressure drop experiments.

Four pressure drop experiments were performed on the test matrix. Data for each experiment were collected and converted using the procedures described in Chapter 4. For each measurement, the process air mass flow rate was tuned to a specific value and kept constant for about 2 minutes. Data were collected at a rate of one set per second and averaged over a total of about 80 readings. During the experiments, an additional measurement of the pressure drop across the test

matrix was made manually with the Dwyer Microtector described earlier. This backup measurement was consistent with the recording of the electronic pressure transducer within the accuracy range of the calibration curve for all measurements.

For each measurement period, an average process air temperature, humidity and pressure are defined as the average of the respective inlet and outlet states over time. The pressure drop across the test matrix and the mass flow rate through the matrix are also averaged. Figure 5.1 shows the pressure drop across the test matrix as a function of the mass flow rate for the four experiments. This figure indicates the ranges for the process air mass flow rate and the overall flow resistance of the matrix for the experiments studied in this work. The experiments are labeled P1-1, P1-2, P1-3, and P2-1, and are analyzed in three combinations of each two experiments: P1-1 and P1-2, P1-2 and P1-3, and P1-2 and P2-1. The numerical data are tabulated in Tables C.1.1 through C.1.4 in Appendix C.

P1-2 and P1-3 are pressure drop experiments performed on the same test matrix with different orifice plates for the flow rate measurement. Using the pressure drop across the matrix as reference, the measured mass flow rates in both experiments can be compared and form a check for the accuracy of the flow rate measurement and conversion. This comparison is presented and discussed in Section 4.2.5 and indicates correct measurement of the mass flow rate.

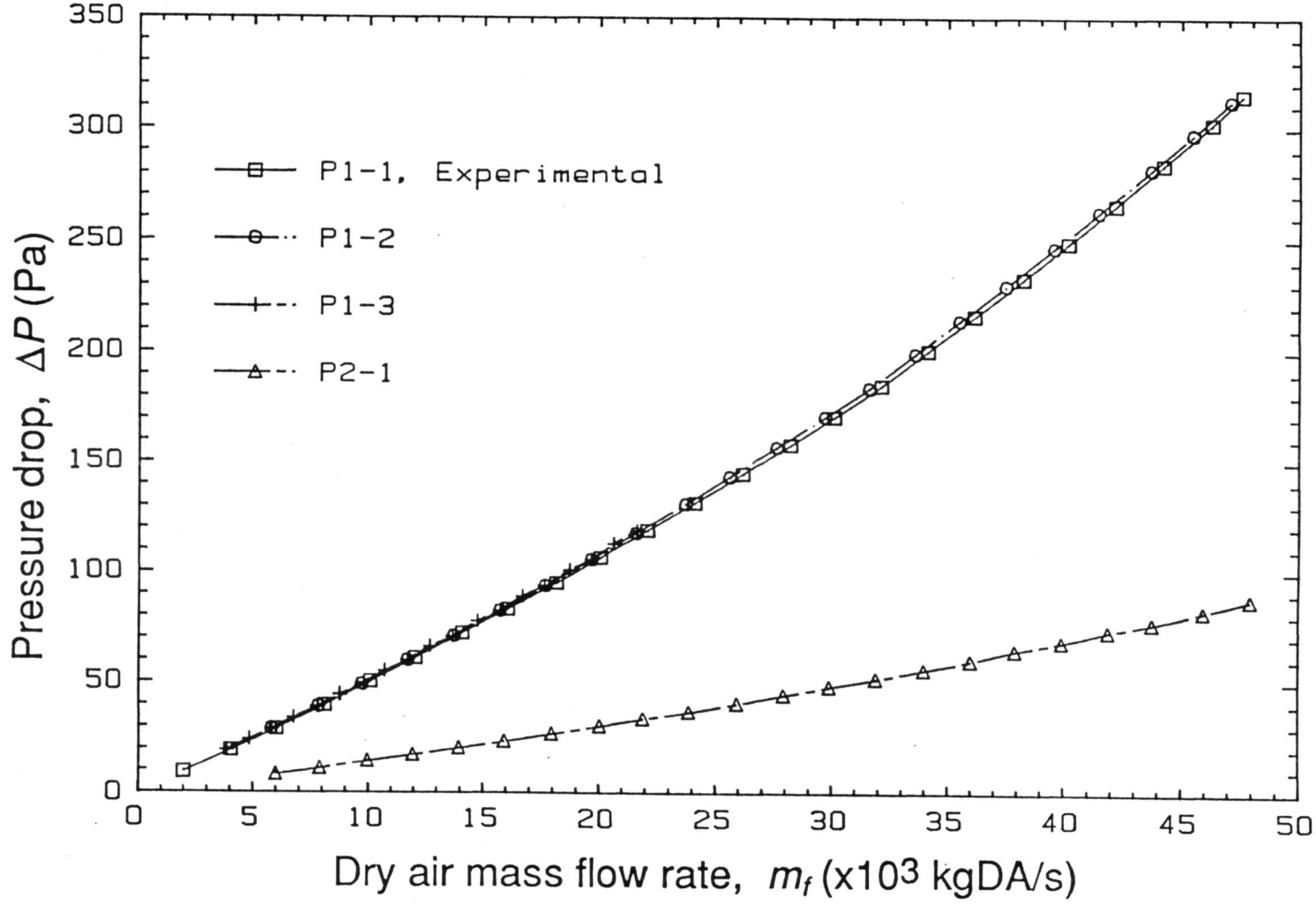

Figure 5.1 Experimental pressure drop across the test matrix as a function of the process air mass flow rate.

P1-1 and P1-2 are pressure drop experiments performed on the same matrix with the same orifice plate for each experiment. P1-1 was recorded before the series of sorption experiments were started, and P1-2 after these experiments were finished. A comparison between these two experiments forms a check on the repeatability of the flow characteristics of the experimental facility.

P1-2 and P2-1 are pressure drop experiments performed on two different test matrices. Both matrices are geometrically related to each other, and, by comparison of the test results, the complete geometry of the test matrices can be determined.

5.2.2 Analysis and Discussion

5.2.2.1 Pressure Drop for Laminar Flow through Passages with Rough Surfaces

A general flow passage can be characterized by three independent parameters: the wetted transfer area A, the free flow area A_c and the flow length L (Kays and London, 1984). The hydraulic diameter D_h is defined as

$$D_h = 4L\frac{A_c}{A} \tag{5.1}$$

The average fluid velocity U for a flow through the passage is computed from the fluid mass flow rate, $\dot{m}_f$,

$$U = \frac{\dot{m}_f}{\rho A_c} \quad . \tag{5.2}$$

and the Reynolds number *Re* for a Newtonian fluid is defined as:

$$Re = \frac{U D_h}{\upsilon} . \tag{5.3}$$

The pressure drop for fully developed flow through the passage is conventionally expressed in terms of a friction factor *f*,

$$\Delta P = \frac{\rho U^2}{2} \left(f \frac{4L}{D_h}\right) ,$$

or, (5.4)

$$\Delta P = \frac{\rho U^2}{2} \left(f \frac{A}{A_c}\right) \quad .$$

These expressions define the friction factor *f*. *f* depends on the geometry of the passage, the Reynolds number and the roughness of the surfaces of the passage. For fully-developed laminar flow and smooth passages, the product of the friction factor and Reynolds number, *fRe*, is a constant depending only upon the geometry of the passages. *fRe* has been computed for well-defined geometries, and theoretical values are 14.2 for square ducts; 16 for circular ducts; and 24 for parallel plates. For rectangular channels with height *b* and width *W* (Cornish, 1928), *fRe* is

$$fRe = \frac{24}{(1+\frac{b}{W})^2[1-\frac{192}{\pi^5}\frac{b}{W}(\tanh(\frac{\pi W}{2b})+\frac{1}{3^5}\tanh(\frac{3\pi W}{2b})+...)]} \quad (5.5)$$

For rectangular passages with aspect ratio $W/b > 3$, this latter formula can be simplified to the following expression with an error of less than 0.01%:

$$fRe \approx \frac{24}{(1+\frac{b}{W})^2(1-0.63025\frac{b}{W})} \quad (5.6)$$

Equation (5.6) is used in the subsequent part of this analysis.

The effect of small surface roughnesses on the flow resistance of passages has been studied by many researchers (Schlichting, 1979). The classic experiments of Nikuradse show the effect of the Reynolds number and the relative wall roughness on the friction factor for flow through artificially-roughened, circular pipes. Moody determined the flow resistance of commercially rough pipes and introduced the concept of an equivalent sand roughness. Both works show that the effect of small surface roughnesses, in the range of 0 to 5%, on the functional relationship between the friction factor and the Reynolds number is negligible for laminar flow. In the region of laminar flow, rough pipes have the same resistance as smooth pipes.

Whereas the wall shear area A and the free flow area A_c are well defined for surfaces with small roughness, the

definition of these areas becomes ambiguous for surfaces with large, irregular roughness. Furthermore, the presence of large wall protuberances may affect the functional relationship between the friction factor and the Reynolds number. Recent experimental research on the flow resistance of rough passages is directed toward the enhancement of single phase convective heat transfer (Bergles, 1981). The surface roughness is produced artificially and ranges from a random sand-grain type to discrete surface protuberances, arranged in a regular pattern. These surface irregularities act as turbulence promoters to increase the convective heat transfer coefficient between the fluid and the passage wall. In their bibliography on augmentation of convective heat and mass transfer, Bergles and Webb (1978) list 200 references to studies on single phase fluid flow over rough surfaces. However, the majority of the publications deals with turbulent flow, and only few study the effect for internal, laminar flow (Brauer, 1961; Molloy, 1967; Zappa and Geiger, 1971).

Brauer (1961) reported pressure drop experiments for laminar flow through an annular gap with an artificially roughened inner tube surface and a smooth outer tube surface. The height of the annular gap is 2.15 mm and the mean radius of curvature is 17.1 mm. The friction factor-Reynolds number product for a smooth circular annulus with these dimensions is 23.7. In a first series of the described experiments, rec-

tangular ribs are machined circumferential around the inner tube. The ribs have a square cross section, 300x300 μm, and are spaced, respectively for three alternate experiments, 300, 600 and 1200 μm apart. The friction factor-Reynolds number product derived from his experimental data agrees with the theoretical value for a smooth annulus formed by the actual outer tube and an imaginary, smooth inner tube, encircling the actual inner tube with ribs. In a second series of Brauer's experiments, 350x300 μm wedge type grooves are machined on the inner tube surface. The grooves are spaced, respectively for 3 alternate experiments, 0, 300 and 600 μm apart. For these annuli, the experimental value of fRe agrees with the theoretical value, 23.7.

The geometry in the work of Molloy (1967) is that of a 12.7 mm I.D. smooth tube with a 178 μm wire spirally wound and brazed to the inside surface of the tube with a pitch of 10 times the diameter. The report describes pressure drop experiments on this rough tube and on a smooth tube with the same inner diameter. Molloy discusses the importance of choosing the proper hydraulic diameter for correlating the friction factor, and recognizes the fact that, under laminar flow conditions, the separation before and after the isolated roughness elements produces 'dead' spaces of still air which affect the mean free flow area. In his analysis, the wire root diameter of the rough tube is used as the base for the friction factor

and it is shown experimentally that the calculated friction factors for the smooth and rough tubes are in good agreement with each other for laminar flow.

Zappa and Geiger (1971) report an experimental investigation of the effect of transverse surface fins in an annulus on the pressure drop of transformer oil in laminar flow. The internal diameter of the outer tube is 38.35 mm and the inner tubes have a root diameter of 26.75 mm. The height of the fins for the inner tubes ranges from 635 to 3175 μm with a pitch of 12.7 and 25.4 mm. The authors determine the friction factor as a function of the Reynolds number and show that the friction factor increases with the fin height. However, in their study, the Reynolds number is based on the hydraulic diameter of a smooth annulus for all experiments. Hence, the variation in friction factor with fin height may be explained by an improper choice of hydraulic diameter.

Based on the work of Brauer and Molloy, this author assumes the following hypothesis with respect to the analysis of the pressure drop data in this work:

> For fully developed, laminar flow through passages having surfaces with large roughness, the friction factor-Reynolds number product is the same as that for smooth passages. The flow area, A_c, appearing in the pressure drop equation (5.4), is the average of the actual flow area of the fluid

over the flow length. The wall transfer area in Eq. (5.4), *A*, is the actual area sheared by the fluid over wall and particle surfaces, and small pockets of still fluid in between the individual particles. The shear area *A* may differ from the total internal surface area of the walls of the flow passage.

5.2.2.2 Analysis of the Pressure Drop Experiments

Experiments P1-1 and P1-2 are pressure drop tests, conducted, respectively, before and after the sorption experiments which took about 3 weeks. The experimental data shown in Figure 5.1 indicate a small difference between the data of these two experiments. An analysis based upon cubic spline interpolation with optimized locations of the spline knots, indicates that the mass flow rate of P1-1 is consistently about 1% higher than the flow rate of P1-2 for the same pressure drop across the test matrix. If the effect of different air state conditions is included, this bias increases to 2%. The analysis further shows that the difference between the two tests can not be contributed to either a relative or absolute bias in the measurement of the flow rate or in the pressure drop measurement. However, the difference in mass flow rates for a given pressure drop across the matrix and including

density effects can be accurately correlated with that matrix pressure drop,

$$\Delta\dot{m}_f = 3.25 \times 10^{-5} \sqrt{(2\rho\Delta P)}, \qquad (5.7).$$

where $\Delta\dot{m}_f$ is the flow rate difference, ρ is the air density at the inlet face of the test matrix, and ΔP is the pressure difference across the test matrix. Because the exhaust of the test matrix leads directly into the laboratory room, ΔP can also be interpreted as the static pressure head at the entrance section of the test section. Equation (5.7) thus shows that the difference in mass flow rates may be attributed to a small flow leak from the section in front of the test matrix. A visual inspection of the experimental facility showed that one of the seals of the windows of the test section had deformed during the course of the sorption experiments due to thermal effects, thus providing a path for air leakage. This flow leak is a maximum of about 2% of the total flow. Equation (5.7) is used as an additional correction for the mass flow rate conversion procedure described in Chapter 4. This correction increases the uncertainty of the mass flow rate measurement by 1%.

Experiment P1-2 is a conventional pressure drop experiment performed on the original test matrix described in section 4.1.2. The main features of this test matrix, relevant

to this discussion, are the presence of 74 flow passages spaced center-to-center 1693 ± 2 μm apart. Experiment P2-1 is a similar pressure drop experiment performed on a modified matrix. This matrix has an identical structure as that of the original matrix, except that it has 48 flow passages which are spaced 2524 ± 2 μm apart. The modified matrix has an additional spacer of thickness 794 ± 2 μm inserted between the spacers holding the desiccant sheets. The same sheets are used in both matrices. The spacings are obtained from the measurement of the total height of all the passages with vernier calipers divided by the total number of passages for each matrix.

In the subsequent discussion, index 1 refers to the original matrix and index 2 refers to the modified matrix. W denotes the measured width of the matrix. It is assumed that the individual desiccant sheets have identical geometrical characteristics. Therefore, there exist geometrical relationships between the transfer area and free flow area of both matrices. The transfer area of one flow passage is the sum of the unknown transfer area of two sides of a desiccant sheet and the wetted area of the side walls of the passage. The functional relationship describing this observation is:

$$\frac{A_1 - 2L(A_{c,1}/W)}{74} = \frac{A_1 - 2L(A_{c,2}/W)}{48} \tag{5.8}$$

The flow area of the modified passage is the sum of the unknown flow area of the original passage and the additional area of a rectangle of known height and width W,

$$\frac{A_{c,2}}{48} = \frac{A_{c,1}}{74} + (0.002524 - 0.001693)W, \qquad (5.9)$$

in which $A_{c,1}$, $A_{c,2}$ and W are expressed in m^2 and m, respectively.

The total pressure drop across the test matrix is the sum of the pressure losses due to the flow through the rectangular passages including entrance effects, and the additional losses at the entrance and exit faces of the matrix. The hydrodynamic entrance length, L_{hy} is defined as the axial distance in the flow direction, measured from the inlet face of the flow passage, at which the maximum fluid velocity reaches 99% of the maximum velocity for fully developed flow. For parallel plates, the hydrodynamic entrance length is given by Shah and London (1978) as a function of the Reynolds number and D_h:

$$\frac{L_{hy}}{D_h} = \frac{0.315}{0.0175Re + 1} + 0.011Re \ . \qquad (5.10)$$

For the experiments reported in this work, the Reynolds number ranges from 100 to 600. Using Eq. (5.10), L_{hy} varies from 3 to 14 mm which is 1 to 7% of the total flow length of the passages. Therefore, for the recorded experiments, the

entrance effects are fully established and the flow is fully developed for the major part of the flow length.

Following Shah and London (1978), the pressure drop for fully developed flow through parallel plates, including entrance effects, is given by:

$$\Delta P = \frac{\rho U^2}{2} \left(fRe \frac{A}{A_c Re} + K_c \right). \tag{5.11}$$

U is the fluid velocity within the flow passage, $fRe = 24$, and $K_c = 0.674$. K_c represents the pressure loss due to entrance effects. The total pressure drop across the test matrix for the analyzed pressure drop experiments can be written in a form equivalent to (5.11),

$$\Delta P = \frac{\rho U^2}{2} \left(fRe \frac{A}{A_c Re} + K \right). \tag{5.12}$$

in which K is the sum of all loss coefficients,

$$K = K_i + K_c + K_f + K_e + K_o. \tag{5.13}$$

K_i represents the pressure loss due to the flow contraction in the conical inlet manifold of the matrix. The inlet manifold forms a smooth contraction for the fluid flow from the rectangular duct area A_d to the matrix rectangular inlet area A_{fr}. The loss coefficient for this configuration is given by White (1979),

$$K_i = 0.064\left(\frac{A_c}{A_{fr}}\right)^2. \tag{5.14}$$

K_c represents the irreversible pressure loss due to entrance effects of the flow entering the individual passages. A general formula for K_c for passages with arbitrary geometries is given by Kays (1950) and Kays and London (1984):

$$K_c = 0.8 - 0.4\left(\frac{A_c}{A_{fr}}\right)^2 \tag{5.15}$$

However, because a more precise value for K_c is known for the particular case of flow through parallel plates, that value is used for this analysis,

$$K_c = 0.674. \tag{5.16}$$

K_f represents the irreversible pressure loss due to the presence of internal wall protuberances within the passages, and is unknown from the literature. The estimated value for this coefficient derived from the experimental results reported is discussed later in this section.

K_e represents the irreversible pressure loss due to an abrupt flow expansion at the exit face of the test matrix, from the internal flow area, A_c, to the matrix face area, A_{fr}. Assuming a uniform velocity profile within the flow passage, a theoretical expression for K_e has been established (Kays, 1950; Kays and London, 1984):

$$K_e = 1.0 - 2.4\left(\frac{A_c}{A_{fr}}\right) + \left(\frac{A_c}{A_{fr}}\right)^2. \tag{5.17}$$

The outlet of the matrix into the duct is a sudden expansion from the matrix outlet face with area A_{fr} to the rectangular duct with area A_d. The pressure taps are mounted in the duct walls near the exit face where it can be assumed that the fluid jet is leaving the matrix at uniform velocity and has not yet expanded. The 'loss' coefficient is then the pressure head due to the flow velocity,

$$K_o = \left(\frac{A_c}{A_{fr}}\right)^2 \left(1 - \left(\frac{A_{fr}}{A_d}\right)^2\right). \tag{5.18}$$

The first factor in the right hand side of Eq. (5.18), which also appears in Eq. (5.14), arises from the definition of the loss coefficient in Eq. (5.12) which is referenced to the average fluid velocity U within the passages.

The pressure drop equation (5.12) can be rewritten in terms of dimensionless groups of known and unknown variables,

$$\frac{\Delta P\, L^3}{m_f \upsilon} = \left(\frac{K L^4}{2A_c^2}\right) \frac{m_f}{\mu L} + \frac{fRe}{8} \frac{L^2 A^2}{A_c^3} \tag{5.19}$$

Equation (5.19) expresses a linear relationship between the two dimensionless groups, $\Delta P\, L^3/m_f \nu$ and $m_f/\mu L$. Both groups contain only variables which can be either directly or indirectly obtained from measurements. Figure 5.2 shows the experimental

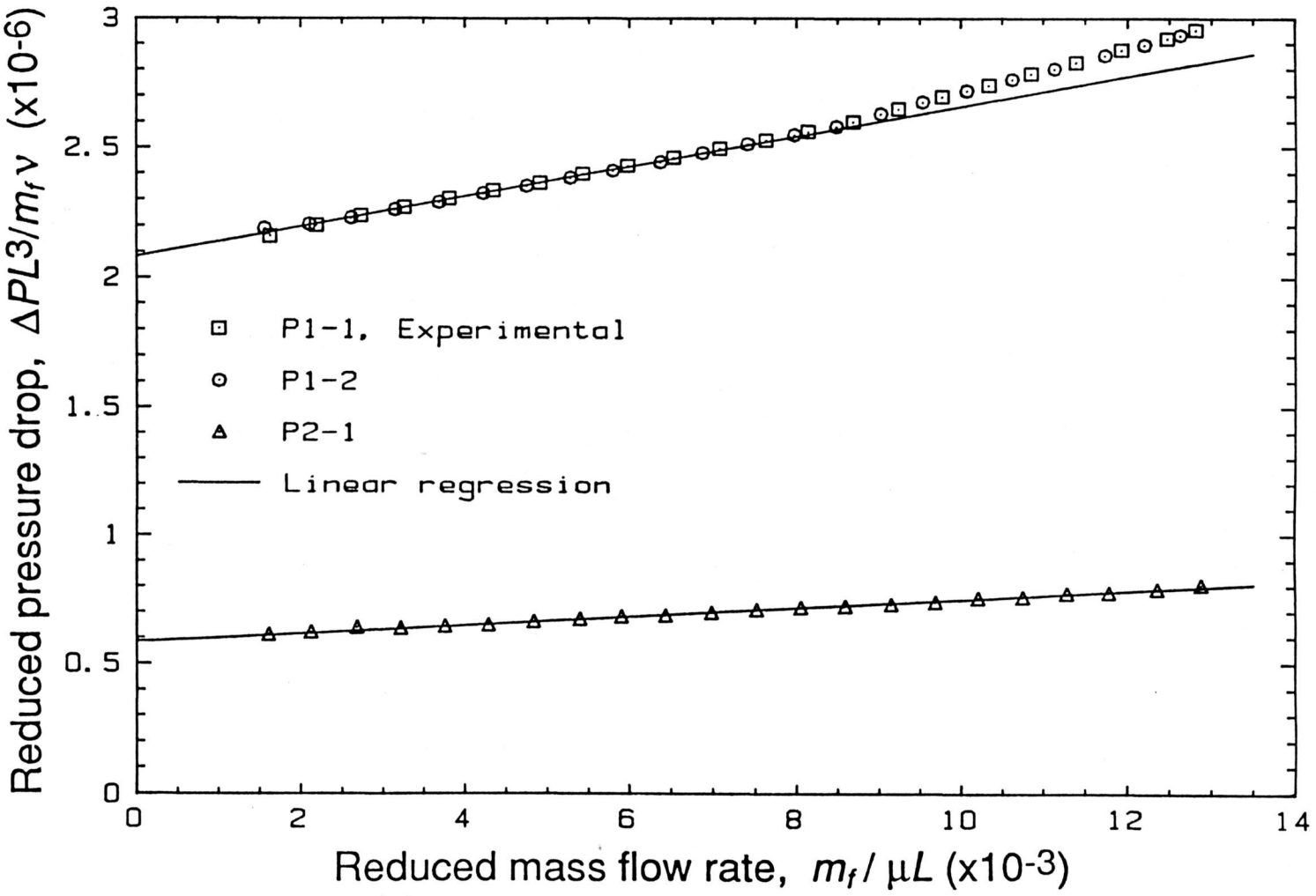

Figure 5.2 Reduced pressure drop across the test matrix as a function of the reduced flow rate.

results of tests P1-2 and P2-1 in a diagram with ordinates, $\Delta PL^3/m_f\nu$ and $m_f/\mu L$. A linear, least squares regression of the experimental data of P2-1 gives a straight line with a slope of 16.75±3%, an intercept of 581,218±0.6%, and the r^2 is 99.6%. The data of test P1-2 indicate a straight line for $m_f/\mu L <$ 9000. Within this region, the experimental data can be fitted with a straight line with a slope of 57.67±1.2%, an intercept of 2,080,920±0.2% and the r^2 is 99.7%.

Outside this region the slope of the curve changes abruptly. The passage Reynolds number at this transition point is about 350. The Reynolds number based upon the particle diameter is given by

$$Re_p = \frac{fRe}{4}\frac{D_p^2}{D_h^2}Re, \qquad (5.20)$$

and is about 24 at the flow at which the pressure drop pattern changes. Separation of external flow about isolated spheres starts at a Re of 24 hence, the change in pressure drop can be explained by the onset of separation of the flow about the individual particles.

From the dimensionless pressure drop equation (5.19), the following expressions are obtained for the intercepts in terms of the experimental data:

for P1-2,

$$\frac{fRe}{8}\frac{L^2A_1^2}{A^3_{c,1}} = 2{,}080{,}920 \pm 0.2\%, \tag{5.21}$$

and for P2-1,

$$\frac{fRe}{8}\frac{L^2A_1^2}{A^3_{c,2}} = 581{,}218 \pm 0.6\%. \tag{5.22}$$

The friction factor-Reynolds number product of each passage is given by the simplified Cornish expression (5.6). The width of the passages for each matrix is known from direct measurement with vernier calipers, and the height of the passages can be computed from the flow area,

$$b = \frac{A_c / Number\ of\ Passages}{W} \tag{5.23}$$

Equations (5.8, 5.9, 5.21, 5.22), supported with Eq. (5.23) in conjunction with Eq. (5.6), can be solved by a successive substitution procedure yielding the unknown matrix areas, $A_{c,1}$, $A_{c,2}$, A_1 and A_2. The results of this iteration for the original test matrix are: $A_{c,1} = A_c = 0.00927 \pm 2\%$ m^2, $A_1 = A = 3.68 \pm 3.5\%$ m^2, and $fRe_1 = fRe = 23.70$. The flow height of each passage is 1080 μm and $D_h = 2061$ μm.

The theoretical values for the loss coefficients K_i, K_c, K_e, and K_o in Eq. (5.13) can now be computed using Eqs. (5.14, 5.16-18) and, excluding the loss coefficient associated with the internal wall effects K_f, is 0.88 for the original matrix.

The total loss coefficient can be computed from the experimental data using the theoretical expression for the slope in Eq. (5.19) and is 5.84±7%, yielding K_f = 5.84 - 0.88 = 4.96. For the second matrix with larger sheet spacings, the experimental total loss coefficient is only 2.23 and K_f = 1.34. A theoretical analysis assuming that K_f is due to incremental pressure drops across individual particles indicates that K_f is proportional to $(L/D_h)(D_p/D_h)^2$. The ratio of this group for the two test matrices is 0.2 whereas the ratio of K_f for both matrices is 0.3. Thus it is shown that a major fraction of the pressure drop across the test matrix is due to the protrusion of the individual particles in the fluid stream. The author could not find published work which supports these quantitative findings.

Finally, the experimental pressure drop data for experiments P1-1 through P2-1 are presented in a diagram with the product $f_{app}Re$ and Re as ordinates in Figure 5.3. f_{app} is the apparent friction factor, and is defined as

$$\Delta P = \frac{\rho U^2}{2} \left(f_{app}Re \frac{A}{A_c Re}\right). \tag{5.24}$$

This figure indicates the repeatability of the pressure drop experiments, the range of Reynolds numbers of interest to this work, and the important effect of internal losses on the total pressure loss in comparison with the pressure drop across a smooth passage with identical dimensions.

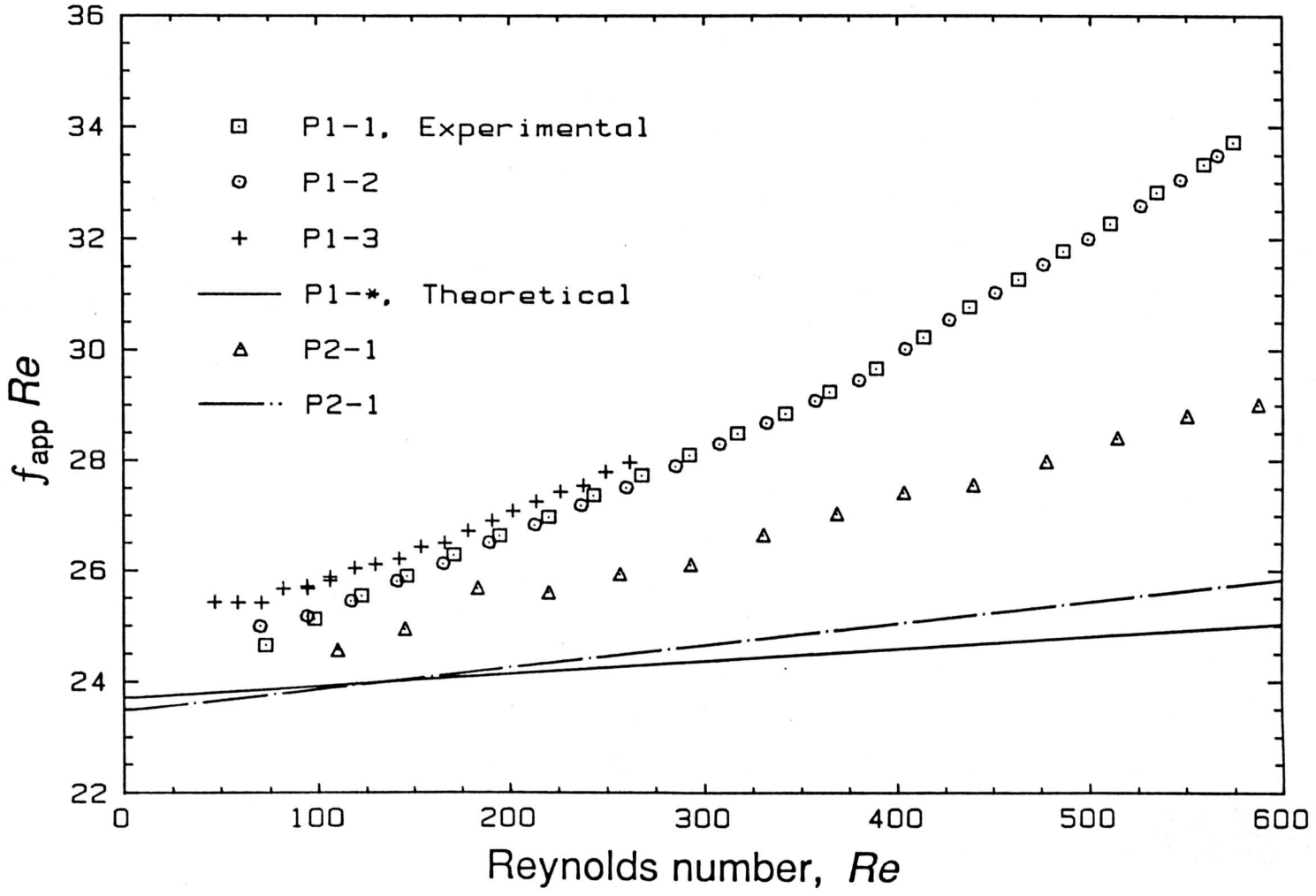

Figure 5.3 Apparent friction factor of the test matrix as a function of the Reynolds number.

5.2.3 Surface and Core Geometry of the Test Matrix

The geometry of a heat exchanger is fully characterized by a set of four parameters (Kays and London, 1984). These parameters are the free flow area A_c, the transfer area A, the frontal area A_{fr} and the flow length L. The flow length and frontal area can be measured directly with high accuracy. The calculation of the free flow area and the transfer area with the pressure drop analysis completes the list of geometric parameters. A complete listing of all geometric parameters of the test matrix is given in Table 5.1.

The free flow area divided by the number of passages and the passage width yields the average height of a flow passage. The center-to-center spacing of the passages is measured directly and the thickness of the carrier sheets with no particles is known from the manufacturer's data. The average desiccant layer thickness can then be computed and is 269 μm. This value should be compared to the desiccant particle diameter which ranges from 177 to 297 μm with an average value of D_p = 217 μm. The geometry of a flow passage is pictorially shown in Fig. 5.4.

The total transfer area A, 3.68 m^2, consists of the shear area along the desiccant sheets and the shear area along the metal walls of the aluminum matrix. Thus, A is the total transfer area for heat and momentum. The transfer area of the

Table 5.1 Surface and core geometry of the test matrix

Exchanger Geometry				
Free Flow Area	A_c	0.00927 ± 3.0%	m^2	(3)
Frontal Area	A_{fr}	0.0146 ± 1.5%	m^2	
Heat & Momentum Transfer Area	A	3.68 ± 4.5%	m^2	(3)
Mass Transfer Area	A	3.65 ± 4.5%	m^2	
Flow Length	L	0.203 ± 0.5%	m	(1)
Hydraulic Diameter	D_h	2.061 ± 6.0%	µm	
Porosity	p	0.635 ± 4.0%	/	
Flow Passage Geometry (Rectangular)				
Average Height	b	1.080	mm	
Width	W	116 ± 0.9%	mm	(1)
Length	L	203	mm	(1)
Number of Passages		74	/	(1)
Center-to-Center Spacing		1.693 ± 0.1%	mm	(1)
Desiccant Sheet Geometry				
Carrier Thickness		25.4	µm	(2)
Adhesive Thickness (2x)		25.4	µm	(2)
Tape Thickness		76	µm	(2)
Particle Size Range		177 - 297	µm	(2)
Average Particle Size	D_p	217	µm	(2)
Avg. Particle Layer Thickness		269	µm	
Sheet Thickness Range		? - 889	µm	(1)
Apparent Sheet Thickness		613 ± 3%	µm	
Sheet Length	L	203	mm	(1)
Total Sheet Width		169	mm	(1)
Sheet Width with Particles	W	116	mm	(1)
Number of Sheets		75		(1)
Center-to-Center Spacing		1.693	mm	(1)
Matrix Geometry				
Spacer Dimensions (WxHxL) (150x)		25.4x0.794x203	mm	(1)
Lid Dimensions (WxHxL) (4x)		83.5x17.0x203	mm	(1)
Rod Dimensions (ϕxL) (6x)		12.7x144	mm	(1)
External Matrix Dimensions (WxHxL)		169x161x203	mm	(1)
Dimensions of Exchanger Part (WxHxL)		116x126x203	mm	(1)
Duct Geometry (Rectangular)				
Dimensions (WxH)		173x166	mm	(1)
Free Flow Area	A_d	0.0286	m^2	

Source
(1) Independent variable(s), measured with vernier calipers.
(2) Independent variable(s), supplied by manufacturer.
(3) Independent variable(s), from pressure drop analysis.

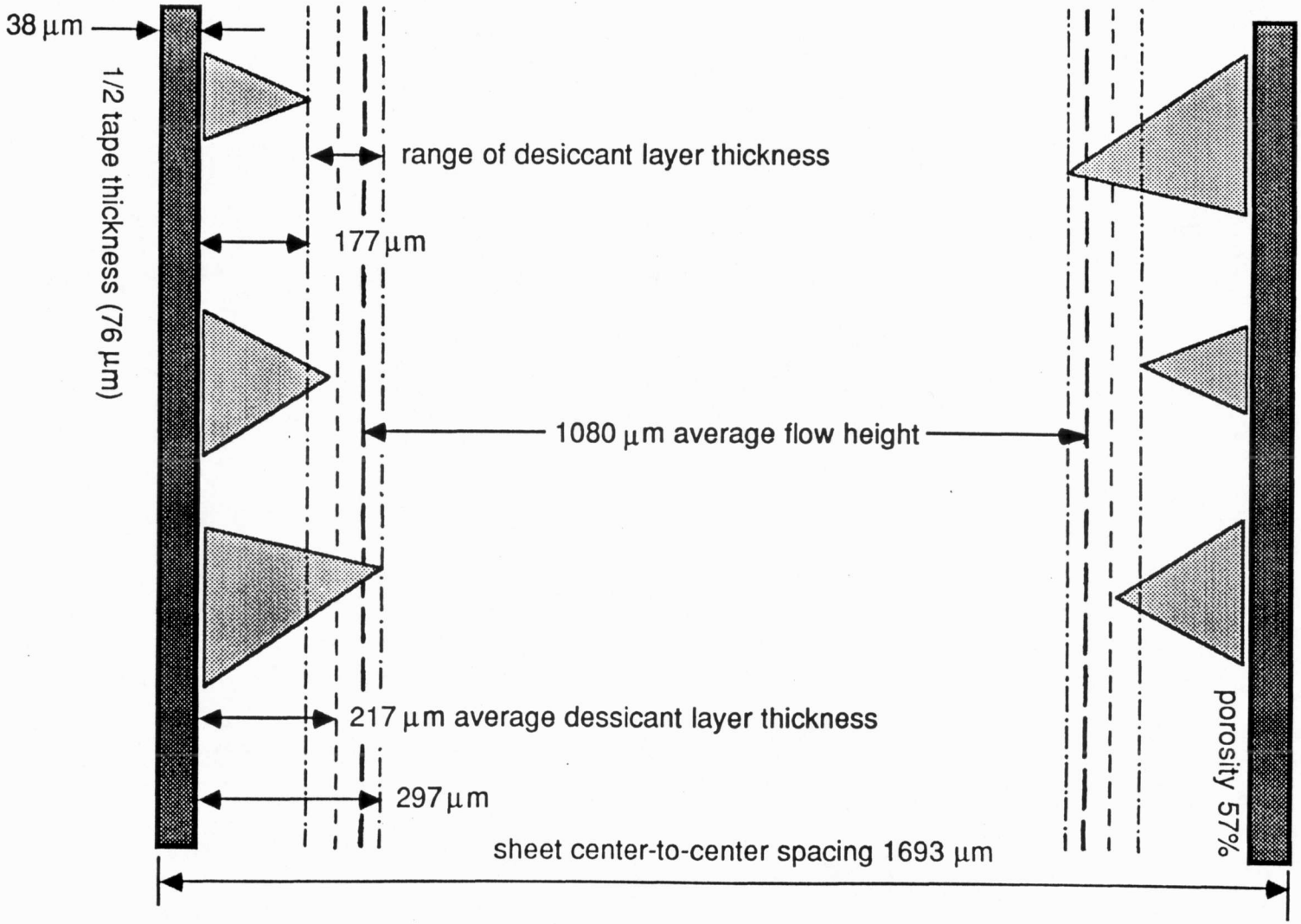

Figure 5.4 Schematic configuration of the flow passages.

desiccant sheets is 3.65 $m^2 \pm 3.5\%$. The difference is within the limits of accuracy of the computed areas. The transfer area A is about 5% higher than the sheet surface areas, computed as if they were flat square surfaces.

The mass of desiccant within the matrix is computed from the heat and mass transfer experiments in the next chapter and is 0.487 kg. The volume of the desiccant layer, computed from the density of silica gel, is 402 cm^3. The external surface area of the particles is given by the manufacturer and is 276.5 cm^2/cm^3 yielding a total particle surface area of 11.13 m^2, which is about 3 times the estimated transfer area of the desiccant layer. This discrepancy indicates that only about 33% of the desiccant particles surface is in contact with the air stream. The remainder of the desiccant surface is in contact with pockets of still air and the carrier substance. The macroporosity of the desiccant layer, i.e. the interparticle porosity, is about 57%.

5.3 Dynamic, Adiabatic Sorption Experiments with Varying Matrix-Initial and Fluid-Inlet States

This section describes the analysis of dynamic sorption experiments in which the thermodynamic equilibrium properties of the desiccant matrix are computed. As for the geometrical

parameters of the matrix, these properties cannot directly be measured with methods that are independent of the nature of sorption experiments. The mass of desiccant, the matrix thermal capacitance, and the sorption-isotherm type of the desiccant are computed from an analysis of a series of specifically designed, dynamic sorption experiments.

The amount of desiccant attached to the desiccant sheets is needed for subsequent parts in the analysis. The desiccant mass determines the external surface area of the particles and the macroscopic porosity of the desiccant layer. This quantity can, however, only be roughly estimated from an account of the silica-gel volume used for the manufacturing of the desiccant sheets. The analysis of the sorption processes requires further the thermal capacitance of the test matrix. The matrix acts as a heat store, and its capacitance determines the heat exchange with the air stream relative to that with the desiccant. The lumped thermal capacitance of the test matrix can be computed from the material properties of the individual structural parts. However, because the aluminum frame of the matrix is only in indirect contact with the air stream, it is uncertain which of these parts participate directly in the energy exchange with the air stream. The variability of the sorption-isotherm of commercial silica gel is discussed in Chapter 3. It is shown that there exist two basic isotherm shapes for regular-density silica gel. The isotherm of the gel

within the test matrix is obtained from sorption experiments performed on the actual test matrix.

5.3.1 Experimental Results

The experiments which form the subject of this second analysis are a series of 8 dynamic sorption experiments. In these experiments, an air stream with fixed inlet conditions is passed through the desiccant matrix which is initially at an established equilibrium state. Parameters for the experiments are the fluid inlet state and the matrix initial state. These conditions are varied systematically for the different experiments. The air flow rate is the same for all experiments. Data for each experiment are collected and converted using the procedures explained in the previous chapter.

The conditions for each experiment are given in Table 5.2. This table lists the matrix preparation conditions, the estimated matrix initial conditions and the air stream inlet conditions for each experiment. These experiments are designed to yield maximum information about the sorption isotherm of the silica gel. Table 5.2 indicates that the water content of the gel for the initial conditions of the desorption experiments and the inlet conditions of the adsorption experiments, are approximately equal for corresponding experiments. These conditions are chosen such that they are uniformly distributed on

Table 5.2 Preparation, initial and inlet conditions for the I-series of dynamic sorption experiments.

The mass flow rate is approximately 0.02 kg-dry-air/s

	PREPARATION CONDITIONS				INITIAL CONDITIONS				INLET CONDITIONS			
ExpID	t_f	w_f	P	W_d	t_f	w_f	P	W_d	t_f	w_f	P	W_d
	°C	kg/kg	Pa	kg/kg	°C	kg/kg	Pa	kg/kg	°C	kg/kg	Pa	kg/kg
					adsorption experiments							
I1-A	65.2	0.03235	81420	0.07803	54.4	0.02230	81430	0.08972	30.5	0.02709	81430	0.33796
I2-A	72.1	0.03235	83330	0.06374	54.3	0.01570	83130	0.07287	30.6	0.02209	83130	0.30975
I3-A	79.5	0.03225	82600	0.04991	64.1	0.01960	82660	0.06032	31.7	0.01797	82660	0.25314
I4-A	85.5	0.03232	82860	0.04054	66.3	0.01750	82870	0.05231	29.5	0.01474	82870	0.23994
I5-A	80.4	0.01705	83150	0.02972	63.3	0.00960	83020	0.03856	30.1	0.01196	83020	0.18955
I6-A	79.5	0.01201	83220	0.02255	65.6	0.00710	83070	0.02729	31.0	0.00981	83070	0.14654
I7-A	**********				TEST FAILED				**********			
I8-A	79.5	0.01202	82610	0.02240	75.0	0.00800	82660	0.01893	67.1	0.02684	82660	0.06623
					desorption experiments							
I1-D	30.1	0.02698	81390	0.34017	30.7	0.02630	81440	0.33278	62.6	0.02708	81440	0.07612
I2-D	30.2	0.02203	82850	0.31293	31.8	0.02230	82730	0.29705	65.0	0.02208	82730	0.06300
I3-D	30.2	0.01792	82950	0.27289	33.2	0.01950	83010	0.25214	67.9	0.01797	83010	0.05042
I4-D	30.2	0.01469	82910	0.23006	34.6	0.01720	82830	0.20683	70.8	0.01473	82830	0.03926
I5-D	30.2	0.01198	83220	0.18915	33.7	0.01370	82950	0.17368	66.9	0.00817	82950	0.02893
I6-D	30.2	0.00985	83270	0.15506	34.3	0.01150	83410	0.14087	76.2	0.00985	83410	0.02201
I7-D	30.2	0.02706	83420	0.34254	29.2	0.02490	83420	0.34019	30.0	0.01207	83420	0.19346
I8-D	71.7	0.03231	82950	0.06430	64.8	0.02540	83050	0.06909	66.6	0.00640	83050	0.02368

the second branch of the sorption isotherm expressed in terms of the desiccant water content as a function of the adsorption potential. This branch is mainly determined by the values of the physical parameters $W_{o,2}$ and $E_{o,2}$. The water content for the initial conditions of the adsorption experiments and the inlet conditions of the desorption experiments scan that part of the isotherm which is determined by the parameters $W_{o,1}$ and $E_{o,1}$. The analysis of the experimental results uses this information to separate the effects of these correlated parameters.

The outlet response for each of the experiments is shown in Figures C.2.1.a through C.2.8.b in Appendix C. These figures show the measured inlet and outlet temperatures and humidities as a function of time. The alternate experiments are labeled I1-A to I8-D, where the indices A and D refer to adsorption and desorption, respectively. Experiments I7 and I8 show the outlet response for a near step change in inlet humidity. The quality of these experiments is poor because of practical limitations of the experimental facility. They are included for completeness to illustrate the principle of closed-cycle sorption air-conditioning systems, in which air is cooled or heated by moisture exchange with the desiccant.

Figures C.2.1 - 8 also show the non-closure of the temperature response for the desorption experiments. This effect can be attributed to heat transfer from the air stream

to the aluminum frame of the test matrix and a small heat loss to the surroundings. The rate of heat transfer to the matrix is determined by heat conduction through the tapes carrying the desiccant and by convection at the sides of the passages. This rate of heat transfer determines the time constant for temperature variations of the metal frame. Assuming the tape carriers act as rectangular fins, the time constant can be computed and is about 2800 s. This is also the time scale of the experiments which is independently determined by the mass of desiccant and the air mass flow rate, and thus temperature variations of the matrix may be expected. Further evidence supporting this hypothesis is the consistent bias between preparation and initial temperatures for the desorption experiments I1-D through I6-D in Table 5.2. During the preparation phase of the experiment, the desiccant sheets are established at a uniform equilibrium temperature, 30.2 °C. During the bypass period, the temperature of the desiccant increases and the increase is larger for higher preparation temperatures of the preceding adsorption experiment, I1-A through I6-A respectively. Following the analysis of Carslaw and Jaeger (1959) for transient temperature distributions within slabs of finite thickness, the dimensionless response time for the desiccant sheets is 0.065. This number is sufficiently large to explain the temperature increase of the desiccant sheets during the bypass phase and the aluminum frame of the matrix thus acts as

a thermal store. The heat exchange between the matrix and the air stream can be twice to three times as large as the heat exchange with the desiccant. It causes nonuniform initial temperature distributions within the desiccant layers and the analysis of the experimental data has to be corrected for the heat loss. This phenomenon is a nuisance and forms a practical limitation of the experimental facility, due to the particular design of the test matrix.

The gradual change in pattern of the breakthrough curves from experiments I1-D to I6-D illustrates the remarkable non-linearity of the sorption isotherm of regular-density silica gel. Breakthrough curves exhibiting both expansion and shock wave behavior, such as in I1-D and I2-D, are rare. This author could not find published work showing this particular behavior for regular-density silica gel. The effect of nonlinearity has major consequences. Dynamic desorption behavior as shown in Figs. C.2.1-8 can only be predicted with functional models for the sorption isotherm that have high accuracy for evaluating the sorption capacity **and** the derivative thereof, including the differential heat of sorption. The Weibull form of the Dubinin-Polanyi model satisfies both criteria, e.g., this model does predict the mixed wave pattern of experiment I1-D. However, the isotherm proposed by Brandemuehl (1982) and subsequently used by many researchers (e.g., Jurinak, Mitchell and Beckman, 1984; Burns, Mitchell and Beckman, 1985; Van den

Bulck, Mitchell and Klein, 1986) predicts a pure shock wave for experiment I1-D. Not recognizing the mixed pattern behavior of the breakthrough curves can result in underestimating the total breakthrough time of the desorption cycle, and consequently, underestimating the required regeneration energy. The most significant conclusion of the series I sorption experiments presented in this study is that, for modeling desiccant systems, it is experimentally shown that a form for the sorption isotherm is required which is accurate in predicting both the amount of sorption and the differential thereof.

5.3.2 Analysis and Discussion

This section describes the calculations of the mass of desiccant, the matrix specific heat, and the sorption-isotherm type. The verification of the isotherm model requires the lumped, matrix specific heat, defined as the overall thermal capacitance of the matrix per unit mass of desiccant. However, evaluation of the matrix specific heat needs an expression for the isotherm and the amount of dry desiccant mass. Computation of the amount of desiccant requires the isotherm expression. Hence, the analysis for determining these parameters is iterative. The desiccant isotherm which gives the best agreement with the experiments is the isotherm with the low

value for $E_{o,2}$. This isotherm expression is used in the analysis presented next.

5.3.2.1 Active Mass of Desiccant

The mass of active dry gel contained within the test matrix is computed from an overall mass balance integrated over time,

$$\int_{o}^{\infty} \dot{m}_f \, (w_{f,1} - w_{f,2}) \, d\theta = M_d \, (W_{d,2} - W_{d,1}), \qquad (5.25)$$

where $(w_{f,1} - w_{f,2})$ is the instantaneous difference between the air stream inlet and outlet humidity, $(W_{d,2} - W_{d,1})$ is the difference between the desiccant final and initial equilibrium water content, and M_d is the mass of dry desiccant. For each experiment, there exist two values for the desiccant water loss computed from the isotherm with the high and low value for $E_{o,2}$, respectively. The integral in Eq. (5.25) is computed from the experimental results using Simpson's integration rule, which has second order accuracy. Small corrections can be applied to the measured values of the air-stream humidity difference to compensate for the non-closure of the outlet-humidity response and thus to provide a limiting value for the integral in Eq. (5.25).

Figure 5.5 shows the integral over time of the air stream humidity difference as a function of the difference in desiccant water content for the sorption experiments of series I and also of series M which are presented in the following section. The desiccant water term is computed with the isotherm with the low value for $E_{o,2}$, and the integral is not corrected for non-closure. The experimental data points fall on a straight line as indicated by Eq. (5.25). The linear least squares regression of the 42 data points, excluding experiments I1-D and I7-D, yields a slope of 0.489, an intercept of -0.0055 and r^2 = 99.6%. Setting the intercept to zero yields a slope M_d = 0.487 ± 3% kg-dry desiccant. This value compares very well with the value of 0.497 kg listed by Pesaran (1985), and obtained from an account of the volume of the silica gel used for the manufacturing of the desiccant sheets.

If corrections for non-closure are applied to the integral, the linear regression of the data points yields a slope of 0.446. For the isotherm with the high value for $E_{o,2}$, these numbers are 0.435 and 0.406, respectively. The differences between these numbers illustrate the sensitivity of the computed desiccant mass to the isotherm shape, and show that the variability of the isotherm can explain the difference between the values for the desiccant mass obtained from sorption experiments and a volume account, respectively. This

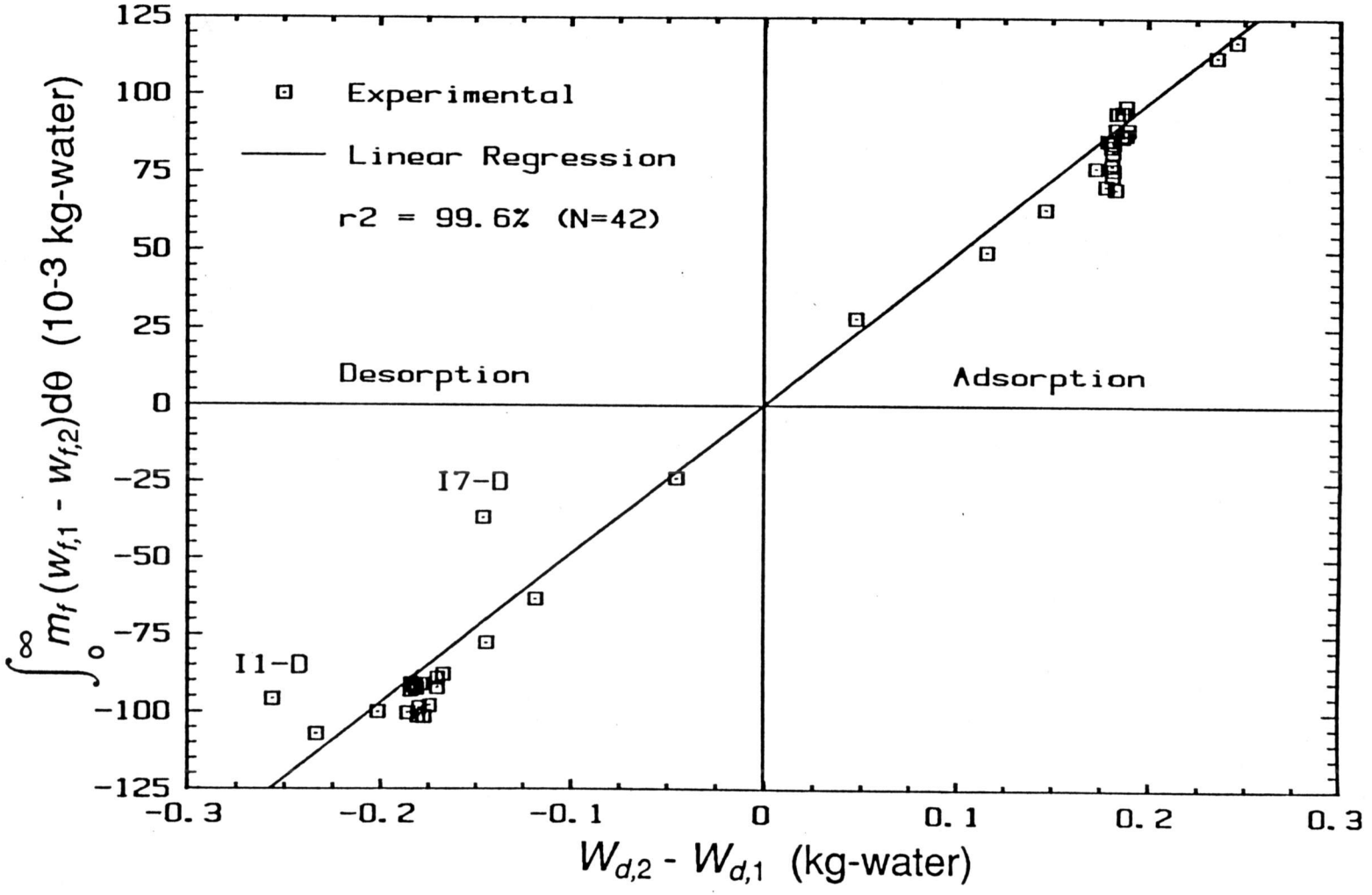

Figure 5.5 Integral of the experimental air stream humidity difference as a function of the desiccant water gain.

difference is often contributed to the hypothesis that certain sections of the desiccant particles become isolated from the water vapor, because the pores connecting these sections to the external particle surface may be blocked by the glue used to adhere the particles to the carrier (Pesaran, 1985). The results of the series I dynamic sorption experiments and the agreement between the experimental and theoretical values for the desiccant mass puts this hypothesis in question, and substantiates the accuracy of the isotherm with the low value for $E_{o,2}$ for computing the sorption capacity.

5.3.2.2 Thermal capacitance of the Matrix

The lumped thermal capacitance of the test matrix is computed from the individual parts of the matrix,

$$C_m = \sum_i M_{m,i}\, c_{m,i}, \tag{5.26}$$

where $M_i\, c_{m,i}$ is given by:

carrier tape:	0.241 kg	x 1350 J/kg·K	=	330 J/K
spacers:	1.540 kg	x 896 J/kg·K	=	1380 J/K
rods:	0.259 kg	x 896 J/kg·K	=	230 J/K
lids:	3.120 kg	x 896 J/kg·K	=	2800 J/K
				4740 J/K

The computed theoretical value of C_m is 4740 J/K.

The lumped thermal capacitance of the matrix can also be estimated from an overall energy balance integrated over time,

$$\int_0^\infty \dot{m}_f (i_{f,1}-i_{f,2})\,d\theta = M_d(I_{d,2}-I_{d,1}) + (C_m+UA)(t_{m,2}-t_{m,1}), \quad (5.27)$$

where $(i_{f,1} - i_{f,2})$ is the difference between the air stream inlet and outlet enthalpy at time θ, $(I_{d,2} - I_{d,1})$ the difference between the desiccant final and initial enthalpy, and $(t_{m,2}-t_{m,1})$ the difference in matrix final and initial temperature. C_m represents the thermal capacitance of the matrix, excluding the desiccant. *UA* represents the heat loss coefficient to the surroundings. Rearranging Eq. (5.27) gives an expression for the thermal capacitance,

$$\int_0^\infty \dot{m}_f (i_{f,1}-i_{f,2})\,d\theta - M_d(I_{d,2}-I_{d,1}) = (C_m+UA)(t_{m,2}-t_{m,1}), \quad (5.28)$$

The integral is computed with Simpson's rule and small corrections can be applied to the air temperature and humidity to compensate for the effect of non-closure of the outlet profiles. The desiccant enthalpy can be computed from the sorption isotherm with the low and high value for $E_{o,2}$, respectively.

Figure 5.6 shows the left hand side of Eq. (5.28) as a function of the temperature swing of the matrix. No corrections are applied to the integral and the low value for $E_{o,2}$ is used for the 44 data points in Fig. 5.6. The experimental

data follow approximately a straight line although the scatter of the data is somewhat larger than for the mass balance. The linear least squares regression of the data in Fig. 5.6 and excluding experiment I8-A, gives a slope of 5380 J/K with an intercept of 6170 J and r^2 = 99.0%. Setting the intercept to zero yields the experimental value $C_m + UA = 5390 \pm 200$ J/K. If the integral is computed with corrections for non-closure, the slope is 4170 J/K. For the isotherm with the high value for $E_{o,2}$, these numbers are 5390 and 4190 J/K, respectively.

Comparing the theoretical value for C_m with the experimental value for $C_m + UA$ shows that corrections to the enthalpy integral yield a negative value for UA, which is physically impossible. In the previous section, it is also shown that applying no corrections to the humidity integral gives a better comparison between experiment and theory. The value for UA is the same for both isotherms, thus no conclusion with regard to the preferred isotherm shape can be drawn from this analysis.

The numbers presented here show that only about 13% of the air-stream enthalpy is exchanged directly with the desiccant. The remainder is exchanged with the structural parts of the matrix, 78%, and the surroundings, 9%. This analysis indicates that the design of the matrix incorporates too much non-desiccant material, and does therefore not adequately represent the design of an actual dehumidifier in which the amount of structural material is minimized.

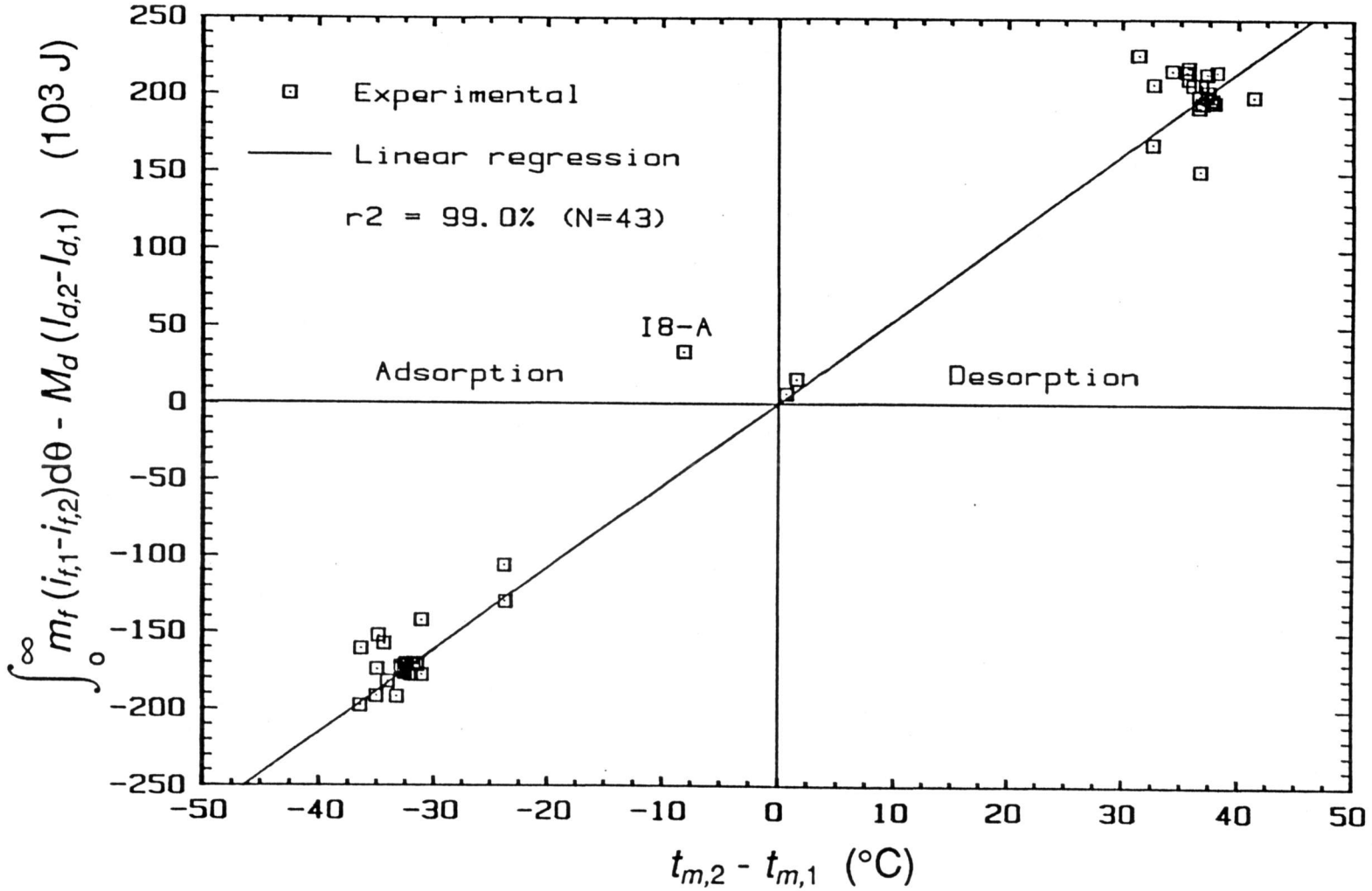

Figure 5.6 Integral of the experimental air stream enthalpy difference as a function of the matrix temperature gain.

5.3.2.3 Sorption-Isotherm Type of the Desiccant

Although the static sorption isotherm is essentially an equilibrium property of the desiccant-water vapor system, the model for the isotherm expression can be verified with dynamic sorption experiments. The breakthrough curves shown in Figs. C.2.1 - 8 indicate the existence of an intermediate outlet state which is constant in time for a small period. It has been shown theoretically (e.g., Ruthven, 1985) that this intermediate state is a true equilibrium state, dependent only upon the sorption isotherm and the lumped matrix specific heat, including desiccant and structural material. Furthermore, the average times at which the first and second wave reach the exit face of the matrix depend also upon these parameters. The computation of the intermediate state properties and average breakthrough times has been studied previously (e.g., Van den Bulck, Mitchell and Klein, 1985a) and is reviewed in Chapter 2.

Table 5.3 gives the comparison of theoretical and experimental intermediate states for experiments I and experiments M. The initial and inlet states needed for the computation of the theoretical intermediate state properties are retrieved from Tables 5.2 and 5.6. The isotherm is the Dubinin-Polanyi expression with the low value for $E_{o,2}$. The matrix specific heat is the theoretical value computed in the previous section, and adiabatic energy exchange between the air stream and the

Table 5.3 Comparison of experimental and predicted intermediate temperature and humidity for the experiments of series I and M.

Percentage deviations are based upon the maximum temperature and humidity swing for each experiment.

* marks experiments for which the intermediate state is not well defined.

Exp	experimental		predicted		deviation	
	$t_{f,int}$	$w_{f,int}$	$t_{f,int}$	$w_{f,int}$	$t_{f,int}$	$w_{f,int}$
	°C	kg/kgDA	°C	kg/kgDA	%	%
			Series I, Adsorption			
I1-A	55.6	0.02060	53.7	0.02060	-7.6	0.0
I2-A	56.3	0.01530	54.4	0.01580	-7.4	7.4
I3-A	60.1	0.01190	60.6	0.01170	1.5	-2.6
I4-A *	59.8	0.00870	61.2	0.00830	3.8	-4.5
I5-A *	59.5	0.00630	60.5	0.00620	3.0	-1.8
I6-A *	58.0	0.00440	62.9	0.00440	14.2	0.0
I8-A *	84.0	0.02200	80.7	0.02510	-19.5	16.5
			Series I, Desorption			
I1-D	33.7	0.03360	33.7	0.03520	0.0	21.9
I2-D	35.0	0.02910	35.5	0.03000	1.5	12.8
I3-D	37.2	0.02540	36.8	0.02570	-1.2	4.0
I4-D	38.3	0.02240	37.9	0.02210	-1.1	-3.9
I5-D	36.1	0.01560	34.6	0.01470	-4.5	-12.1
I6-D	41.2	0.01760	38.8	0.01650	-5.7	-14.2
I7-D	22.5	0.01570	22.8	0.01440	4.0	-10.1
I8-D	53.4	0.01060	56.3	0.00770	22.0	-15.3

(continued)

Table 5.3 (continued)

Exp	experimental		predicted		deviation	
	$t_{f,int}$ °C	$w_{f,int}$ kg/kgDA	$t_{f,int}$ °C	$w_{f,int}$ kg/kgDA	$t_{f,int}$ %	$w_{f,int}$ %
Series M, Adsorption						
M13-A	58.2	0.01030	58.7	0.00960	1.5	-9.6
M14-A	57.9	0.01010	58.8	0.00970	2.8	-5.3
M15-A	57.9	0.01020	58.0	0.00970	0.3	-7.1
M16-A	58.0	0.01020	58.5	0.00970	1.5	-6.8
M18-A	58.0	0.01020	57.9	0.00970	-0.3	-7.2
M20-A	58.3	0.01010	59.6	0.00970	3.9	-4.9
M22-A	58.6	0.01020	59.6	0.00950	2.9	-8.0
M25-A	58.2	0.01010	60.4	0.00940	6.2	-7.4
M28-A	58.1	0.01020	58.8	0.00950	2.1	-9.5
M32-A	57.9	0.00980	60.3	0.00940	6.8	-4.3
M36-A	56.4	0.00970	57.4	0.00970	3.2	0.0
M39-A *	58.0	0.00980	61.3	0.00930	9.0	-4.7
M22-A-R	58.0	0.01010	58.8	0.00960	2.4	-6.5
M28-A-R*	57.5	0.00990	57.3	0.00963	-0.6	-4.3
M36-A-R*	58.0	0.00980	59.8	0.00940	5.2	-4.2
Series M, Desorption						
M13-D	36.8	0.02260	35.9	0.02330	-2.4	8.2
M14-D	36.9	0.02270	35.8	0.02340	-2.9	7.9
M15-D	36.7	0.02250	35.5	0.02330	-3.2	8.8
M16-D	37.1	0.02270	36.4	0.02310	-1.9	4.9
M18-D	36.9	0.02270	35.7	0.02340	-3.1	7.4
M20-D	37.0	0.02270	36.0	0.02330	-2.6	6.7
M22-D	37.1	0.02270	36.6	0.02290	-1.4	2.4
M25-D	37.1	0.02260	36.8	0.02290	-0.8	3.7
M28-D	37.2	0.02310	36.4	0.02310	-2.2	0.0
M32-D	37.0	0.02330	35.9	0.02330	-2.9	0.0
M36-D	37.4	0.02340	36.2	0.02320	-3.2	-2.2
M39-D	37.4	0.02340	36.4	0.02310	-2.7	-3.4
M22-D-R	37.2	0.02280	36.0	0.02330	-3.2	6.0
M28-D-R	37.0	0.02320	35.7	0.02340	-3.4	2.1

average and standard deviations

$t_{f,int}$: 0.3%, σ = 6.1%, without * σ = 3.5%
$w_{f,int}$: -0.9%, σ = 7.9%, without * σ = 7.5%

test matrix is assumed. The average deviation between theory and experiment is 0.3% with σ = 6.1% for the intermediate temperature, and -0.9% with σ = 7.9% for the intermediate humidity ratio. These percentage deviations are based upon the maximum temperature or humidity swing for each individual experiment. The intermediate state is not well defined for the indicated experiments in Table 5.3 because the first and second wave overlap for these experiments. This is due to the limited rate of mass transfer to the desiccant and is further discussed in the following section. Ignoring the indicated experiments reduces the standard deviation of the temperature error to 3.5%, and to 7.5% for the humidity error.

Table 5.4 lists the uncertainty in computing the intermediate state due to uncertainties in the independent parameters determining the intermediate state properties. The indicated relative uncertainties are based upon the same basis as the relative errors in Table 5.3. The expected uncertainty in intermediate temperature is 3% and in intermediate humidity is 8%. Thus it is shown that the model for the isotherm expression and the value for the matrix specific heat used in this analysis are physically correct within the margins of uncertainty of the experiments. Table 5.4 also indicates that the uncertainty levels due to the initial state are much higher than those due to the inlet state. This is the immediate consequence of the procedures of operation of the experimental

facility. The initial state of the matrix can only be approximately estimated from the preparation conditions, whereas the inlet state properties are measured directly with high accuracy. State of the art single blow facilities use a different design in which this phenomenon is avoided (Rapley and Webb, 1983).

The average breakthrough times are expressed as dimensionless variables, $\theta^*_i = \theta_i \dot{m}_f / M_d$, where θ_i is the average time at which the first, i=1, or second, i=2, wave reaches the exit face of the matrix. The average breakthrough times are not well-defined for the adsorption experiments because the waves associated with these experiments are expansion waves, continuously spreading due to the nonlinear equilibrium property relationships, and finite rates of heat and mass transfer between the desiccant and the air stream. Furthermore, the experimental breakthrough times of the series I-D are not well-defined because of either the mixed character of the waves, or the poor quality of the experiments. However, the breakthrough times of the series M-D experiments are all about equal and well-defined. The average dimensionless experimental times for these experiments are about 0.77 ± 0.04 for the first thermal wave and 26.7 ± 0.4 for the second wave. This latter value is obtained from the analysis of the data presented in the next section, and is the average of 14 different desorption experiments. The average predicted breakthrough times are 2.55 ±

0.03 and 27.2±0.6, respectively. The uncertainty level of the theoretical breakthrough times is listed in Table 5.4. The theoretical and experimental breakthrough times for the second wave are in very close agreement with each other, and the difference is well within the margins of expected uncertainty.

The speed of the first wave, however, is more than 3 times the predicted value and is outside the range of experimental uncertainty. The first wave is a thermal wave, i.e., the driving potential for the propagation of the wave is determined by the rate of change of the air stream temperature relative to the rate of change of matrix temperature. For the

Table 5.4 Relative uncertainty levels for the estimation of the intermediate state properties and dimensionless breakthrough times

independent variable	t_{int} %	w_{int} %	θ_1^* %	θ_2^* %
air stream flow rate			2.5	2.5
mass of desiccant			3.0	3.0
initial temperature	2.2	3.6	0.3	2.7
initial humidity	2.0	3.2	2.6	2.1
inlet temperature	0.0	0.4	0.2	0.3
inlet humidity	0.6	4.8	0.8	0.4
isotherm	0.6	3.4	4.2	6.9
specific heat	0.3	1.0	3.3	1.6
combined %	3.0	8.0	7.2	8.8

studied experiments, only the desiccant and the tape carrier participate directly in the heat exchange with the air stream. The theoretical breakthrough time of the first wave for the system: desiccant + tape carrier excluding the other structural parts and air stream is only 0.47 ± 0.01 because of the smaller thermal capacitance. This theoretical value is in much better agreement with the experimental value. The metal parts of the matrix, spacers, rods and lids, exchange thermal energy with the air stream only indirectly through heat conduction, as discussed earlier. The rate of heat conduction is too small to change the temperature of these parts during the small time interval in which the fast first wave passes through the matrix. Hence, the matrix acts as a distributed system for fast temperature swings. The concept of lumped thermal capacitance as used in conventional dehumidifier theories and discussed in Chapter 2 does not apply for this situation, and the breakthrough times cannot be estimated with the simplified theories of Chapter 2. Enthalpy exchangers operate at rotational speeds synchronized with the breakthrough of the first wave. The experimental results presented in this work indicate that the performance of these devices may not be modeled similar to dehumidifiers, especially if the exchanger has distributed thermal capacitances. Furthermore, the graphical presentation of the breakthrough curves in Appendix C show that the humidity response of the first wave is lagging the thermal

response. This is explained by the fact that the thermal diffusivities of desiccants and structural parts is about 100 to 1000 times the mass diffusivities of desiccants. The finite rate of mass transfer causes an appreciable spread of the mass-transfer wave, which is absent in the thermal wave. This effect is further discussed in the following section of this chapter.

Dehumidifiers are synchronized with the breakthrough of the second wave, which determines their performance. Because the second wave is a mass transfer wave and only the desiccant layer, in direct contact with the air stream, adsorbs the water vapor, and because this wave is a slow wave, the matrix acts generally as a more homogeneous system for this wave. Thus, for the second wave, the assumption of lumped capacitance for computing the intermediate state properties are more closely satisfied.

5.3.3 Thermodynamic Equilibrium Properties of the Test Matrix

Table 5.5 summarizes the values for the thermodynamic properties of the test matrix. They are derived from the experimental data of the series I experiments or obtained from property data literature. The correlation for the desiccant isotherm has been compared with experiments. It is found that

Table 5.5 List of the thermodynamic properties of the test matrix

	mass kg	thermal capacitance J/K
silica gel	0.487	450
carrier	0.242	330
spacers	1.540	1380
rods	0.259	230
lids	3.120	2800
Total	5.583	5190

isotherm correlation

$$W_d = W_{o,1} \exp(-A/E_{o,1})^2 + W_{o,2} \exp(-A/E_{o,2})^2$$

where: $W_{o,1} = 0.117$ and $W_{o,2} = 0.237$ kg/kg-dry-silica

$E_{o,1} = 7740$ and $E_{o,2} = 2500$ J/mole-water

this correlation accurately predicts both the mass of desiccant within the matrix, and thus the sorption capacity of the desiccant, and the breakthrough time of the second mass transfer wave, which is strongly dependent upon the derivative of the isotherm with respect to temperature and humidity ratio. This experimental work therefore substantiates the accuracy of the Dubinin-Polanyi isotherm for regular-density silica gel, with the parameters developed and presented in this work.

Combined with the geometric data of Table 5.1, the data in Table 5.5 form the complete set of parameters which determine the matching of the mass and energy transport fluxes in the air stream with the corresponding transport fluxes in

the desiccant sheet. That discussion forms the subject of the section presented next.

5.4 Dynamic, Adiabatic Sorption Experiments with Varying Process Mass Flow Rate

This section describes the analysis in which the heat and mass transfer coefficients for laminar flow through parallel plates with dynamic sorption at the wall are computed. The Nusselt and Sherwood numbers are determined from a specific series of dynamic sorption experiments with constant initial conditions of the desiccant bed, constant inlet conditions of the air stream, and in which the process air mass flow rate varies in a systematic pattern.

The resistance to mass and energy exchange between the air stream and the desiccant is composed of two resistances acting in series. The first resistance is determined by the finite rates of convective heat and mass exchange between the laminar air stream and the desiccant surface at the walls. The air-side transfer coefficients depend upon the boundary conditions for the temperature and water vapor mass fraction at the wall and the geometry of the duct. The complete geometry of the parallel plate test matrix is derived from an independent set of pressure drop experiments. Except for the

presence of small desiccant particles with irregular shape protruding into the air-stream shear layer, this test matrix has a well-defined geometry. This is unlike conventional sorbent matrices such as packed beds, for which the exact geometry is usually poorly defined. The boundary conditions at the wall are established by the match of the mass and energy transport fluxes in the air stream and desiccant particles, respectively.

The second transfer resistance is determined by the finite rates of mass and energy diffusion within the individual desiccant particles. These diffusion rates depend upon the boundary conditions at the external surface of the particles and the particle geometry. The shape and dimensions of the desiccant particles are not exactly known, and are discussed further in this section.

The transfer rates can be obtained from the solution of two sets of equations of change expressing the conservation of mass, momentum and energy in the air stream and desiccant, respectively. Because the common boundary conditions at the wall for both sets are unknown, the conservation equations must be solved simultaneously. The solution can then be compared to the experimental data. However, this approach suffers from several major disadvantages. If the number of simplifying assumptions is kept small, the combined solution of the conservation equations requires a major computational effort, mainly

due to the nonlinearity of the equations and the physical material properties. Furthermore, there are a number of parameters that determine the solution of the conservation equations which are often not well known, e.g., the diffusivities and sorption properties of the desiccant. Usually, the effects of the variability of these parameters on the solution of the conservation equations are intermixed, and if the solution is in error with the experimental data, the deviation can often be explained by the variability of more than one specific parameters (Schneider and Smith, 1968; Kim, Biswas and Mills, 1984).

To reduce the computational effort, Ghezelayagh and Gidaspow (1982) used a technique to separate the solutions of the two sets of conservation equations. This technique determines the boundary conditions at the interface between the air stream and the desiccant layer from an analysis of a specifically designed set of dynamic sorption experiments. The experimental data are input to a model that solves the conservation equations for the air stream. The results of this model yield the complete set of boundary conditions, fluxes and properties, at the wall. In a second step, the fluxes are input to a model that solves the conservation equations for the desiccant particles. The boundary conditions for this model are overdetermined, and thus allow a check on the accuracy of the model. The advantage of this approach is that the boundary

conditions can be checked for intermediate accuracy. The models for the desiccant- and air side transfer resistances can thus be verified sequentially. This approach is followed in the third subanalysis of this study and is presented next.

5.4.1 Experimental Results

The series of experiments which is analyzed in this part of the analysis consists of 15 dynamic, adsorption-desorption tests. The initial state of the matrix and the inlet state of the air stream are the same for all adsorption and desorption experiments, respectively. The flow rate varies systematically for the alternate experiments. Data for each test are collected and converted using the procedures explained in the previous chapter.

The various test conditions for the experiments are listed in Table 5.6. The matrix preparation conditions, the estimated matrix initial conditions and the air stream inlet conditions are given for each experiment. The adsorption and desorption tests are labeled M-A and M-D, respectively. The choice of initial and inlet conditions is obtained from a compromise between the limited operating range of the experimental facility, the wave type of the breakthrough curves, and the strength of the breakthrough response. The accuracy of the

Table 5.6 Preparation, initial and inlet conditions for the M series of dynamic sorption experiments

	PREPARATION CONDITIONS			
ExpID	t_f	w_f	P	W_d
	°C	kg/kgDA	Pa	kg/kg
		adsorption		
M13-A	80.8	0.03229	83260	0.04807
M14-A	80.9	0.03235	81840	0.04737
M15-A	80.7	0.03230	81480	0.04749
M16-A	80.7	0.03230	81690	0.04758
M18-A	80.7	0.03235	82880	0.04813
M20-A	80.8	0.03227	81730	0.04740
M22-A	80.8	0.03230	81770	0.04745
M25-A	80.8	0.03229	82300	0.04766
M28-A	80.8	0.03230	82300	0.04767
M32-A	80.8	0.03234	81610	0.04742
M36-A	81.0	0.03225	81820	0.04710
M39-A	80.8	0.03223	82330	0.04762
M22-A-R	80.8	0.03231	83230	0.04807
M28-A-R	80.8	0.03229	83300	0.04808
M36-A-R	80.9	0.03226	82940	0.04774
		desorption		
M13-D	27.1	0.01322	83000	0.24889
M14-D	27.2	0.01332	82590	0.24808
M15-D	27.2	0.01327	81640	0.24473
M16-D	27.2	0.01323	83130	0.24806
M18-D	27.3	0.01326	82450	0.24540
M20-D	27.2	0.01324	82520	0.24660
M22-D	27.3	0.01324	81500	0.24253
M25-D	27.3	0.01325	82350	0.24497
M28-D	27.2	0.01325	82020	0.24543
M32-D	27.2	0.01324	81440	0.24371
M36-D	27.3	0.01325	82280	0.24478
M39-D	27.2	0.01325	82280	0.24612
M22-D-R	27.2	0.01326	82580	0.24709
M28-D-R	27.2	0.01332	82990	0.24914
M36-D-R	*****	NOT PERFORMED		********

(continued)

TABLE 5.6 (continued)

	INITIAL CONDITIONS			
ExpID	t_f	w_f	P	W_d
	°C	kg/kgDA	Pa	kg/kg
		adsorption		
M13-A	62.9	0.01760	83220	0.05900
M14-A	62.9	0.01760	82210	0.05855
M15-A	61.9	0.01720	81570	0.05937
M16-A	62.6	0.01760	81720	0.05890
M18-A	61.8	0.01710	82920	0.05996
M20-A	63.9	0.01820	82070	0.05777
M22-A	64.4	0.01900	81300	0.05800
M25-A	65.4	0.01950	82230	0.05745
M28-A	63.0	0.01760	82050	0.05828
M32-A	65.2	0.01910	81710	0.05686
M36-A	60.9	0.01610	81960	0.05911
M39-A	66.7	0.02050	82020	0.05669
M22-A-R	63.0	0.01780	82740	0.05900
M28-A-R	60.9	0.01620	83280	0.05993
M36-A-R	64.8	0.01930	83100	0.05861
		desorption		
M13-D	29.4	0.01410	83090	0.23230
M14-D	29.0	0.01380	82830	0.23230
M15-D	28.4	0.01340	81630	0.23078
M16-D	30.4	0.01460	83210	0.22692
M18-D	28.4	0.01330	82400	0.23122
M20-D	29.1	0.01370	82670	0.22901
M22-D	30.6	0.01450	81540	0.21847
M25-D	30.8	0.01450	82420	0.21820
M28-D	30.2	0.01430	81930	0.22175
M32-D	28.9	0.01360	81580	0.22719
M36-D	30.0	0.01440	82460	0.22724
M39-D	30.3	0.01450	82320	0.22442
M22-D-R	29.8	0.01450	82680	0.23193
M28-D-R	28.9	0.01380	82890	0.23379
M36-D-R	*****	NOT PERFORMED		********

(continued)

TABLE 5.6 (continued)

	INLET CONDITIONS				
ExpID	t_f	w_f	P	W_d	m_f
	°C	kg/kgDA	Pa	kg/kg	kgDA/s
			adsorption		
M13-A	30.2	0.01572	83220	0.24548	0.01286
M14-A	30.5	0.01573	82210	0.23894	0.01388
M15-A	30.0	0.01573	81570	0.24383	0.01486
M16-A	30.1	0.01574	81720	0.24305	0.01617
M18-A	30.2	0.01572	82920	0.24468	0.01755
M20-A	30.9	0.01570	82070	0.23288	0.01935
M22-A	30.1	0.01573	81300	0.24177	0.02153
M25-A	30.1	0.01572	82230	0.24416	0.02434
M28-A	29.7	0.01573	82050	0.24912	0.02783
M32-A	30.1	0.01572	81710	0.24275	0.03233
M36-A	29.7	0.01572	81960	0.24874	0.03590
M39-A	30.2	0.01572	82020	0.24226	0.03882
M22-A-R	30.3	0.01573	82740	0.24301	0.02155
M28-A-R	29.7	0.01571	83280	0.25214	0.02783
M36-A-R	29.9	0.01572	83100	0.24914	0.03582
			desorption		
M13-D	67.1	0.01567	83090	0.04734	0.01283
M14-D	67.2	0.01569	82830	0.04710	0.01385
M15-D	66.4	0.01568	81630	0.04798	0.01483
M16-D	67.1	0.01570	83210	0.04745	0.01620
M18-D	67.2	0.01570	82400	0.04695	0.01750
M20-D	67.0	0.01570	82670	0.04740	0.01935
M22-D	66.6	0.01571	81540	0.04766	0.02154
M25-D	66.9	0.01570	82420	0.04747	0.02434
M28-D	67.1	0.01571	81930	0.04695	0.02787
M32-D	67.2	0.01570	81580	0.04662	0.03235
M36-D	67.1	0.01571	82460	0.04717	0.03582
M39-D	67.1	0.01571	82320	0.04711	0.03887
M22-D-R	67.1	0.01571	82680	0.04726	0.02152
M28-D-R	66.9	0.01570	82890	0.04766	0.02780
M36-D-R	**********	NOT PERFORMED		**********	

analysis increases with the magnitude of the temperature and humidity swings of the outlet response. This can be achieved by increasing the desorption-inlet or adsorption-preparation temperature and increasing the desorption-preparation or adsorption-inlet humidity. However, as this latter variable increases, the response type of the second wave gradually changes from a pure shock wave to a pattern with both shock and expansion wave behavior, as discussed in the previous section. This mixed pattern is undesirable for practical dehumidifier operation, and is therefore avoided for the experiments in this study. As the desorption-inlet temperature or adsorption-preparation temperature increases, the heat loss to the duct and to the frame of the test matrix becomes relatively more important and complicates the analysis. These considerations limit high regeneration temperatures and process humidities. A good compromise is achieved by the conditions for temperature and humidity of 67 °C - 0.0157 kg/kgDA and 30 °C - 0.0157 kg/kgDA, respectively.

The mass flow rate varies for the different experiments such that the inverse of the mass flow rate forms an arithmetic progression of numbers. The characteristic length in the flow direction for laminar, boundary-layer type flow in ducts is inversely proportional to the mass flow rate, and this information forms the rational for the sequence of mass flow rates in Table 5.6.

The transient response for each of these dynamic sorption experiments is graphically shown in Figs. C.3.1.a through C.3.15.a in Appendix C. The measured inlet and outlet air-temperature and humidity are plotted as functions of time. The experiments M-R are repeated experiments. The comparison of the transient response in graphical form and of the intermediate states in Table 5.3 for these repeated experiments indicates that the experiments are repeatable within the limits of accuracy of the installation, as indicated in Table 5.4. The non-closure of the temperature response is apparent for the desorption experiments and is due to the effect of the large matrix thermal capacitance and a small heat loss as explained previously.

The different response behavior for respectively the adsorption and desorption experiments is illustrated in Figs. C.3.1-C.3.15, and explained by the nonlinearity of the sorption isotherm of the desiccant. The second wave or mass transfer wave is much better defined for the desorption experiments than for the adsorption experiments, i.e., this wave is completely separated from the first or thermal wave for the desorption experiments, in contrast to the adsorption tests where the waves overlap. This overlap is due to a mismatch of the amount of desiccant in the matrix relative to the air stream mass flow rates. The mass of desiccant is too small for the range of air stream mass flow rates of the experimental facility. These

observations make the second wave of the desorption experiments the subject of the analysis presented next.

5.4.2 Analysis and Discussion I: Air Side Heat and Mass Transfer Coefficients

This discussion is divided and presented in three subsequent parts. In the first part, the model is formulated and the assumptions are declared. Part 2 describes the preparation of the experimental data for input to the model. The last part presents the results of the analysis.

5.4.2.1 Model Formulation and Assumptions

The model describes the conservation of momentum, energy and mass for the flow of humid air through a parallel plate configuration. The conservation equations are derived from the general equations of change for a multicomponent mixture in terms of the transport fluxes (Bird, Stewart and Lightfoot, 1960). These general equations are simplified by a limited set of assumptions and order of magnitude estimates of the various terms appearing in the equations. The number of assumptions is kept minimal as an effort to verify the conventional set of assumptions in modeling rotary dehumidifiers.

ASSUMPTIONS.

For the gas mixture:

1. Humid air is a dilute, binary, ideal gaseous solution of water vapor in air.

2. The fluid is Newtonian. The bulk viscosity is small. The viscosity, diffusivity, thermal conductivity and thermal diffusivity are well-defined properties of the mixture.

For the continuity equation:

3. Ordinary diffusion due to concentration gradients can be described by Fick's first law of binary diffusion.

For the equation of motion:

4. The stress tensor can be described by Newton's law of viscosity.

For the equation of energy:

5. The conductive energy flux can be described by Fourier's law of heat conduction.

6. Changes in potential energy of the gas are negligible.

7. Radiative heat fluxes are neglected.

For the flow:

8. The humid air flows through parallel passages with complete symmetry around the middle axis. Corner effects due to the rectangular geometry are neglected due to the small aspect ratio of the duct.

9. The flow is two-dimensional. The major velocity component is in the x-direction.

10. *Quasi steady-state approximation.* The dwell time of the fluid within the test matrix ranges from 0.06 to 0.11 s and is small compared to the time scale of the experiments, 3600 s. Local changes of air-density, momentum and temperature with respect to time are therefore negligible compared to the convective changes.

11. *Boundary layer assumption*. The gradients of the diffusive mass flux, the viscous momentum flux and the conductive energy flux are much larger in the y-direction than in the x-direction, i.e., axial diffusion is neglected.

The equations of change are further simplified by neglecting the terms described in the following order of magnitude analysis

ORDER OF MAGNITUDE ANALYSIS

1. Buoyancy forces

The magnitude of the buoyancy forces relative to the viscous and inertial forces which appear in the equation of motion is given by the Grashof number,

$$G = \frac{g D_h^3 \Delta T}{\nu^2 T_0}, \tag{5.29}$$

where ΔT is a characteristic temperature difference between the wall and the fluid. Because the air flow is horizontal, the buoyancy forces act in the same direction as the inertia forces produced by the transverse flow field. The order of the Grashof number is 1 for the experiments under consideration and thus the buoyancy forces are of the same magnitude as the inertial forces acting in the y-direction. However, these forces scale as Re^{-1} with the inertial and viscous forces in the flow direction and are neglected as part of the boundary

layer assumption. Hence, the buoyancy forces can be neglected and the heat and mass transfer is that of forced convection only.

2. Viscous Heating

The effect of viscous heating on the temperature distribution in the flow field is indicated by the magnitude of the Brinkman number,

$$Br = Pr\frac{U^2}{c_p \Delta T}. \tag{5.30}$$

This number is the ratio of heat production by viscous dissipation to heat tranport by conduction. For the experiments under consideration, Br is of the order of $5\text{x}10^{-5}$. Hence, the effect of viscous heating is negligible and the corresponding term in the energy equation can be omitted

3. Heating by compression

The effect of fluid expansion due to pressure changes on the temperature distribution within the flow direction is determined by the work done on the fluid by the pressure forces. For viscous flow through ducts, the ratio of the rate of temperature increase due to compression to the rate of heat conduction is given by $(fRe)Br$. For parallel plates, fRe = 24 and thus heating by compression has the same order of magnitude

as viscous heating and can be neglected. The corresponding term in the energy equation is omitted.

4. Thermo-diffusion, pressure and forced diffusion mass flux

A complete description of the mass diffusion fluxes occurring in binary gases is given in Appendix A. The ratio of the thermo-diffusion to ordinary diffusion mass flux is given by

$$\frac{j^{(T)}}{j^{(x)}} = \alpha_T(1-\omega)\frac{\Delta \ln(T)}{\Delta \ln(\omega)}, \tag{5.31}$$

in which α_T is the thermal diffusion factor. For water-vapor air mixtures, α_T ranges from 0.01 to 0.03 (Mason and Monschick, 1965). The thermo-diffusion flux is less than 1% of the ordinary diffusion flux for the studied experiments and therefore neglected in this analysis.

Because of the boundary layer assumption, the pressure gradient is directed in the flow direction. The pressure diffusion flux is in the direction of the pressure gradient and thus also directed in the flow direction. Because of the boundary layer assumption, the divergence of this flux is neglected with respect to the convective changes and pressure diffusion is neglected.

Forced diffusion occurs only in the presence of external force fields other than gravity and is not considered in this analysis.

5. Dufour energy flux

Appendix A describes the energy fluxes that occur in multicomponent gas mixtures. The energy flux due to concentration gradients relative to the energy flux by conduction for dilute binary mixtures is given by

$$\frac{q^{(x)}}{q^{(T)}} = \frac{Pr}{Sc}\frac{k_T}{(1-\omega)}\frac{R}{C_p}\frac{\Delta \ln(\omega)}{\Delta \ln(T)}, \qquad (5.32)$$

where k_T is the thermal diffusion ratio. For air-water vapor mixtures, k_T is about 5×10^{-4} and R/C_p is 0.4/1.4. The Dufour energy flux for the conditions of the experiments is less than 1% of the energy flux by conduction and is neglected for the analysis of the experimental data.

CONSERVATION EQUATIONS IN DIFFERENTIAL FORM

The equations of change in terms of the transport fluxes are presented by Bird, Stewart and Lightfoot (1960). Expressions for the transport fluxes in binary gas mixtures are reviewed in Appendix A. With the assumptions and approximations of this analysis, the conservation equations which model the flow of air through the test matrix with dynamic sorption at the wall can be expressed in terms of the transport properties as follows. x measures the position in the flow direction and y the transverse position away from the wall. The velocity components in the x- and y-directions are u and v,

respectively. The flow is laminar for the range of Reynolds numbers of the experiments.

1. Continuity Equation:

$$\frac{\partial(\rho u)}{\partial x} + \frac{\partial(\rho v)}{\partial y} = 0$$

2. Equation of Motion:

$$\rho\left(u\frac{\partial u}{\partial x} + v\frac{\partial u}{\partial y}\right) + \frac{dP}{dx} = \frac{\partial}{\partial y}\left(\mu\frac{\partial u}{\partial y}\right)$$

3. Diffusion Equation: (5.33)

$$\rho\left(u\frac{\partial \omega}{\partial x} + v\frac{\partial \omega}{\partial y}\right) = \frac{\partial}{\partial y}\left(\rho D_{aw}\frac{\partial \omega}{\partial y}\right)$$

4. Equation of Energy:

$$\rho c_p\left(u\frac{\partial t_f}{\partial x} + v\frac{\partial t_f}{\partial y}\right) = \frac{\partial}{\partial y}\left(k\frac{\partial t_f}{\partial y}\right) + \rho D_{aw}\frac{\partial \omega}{\partial y}\left(c_{p,w} - c_{p,a}\right)\frac{\partial t_f}{\partial y}$$

BOUNDARY CONDITIONS

This set of conservation equations forms a set of parabolic partial differential equations. The boundary conditions for the variables u, v, ω and t_f for integration in the y-direction need to be specified at the wall, $y = 0$, and at the center of the channel, $y = D_h/4$. The hydraulic diameter is twice the height of the channel. The conventional boundary conditions that specify the property or flux of temperature and humidity at the wall are absent because they are not known. These boundary conditions are replaced by local integral conditions and matched with experimental data.

For all x,

$$\text{at } y = 0: \qquad u = 0,$$

$$\rho v = -\frac{\rho D_{aw}}{(1-\omega)} \frac{\partial \omega}{\partial y},$$

$$\text{at } y = D_h/4: \qquad \frac{\partial u}{\partial y} = 0,$$

$$v = 0,$$

$$\frac{\partial \omega}{\partial y} = 0, \tag{5.34}$$

$$\frac{\partial t_f}{\partial y} = 0,$$

EQUATIONS OF CHANGE IN INTEGRAL FORM

With these boundary conditions, the equations of change can be integrated in the y-direction. Upon inserting the integrated continuity equation, the resulting integral conservation equations read as follows.

1. Equation of continuity:

$$\frac{d}{dx} \int_0^{D_h/4} (\rho u)\, dy = -\frac{\rho D_{aw}}{(1-\omega)} \frac{\partial \omega}{\partial y}\Big|_{wall}$$

2. Conservation of momentum:

$$\frac{d}{dx} \int_0^{D_h/4} (\rho u)\, u\, dy + \frac{D_h}{4} \frac{dP}{dx} = -\mu \frac{\partial u}{\partial y}\Big|_{wall}$$

3. Conservation of water vapor: (5.35)

$$\frac{d}{dx} \int_0^{D_h/4} (\rho u)\, \omega\, dy = -\frac{\rho D_{aw}}{(1-\omega)} \frac{\partial \omega}{\partial y}\Big|_{wall}$$

4. Conservation of energy:

$$\frac{d}{dx}\int_{o}^{D_h/4} (\rho u)\, i_f\, dy = -k\frac{\partial t_f}{\partial y} - i_w \frac{\rho D_{aw}}{(1-\omega)}\frac{\partial \omega}{\partial y}\Big|_{wall}$$

INTEGRAL CONDITIONS

The integral conditions which complete the set of boundary conditions can be formulated in terms of the experimental data.

for all x,

for the diffusion equation:

$$\int_{o}^{D_h/4} (\rho u)\, \omega\, dy = \omega_{exp}\int_{o}^{D_h/4} (\rho u)\, dy \qquad (5.36)$$

for the energy equation:

$$\int_{o}^{D_h/4} (\rho u)\, i_f\, dy = i_{f,exp}\int_{o}^{D_h/4} (\rho u)\, dy$$

ω_{exp} and $i_{f,exp}$ are the experimental average values of the water-vapor mass fraction and enthalpy of the humid air stream at position x in the flow direction. To obtain these experimental values as functions of x, simultaneous measurements would have to be taken at multiple positions inside the flow channel. Not only would this require an extremely complicated experimental apparatus, the presence of instrumentation within the flow channel would disturb the flow significantly.

However, because axial diffusion is neglected in this analysis, there exists an appropriate scaling technique which does not require local measurements.

The conservation equations in differential (5.33) and integral form (5.35), and the scalar boundary conditions (5.34) can be expressed in terms of the reduced variables x^+, y^+, u^+, and v^+. These variables are defined as:

$$
\begin{aligned}
x^+ &= \frac{x}{D_h Re_o}, \\
y^+ &= \frac{y}{D_h} \\
u^+ &= \frac{u}{U}, \\
v^+ &= \frac{v D_h \rho_o}{\mu_o}
\end{aligned}
\qquad (5.37)
$$

where the reference variables are defined as:

$$
\rho_o U = 4 \int_o^{1/4} (\rho u)\, dy^+ , \qquad (5.38)
$$

and

$$
Re_o = \frac{U D_h \rho_o}{\mu_o}
$$

The integral conditions (5.36) can be expressed in terms of these reduced variables if and only if the distributions of

the mass and energy fluxes at the wall do not include a characteristic length in the flow direction, enforced independently by the desiccant layer. These fluxes are obtained from the match of the conservation equations for respectively the air stream and the desiccant layer at the wall. Thus only if there does not exist a characteristic length in the x-direction in the desiccant layer, then and only then are the spatial distributions of temperature and humidity determined only by the rate of change of the air stream conditions and enforced upon the desiccant system by the boundary conditions. The desiccant layer is composed of individual particles with dimensions ranging from 160 to 300 μm. These particles are isolated from each other and there is negligible axial diffusion of heat or mass. The characteristic length in the air stream, $D_h Re_o$, ranges from 0.2 to 1 m. Because this length is much larger than the particle size, this length determines the global spatial distributions of temperature and humidity of interest to this study. Thus the integral boundary conditions (5.36) can be expressed in terms of the reduced variables x^+, y^+, u^+, and v^+.

5.4.2.2 Preparation of Experimental Data for Input to Model

To obtain the combined heat and mass transfer coefficients in the air flow from the experimental data, the measured

average outlet temperature and humidity ratio must be expressed as functions of x^+.

Table 5.7 lists the air stream-inlet conditions of temperature, humidity, fluid pressure, and flow rate for the 14 experiments of series M-D. This table also lists the values for the reference velocity u_o, the Reynolds number Re_o, and the dimensionless flow length L^+. The formulas to compute these variables are reviewed in Table 5.7. The reference properties ρ_o and μ_o are the properties defined for the average inlet state of all experiments. The average outlet conditions are measured at the exit face of the matrix at which $x^+ = L^+$. If the initial conditions of the test matrix and the inlet conditions of the air stream are respectively the same for all experiments, then the combined set of measured air-stream outlet conditions at a specified time θ and flow length L^+ correspond to the set of state properties of an air stream in a single fictitious experiment with the same matrix-initial and air-inlet conditions, and measured at the corresponding locations $x^+ = L^+$ and time θ.

The study of the experimental data is focused on the second wave of the desorption experiments. The intermediate state in between the thermal wave and the mass transfer wave for each of the experiments is an equilibrium state and can therefore be interpreted as the initial state of the matrix at the start of the second wave for that particular experiment.

Table 5.7 Reference conditions and dimensionless flow lenghts for the experiments of series M-D

	ExpID	$t_{f,in}$	$w_{f,in}$	P	m_f	U	Re_o	L^+
		°C	kg/kgDA	Pa	kgDA/s	m/s	/	/
	M13-D	67.078	0.015674	83052	0.01283	1.657	140.4	0.7018
	M14-D	67.178	0.015688	82787	0.01385	1.789	151.5	0.6501
*	M15-D	66.384	0.015682	81579	0.01483	1.916	162.2	0.6072
	M16-D	67.109	0.015703	83153	0.01620	2.093	177.2	0.5558
	M18-D	67.217	0.015695	82345	0.01750	2.261	191.4	0.5145
	M20-D	66.990	0.015695	82604	0.01935	2.500	211.7	0.4653
*	M22-D	66.558	0.015710	81463	0.02154	2.783	235.6	0.4180
	M25-D	66.936	0.015701	82333	0.02434	3.144	266.3	0.3699
	M28-D	67.113	0.015708	81825	0.02787	3.600	304.9	0.3231
	M32-D	67.195	0.015699	81458	0.03235	4.179	353.9	0.2783
	M36-D	67.076	0.015708	82323	0.03582	4.628	391.8	0.2514
	M39-D	67.075	0.015705	82163	0.03887	5.022	425.2	0.2317
	M22-D-R	67.098	0.015709	82608	0.02152	2.780	235.4	0.4184
	M28-D-R	66.930	0.015700	82788	0.02780	3.591	304.1	0.3239
	average	67.083	0.015699	82320				
	st. dev.	0.093	0.000010	560				

*experiments M15-D and M22-D not included in averages for $t_{f,in}$

reference conditions:

$t_{f,o}$	= 67.083	°C	(average values, this table)
$w_{f,o}$	= 0.0157	kg/kgDA	
P_o	= 82320	Pa	
ρ_o	= 0.8351	kg/m^3	(from property relationships)
μ_o	= 2.0325x10^{-5}	kg/m·s	(Appendix B)
A_c	= 0.00927	m^2	(from Table 5.1)
D_h	= 0.002061	m	
L	= 0.203	m	

formulas:

$$U = \dot{m}_f/\rho_o \cdot A_c \qquad Re_o = UD_h\rho_o/\mu_o \qquad L^+ = L/Re_o \cdot D_h$$

Table 5.8 lists the inlet and initial temperature and humidity for the alternate experiments. There exists a small variability of the inlet and intermediate state properties about average values. The standard deviations of the inlet temperature and humidity fluctuations are 0.1 °C and 0.00001 kg/kgDA, respectively, which is well within the accuracy of the measurements. The variability of the intermediate state properties is larger, as indicated in Table 5.8. The standard deviation of the intermediate temperature about the average value is 0.2 °C, which is the accuracy of the experiment and is acceptable. The intermediate humidity has a constant value for $Re_o < 300$, increases slightly in the range to $Re_o = 360$, and then stays constant with increasing Re_o. This pattern resembles the pattern of the pressure drop as a function of the Reynolds number, Fig. 5.3, which is explained by the protrusion of desiccant particles from the wall into the air stream and the onset of flow separation about the individual particles. However, this reasoning cannot explain the intermediate humidity behavior. Fortunately, the intermediate state is interpreted as the initial state and, for this study, is only needed at the end of the mass transfer wave, i.e., high values of x^+. In this range, the variability of the humidity is acceptable.

To determine the spatial distributions of temperature and humidity, small corrections must be applied to the experimental

Table 5.8 Experimental inlet and intermediate temperatures and humidities for the experiments of series M-D

ExpID	x^+	$t_{f,in}$	$w_{f,in}$	$t_{f,int}$	$w_{f,int}$
	/	°C	kg/kgDA	°C	kg/kgDA
M13-D	0.7018	67.078	0.015666	36.79	0.02260
M14-D	0.6501	67.178	0.015723	36.86	0.02267
M15-D	0.6072	66.384	0.015723	36.71	0.02252
M16-D	0.5558	67.109	0.015749	37.06	0.02268
M18-D	0.5145	67.217	0.015757	36.94	0.02274
M20-D	0.4653	66.990	0.015629	36.99	0.02272
M22-D	0.4180	66.558	0.015686	37.10	0.02266
M22-D-R	0.4184	67.098	0.015694	37.19	0.02279
M25-D	0.3699	66.936	0.015731	37.09	0.02262
M28-D	0.3231	67.113	0.015719	37.19	0.02314
M28-D-R	0.3239	66.930	0.015727	37.00	0.02318
M32-D	0.2783	67.195	0.015721	37.04	0.02328
M36-D	0.2514	67.076	0.015702	37.37	0.02337
M39-D	0.2317	67.075	0.015696	37.40	0.02337
avg.		67.083[1]	0.015709	37.05	0.02267[2]
st. dev.		0.009	0.000010	0.20	0.00008

[1] experiments M15-D and M22-D not included

[2] for $x^+ > 0.35$

data to correct for the variability of the initial, i.e., intermediate, and inlet states. For each experiment and measurement time θ, the corrected outlet temperature t_f^* is obtained from the measured outlet temperature t_f using a proportional relationship which preserves the shape of the breakthrough wave,

$$\frac{t_f^* - t_{f,int}^*}{t_{f,in}^* - t_{f,int}^*} = \frac{t_f - t_{f,int}}{t_{f,in} - t_{f,int}}$$

and similarly for the humidity ratio: (5.39)

$$\frac{w_f^* - w_{f,int}^*}{w_{f,in}^* - w_{f,int}^*} = \frac{w_f - w_{f,int}}{w_{f,in} - w_{f,int}}$$

The superscript * denotes the corrected value. The corrected values for the inlet and intermediate states are the average values, as listed in Tables 5.8. Absolute corrections to the outlet temperatures and humidities are of the order of 0.2 °C and 0.00005 kg/kg, respectively. For the remainder of the analysis, corrected values are used to represent the measured, experimental properties.

Figures 5.7a-b show the outlet temperature and humidity as a function of x^+ for 6 measurement times. These transient, spatial distributions still show a small scatter about a smooth profile, as indicated in the figures. Graber (1970) has shown with a theoretical analysis that the Nusselt number for forced convection, laminar flow through ducts is dependent upon the second derivative of the average temperature with respect to position in the flow direction. Therefore, the experimental data need to be represented with a distribution form which has a smooth second derivative. Neither cubic splines or continuous polynomials of fourth degree or higher satisfy these requirements. To assure a smooth second derivative, the experimental data are curve-fitted with the integral of a distribution form which has a smooth first derivative. For constant

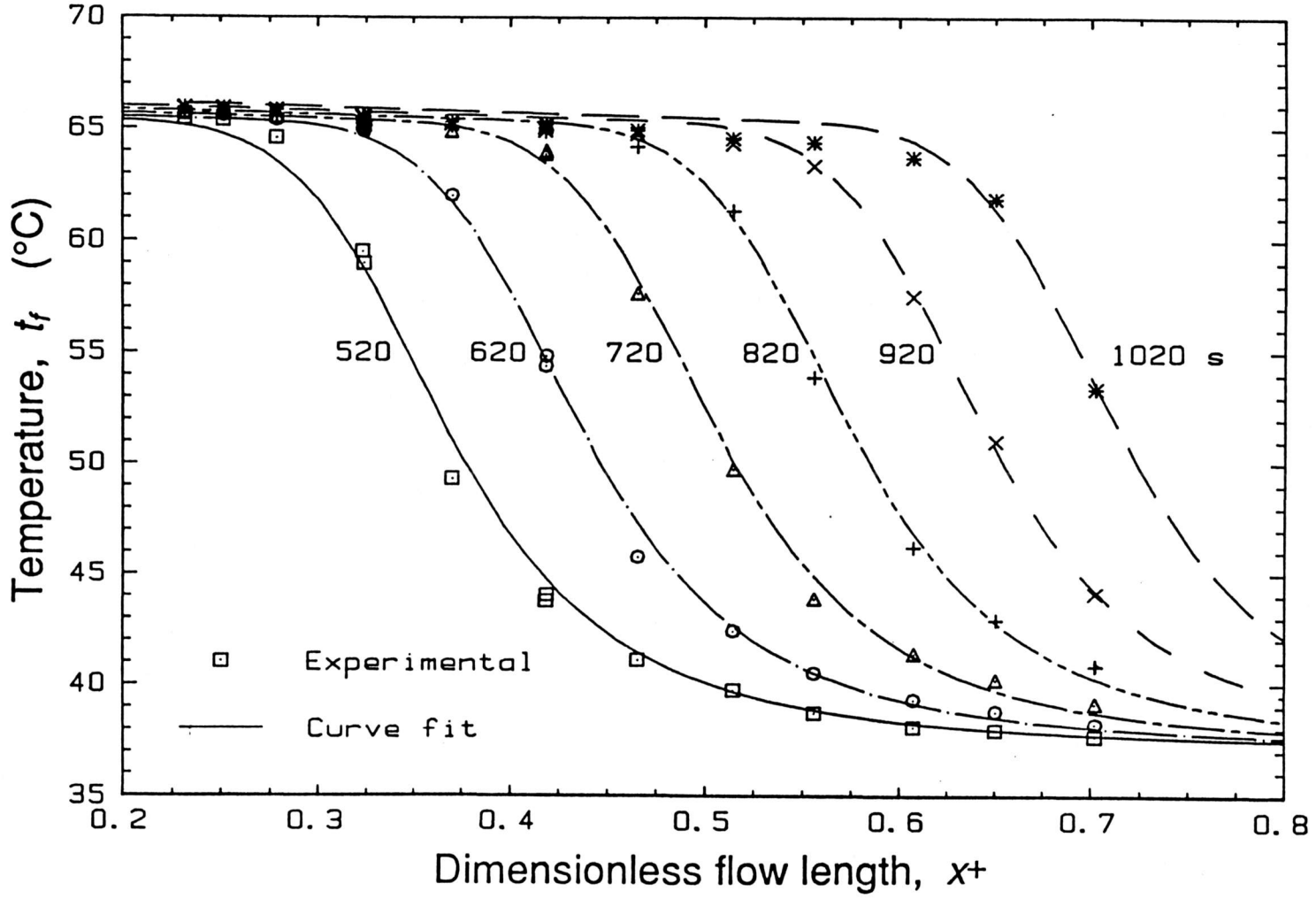

Figure 5.7a Experimental temperature distributions with the dimensionless flow length.

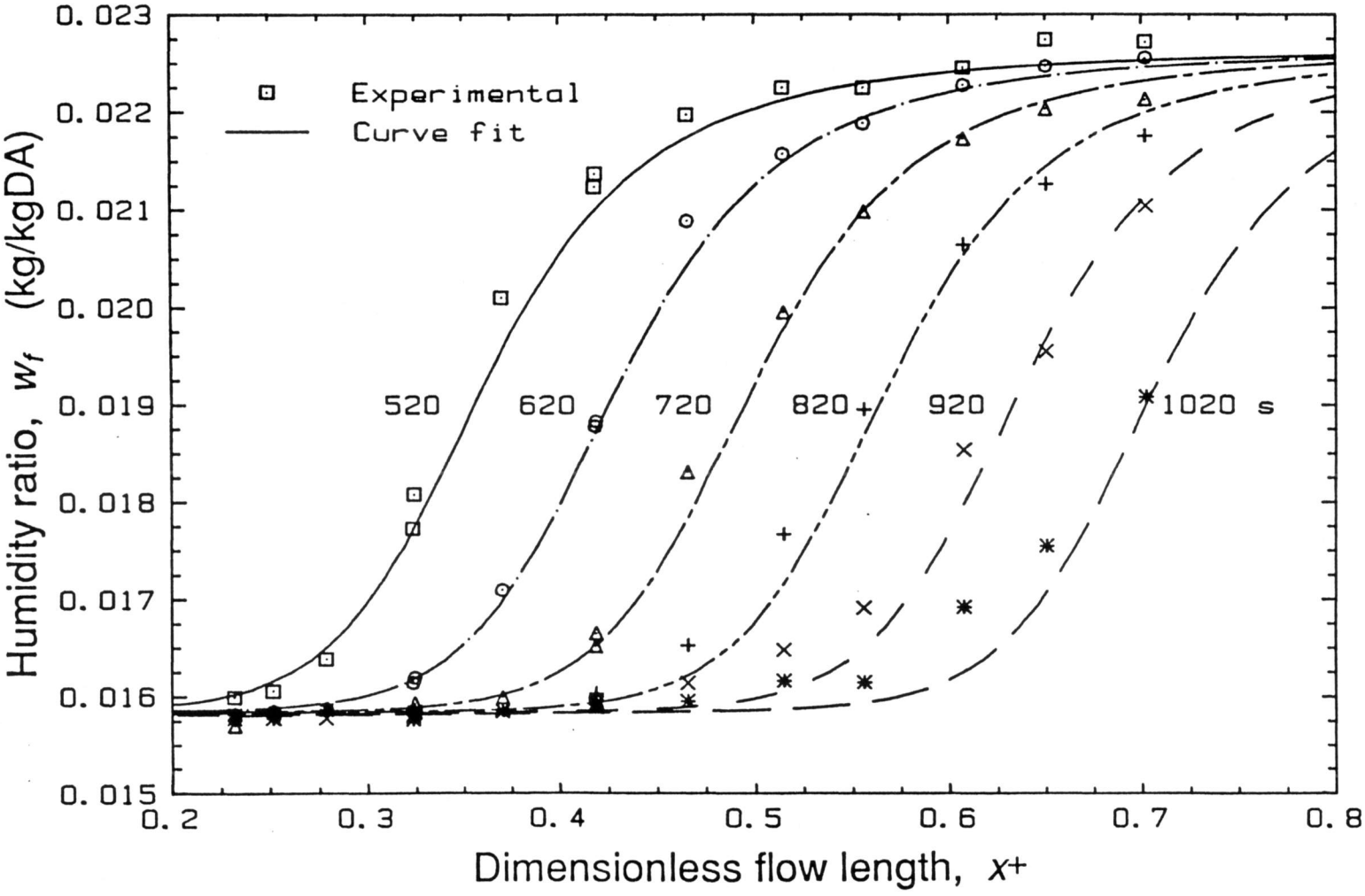

Figure 5.7b Experimental humidity distributions with the dimensionless flow length.

overall transfer coefficients and a Langmuir-type isotherm, Ruthven (1984) reviews analytical solutions for the constant-pattern breakthrough curves for dynamic, isothermal sorption. The listed solutions indicate that the derivative of the fluid stream concentration can be approximated as:

$$\frac{\partial \omega}{\partial x^+} \propto (\omega-\omega_1)(\omega_2-\omega), \tag{5.40}$$

where ω_1 and ω_2 are the bounds for the concentration at the beginning and end of the breakthrough curve, respectively. To incorporate the effects of nonisothermal transfer, non-constant overall transfer coefficients and heat loss to the matrix, the distribution form indicated in Eq. (5.40) is generalized as follows. Define $F(x;p,q)$ as the solution to the initial value problem:

for all x,

$$\frac{dF}{dx} = \frac{[(1+F)+\sqrt{((1+F)^2+\varepsilon^2)}]^p \; [(1-F)+\sqrt{((1-F)^2+\varepsilon^2)}]^q}{(dF/dx)\,|_{x=0}}$$

for $x = 0$, (5.41)

$$F(0;p,q) = \frac{p-q}{p+q}$$

where ε is small, say ≤ 0.01.

This function F is continuous and has an infinite number of continuous derivatives for all x. Its second derivative is smooth and does not show wiggles. The parameters p and q are

shape parameters which determine the skewness of the distribution form, and the tendency of the distribution to tail at F = +1 and -1, respectively. For $p = q = 1$, F' approximates a symmetrical, Gaussian distribution, and F has the shape of the error function.

The experimental data for the temperature and humidity distributions are fitted with the function F defined in Eq. (5.41),

$$\frac{dt_f}{dx^+} = -h_t\,(t_f - t_m) + (t_{f,2} - t_{f,1})\,b\,F'_t(x^+ - x_o; p_t, q_t), \tag{5.42}$$

where,

$$F_t = \frac{2t_f - t_{f,1} - t_{f,2}}{t_{f,2} - t_{f,1}}.$$

A similar form is chosen for the humidity distribution. The first term in Eq. (5.42) describes the heat exchange of the air stream with the test matrix. The parameters h_t and t_m are obtained from the slope of the experimental outlet temperature as a function of x^+ after the second wave has passed through the matrix, and are not part of the curve fit procedure. h_t represents the heat transfer coefficient between the air stream and the matrix and t_m represents the matrix temperature. The second term in Eq. (5.42) represents the dynamic exchange with the desiccant. The parameter b describes the scale of the distributions in the x^+-direction. $t_{f,2}$ and $t_{f,1}$ are the temperatures at the start and end of the wave, and are known

from the average inlet and intermediate conditions. The derivative of the distributions is maximal at $x^+ = x_o$. A similar description holds for the functional form for the curve fit of the experimental humidity distributions.

The curve fit problem can now be posed as follows. For each of the 6 experimental temperature and humidity distributions shown in Figs. 5.7a-b, assume that x_o and b are respectively the same for temperature and humidity. Assume further that the shape parameters (p_t, q_t) and (p_w, q_w) and the scale parameter b are respectively the same for the 6 alternate distributions. There exist then 5 + 6 curve fit parameters which determine the RMS error of the fit with the 2 x 84 experimental data points. This curve fit belongs to the class of large residual minimization problems (Scales, 1985) for which conventional algorithms such as the common Levenberg-Marquardt method are not applicable. Rather a global minimization routine using a quasi-Newton's method with constraints has to be used. The actual calculations were performed by a CRAY X-MP/48 computer using the ZXMWD routine from the IMSL library of mathematical subroutines (IMSL, 1982).

The results of the curve fit procedure indicate that x_o varies linearly with time for the 6 alternate distributions, indicating that the temperature and humidity distributions propagate at a constant speed in the flow direction and that the shape and scale of the distributions are steady or fully

developed. This result confirms with the theoretical prediction that, for the conditions of the reported experiments, the desorption wave is a sharp shock wave for infinite transfer coefficients, and a constant-pattern wave for finite transfer coefficients. The alternate distributions shown in Figs. 5.7a-b can be shifted to the left over a corresponding distance x_o to overlap with a single distribution curve. Figures 5.8a and b show the shifted experimental data points of Figs. 5.7a-b in comparison with the computed curve fits. The RMS error of the experimental data points about the normalized distribution curves obtained from the integration of Eqs. (5.42) is 0.49 °C for the temperature and 0.00020 kg/kg for the humidity.

The shifts for the temperature distributions and the humidity distributions differ with a small constant. This difference indicates that the experimental temperature distributions lag the humidity distributions in time. This effect is small and ignored for this analysis. The nature of this time lag is discussed in detail later in this chapter.

The shifted experimental data can also be fitted with a cubic spline with variable knots at optimized locations. The scatter of the data about this 'best' fit are 0.34 °C for temperature and 0.00012 kg/kg for humidity. These spline RMS errors are of the order of the measurement accuracy, and therefore show that the experimental distributions are indeed fully established.

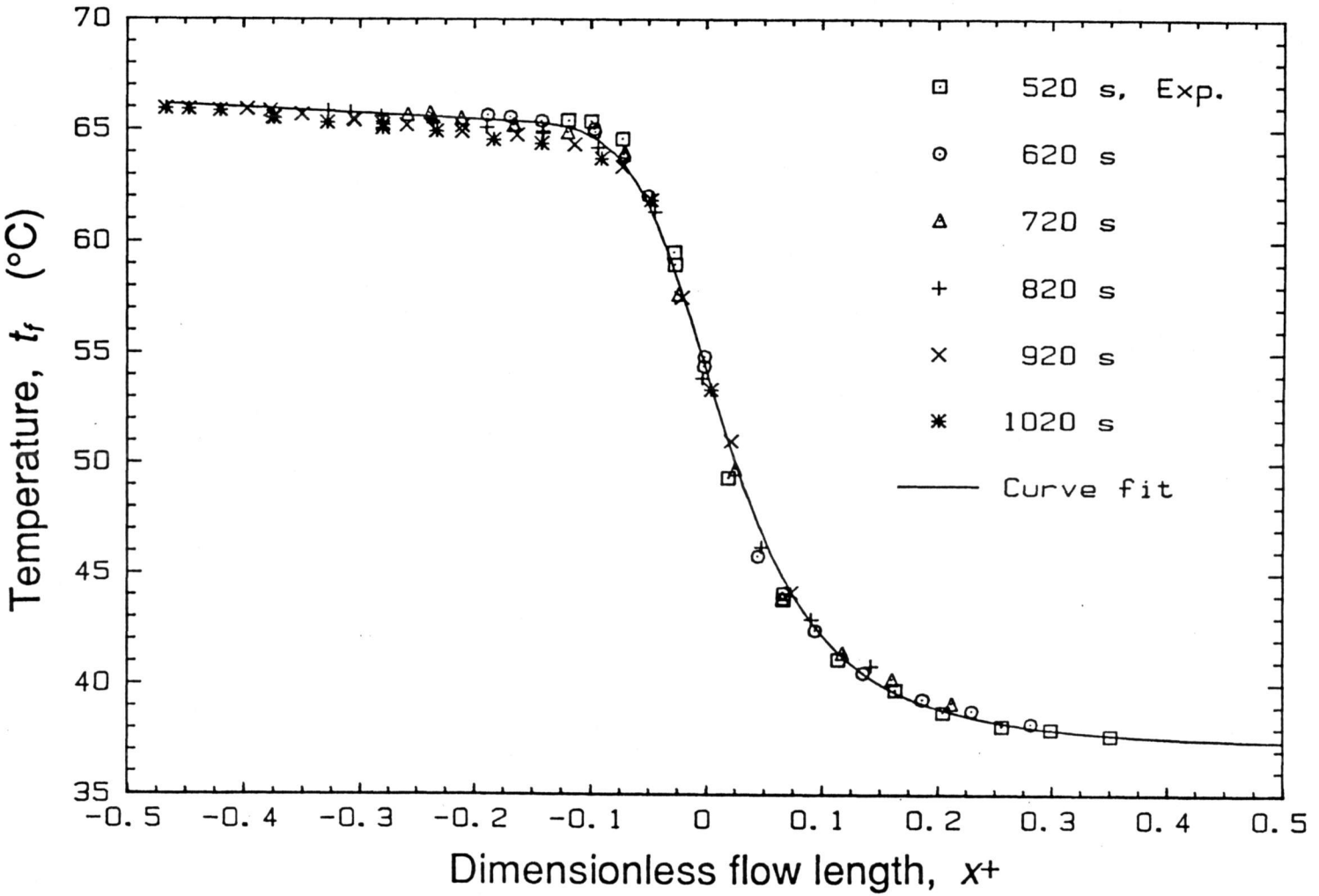

Figure 5.8a Shifted experimental temperature distributions with the dimensionless flow length.

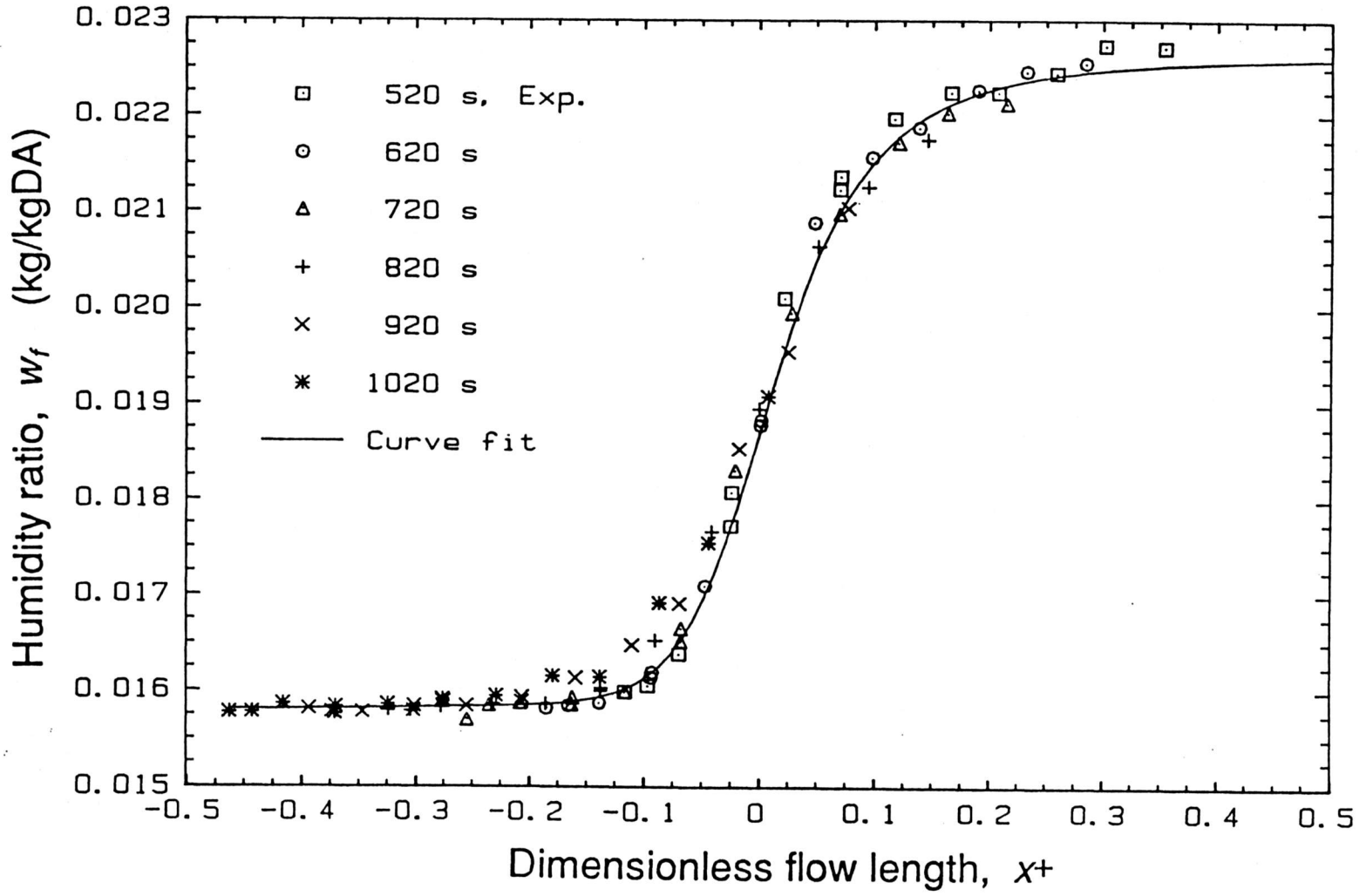

Figure 5.8b Shifted experimental humidity distributions with the dimensionless flow length.

The scale of the wave distribution is determined by the finite rates of mass transfer and is about 12.03 ± 0.03. For the fast thermal wave, this parameter is about 30 times higher. The shape parameters (p_t, q_t) and (p_w, q_w) are respectively (0.9, 1.4) and (1.0, 1.4). The speed at which the distributions move along the channels, $dx_o/d\theta$, is $6.93 \pm 0.08 \times 10^{-4}$/s. This speed relates through the definition of x^+ in Eq. (5.37) to the dimensionless shock speed S_2 discussed in Chapter 2,

$$S_1 = \frac{D_h^2 M_d}{\mu_o A_c L} \frac{dx_o}{d\theta}. \tag{5.43}$$

The computed value of S_2 from the experimental data is $0.0375 \pm 3\%$. The theoretical value, obtained from the shock wave equations with the isotherm with low $E_{o,2}$, is $0.0368 \pm 3\%$. This good agreement between theory and experiment substantiates the presented analysis and also the accuracy of the isotherm correlation introduced in this work.

The cubic spline with variable knots and the integral of the distribution form in Eq. (5.42) provide two analytical expressions which can be used for input to the integral boundary conditions (5.36).

5.4.2.3 Air Side Heat and Mass Transfer Coefficients

The problem of determining the air-side heat and mass transfer coefficients is completely posed at this stage of the analysis. The transfer coefficients are based upon the following conventional definitions;

for the mass transfer coefficient h_m:

$$j = -\rho D_{aw} \frac{\partial \omega_f}{\partial y}\Big|_{wall} = h_m(\omega_{wall} - \omega_{avg}), \tag{5.44}$$

and similarly for the heat transfer coefficient h:

$$q = -k \frac{\partial t_f}{\partial y}\Big|_{wall} = h(t_{f,wall} - t_{f,avg}),$$

in which k and D_{aw} are the thermal conductivity and mass diffusivity of the humid air at the wall. Note that j_w is the water vapor diffusion flux at the wall, rather than the total mass flux m_w, and that q is the energy flux by conduction, rather than the total energy flux e. The Nusselt and Sherwood numbers are defined as conventional,

$$Nu = \frac{h D_h}{k}, \text{ and } Sh = \frac{h_m D_h}{\rho D_w}. \tag{5.45}$$

Nu and Sh are obtained from the solution of the conservation equations in differential and integral form (5.33, 5.35), with

the differential and integral boundary conditions (5.34, 5.36). The initial conditions are those of fully developed Hagen-Poiseuille flow through parallel plates with uniform temperature and humidity. The thermo-physical properties, ρ, c_p, μ, k, D_{aw}, are obtained from the most recent published standards for property evaluation for air-water vapor mixtures. These property standards are reviewed in Appendix B.

Conventional second-order finite difference solutions of the system of continuity and momentum equations give fluctuations in the velocity and pressure terms. The nature of these fluctuations is the same as those that appear in finite difference solutions of the Navier-Stokes equations and are described by Patankar (1980). The fluctuations are generated by the difference expression for the pressure differential dP/dx^+, which is unknown for internal duct flow. They are of the order of magnitude of the transverse velocities generated by the mass transfer at the wall. Rather than using difference algorithms specifically developed to smooth these fluctuations, such as upwind differencing, the method of orthogonal collocation with cubic Hermite splining over finite elements is used. This method inherently gives smooth profiles for the velocities and fluxes. Also the nonlinearity of the momentum-convection terms and the change of thermo-physical properties with temperature and water vapor mass fraction is included without the need for iteration. The integral of the conser-

vation equations gives increased accuracy for the numerical solution and can be incorporated without adding to the complexity or computation time of the solution. In finite difference schemes, this integral is needed because it serves as an additional equation to compute the pressure differential, however, the expression for the integral destroys the bandness of the nodal coefficient matrix and therefore increases the computation time substantially.

The algorithm for the method of orthogonal collocation for solving one dimensional, parabolic partial differential equations is described in detail by Lapidus and Pindar (1982). In essence, this method approximates the various profiles in the y-direction of the velocity u^+, temperature t_f, and water vapor mass fraction ω, with splines of cubic Hermite polynomials defined over a sequence of finite elements. With this representation, the partial differential equations, expressed at the Gaussian quadrature points within each element, are reduced to a system of ordinary differential equations in the nodal variables u^+, t_f, ω, and P. This system of equations can be solved with a conventional ODE solver. In this analysis, 5 finite elements are used in combination with the fourth order Runga-Kutta method. The multidimensional collocation vectors which appear in the numerical scheme are structured to minimize the number of page faults during computation and thereby maximizing execution speed. The actual

calculations were performed by a CRAY X-MP/48 computer and took in all about 20 minutes of CPU time for a complete integration in the x^+-direction. The large CPU time is the result of the small step size, $5x10^{-5}$, which was needed to make the integrator stable. Collocation schemes in general add stiffness to the ODE system.

Solutions are obtained and presented for the cubic spline and the *F* distribution function representing the experimental data. Figures 5.9a-c show the distributions in the x^+-direction of, respectively, the air-side Nusselt and Sherwood numbers, the average- and wall temperature and water-vapor mass fraction, and the conductive- and total energy and mass diffusion fluxes, for the *F* distribution input. The variation of the local Nusselt and Sherwood numbers is due to the nonuniform distributions of the wall fluxes. These flux distributions have the shape of a skewed Gaussian distribution, as shown in Fig. 5.9c. The fluxes are constant in the region $x^+ < -0.3$ prior to the start of the wave. In this region the computed *Nu* and *Sh* numbers agree with the asymptotic value for constant fluxes, 8.235 (Shah and London, 1978), as indicated in Fig. 5.9a and this agreement substantiates the accuracy of the numerical model.

The Sherwood number starts to increase at $x^+ \approx -0.3$, and the Nusselt number increases at $x^+ \approx -0.2$ in Fig. 5.9a. This difference is due to the sensitivity of the Nusselt and

Sherwood numbers to the representation of the experimental data with interpolating functions. Figure 5.10a shows the *Nu* and *Sh* distributions for the cubic spline input. These latter figures illustrate the effect of the curve fit representation on the results of the calculations. The local Nusselt and Sherwood numbers depend mainly on the distributions of the **derivatives** of the wall fluxes, and the discontinuity of the third derivative of the cubic splines at the knots has a major effect on the computed transfer coefficients. This result shows that the experimental data for input to the analysis need to be represented with a curve fit which is smooth and has continuous, smooth derivatives up to at least second order. These requirements are approximately met by the integrated *F* distribution as introduced in Eqs. (5.41-42). Furthermore, the second derivative of the curve fit should approximate the second derivative of the experimental temperature- and humidity distributions with good accuracy. Such a curve fit requires (a) extremely accurate measurements of the air stream temperature, humidity and mass flow rate, and (b) a large series of highly repeatable experiments for a wide range of the air stream mass flow rate. These requirements can be met with state-of-the-art single blow facilities, however, with the experimental facility used in this study, the scatter of the measurements is too large to assure good accuracy in the second derivative.

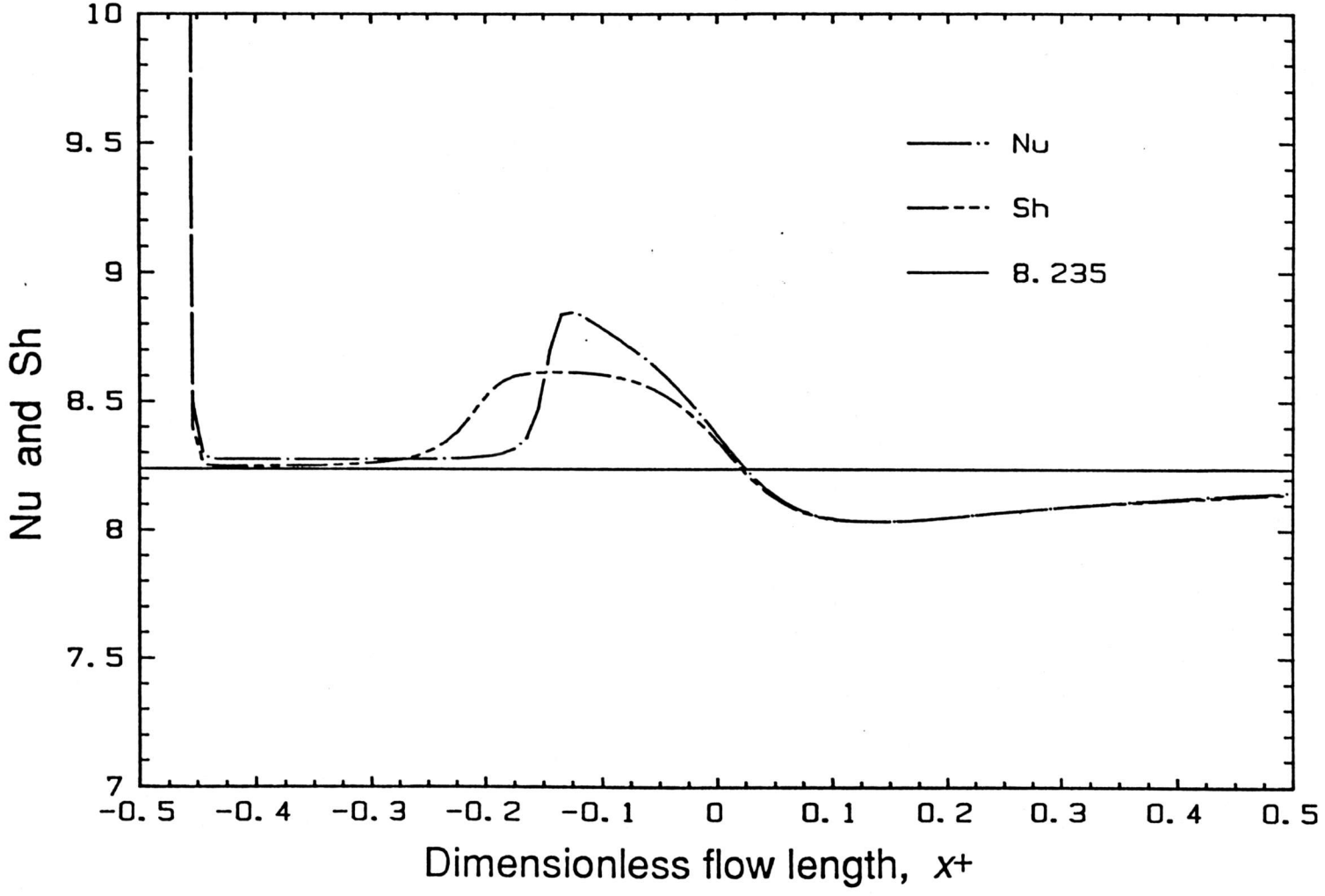

Figure 5.9a Air Nusselt and Sherwood number distributions with the dimensionless flow length.

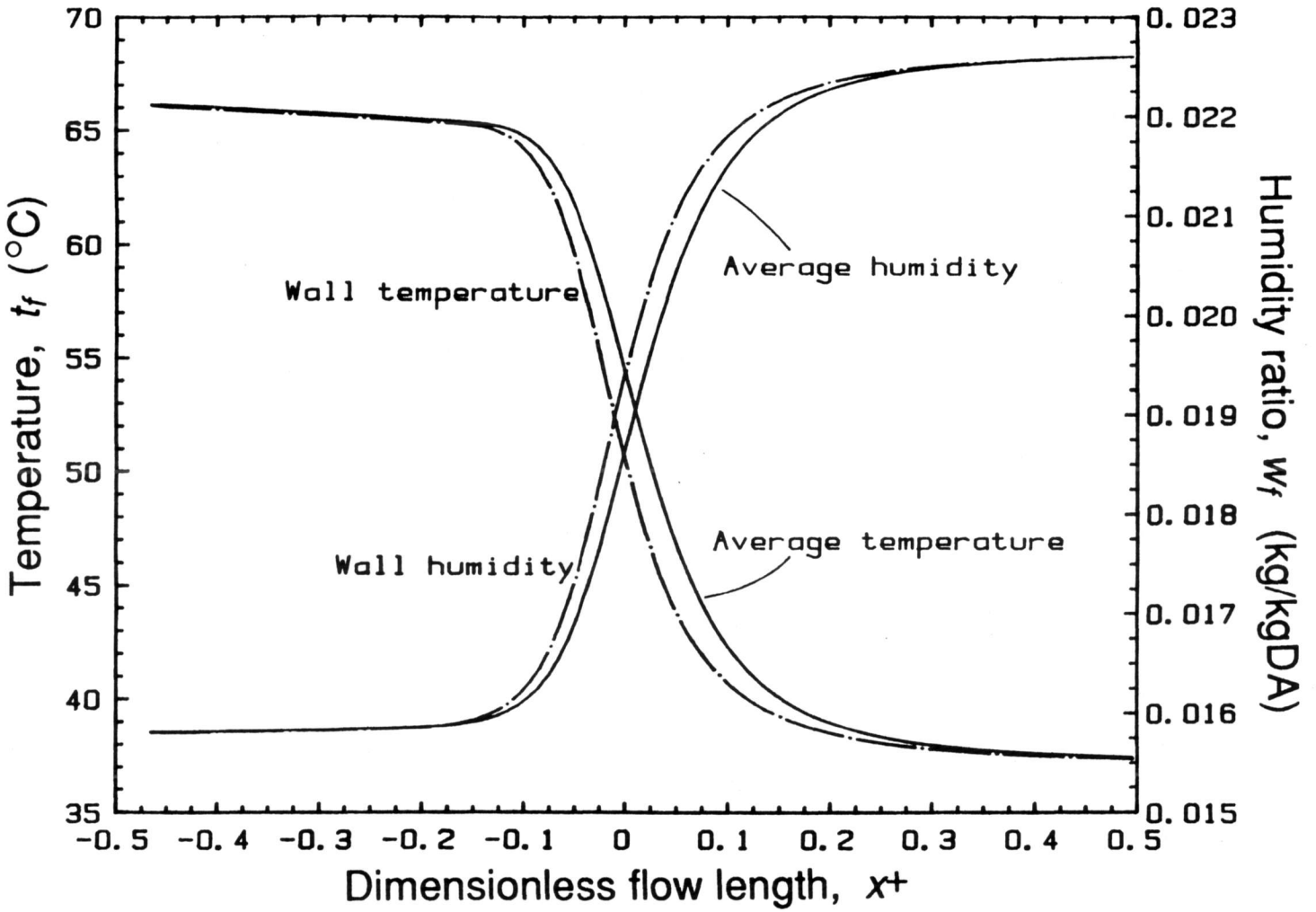

Figure 5.9b Air temperature and humidity distributions with the dimensionless flow length.

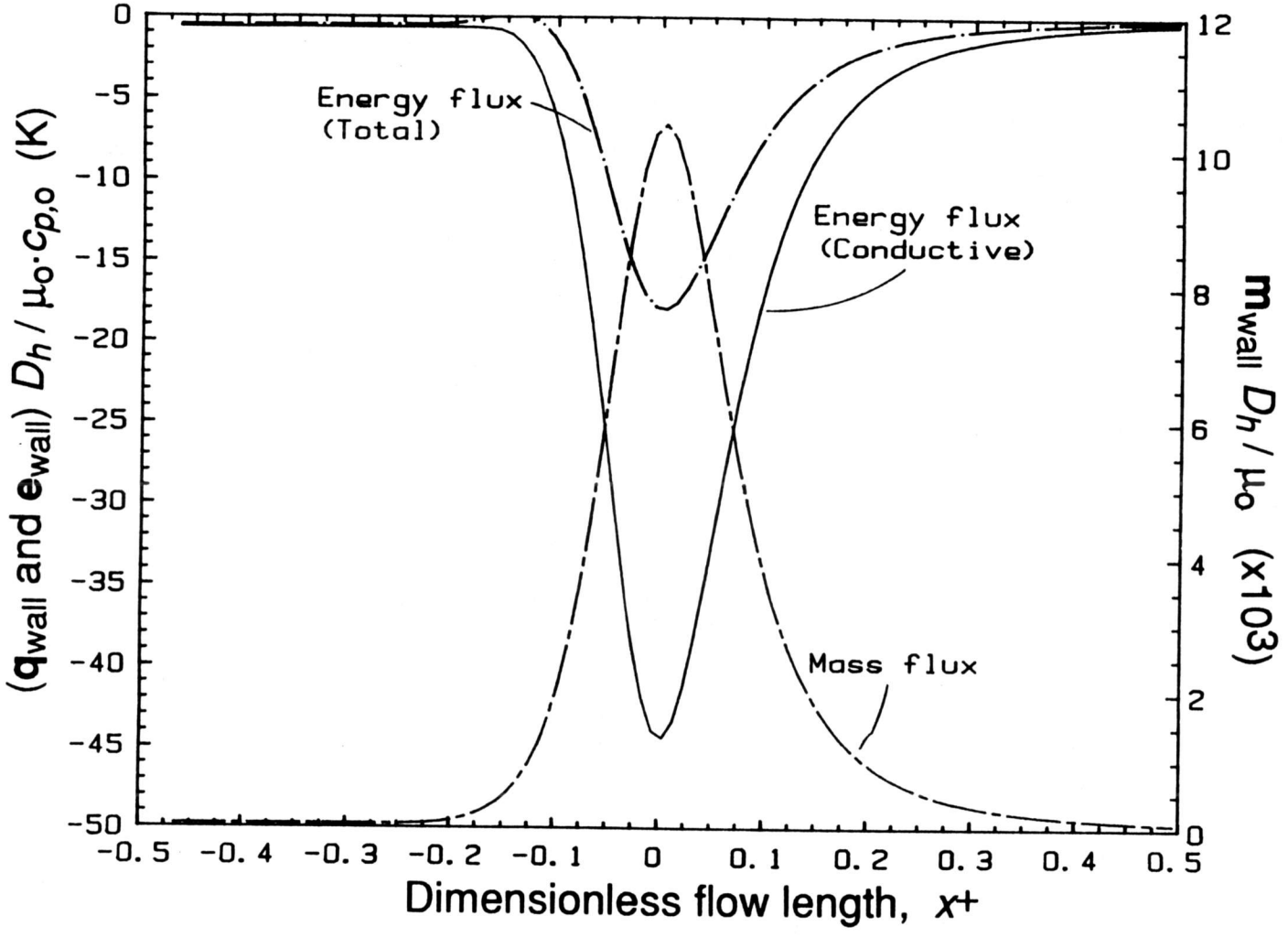

Figure 5.9c Air mass and energy flux distributions with the dimensionless flow length.

The variations of *Nu* and *Sh* with position is important in the window $-0.1 \leq x^+ \leq 0.2$ where the magnitudes of the mass and energy transfer fluxes are largest. In this region, Fig. 5.9a indicates that the variations of *Nu* and *Sh* about the average value are similar and small, about ± 5%. The average numbers compare with the solution for a constant heat or mass flux, 8.235. To check these results, the computed distributions can be compared with theoretical distributions obtained from an analogy theory. Graber (1970) showed that the Nusselt number for forced convection, laminar flow in ducts depends on the derivative of the heat flux. For an exponential distribution of the local wall heat flux, the temperature profile is fully developed, the Nusselt number is constant and, for flow through parallel plates, can be approximated with the following linear equation,

$$\mathrm{Nu} = 8.235 + 0.0222 \frac{1}{q}\frac{dq}{dx^+} \tag{5.46}$$

For non-exponential flux distributions, the temperature profile is continuously developing. However, it may be expected that the local Nusselt number can still be approximated by Eq. (5.46). The local wall heat flux is proportional to the derivative of the average fluid temperature with respect to x^+, and, in this study, can be directly obtained from the curve fit of the experimental data, Eq. (5.42). The estimated distri-

butions of the Nusselt and Sherwood numbers computed with Eq. (5.46) are compared with the complete solution of the conservation equations in Fig. 5.10b. The respective profiles do not exactly overlap because the local wall fluxes do not vary exponentially with x^+, and the local temperature and humidity profiles are continuously developing. However, the corresponding curves show the same variation and that fact substantiates the results of this analysis. The main conclusion of this part of the analysis is that the air-side Nusselt and Sherwood numbers are approximately constant for the mass transfer wave of the desorption experiments, and about equal to the value for constant wall fluxes.

The local energy and water-vapor mass fluxes shown in Fig. 5.9c can be integrated over x^+. These experimental airstream mass and energy integrals can be verified by comparison with a theoretical thermodynamic model of the desiccant layer. This further check on the accuracy of the presented analysis is given in the second part of the analysis of the M-D experiments, introduced next.

5.4.3 Analysis and Discussion II: Desiccant Side Transient Heat and Mass Transfer Coefficients

This second analysis is structured similar to the previous discussion and is also presented in three parts. The

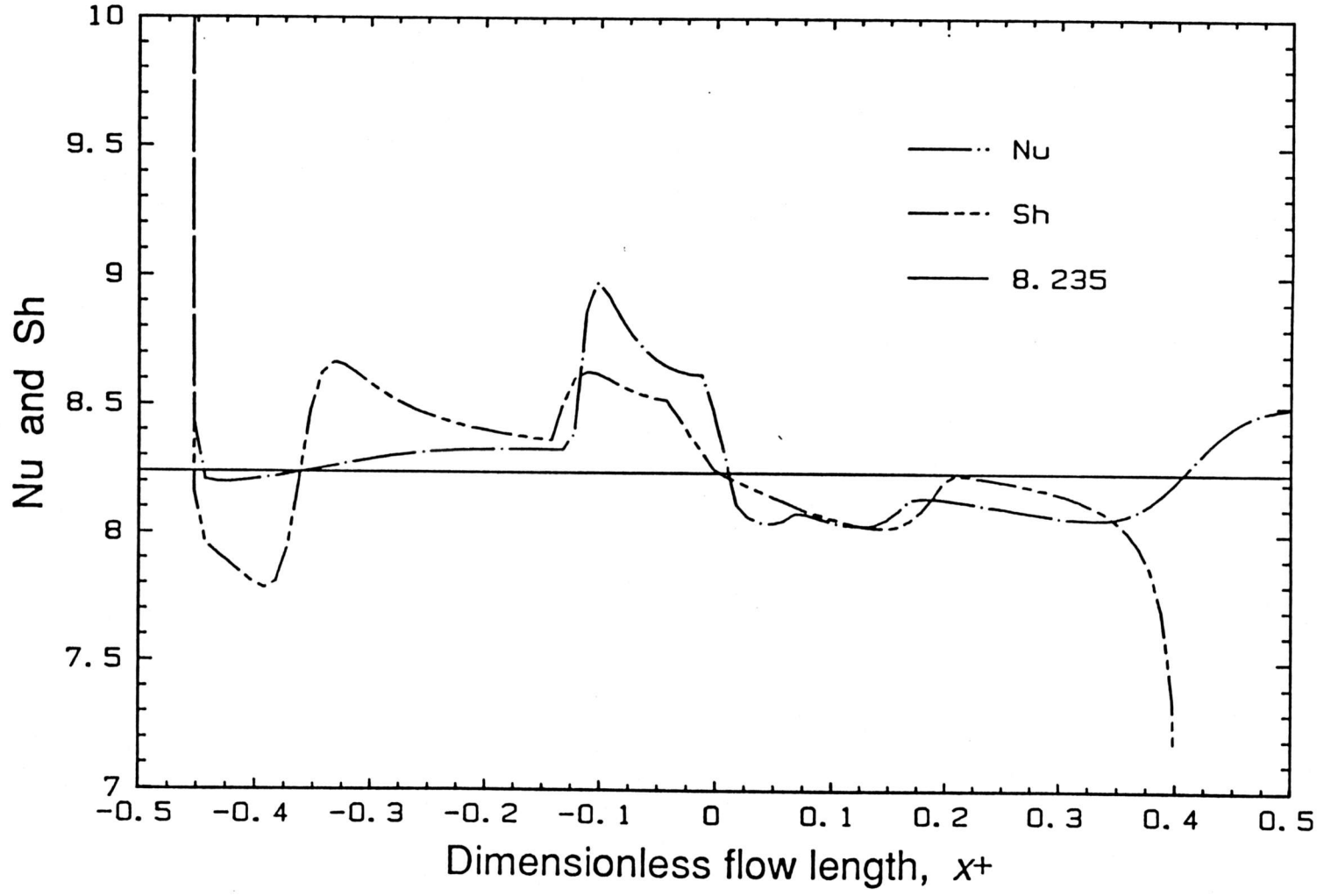

Figure 5.10a Air Nusselt and Sherwood number distributions with the dimensionless flow length for the cubic spline curve fit.

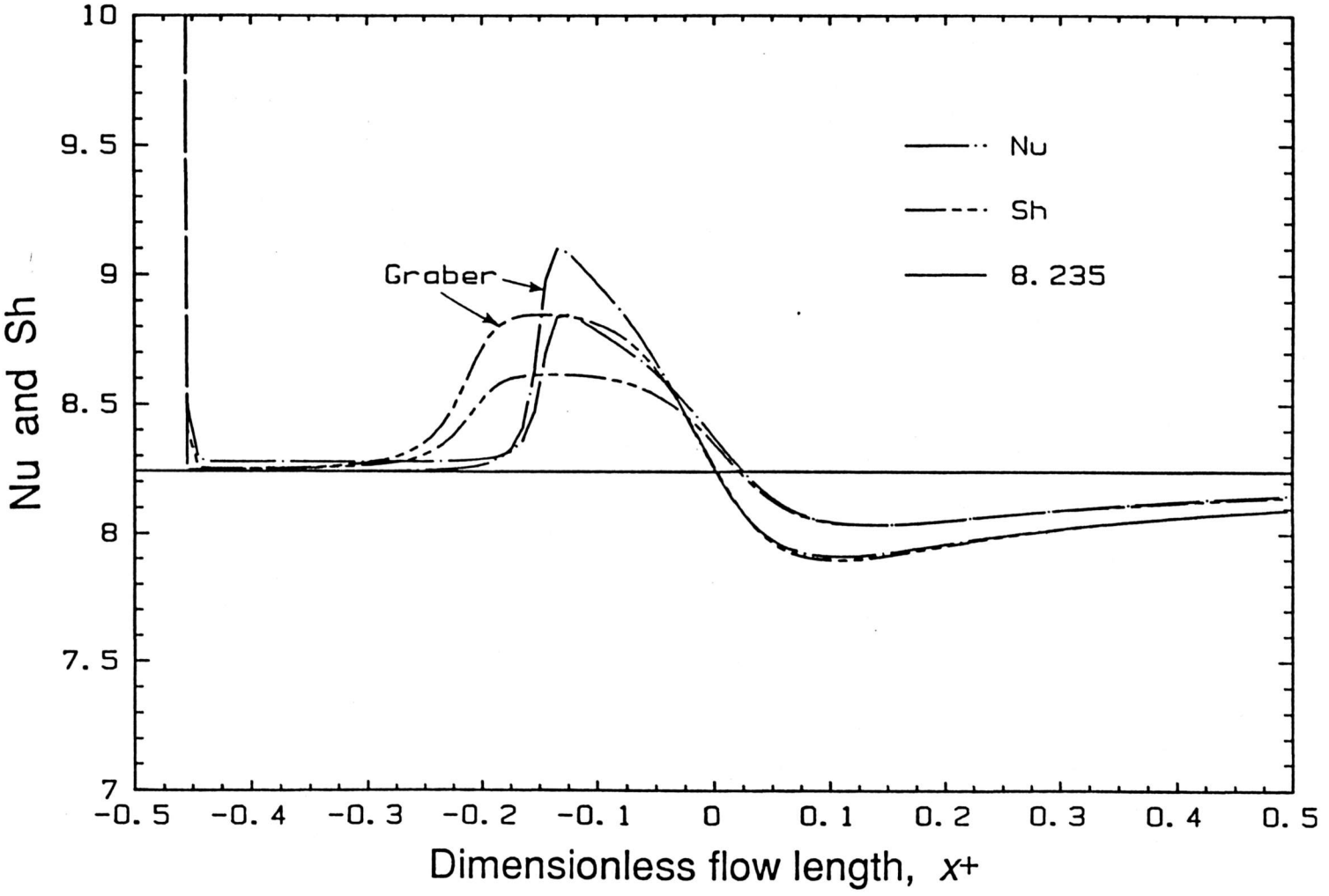

Figure 5.10b Air Nusselt and Sherwood number distributions with the dimensionless flow length compared with Graber's analysis.

first section describes the model formulation and assumptions. The wall heat and mass fluxes obtained from the previous analysis are prepared for input to the model in the second part. The third section presents the results of the analysis.

5.4.3.1 Model Formulation and Assumptions

The model for analyzing the experimental results is based upon the conservation of mass and energy for transient, adiabatic diffusion of water vapor inside regular-density silica gel particles. The general equations of change for the molecular transport of species through a porous media are simplified with a set of assumptions and order of magnitude estimates for the terms that appear in the conservation equations.

ASSUMPTIONS

1. The local kinetic rate of sorption is much larger than the rates of mass diffusion within the gas or adsorbed phase. Therefore, there is local equilibrium between the gas and adsorbed phases at all times.

2. The porous desiccant particles are considered as a continuum. The average diameter of the internal pores is about 22×10^{-10} m, and is small compared to the average diameter of the particles, 22×10^{-5} m. The distribution of the phases and the temperature within the particles are considered continuous.

3. The porosity of the desiccant is constant throughout the volume of the particles.

4. Air present within the internal pores of the desiccant is stagnant and inert, and does not affect the local thermodynamic equilibrium of the water molecules in the gas and adsorbed phases.

5. The geometry of the particles is approximated as spheres.

This last assumption is the critical part of this analysis. The transfer resistances of the desiccant particles are mainly determined by their geometry, and the results of this analysis is consequently only applicable to spherical particles. The effect of the shape of desiccant particles on the overall transfer resistance for linear rate equations is investigated in the next chapter.

ORDER OF MAGNITUDE ESTIMATES

1. Pressure and Ordinary Diffusion in the Gas Phase

A complete description of the various mass-diffusion fluxes occurring within porous adsorbents is reviewed in Appendix A. The magnitude of Knudsen diffusion relative to ordinary diffusion depends on the ratio of the mean free path length of the diffusing gaseous molecules to the pore diameter of the channels in which the transport occurs. For regular-density silica gel and water vapor at room temperature, the pore diameter is 22×10^{-10} m which is much smaller than the mean free path of the water molecules, 12×10^{-8} m. The dominating diffusion mechanism in the gas phase is thus Knudsen diffusion.

Pressure diffusion due to Poisseuille flow through the pores is negligible compared to Knudsen diffusion for pores with diameters less than 10^{-8} m (Ruthven, 1984). This condition is satisfied for regular-density silica gel.

CONSERVATION EQUATIONS IN DIFFERENTIAL FORM

The equations of change for mass and energy in terms of the transport fluxes are described by Bird, Stewart and Lightfoot (1960). Expressions for the transport fluxes in terms of the transport coefficients for porous adsorbents are reviewed in Appendix A. The equations which model the transient diffusion of water vapor and energy for the set of assumptions declared above and with the simplifications of the order of magnitude analysis are expressed in terms of the transport properties as follows.

1. Continuity of the water vapor:

$$\frac{\varepsilon_p \rho}{1-\omega}\frac{\partial \omega}{\partial \theta} = - R_w + \nabla\cdot\left(\frac{\varepsilon_p \rho}{1-\omega} D_{K,e}\nabla\omega\right)$$

2. Continuity of the adsorbed phase:

$$(1-\varepsilon_p)\rho_s\frac{\partial W_d}{\partial \theta} = R_w + \nabla\cdot\left((1-\varepsilon_p)\rho_s D_{S,e}\nabla W_d\right)$$

3. Conservation of energy equation: (5.47)

$$\rho c\frac{\partial t_d}{\partial \theta} + i_w\frac{\varepsilon_p \rho}{1-\omega}\frac{\partial \omega}{\partial \theta} + I_W(1-\varepsilon_p)\rho_s\frac{\partial W_d}{\partial \theta}$$

$$= \nabla\cdot k\nabla t_d + \nabla\cdot\left(i_w\frac{\varepsilon_p \rho}{1-\omega} D_{K,e}\nabla\omega + I_W(1-\varepsilon_p)\rho_s D_{S,e}\nabla W_d\right)$$

R_w is the local volumetric rate of adsorption. ρc is the average specific heat of the desiccant particle,

$$\rho c = \varepsilon_p \rho c_{aw} + (1-\varepsilon_p)\, c_{sw} \tag{5.48}$$

where c_{aw} and c_{sw} are the specific heats of humid air and wet silica gel. The enthalpies i_w and I_W are the partial molal enthalpies of respectively the water vapor in the gas phase and liquid water in the sorbed phase. Correlations for these thermodynamic properties and the transport coefficients $D_{S,e}$, $D_{K,e}$ and k are retrieved from the latest available data published in the literature and listed in Appendix B.

The assumption of local equilibrium between the adsorptive and adsorbate phases yields an additional relationship for the variables t_d, ω and W. The relationship used in this work is the Dubinin-Polanyi expression for the sorption isotherm of water vapor on regular density silica gel. The low value for $E_{o,2}$ is chosen.

BOUNDARY CONDITIONS

This set of conservation equations forms a set of non-linear, parabolic partial differential equations. The boundary conditions for the variables t_d and W need to be specified at the external surface of the desiccant particles. An additional boundary condition of symmetry in the center of the spherical particles closes the set of equations. The boundary conditions

at the surface are the fluxes from the air stream into the desiccant,

for the water vapor mass flux,

$$-\frac{\varepsilon_p \rho}{1-\omega} D_{K,e} \nabla\omega - (1-\varepsilon_p)\rho_s D_{S,e} \nabla W_d = \boldsymbol{m}_{wall}$$

and for the energy flux, (5.49)

$$-k\nabla t_d - i_w \frac{\varepsilon_p \rho}{1-\omega} D_{K,e} \nabla\omega - I_W (1-\varepsilon_p)\rho_s D_{S,e} \nabla W_d = \boldsymbol{e}_{wall}$$

The gradients are normal to the surface and directed outward of the particle into the air stream.

CONSERVATION EQUATIONS IN INTEGRAL FORM

The conservation equations (5.47) can be integrated over the volume of the particle. The integrals of the divergences of the transport fluxes are related to the boundary conditions for the gradients (5.49) through the Gauss-Ostrogadskii divergence theorem. The overall conservation balances can be expressed as,

for the conservation of mass:

$$\frac{\partial}{\partial\theta} \iiint (\varepsilon_p \rho\omega + (1-\varepsilon_p)\rho_s W_d)\, dV = -\boldsymbol{m}_{wall}$$

(5.50)

and for the conservation of energy:

$$\frac{\partial}{\partial\theta} \iiint (\varepsilon_p \rho i_{aw} + (1-\varepsilon_p)\rho_s I_{sw})\, dV = -\boldsymbol{e}_{wall}$$

where the triple integrals denote integration over the particle volume.

Depending on the algorithm for integration of the differential equations of change (5.47), the accuracy of the numerical solution of conservation equations can usually be increased if the integral equations (5.50) are solved simultaneously. These equations assure the overall conservation of mass and energy at each level of the marching-type integration for these parabolic systems..

The conservation equations (5.47) and (5.50) and the boundary conditions (5.49) form a closed set of transient diffusion equations. There exist two fundamental characteristic diffusivities for the transport of mass and energy, respectively. For the conditions of the studied desorption tests, the mass diffusivity ranges from 1 to 2.4×10^{-9} m^2/s, and the thermal diffusivity ranges from 2.8 to 3.4×10^{-7} m^2/s. These diffusivities define two characteristic time constants. The time constant related to the mass diffusion is the larger one and determines the scale for the reduced time variable,

$$\theta^+ = \frac{\theta D_{sw}}{D_p^2} \tag{5.51}$$

where D_{sw} is the total effective diffusivity for diffusion of water through silica gel, defined by Eq. (A.26). Because this property varies over a range of 2.5, the diffusivity used for

the definition of θ^+ is a reference diffusivity, and by definition set to 10^{-9} m^2/s.

5.4.3.2 Preparation of Experimental Data for Input to the Model

The mass and energy fluxes which form the boundary conditions (5.49) need to be expressed in terms of the reduced time variable defined in Eq. (5.51). The analysis of the experimental data for input into the air-side model shows that the distributions of temperature and humidity shift with time in the direction of the air flow at a constant speed, Eq. (5.43). The relationship between the dimensionless distance in the flow direction and the real time for the reported experiments is:

$$\theta = 1443\,(0.5 - x^+)\,. \tag{5.52}$$

Using the definitions for θ^+ (5.51) and x^+ (5.37), Eq. (5.52) can be used to express the wall fluxes presented in Fig. 5.9c in terms of θ^+. These intermediate flux distributions need to be checked for accuracy and correctness of conversion from dimensionless form scaled with air stream properties to dimensionless form scaled with desiccant properties. Three independent checks exist and can be presented as follows.

Table 5.9 lists selected air stream and desiccant properties at the start and end of the desorption wave. The prop-

Table 5.9 Selected air-stream and desiccant properties at the start and end of the desorption wave

	Time (s) 0	1392	Δ	
x^+	0.5	-0.465		
t_f, t_d	37.325	66.097	28.772	°C
ω	0.02210	0.01555		kg/kg
w_f	0.02260	0.01575	-0.006855	kg/kgDA
i_f	360985	375530	14545	J/kgDA
P	82320	82320		Pa
rh	0.449	0.0772		
W_d	0.2286	0.04903	-0.1795	kg/kgDD
I_d	6378	49637	43259	J/kgDD

INTEGRALS

$\int_0^{1392} \dot{m}_{wall} d\theta$	-0.024827 kg-water/m^2
$\int_0^{1392} \dot{e}_{wall} d\theta$	45094 J/m^2

erties at start of the wave are those of the intermediate state, and at the end those of the inlet state. The ratio of the air-stream water-vapor gain to the desiccant water loss can be evaluated from the data listed in this table,

$$\frac{\Delta w_f}{\Delta W_d} = \frac{0.006855}{0.179551} = 0.0382 \pm 3\%. \qquad (5.53)$$

From the rotary dehumidifier theory reviewed in Chapter 2, this ratio should be equal to the dimensionless shock-wave speed S_2

obtained from the experiments, Eq. (5.43), which is 0.0375 ± 3%. These two values agree with each other well within the ranges of experimental uncertainty.

The integral over time of the water-vapor mass flux at the walls of the flow passages can be computed from the results of the previous analysis and is 0.02483 kg-water/m^2-transfer-area. The transfer area between the air stream and the desiccant layer can be estimated from this integral,

$$A = \frac{M_d \Delta W_d}{\int \dot{m}_{wall} d\theta} = \frac{(0.487)(-0.1795)}{-0.024827} = 3.52 \text{ m}^2. \qquad (5.54)$$

This value can be compared with the experimental value obtained from the pressure drop tests, 3.65 m^2 ± 4.5%, and the theoretical value computed from the geometry of the matrix, 3.49 m^2. Again these values agree within the ranges of accuracy.

The integral over time of the total energy flux at the walls of the flow passages can be computed from the results presented in Fig. 5.9c with Simpson's integration rule and is -45094 J/m^2-transfer-area. The fraction of energy which is exchanged with the desiccant can be computed from an integral energy balance,

$$f = \frac{M_d \Delta I_d}{-A \int \dot{e}_{wall} d\theta} = \frac{(0.487)(43259)}{(3.52)(45094)} = 0.133, \qquad (5.55)$$

indicating that only 13% of the energy is exchanged with the desiccant. The remainder is exchanged with the structural material of the matrix. The thermal capacitance associated with this structural material can be computed from the energy integral,

$$C_m = \frac{-(1-f)A\int \dot{e}_{wall}\,d\theta}{\Delta t_d} = \frac{(0.867)(3.52)(45094)}{(66.98-37.32)} = 4640\ \text{J/K}. \qquad (5.56)$$

This experimental value can be compared with the theoretical value computed from the matrix geometry and the thermo-physical properties of the matrix materials, 4740 J/K. The agreement is again well within the ranges of experimental uncertainty.

These three independent checks substantiate the analysis of the experimental results presented so far. The flux distributions are thus ready to be input to the desiccant model to proceed with the analysis. The local air-stream wall fluxes, mass and energy, are related to the desiccant fluxes per unit external surface area by:

$$\phi_{des} = \frac{A}{A_p}\phi_{air}, \qquad (5.57)$$

in which ϕ is either $\dot{m}_{wall}$ or $\dot{e}_{wall}$, and where A is the air-to-desiccant transfer area and A_p is the total external surface area of the desiccant particles. This external surface area is, by definition of the particle diameter D_p, equal to:

$$A_p = 6\frac{V_p}{D_p} = 6\frac{(0.487/1210)}{217 \times 10^{-6}} = 11.12 \text{ m}^2 \qquad (5.58)$$

Equation (5.57) assumes that the air fluxes are uniformly distributed over the external surface area of the desiccant particles. Figure 5.4 illustrates the configuration of the desiccant particles within the desiccant sublayer with respect to the air stream. The desiccant layer is composed of individual, separated particles surrounded by a continuous layer of stagnant air. The macroscopic porosity or void fraction of the particle layer is 56%. The mass diffusivity of water vapor in air, D_{aw}, is about 2.8×10^{-5} m^2/s, and the effective *mass diffusion coefficient* of water vapor in regular-density silica gel, based upon the gradient of the water vapor mass fraction, is about 1.0×10^{-5} m^2/s. These numbers indicate that the mass fluxes through the stagnant air are comparable to the interparticle diffusion fluxes for equal mass fraction gradients. However, the effective *mass diffusivity* of silica gel is much smaller, 1.2×10^{-9} m^2/s, due to the larger density of the solid phase. Thus, the response time for transient wall fluxes of the pockets of still air is much smaller than the response time of the particles, and it can be assumed that, on the time scale of the desiccant particles, the surrounding air has homogeneous properties. Also, the thermal diffusivity of the particles is about 2.8×10^{-7} m^2/s which is an order of magnitude smaller than

that of humid air. Hence, thermal energy will be distributed more rapidly within the air phase than within the particles.

Figure 5.4 shows that part of the external desiccant surface is attached with adhesive to the tape carriers. These surfaces act as adiabatic walls for heat transfer and as vapor barriers for mass transfer. The effect of the presence of such surfaces on the transient response of the individual particles is discussed in next chapter.

5.4.3.4 Desiccant Side Heat and Mass Transfer Coefficients

The problem of determining the desiccant particles heat and mass transfer resistance is completely posed at this stage of the analysis. The particle transfer coefficients are based upon the following definitions,

for the mass transfer coefficient h_m:

$$j_W = -(1-\varepsilon_p)\rho_s D_{W,e}\frac{\partial W_d}{\partial \eta}\Big|_{wall} = h_m(W_{d,wall} - W_{d,avg})$$

and similarly for the heat transfer coefficient h: (5.59)

$$q = -k\frac{\partial t_d}{\partial \eta}\Big|_{wall} = h(t_{d,wall} - t_{d,avg}),$$

in which $D_{W,e}$ and k are the effective diffusivity and thermal conductivity of the desiccant at the external surface of the particles. The transfer coefficients are based upon rate expressions for the diffusion fluxes, rather than the total

mass and energy fluxes with respect to a stationary coordinate system. The conductive Nusselt and Sherwood numbers are defined in analogy with convective heat transfer,

$$Nu = \frac{hD_p}{k} \quad \text{and} \quad Sh = \frac{h_m D_p}{(1-\varepsilon_p)\rho_s D_{W,e}}. \tag{5.60}$$

The Nusselt and Sherwood numbers are obtained from the solution of the conservation equations in differential and integral form. These equations are very similar to the parabolic, one-dimensional Navier-Stokes equations (5.33-36), and the numerical procedures programmed by the author for the solution of these equations are applicable for the desiccant equations with only minor modifications. The method of orthogonal collocation with cubic Hermite splining reduces the differential and integral conservation equations to a system of ordinary differential equations in the nodal variables: temperature, gel-water load, conductive energy flux and mass diffusion flux. The most recent correlations for the thermo-physical properties of regular-density silica gel as described in Appendix B are used to evaluate the desiccant properties at the collocation points. The gradients and divergences are expressed in spherical coordinates.

The system of differential equations is a typical system of stiff equations due to the different time constants of the mass and energy equation. Therefore, Gear's method with

variable order for stiff O.D.E.'s is used to integrate the system of equations. The actual numerical computations were done by a Digital Equipment Corp. MicroVAX computer and took in all less than 5 minutes of CPU time for a complete integration. The numerical subroutine DGEAR from IMSL was used as integrator (IMSL, 1982).

The results of the computations are presented in graphical form in Figures 5.11a-b. Fig 5.11a shows the particle conductive Nusselt and Sherwood numbers as functions of the reduced flow length x^+. The computed Nusselt number is constant and equal to 10, the theoretical value for steady state heat conduction into spherical particles with a constant heat flux boundary condition. The agreement between this theoretical value and the computed value substantiates the accuracy of the numerical model. The Sherwood number varies slightly about the average value, 10. The variation is due to the non-constant surface fluxes, which have a skewed Gaussian distribution in time. The effect of non-constant boundary conditions can be estimated with the analogy method discussed in analysis part I. For spherical particles and exponential mass fluxes, the Sherwood number is constant and given by:

$$Sh = 10.0 + 0.052 \frac{\partial j}{j \partial \theta^+} \tag{5.61}$$

Although the sensitivity coefficient in Eq. (5.61) is more than twice that for convective heat transfer in parallel plates,

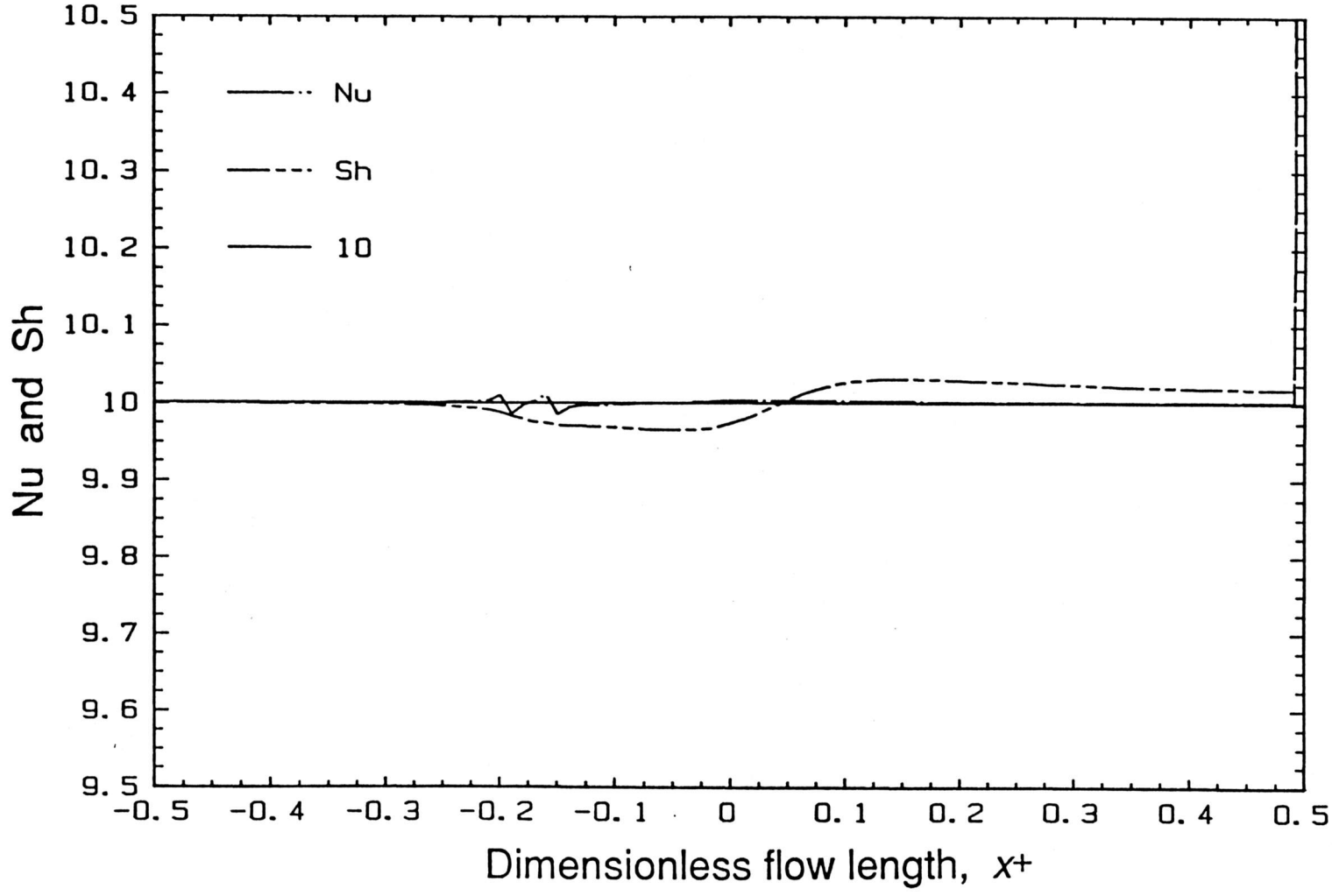

Figure 5.11a Desiccant Nusselt and Sherwood number distributions with the dimensionless flow length.

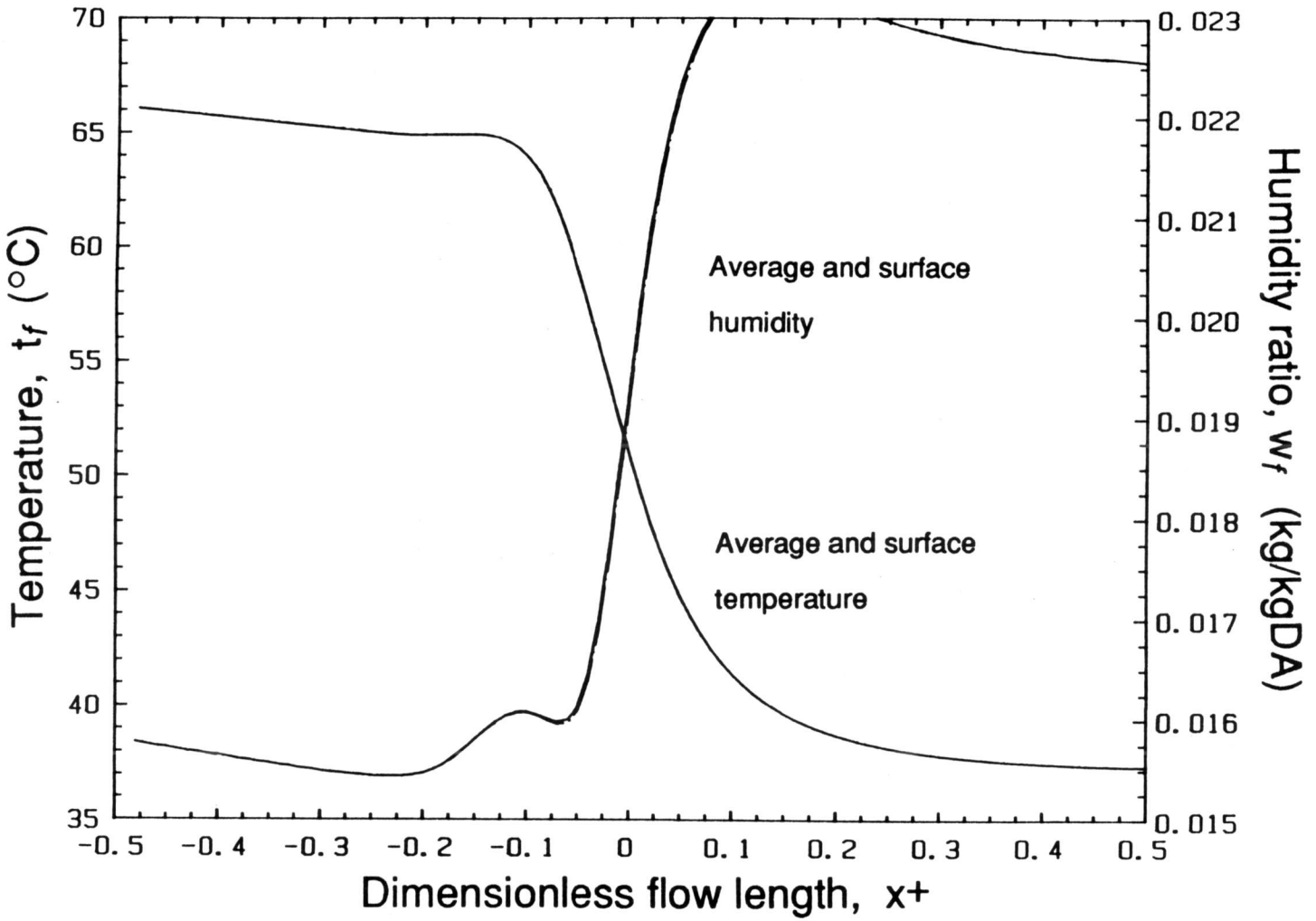

Figure 5.11b Desiccant temperature and humidity distributions with the dimensionless flow length.

Eq.(5.46), the effect of the actual flux distributions on the Sherwood number is much smaller than for the air stream, Fig. 5.10b, because the reduced time scale for θ^+ is about 30 times the reduced length scale for x^+. Hence it can be concluded that for the desorption experiments reported here, the variation of the particle-conductive Nusselt and Sherwood numbers is negligible, and their average values agree with the asymptotic value for a constant flux boundary condition. However, this does not imply that the transfer coefficients are constant. For the conditions of the studied experiments, the particle conductivity decreases about 20% and the mass diffusivity increases with a factor of 2.5 over the course of the desorption process. It may be expected that in particular the desiccant-side mass transfer coefficient will vary over a wide range for typical operating conditions of rotary dehumidifiers.

Figure 5.11b shows the particle average- and surface temperature and humidity ratio in equilibrium with the silica gel water load as functions of x^+. This plot indicates that there exist no temperature gradients within the particles. The thermal conductivity of the silica is large enough to establish a uniform temperature distribution over the particle volume at all times. Also the humidity ratio differences are small and insignificant compared to the humidity differences in the air stream, Fig. 5.9b. Comparing these two figures shows that the temperature profiles for the desiccant and the air stream are

similar; however, the humidity distributions have different shapes. This odd behavior of the humidity distribution is explained primarily by the relative shift of the mass and energy fluxes. In the model, it is assumed that the energy flux is distributed evenly between the desiccant mass and the large thermal capacitance of the structural material of the matrix. It is shown by a third analysis method presented in the next section that this assumption is wrong. The effect of lumping the thermal capacitance is that the temperature response of the desiccant particles is synchronized with the energy flux, whereas the actual temperature response of the desiccant layer will precede the computed response by about 40 s. Although the effect can in part be compensated by artificially shifting the mass and energy flux distributions during input to the integral and boundary conditions, Eqs. (5.49-50), the effect is still noticable in the humidity ratio response.

Figure 5.12 shows the temperature and water load at the surface of the silica particles, computed by the numerical solution of Eqs. (5.47-5.50) in comparison with the air-stream wall temperature and gel-water load in equilibrium with the air-stream humidity ratio, computed by the solution of Eqs. (5.33-5.36). The respective profiles should overlap if the analysis were exact and the thermodynamic capacitances were correct. Figure 5.12 indicates small differences between the temperature and water load profiles. The largest deviations

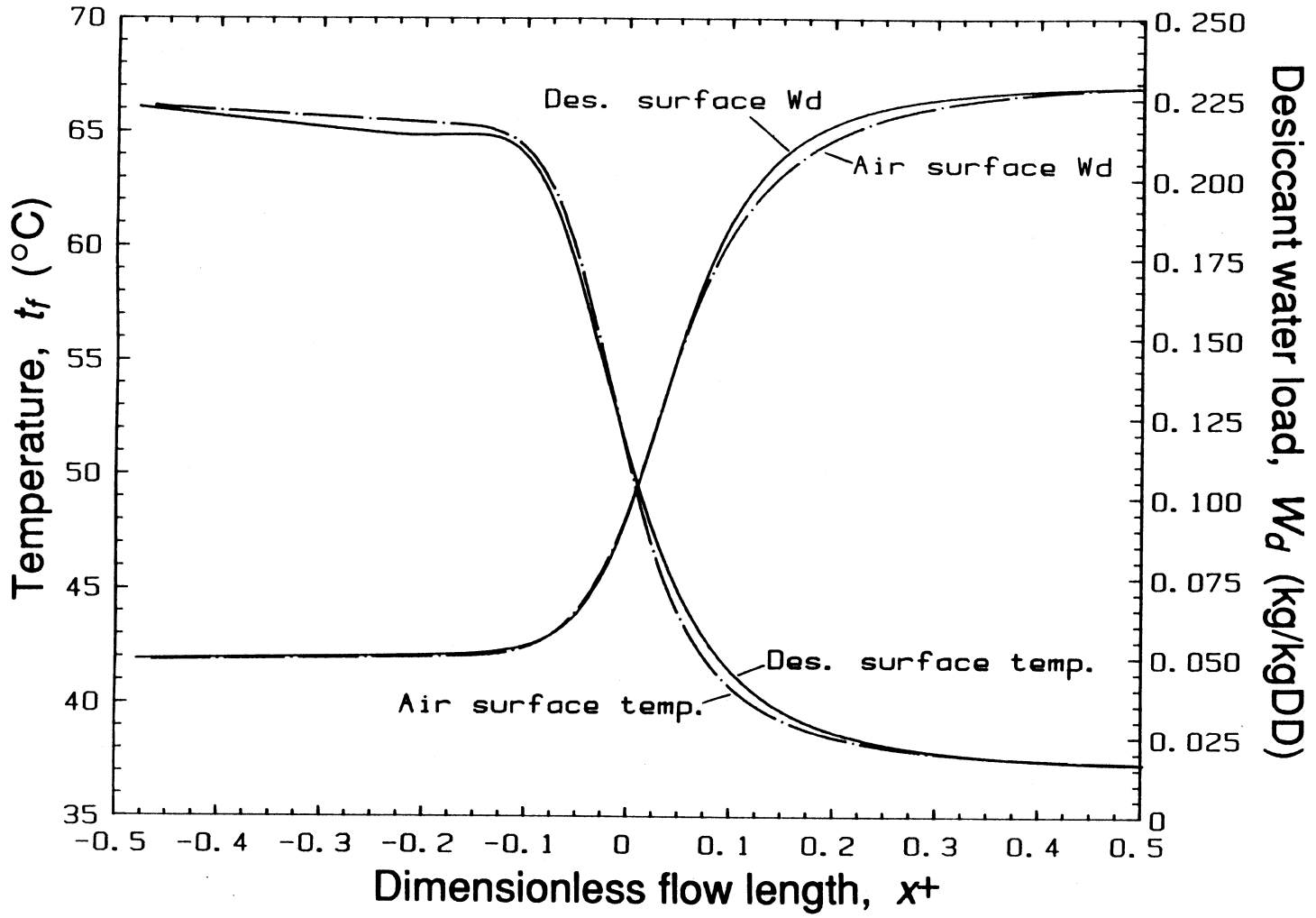

Figure 5.12 Comparison of air and desiccant temperature and water load distributions with the dimensionless flow length.

appear in the region $x^+ > 0$ where there is a difference in curvature between the respective profiles. This difference is explained by the phenomena explained above, and also in part by the inaccuracy of the curve fit to the experimental data, Figs. 5.8a-b. Evidence of this explanation is provided by the abrupt change of slope in the desiccant-temperature profile in Fig. 5.12 at $x^+ \approx -0.2$. This change of slope, which is absent in the air-stream temperature profile, is caused by matching the S-shaped distribution of the wave to the exponentially decaying distribution of the heat loss in the curve fit procedure, Eq. (5.42). Thus the curve fit of the experimental data has different effects on the computed air-stream- and desiccant temperature response. The difference is explained by the numerical inaccuracy of the integration scheme of the desiccant model. The air-stream fluxes are input to the integrator in tabular form and small round-off errors may occur.

The effect of the desiccant diffusivities on the surface temperature and water content distributions of the desiccant particles is negligible. The temperature and humidity responses of the desiccant layer are completely determined by the flux distributions through the conservation equations, and therefore by the curve fit of the experimental data. These curve fits already incorporate the entire effect of the diffusivities, because the spread or dispersion of the wave front is completely determined by the magnitude of the diffusivities

in the desiccant and air stream. Thus the desiccant surface temperature and humidity distributions cannot be matched to the corresponding air-stream distributions by adjusting the values of the mass or thermal diffusivities. The approach of this analysis does not give any information on the values of the diffusivities. These values have to obtained from a proper interpretation of the wave dispersion, and such an analysis is presented next.

5.4.4 Analysis and Discussion III: Overall Heat and Mass Transfer Coefficients

This third and last part of the analysis of the experimental data follows up on the conclusions of the preceeding discussions, in which it is shown that the average values of the Nusselt and Sherwood numbers are the asymptotic values for constant flux boundary conditions. The variation of these transfer parameters about their average values is small. This discussion investigates the magnitude and variation of the overall heat and mass transfer coefficients.

The first section describes the model formulation and assumptions. The theoretical results of the model are compared with the experimental data, and a curve matching procedure leads to the overall heat and mass transfer coefficients.

5.4.4.1 Model Formulation and Assumptions

The model for analyzing the experimental results follows the classical Schumann model. The equations of change are based upon overall conservation equations for the air stream and test matrix. The transfer-rate equations are linear and expressed in terms of overall heat and mass transfer coeffi cients. Diffusion equations are not included in the model.

ASSUMPTIONS

1. The matrix-flow area, the transfer area per unit length, and the distribution of desiccant mass are constant with respect to position in the flow direction.

2. The axial diffusion of heat and mass in the air stream is negligible compared to the transport by forced convection. Axial diffusion in the desiccant layer is neglected because the layer consists of isolated particles with small dimensions.

3. The pressure drop through the bed is small with respect to absolute pressure and is neglected for evaluating the sorption equilibrium conditions. For the investigated experiments, the pressure drop is less than 0.5% of the atmospheric pressure and less than the accuracy with which this pressure is measured.

4. The rate of heat and mass transfer can be modeled with constant overall heat and mass transfer coefficients.

5. The temperature distributions in the desiccant layer and structural parts of the test matrix are assumed to be uniform, and the average temperatures of both systems are equal at all times.

Assumption 1 and 2 are consistent with the assumptions of the previous models. Assumption 4 converts the model equations

from the Rosen-type diffusion equations into the Schumann-type overall rate equations. This assumption is crucial in modeling regenerative dehumidifiers, because it simplifies the resulting model equations substantially. Part I of this analysis investigates the effect of nonuniform, transient distributions of the wall mass and energy fluxes on the air-side Nusselt and Sherwood numbers. The analysis of the experimental data shows that the effect is small for the mass transfer wave, which is slower and has a wider distribution than the preceeding thermal wave. Part II investigates the effect of the transient wall flux distributions on the desiccant-particle Nusselt and Sherwood numbers. It is experimentally verified that the effect is small for the region in which there is significant heat and mass exchange between the desiccant and the air stream. Although the Nusselt and Sherwood numbers are relatively constant, the actual particle heat and mass transfer coefficients may vary substantially due to the variation of the diffusivities with temperature and water concentration. It is investigated in this analysis if these variations are small enough to be neglected.

Assumption 5 lumps the desiccant mass with the structural parts of the test matrix into a homogeneous solid. This assumption is also standard in modeling regenerative dehumdifiers. However, Part I and II have indicated that, for the studied experiments, there exist time delays between the

temperature and humidity distributions. These time delays are contributed to the distributed capacitances that exist in the test matrix. The applicability of assumption 5 is further discussed later in this section.

With assumptions 1-5, the overall equations of change for the air stream and test matrix can be written as follows. x measures the distance in the flow direction and θ measures the real time.

1. Overall water vapor conservation:

$$\dot{m}_f L \frac{\partial w_f}{\partial x} + m_f \theta_d \frac{\partial w_f}{\partial \theta} + M_d \frac{\partial W_d}{\partial \theta} = 0$$

2. Overall energy conservation:

$$\dot{m}_f L \frac{\partial i_f}{\partial x} + m_f \theta_d \frac{\partial i_f}{\partial \theta} + M_d \frac{\partial I_m}{\partial \theta} = 0 \qquad (5.62)$$

3. Rate of overall water vapor mass transfer:

$$M_d \frac{\partial W_d}{\partial \theta} = h_m A (w_f - w_d)$$

4. Rate of overall thermal energy transfer:

$$M_d \frac{\partial I_m}{\partial \theta} = h A (t_f - t_m) + h_m A (w_f - w_d) i_w$$

Different subscripts d and m indicate the implications of the one-capacitance model. The subscript m refers to the lumped system, structural parts and desiccant, whereas the subscript d refers to the desiccant alone. w_d is the humidity ratio of the

air stream in equilibrium with the silica gel at the temperature t_d and water content W_d.

The analysis of the experimental data for the mass transfer wave of the desorption experiments shows that the temperature and humidity distributions are constant-pattern waves, i.e., the shape of the distributions is preserved as the wave progresses through the matrix. This experimental finding is in accordance with well-established theories about wave dispersion for systems with a favorable isotherm (Ruthven, 1984). Michaels (1952) and Garg and Ruthven (1975) succesfully used a specific tranformation technique introduced by Glueckauf (1947) for analysis of experimental breakthrough curves with constant patterns. This transformation technique is based upon the argument that an observer translating at the speed of the wave will not measure a change of shape of the wave. For the system of equations (5.62), the speed of the second wave is given by:

$$\frac{dx}{d\theta} = \frac{\frac{\dot{m}_f L}{M_d} S_2}{1 + \frac{\dot{m}_f \theta_d}{M_d} S_2} \qquad (5.63)$$

where S_2 is the constant dimensionless wave speed. As discussed in Chapter 2, S_2 is a parameter dependent only upon the thermodynamic properties of the fluid and matrix system, and the inlet and initial conditions. Based upon expression (5.63) a new position coordinate z can be defined as:

$$z = x - \frac{\frac{\dot{m}_f L}{M_d} S_2}{1 + \frac{\dot{m}_f \theta_d}{M_d} S_2} \theta \tag{5.64}$$

The partial differential equations expressed in the stationary coordinate system (x,θ) can be written in terms of the coordinates (z,θ). The condition for a constant pattern wave translates into:

$$\left.\frac{\partial}{\partial \theta}\right)_z = 0 \tag{5.65}$$

Hence, the system of partial differential equations (5.62) reduces to a system of ordinary differential equations in a coordinate system, moving with the wave. The model equations in terms of the new variable z become:

1. Water vapor conservation:

$$\frac{dw_f}{dz} - S_2 \frac{dW_d}{dz} = 0$$

2. Energy conservation:

$$\frac{di_f}{dz} - S_2 \frac{dI_m}{dz} = 0 \tag{5.66}$$

3. Rate of water vapor mass transfer:

$$\frac{-\dot{m}_f L}{1 + \frac{\dot{m}_f \theta_d}{M_d} S_2} \frac{dw_f}{dz} = h_m A (w_f - w_d)$$

4. Rate of energy transfer:

$$\frac{-\dot{m}_f L}{1 + \dfrac{m_f \theta_d}{M_d} S_2} \frac{di_f}{dz} = h A (t_f - t_m) + h_m A (w_f - w_d) i_w$$

In this form, the equations become analogous to the model equations for counterflow cooling towers or wet-surface cooling coils. The conservation equations in (5.66) can be readily integrated because S_2 is constant. Along the continuous property distributions of the wave, the condition for constant pattern translates as:

$$\frac{(w_f - w_{f,1})}{(W_d - W_{d,1})} = \frac{(w_{f,2} - w_f)}{(W_{d,2} - W_d)} = \frac{(w_{f,2} - w_{f,1})}{(W_{d,2} - W_{d,1})} = S_2$$

$$\frac{(i_f - i_{f,1})}{(I_m - I_{m,1})} = \frac{(i_{f,2} - i_f)}{(I_{m,2} - I_m)} = \frac{(i_{f,2} - i_{f,1})}{(I_{m,2} - I_{m,1})} = S_2 \qquad (5.67)$$

where the subscripts 1 and 2 refer to the conditions at the start and finish of the wave. For the first thermal wave, 1 is the matrix initial state and 2 is the intermediate state. For the second mass transfer wave, 1 is the intermediate state and 2 is the fluid stream inlet state. Equations (5.67) were established by Van den Bulck, Mitchell and Klein (1986) for modeling regenerative dehumidifiers with infinite transfer conditions. This work extends the application of these equations to dehumdifiers with finite transfer coefficients. They can be used to compute the intermediate state properties and the wave speeds S_1 and S_2.

The system of ordinary differential equations (5.66) can be further simplified by using the time variable τ introduced by Anzelius (1926) for modeling fluid flow through porous matrices,

$$\tau = - (1 + \frac{\dot{m}_f \theta_d}{M_d} S_2) \frac{h A}{c_p \dot{m}_f} \frac{z}{L} \tag{5.68}$$

In terms of the dimensionless time τ, the model equations become:

1. Water vapor conservation:

$$\frac{dw_f}{d\tau} - S_2 \frac{dW_d}{d\tau} = 0$$

2. Energy conservation:

$$\frac{di_f}{d\tau} - S_2 \frac{dI_m}{d\tau} = 0 \tag{5.69}$$

3. Rate of water vapor mass transfer:

$$\frac{dw_f}{d\tau} = \frac{1}{Le} (w_f - w_d)$$

4. Rate of energy transfer:

$$\frac{dt_f}{d\tau} = (t_f - t_m)$$

Le is the effective, overall Lewis number defined as:

$$Le = \frac{h}{h_m c_p} \tag{5.70}$$

and indicates the magnitude of the resistance for mass transfer relative to that for heat transfer.

The nature of the new time variable can be shown by relating τ and θ in terms of dimensionless groups. Inserting Eq. (5.64) into (5.68) gives:

$$\Delta\tau = \frac{h A}{c_p M_d} (S_2 \Delta\theta), \tag{5.71}$$

where $\Delta\theta$ measures the elapsed real time at a specified location within the flow channel, e.g., the exit face of the matrix. Using the definition expressions for the Nusselt number, the transfer area A, and the thermal diffusivity of the fluid stream, α_f, Eq. (5.71) can be written as:

$$\Delta\tau = 4\, Nu\, S_2 \frac{M_f}{M_d} \frac{\alpha_f \Delta\theta}{D_h^2}$$

and the inverse relation is: (5.72)

$$\Delta\theta = \frac{1}{Nu} \frac{M_d}{M_f} \frac{D_h^2}{4\alpha_f} \frac{\Delta\tau}{S_2}.$$

This last expression describes the spread of the wave in real time as proportional to:

1. $(D_h^2/4\alpha_f)$, which is the characteristic time scale for transverse diffusion within the fluid stream from the core of the flow channel to the channel walls. For the experiments reported in this work, this time is about 0.0339 s ± 15%.

2. $(1/Nu)$. Nu is a parameter depending upon the geometry of the flow passage. The shorter the average distance between the core and the walls, the higher is Nu. For the studied experiments, it is shown that the heat transfer resistance of the desiccant particles is negligible compared to the convective resistance in the fluid stream. The overall Nusselt number can thus be put equal to the fluid Nusselt number, i.e., $Nu = 8.235 \pm 5\%$.

3. (M_d/M_f), the ratio of desiccant to fluid mass within the exchanger. With increasing matrix porosity, this parameter decreases, and the transfer wave becomes more confined. M_d is obtained from the I-series sorption experiments, and M_f is computed from the core geometry of the test matrix, which is independently obtained from the pressure drop experiments. For the studied experiments, the mass ratio is $0.487/0.00167 = 292 \pm 5\%$.

4. $(\Delta\tau/S)$. S is a semi-thermodynamic property of the fluid and matrix system, dependent upon the matrix-initial and fluid-inlet conditions. For the first, thermal wave, $S_1 = 1.30 \pm 5\%$ and for the second mass wave, $S_2 = 0.0378 \pm 2\%$, for the desorption experiments of series M. These numbers explain why the first wave is more confined than the second wave. $\Delta\tau$ measures the width of the wave in the dimensionless form. Equations (5.69) show that this parameter can be obtained by

integrating the model equations. $\Delta\tau$ has the same nature as S, and depends in addition on the Lewis number.

The system of equations (5.69) is non-stiff and can be readily integrated with the conventional Runga-Kutta algorithm. The ordinary differential equations are consistent with the system of partial differential equations, however, integration of this latter system requires a two-dimensional finite difference scheme which proves a major computational effort. The ease with which the model equations can be integrated in terms of τ forms the rationale for the experimental test procedure proposed in next chapter. All parameters appearing in the conversion formula (5.72) have been carefully determined in this work by analyses and experiments independent of the present model. The only unknown parameter in Eq. (5.69) is the effective overall Lewis number. This parameter contains the mass transfer coefficient and thus most of the effect of variable properties.

The effect of the Lewis number on the shape of breakthrough curves is illustrated in Figure 5.13. The initial and final conditions for the integration are, respectively, the intermediate and inlet state of the experimental data of the mass transfer wave of the desorption experiments. The alternate curves in Fig. 5.13 indicate that the Lewis number acts both as a skewness and scale parameter. The total width

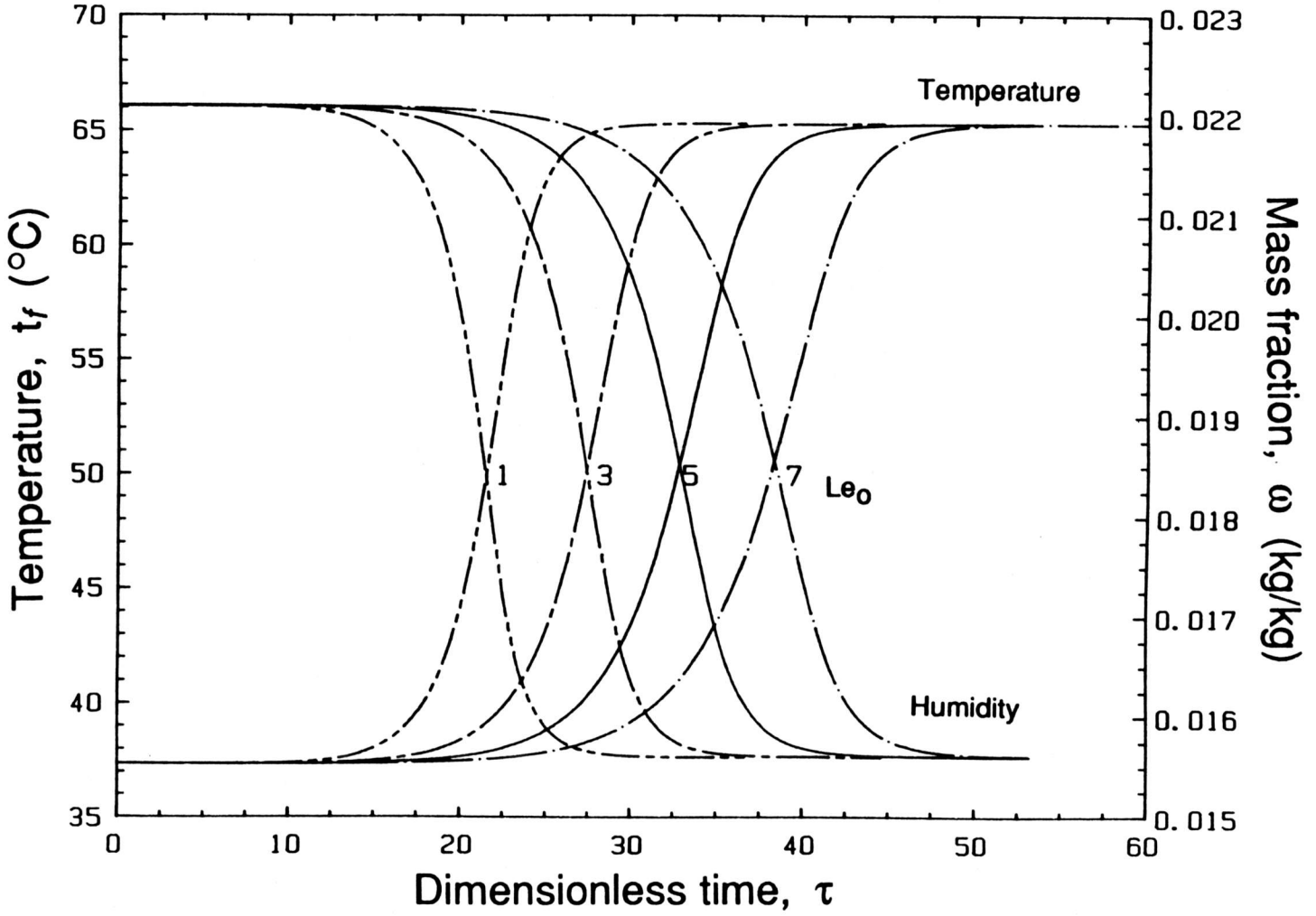

Figure 5.13 Effect of Lewis number on the air temperature and humidity response with time.

of the wave, i.e., the duration of breakthrough at a specified location, increases proportionally with the Lewis number. In principle, this information can be used to estimate the Lewis number. The total width of the wave in real time, $\Delta\theta$, can be measured from the experimental breakthrough curve, and the width $\Delta\tau$ can be computed using Eq. (5.72). This experimental value can then be compared with the theoretical value with Le_o as a parameter, and the Lewis number can be computed from matching the theoretical with the experimental value. However, the total width of a breakthrough curve for an S shaped distribution is not well defined, and this procedure leads to a range for the Lewis number. An alternate procedure is recommended.

With increasing Lewis number, the skewness of the breakthrough curve increases. This effect is illustrated by the alternate breakthrough curves shown in Figure 5.13. The shape of the branches connecting the breakthrough curves with the inlet properties are almost independent of Le, however, the branches leading to the intermediate state expand with increasing Le_o. The breakthrough curves become more asymmetric and this quantity is measured by the skewness of the curve. From the theory of moments, it is well known that the skewness of a distribution is a third order parameter, whereas the width is second order and the position of the wave is first order. The accuracy with which these respective parameters can be derived from experimental data decreases in that order. Again,

this insensitivity leads to a range for the Lewis number which matches the experimental data.

5.4.4.2 Effective Lewis Number

The effective Lewis number is defined by Eq. (5.70). A theoretical expression for Le can be derived by matching the wall fluxes at the air side with those at the desiccant side. The air side wall fluxes are given by:

for mass transfer:

$$m_f = \frac{\rho D_{aw}}{D_h} Sh_a \frac{(\omega_{avg} - \omega_{wall})}{(1 - \omega_{wall})}$$

and for heat transfer: (5.73)

$$q_f = \frac{k_a}{D_h} Nu_a \, (t_{f,avg} - t_{f,wall})$$

and the desiccant side particle fluxes are given by:

for mass transfer:

$$m_p = \frac{(1-\varepsilon_p)\rho_s D_{W,e}}{D_p} Sh_p \, (W_{d,wall} - W_{d,avg})$$

and for heat transfer: (5.74)

$$q_p = \frac{k_d}{D_p} Nu_p \, (t_{d,wall} - t_{d,avg})$$

The mass fluxes are conventionally based on gradients of the water mass fraction in the air stream, ω, and the water content of the desiccant, W_d. These definitions lead to diffusivities

which are in general least dependent upon temperature or species concentration. In the dehumidifier theory, the overall mass transfer coefficient is expressed in terms of humidity ratio gradients, which result in less complicated conservation equations. Theoretical expressions for the transfer coefficients can be obtained by matching the fluxes:

for mass transfer:

$$\dot{m}_f A = \dot{m}_p A_p = h_m A(w_{f,avg} - w_{d,avg})$$

and for heat transfer: (5.75)

$$q_f A = q_p A_p = h A(t_{f,avg} - t_{d,avg})$$

These expressions lead to the following theoretical expressions for the overall transfer coefficients:

$$h_m = \frac{\frac{\rho D_{aw}}{D_h} Sh_a \frac{1}{(1-\omega)} \frac{\partial \omega}{\partial w_f}}{1 + \frac{\rho D_{aw}}{(1-\varepsilon_p)\rho_s D_{w,e}} \frac{D_p}{D_h} \frac{Sh_a}{Sh_p} \frac{A}{A_p} \frac{\partial \omega / \partial w_f)_T}{(1-\omega)\partial \bar{W}/\partial w_f)_T}}$$

and (5.76)

$$h = \frac{\frac{k_a}{D_h} Nu_a}{1 + \frac{k_a}{k_p} \frac{D_p}{D_h} \frac{Nu_a}{Nu_p} \frac{A}{A_p}}$$

The thermal conductivity of silica gel, k_p, is about 40 times the thermal conductivity of air, the hydraulic diameter is about 10 times the particle diameter, and the external particle area is about 3 times the transfer area. The denominator in

the expression for the heat transfer coefficient is 1.00 ± 0.003, and the overall transfer coefficient is equal to the air-side transfer coefficient.

The expression for the overall mass transfer coefficient is more complicated. The effective desiccant diffusivity, $D_{W,e}$, can vary by a factor of 2 to 3 over the course of the sorption process. Furthermore, this diffusivity is only known within a factor of 5 to 10. The derivative of the water content with respect to the humidity ratio varies substantially with temperature and water content. The particle Sherwood number ranges from 2 to 10 depending on the particle shape and percentage of external surface covered by the adhesive. These factors make a theoretical estimate of the average transfer coefficient extremely ambiguous, and an uncertainty range of one order of magnitude is not unusual.

These considerations support procedures to derive the effective Lewis number directly from experimental results. The model equations presented in the previous section lead to two such procedures. These procedures are applied to the experimental data of the mass transfer wave of the desorption experiments.

Point Matching Method

For the curves in Fig. 5.13, a linear regression of $\Delta\tau_{10-90}$ with Le yields:

$$\Delta\tau_{10-90} = 6.007 + 0.766\,Le,\ r^2 = 99.97\% \qquad (5.77)$$

where $\Delta\tau_{10-90}$ is the 10-90% spread of the wave. Equation (5.72) presents a linear relationship between $\Delta\tau$ and $\Delta\theta$, and for the conditions of the mass transfer wave of the desorption experiments, $\Delta\theta/\Delta\tau = 31.82 \pm 20\%$. Combining Eq. (5.77) with this ratio gives a theoretical expression for the 10-90% spread of the wave in real time.

$\Delta\theta_{10-90}$ can also be estimated directly from the experimental distributions in x^+ presented in Fig 5.8 The scatter of the experimental data about the curve fit results in $\Delta x^+_{10-90} = 0.205 \pm 0.020$, and with the accurate linear relation between θ and x^+, Eq. (5.52), the experimental value of $\Delta\theta_{10-90}$ is 295 ± 30 s. With the point matching method for $\Delta\theta_{10-90}$, the Lewis number can be estimated from the relationship (5.77) which yields 4.3 ± 1.3.

Curve Matching Method

The integration of the reduced model equations (5.69) yields the theoretical distributions of temperature and humidity in the variable τ, with the Lewis number as a parameter. There exists a linear relationship between τ and x^+, and the theoretical distributions can thus be compared with the experimental distributions presented in Figs. 5.8a-b. This comparison is shown in Fig. 5.14a for the temperature, and in Fig. 5.14b for the water-vapor mass fraction. The parameter in this comparison is the Lewis number.

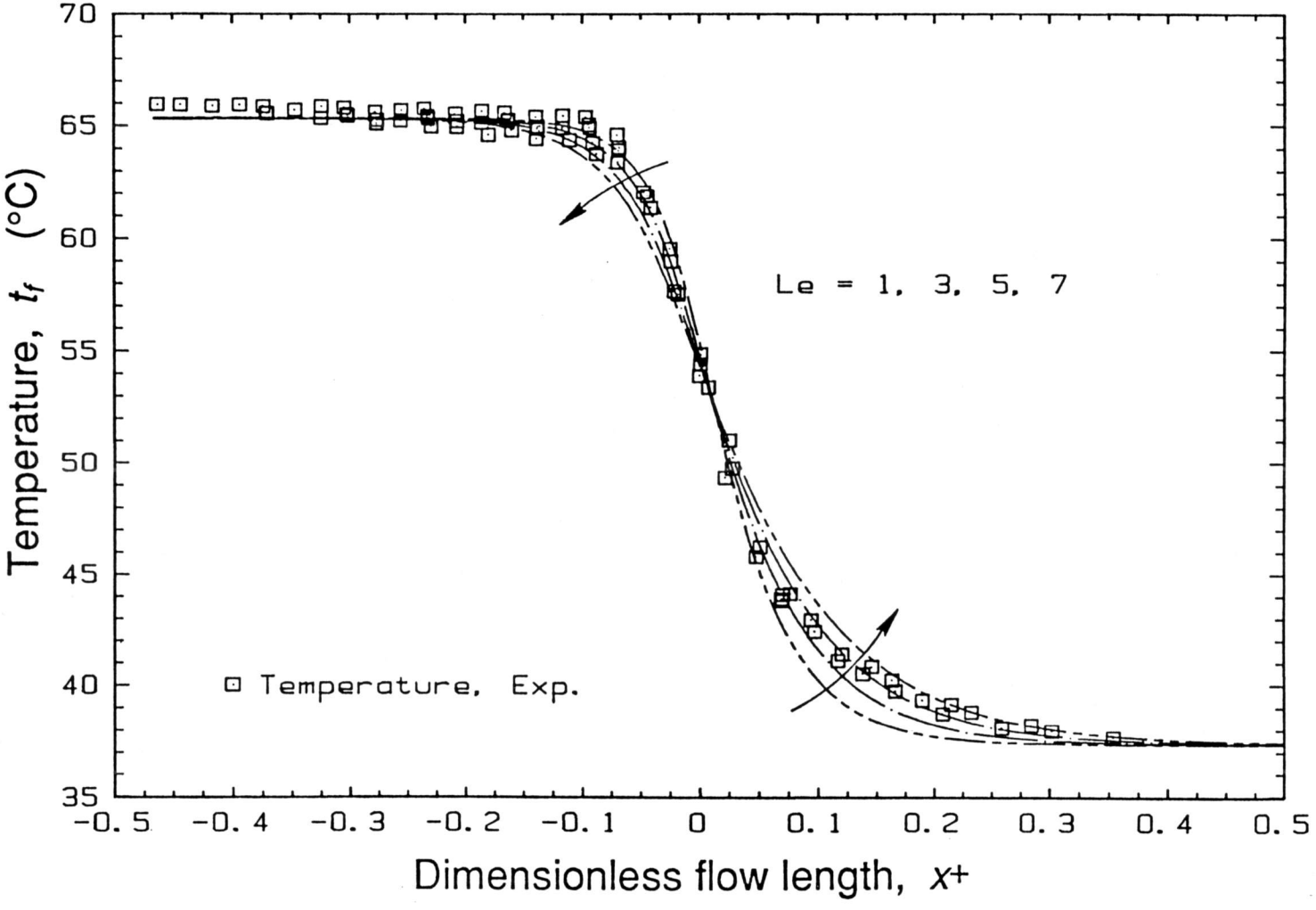

Figure 5.14a Experimental air temperature distributions in comparison with theoretical distributions with Le_0 as parameter.

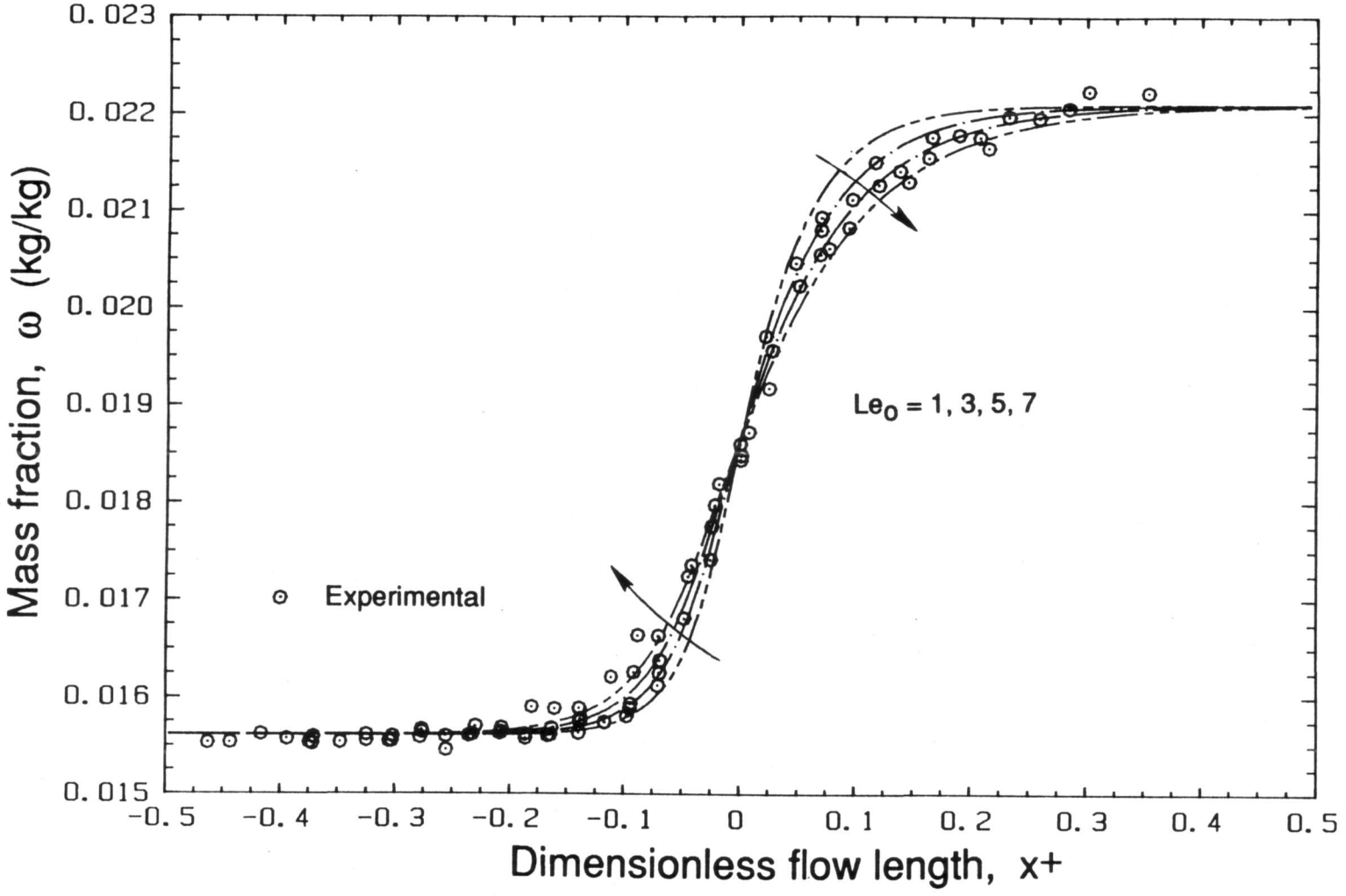

Figure 5.14b Experimental air humidity distributions in comparison with theoretical distributions with Le_0 as parameter.

The alternate curves in Figs. 5.14a-b illustrate that the Lewis number acts more as a skewness parameter than as a scale parameter, and is therefore harder to extract from the experimental results with high accuracy. For the branch connecting the distribution curves with the inlet state, the scatter of the data is larger than the variation caused by varying Lewis numbers, and no conclusion with respect to the magntitude of this parameter can be made. However, for the opposite branch, connecting the curves with the intermediate state, the scatter of the experimental data is confined within a range corresponding to Le_o = 3-7 for both temperature and humidity. This range is consistent with the result of the point matching method.

The large uncertainty level of the Lewis number is mainly due to the scatter of the experimental datapoints about average values. This scatter is not as much due to measurement inaccuracies as it is to the limit with which the series M experiments are repeatable with the experimental facility. This analysis shows that a high-quality experimental apparatus is needed to predict third order parameters, such as the Lewis number. This is also true if effects such as axial diffusion were to be investigated.

5.4.4.3 One-Capacitance Models

Finally, the reduced model equations (5.69) can be used to investigate the validity of the one-capacitance type models, in which the desiccant and matrix-structural parts are lumped into a single thermal capacitance. Figure 5.15 shows the temperature and humidity distributions obtained from integrating the reduced model equations in comparison with the experimental data for $Le_o = 4$. The RMS error of the humidity is 0.16 g/kg, which is only slightly higher than the scatter of the humidity data about a cubic spline with optimized knots, 0.13 g/kg. If the temperature curve were to be shifted over a distance $\Delta x^+ = 0.0293$, or $\Delta\theta = -42$ s, the RMS error of the experimental data about the theoretical distribution is 0.58 °C, which is comparable to the scatter about a cubic spline with optimized knots, 0.3 °C. Thus the distribution predicted by the one-capacitance model lags the experimental data in time by about 42 s. This time lag is solely due to lumping the desiccant mass with small thermal capacitance with the structural parts of the test matrix with large thermal capacitance. For estimating the effect of the one-capacitance assumption on the performance prediction of dehumdifiers, $\Delta\theta_{10-90}$ of the distributions is about 300 s. The total breakthrough time varies with the mass flow rate, and ranges from 9 to 20 minutes for the series M desorption experiments.

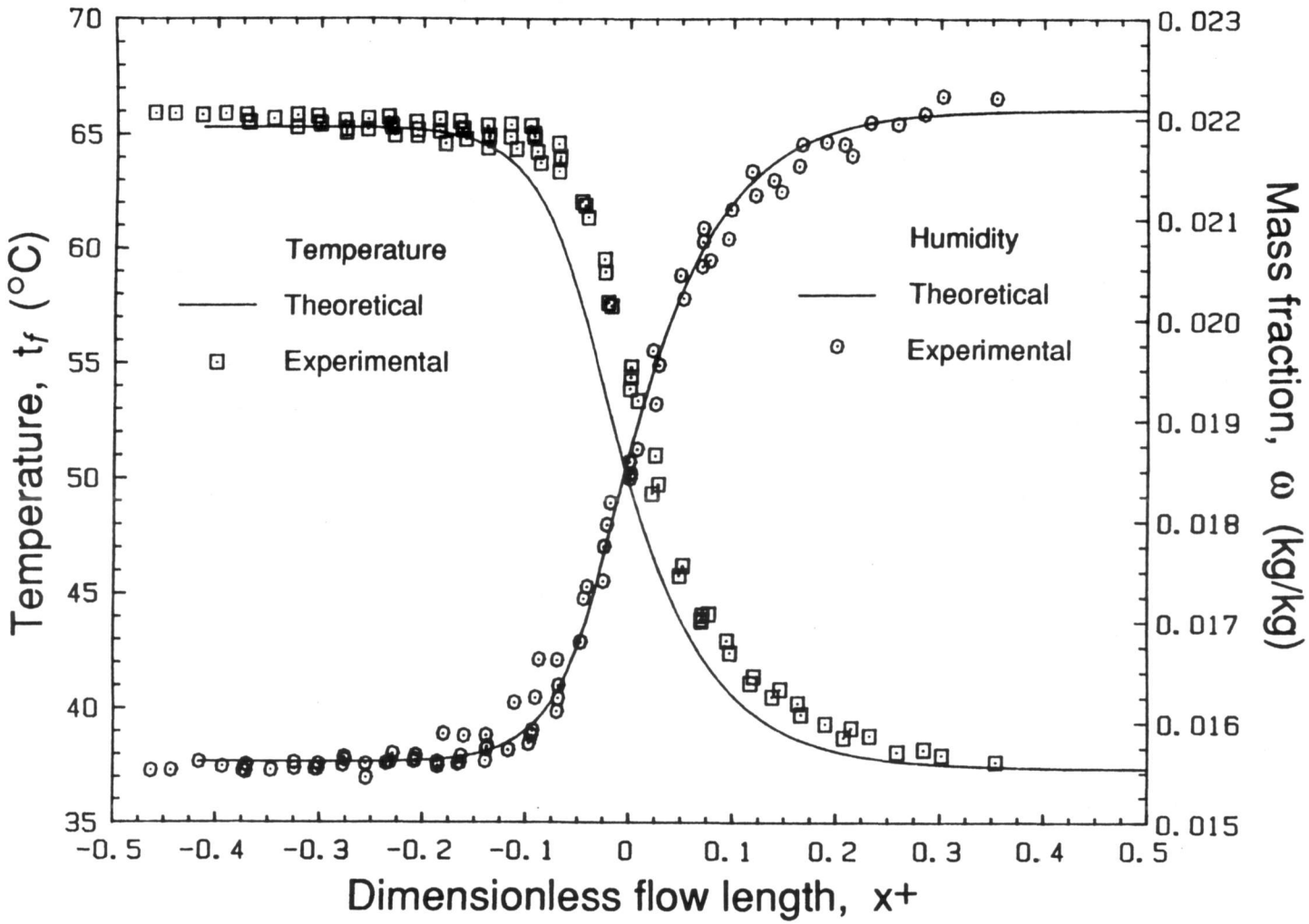

Figure 5.15 Experimental air temperature and humidity distributions in comparison with the theoretical distribution for a one-capacitance model and $Le_0 = 4$.

This analysis shows that errors may occur in predicting the position of the breakthrough wave if a one-capacitance model is applied. However, in that case the total breakthrough time would be overestimated, which would lead to a conservative estimate of the energy required to regenerate the desiccant within the dehumidifier. The conclusion of this analysis is that caution should be taken when applying one-capacitance models to regenerative dehumidifiers with 'large' thermal capacitance. Synchronization of dehumidifier wheels with the breakthrough of the second humidity wave for on-line speed control may lead to small energy savings when compared to synchronization with the second temperature wave, for dehumdifiers with large distributed capacitances. For regenerative dehumdification, it suffices to regenerate the desiccant, not the entire matrix.

CHAPTER 6

COMPACT DEHUMIDIFIERS

The preceding chapter presents a detailed analysis of single blow experiments in compact dehumidifiers. This chapter summarizes the conclusions from that work, and formulates guidelines for the design and analysis of rotary dehumidifiers.

The first section describes how the results of the presented work can be applied to the design and analysis of regenerative dehumidifiers. The pressure drop, transfer rate resistance and capacitance distribution are discussed for future modeling of regenerative dehumidifiers.

The second section discusses an experimental, single-blow test procedure for compact dehumidifier matrices. The nonlinearity of the sorption isotherm creates constant-pattern breakthrough curves with distinct properties from those of heat exchanger matrices. Proper interpretation of the experimental results can lead to a fast and accurate estimate of the performance characteristics of desiccant exchangers. A procedure and analysis tool is presented in the second part of this chapter.

6.1 Design and Analysis of Compact Dehumidifiers

The design procedures of compact heat exchangers have been well established and are presented in the reference work by Kays and London (1984). Periodic flow-type heat exchanger matrices are characterized by their porosity, free flow area, transfer area, flow length, the internal passage geometry that determines the asymptotic value for the Nusselt number and the constant value of the product fRe, and the thermal capacitance per unit volume. The performance of rotary dehumidifier matrices is, in addition to the parameters listed above, determined by the sorption capacitance per unit volume, the equilibrium isotherm correlation for the desiccant, and the relative distribution of the thermal and sorption capacitances.

The optimum design of rotary dehumidifiers is challenging because it involves the specification of many parameters. The stringent criteria is the minimization of the life cycle cost of the installation of a dehumidifier (Mitchell, 1983), although criteria such as manufacturability and exchanger volume may be equally important. The thermal capacity of the dehumidifier is proportional to the transfer area,

$$Q \propto \frac{Nu\,A}{D_h} \tag{6.1}$$

and the fan power is the friction power expended by the flow through the matrix,

$$E \propto \frac{f_{app} Re^3}{D_h 3} \qquad (6.2)$$

To compute the life cycle cost of the dehumidifier in a specified installation, correlations are required for the apparent friction factor and the Nusselt or Sherwood numbers. The experimental and analytical work presented in this volume provide the following contributions to the ongoing task of optimizing rotary dehumidifiers (Ingram and Vliet, 1982; Jurinak and Mitchell, 1982; Jurinak and Mitchell, 1984a; Grolmes and Epstein, 1985; Van den Bulck, Mitchell and Klein, 1986).

6.1.1 Pressure Drop Equation

Jurinak, Mitchell and Beckman (1984b) analytically investigated the economic feasibility of desiccant air-conditioning systems in comparison with conventional vapor compression cooling. Their study indicates the important contribution of the mechanical fan power to the total operating cost of rotary dehumidifiers. It is shown that, for a specified cooling load on the system, a high or low fan power can make the difference between a competitive or unprofitable investment. It is thus important to have an accurate estimate of the pressure drop for flow through dehumidifier matrices.

The computation of the pressure drop for flow through compact dehumidifiers follows the same procedures as for compact heat exchangers (Kays and London, 1984). However, the analysis of the pressure drop experiments presented in this work indicates that for desiccant matrices with small hydraulic diameters, there may be a significant additional pressure drop associated with the protrusion of individual desiccant particles into the fluid-shear layer. The magnitude of the additional pressure loss depends on the shape and dimensions of the particles relative to the total flow height. For crushed particles with sharp edges, correlation of the experimental data presented in this work yields the following formula for the frictional loss coefficient,

$$K_f = C\frac{L}{D_h}\left(\frac{D_p}{D_h}\right)^2, \quad \text{where } C = 5.7 \pm 1. \tag{6.3}$$

This formula can be used as a correction factor for the pressure drop through very rough passages, i.e.,

$$\Delta P_{rough} = \Delta P_{smooth} + K_f\frac{\rho U^2}{2}. \tag{6.4}$$

where U is the average velocity within the passages. ΔP_{smooth} is the conventional pressure drop for smooth passages with the same geometry as the rough passages.

The effect of the particle protrusion is a wall effect and should therefore not depend on the core geometry of the

passages. Equation (6.3), although derived from experiments for the parallel-plate geometry, should therefore hold for other passage geometries as well. However, the numerical constant may depend on the geometry of the desiccant particles, either crushed or spherical.

6.1.2 Transfer rate correlations

Jurinak and Mitchell (1982) analytically studied the effect of the overall Lewis number on the performance of rotary dehumidifiers. Their study indicates that increasing the Lewis number from 1 to 4 yields the same decrease in drying performance as halving the overall heat transfer coefficient with $Le_o = 1$. The volume and thus the pressure drop of a dehumidifier with $Le_o = 4$ is thus twice that of a matrix with $Le_o = 1$. Van den Bulck, Mitchell and Klein (1985b) established effectiveness curves of rotary dehumidifiers with Le_o as parameter. Their study indicates that high performance dehumidifiers with $Le_o = 5$ may require transfer areas that are 3 to 4 times the transfer area of $Le_o = 1$ dehumidifiers. Even a Lewis number of 2 causes a 30% increase in transfer area for the same capacity. The value of Le_o is therefore extremely important for the economic feasability of desiccant cooling systems.

6.1.2.1 Fluid-stream transfer rate resistance

The analysis of the second or mass transfer wave of the series M desorption experiments shows that the effect of variable wall fluxes on the fluid side heat and mass transfer coefficients is small. An analogy method based upon Graber's work provides a formula to estimate the amplitude of the oscillatory behavior of the transfer coefficients, Eq. (5.46). The effect may be appreciable for the first or thermal wave because this wave is more confined in the flow direction. For the experiments reported in this work, the amplitude of the oscillation in the fluid-side Nusselt and Sherwood number for the first wave may be estimated at about 30 times that of the second wave.

However, because the first wave is more confined, the shape and width of the temperature and humidity distributions are less important than their position with time. The speed of the first wave is mainly determined by the distribution of the thermal capacitances within the matrix, and whether these individual parts exchange heat directly or indirectly with the fluid stream. The challenge for the first wave is not as much in predicting the shape of the wave, as predicting the time of breakthrough of the wave. Therefore, it may still be assumed that the Nusselt and Sherwood numbers are constant with respect to time and position even for the first wave.

6.1.2.2 Desiccant-layer transfer rate resistance

The analysis of the particle transfer resistance presented in this work shows that the conductive Nusselt and Sherwood numbers are constant with respect to time and position. This constant is the asymptotic value for constant flux boundary conditions for spherical particles, 10. However, if, say, a cubical geometry rather than a spherical geometry is used in the model for solving the conservation and diffusion equations, the constant value would be 6. Thus it remains to be determined which is the appropriate value for the actual geometry of the desiccant particles.

The transient, three dimensional heat conduction equation in solids is:

$$\rho c \frac{\partial T}{\partial \theta} = k \nabla^2 T \tag{6.5}$$

This equation needs an initial condition, specifying the temperature over the particle volume, and a boundary condition of the type:

$$a \frac{\partial T}{\partial \eta} + b\,\mathrm{T} = f \tag{6.6}$$

where a, b and f are functions defined on the surface of the particles, and T and $\partial T/\partial \eta$ are evaluated at the surface.

For engineering purposes, the parabolic heat equation (6.5) can be replaced by an overall energy rate equation:

$$\rho c V_p \frac{dT_{avg}}{d\theta} = hA_p(T_{surf,avg} - T_{avg}) \tag{6.7}$$

where V_p and A_p are the volume and total external particle area, respectively. For the purpose of this analysis, T_{avg} is defined as the volume-average temperature, and $T_{surf,avg}$ is defined as the transfer-area average temperature, **not** including adiabatic, external transfer areas. $T_{surf,avg}$ is the temperature of a well-stirred fluid surrounding the particle, which may or may not have part of its external area insulated. Equation (6.7) defines the heat conduction coefficient, h. The particle conductive Nusselt number is written in analogy with convective heat transfer,

$$Nu_p = \frac{h D_p}{k} \tag{6.8}$$

where D_p is the particle diameter,

$$D_p = 6 \frac{V_p}{A_p}. \tag{6.9}$$

The particle Nusselt number depends on the particle geometry and the boundary conditions at the external surface, Eq. (6.6). Standard boundary conditions are constant heat flux or temperature at the surface of the particle. Table 6.1 lists

the asymptotic values of the Nusselt number for these two boundary conditions, respectively, $Nu_{(H)}$ and $Nu_{(T)}$, for various particle geometries. The numbers shown in Table 6.1 were computed with standard analytical techniques (Carslaw and Jaeger, 1959). The effect of the particle geometry is indicated by the value of the particle shape factor, ϕ_p, defined as

$$\phi_p = \frac{D_p}{D_s}, \tag{6.10}$$

where D_s is the diameter of a sphere with the same volume as the particle. ϕ_p is 1 for spherical particles and less than 1 for other geometries. The smaller ϕ_p, the larger is the average distance between the external surface and the core volume of the particle, and thus the larger the transfer resistance and the smaller the Nusselt number. The presence of corners also decreases the conductive Nusselt number.

Crushed silica gel particles have the shape of polyhedrons with nearly plane faces and sharp edges and corners. The number of major faces varies and ranges from 4 to 7. The experimental value of the shape factor of crushed glass particles is about 0.65 (Perry and Chilton, 1973). The numbers in Table 1 indicate that $Nu_{(H)}$ for these geometries ranges from 1/2 to 1/5 of the value for a spherical geometry. Table 6.1 also indicates the effect of an adiabatic surface on the

Table 6.1 Asymptotic Nusselt numbers for transient diffusion in solids

GEOMETRY	$D_p = 6\frac{V_p}{D_p}$	$\phi_p = \frac{D_p}{D_s}$	$Nu_{(T)}$	$Nu_{(H)}$
sphere 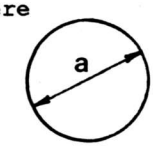	a	1.00	6.58	10.0
cube 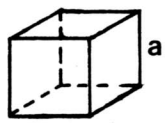	a	0.81	4.93	6.0
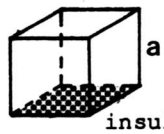			3.70	4.17
parallelepiped 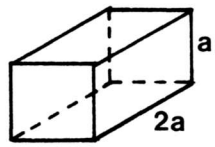	1.2 a	0.64	5.33	6.0
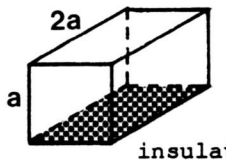			3.55	3.84
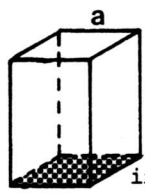			4.89	4.86

(continued)

Table 6.1 (continued)

GEOMETRY	$D_p = 6\frac{V_p}{D_p}$	$\phi_p = \frac{D_p}{D_s}$	$Nu_{(T)}$	$Nu_{(H)}$
cone 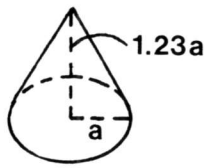	0.95 a	0.704	2.93	
			1.36	
tetrahedron 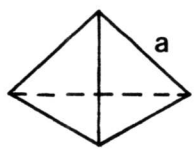	0.41 a	0.67		
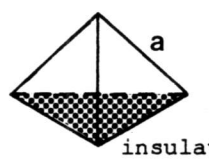				

particle Nusselt number. Typically, $Nu_{(T)}$ is reduced by about 50 to 70% of the value of the non-insulated particle. For particles with an insulated surface and low ϕ_p, the ratio of $Nu_{(H)}$ to $Nu_{(T)}$ approaches 1. Applied to desiccant particles, the external surface area adhering the particle to the carrier with

glue acts as an insulated area or a vapor barrier. The values listed in Table 6.1 thus represent the increase in the particle transfer rate resistance, due to a non-spherical geometry and the presence of an insulated wall. For crushed silica gel particles, the transfer rate resistance increases by a factor of 2 to 3 due to its geometry, and by a factor of about 2 due to adherence to the carrier tape. Spherical particles may thus have 4 to 6 times the diameter of crushed silica gel for the same particle resistance, and obviously this geometry is recommended for the design of dehumidifiers.

6.1.2.3 Overall transfer rate resistance

The overall transfer coefficients can be estimated with Eqs. (5.67). The overall heat transfer coefficient is the fluid-side transfer coefficient, due to the high conductivity of the desiccant particles. Because the transport coefficients of gases are well known and are only weak functions of temperature, the overall heat transfer coefficient can be accurately estimated.

The overall mass transfer coefficient may be less than the fluid-side transfer coefficient, due to the effect of solid side resistance. The particle transfer rate resistance can be estimated if the effective mass diffusivity of the desiccant is

known. This diffusivity is only known within an order of magnitude for regular density silica gel, and can vary with an order of magnitude during the course of a sorption process. The overall mass transfer coefficient may thus not be constant if the solid-side diffusion resistance is dominant. In that case, the variation is due to property effects rather than non-uniform or transient boundary conditions. Until an accurate correlation for the mass diffusivity of regular density silica gel is established, it is best to rely on experimental data to estimate the overall transfer rate resistance, or Lewis number. For crushed silica gel particles with an average particle diameter of 217 μm, the experimental data presented in this work show a Lewis number of 4 to 5 in a parallel-plate geometry with an hydraulic diameter of 2 mm.

6.1.3 Sorption and thermal capacitance distribution

Previous studies of the dynamic sorption capacity of silica gel in a geometry similar to the one used in this work, have introduced the hypothesis that the penetration of adhesive into the desiccant particles may reduce the adsorption capacity of the desiccant by 10 to 40 % (Pesaran and Zangrando, 1985; Kim, Biswas and Mills, 1985). The use of a new isotherm correlation developed in this work indicates that the effect of

the adhesive on the sorption capacity and the thermo-physical properties of the silica gel is negligible. Thus, the reported reduction in sorption capacitance is in fact due to the use of an inaccurate isotherm, or experimental inaccuracy.

The experiments analyzed in this work indicate the effect of distributed thermal capacitances. The analysis of regenerative dehumidifiers may be in error if the thermal capacitance is distributed, and the analysis assumes an one-capacitance model. A complete discussion of this effect is outside the scope of this work.

6.2 A Single Blow Technique for Heat and Mass Exchangers

The survey of single blow techniques presented in the preceding chapter discusses the established methods for characterizing heat exchanger matrices. Whereas the methods for heat transfer alone have evolved into *de facto* standards, the methods for isothermal or adiabatic mass transfer are less developed. The application of point-matching methods, such as the method of moments, is in general restricted to linear systems, and adsorbers have often nonlinear thermodynamic equilibrium properties. The curve-matching techniques applied to mass transfer involve many parameters, and agreement with experimental data can often be obtained with more than one set

of these parameters. Thus it seems that the single blow technique may not be a useful experimental tool for obtaining the performance characteristics of heat and mass exchangers.

The thermal wave in heat exchangers is an expansion wave, continuously spreading as it progresses through the exchanger passages. The shape of this wave does never become 'fully developed' and therefore depends at all times on its initial shape, that is, the change of the inlet conditions with time. In single blow experiments for heat transfer alone, it is therefore crucial to produce a high-quality step change in inlet temperature with a very small response time.

For mass transfer, however, the nonlinearity of the sorption isotherm introduces favorable wave patterns which are not encountered in heat transfer. For selected initial and inlet conditions, desorption waves are constant pattern waves which become rapidly fully established after they originate at the inlet face of the test matrix. The shape and width of the mass transfer wave in desorption processes are constant, and, for reasonable-quality inlet steps and sufficiently long bed lengths, are independent of the sharpness of the step change in inlet conditions. Furthermore, the wave dispersion is well-defined and independent of the air stream mass flow rate. These considerations lead to the formulation of an experimental single blow technique for dehumidifier matrices.

6.2.1 Design criteria for experimental facilities

The design criteria for the experimental facility for isothermal or adiabatic mass transfer are different from those for heat transfer alone.

1. Of utmost importance is the repeatability of the experimental facility for mass transfer. Repeatability creates the possibility of repeated experiments with identical inlet and initial conditions, and varying process air mass flow rates. Such a series of experiments is necessary for the analysis technique paired with the experimental procedure. The repeatability requirement almost excludes the use of manually operated flow valves as used in the facility for this work.

2. The squareness of the step change in inlet conditions is less important, because the effect of the inlet step disappears when the wave becomes fully developed. The change of inlet conditions with time is determined by the temperature- and humidity controllers of the experimental facility. The constant pattern behavior allows the specification requirements for the controllers to be less stringent, and therefore the controllers to be less expensive. However, manual control is stymied by the requirement of repeatability, and computer control with the actual measurements as input variables is mandatory.

3. The requirements for temperature measurements are identical to those for heat transfer, and are not commented upon. The response time of the sensors for humidity measurements should be considered in the design of the facility. The 10-90% duration of the second, mass transfer wave should be about 10 times the response time of the hygrometers. This duration increases linearly with the mass of desiccant in the test matrix, and this requirement puts a lower limit on the amount of desiccant mass.

4. The mass of desiccant should further be in tune with the range for the air stream flow rates facilitated by the experimental apparatus. The duration of the sorption experiment increases linearly with the mass of desiccant and is inversely proportional with the air flow rate. This duration should be in tune with the rate at which the measurements are recorded with time, which put a upper limit on the process mass flow rate or a lower limit on the desiccant mass.

5. The facility should enable the use of a wide range of flow rates and the resolution of the flow rate measurements should be high. Low mass flow rates should be measured with equal accuracy as high mass flow rates.

6. The design of the test matrix should avoid distributed thermal capacitances. Distributed capacitances cause the measured temperature response to desynchronize with the actual temperature response of the desiccant mass. The resulting

shift between the measured temperature and humidity distributions complicates the analysis and increases the uncertainty level of the computed performance parameters.

6.2.2 Experimental Procedure

The experimental procedure follows the principles of the M-series desorption experiments presented in this work. The objective of the experiments is to determine independently in the following order: the core geometry of the test matrix, the mass of desiccant within the matrix, and the spatial distributions of the temperature and humidity response of the second, mass transfer wave.

1. Core Geometry of Test Matrix

A series of pressure drop experiments should be performed to determine the hydraulic diameter and flow area or transfer area of the passages. The measurement of matrix dimensions with Vernier calipers can provide necessary information for the analysis of the pressure drop.

2. Mass of Desiccant

A series of dynamic, single blow adsorption and desorption experiments should be performed to determine the active mass of desiccant within the test matrix. The overall mass balance requires an accurate expression for the isotherm

correlation, which should be established preferably by static sorption experiments. For regular density silica gel, an isotherm is introduced in this work of which the accuracy has been verified by experiments. An independent count of the desiccant volume used for the manufacturing of the test matrix can substantiate the computed value.

3. Outlet Response

A series of repeated desorption experiments should be performed with identical matrix-initial and fluid-inlet conditions, and varying process air mass flow rates. The choice of the fluid-inlet and matrix-initial conditions is determined by a compromise between the operating range of the experimental facility, the pattern type of the breakthrough wave, and the strength of the outlet response. The pattern of the mass transfer wave should be constant. The range of inlet and initial conditions which produce constant pattern waves can easily be determined by the equilibrium theory for regenerative dehumidifiers. Furthermore, the accuracy of the analysis of the experimental data increases with the magnitude of the swing in outlet conditions. In general, high regeneration temperatures and high process humidities produce well-defined outlet responses. Regeneration temperatures are limited on the upper scale by the increase in heat loss which obscures the quality of the analysis of the experimental data.

The inverses of the sequential mass flow rates should form an arithmetic series of numbers because the dimensionless flow length is inversely proportional with the mass flow rate. The maximum and minimum mass flow rates are determined by the width of the mass transfer wave. The elapsed time at which the leading edge of the mass transfer wave reaches the exit face of the test matrix for the lowest flow rate should be equal to the elapsed time at which the trailing edge of the wave reaches the exit face for the highest mass flow rates. The number of intermediate mass flow rates determines the resolution for interpolation in between the inlet and intermediate state properties.

6.2.3 Analysis Technique

The principle of the analysis technique is based upon the transformation of the model partial differential equations into a set of ordinary differential equations for the constant pattern condition of the desorption wave. The transformation is defined by

$$\Delta\tau = 4Nu\frac{M_f}{M_d}\frac{\alpha_f}{D_h{}^2}S\,\Delta\theta \qquad (6.11)$$

where θ is the real time and τ is the dimensionless time in which the conservation and transfer rate equations are

expressed. The idea is to determine independently and sequentially the values of the parameters which appear in Eq. (6.11), except for one: the Nusselt number.

α_f is the thermal diffusivity of the fluid stream and can be accurately determined from existing relationships for the thermo-physical properties of humid air.

D_h is the hydraulic diameter. This parameter can be determined from the independent set of pressure drop experiments with reasonable accuracy. For flow through rough passages, it may be assumed that the product fRe is the same as for smooth passages with the same geometry.

M_f is the fluid mass within the test matrix. This parameter can also be computed from the core geometry of the test matrix, established by the pressure drop analysis.

M_d is the amount of mass of desiccant in the test matrix. The desiccant mass can be computed with reasonable accuracy from overall mass balances for the sorption experiments.

S is the dimensionless shock speed and determined by:

$$S = \frac{M_d}{\dot{m}_f L} \frac{dx}{d\theta} \tag{6.12}$$

where $dx/d\theta$ is the physical wave speed in real-time coordinates. This wave speed can be obtained directly from the repeated sorption experiments with high accuracy. Inserting Eq. (6.12) into (6.11) shows that the mass of desiccant is actually not required for the transformation,

$$\Delta\tau = 4Nu \frac{M_f}{\dot{m}_f L} \frac{\alpha_f}{D_h^2} \frac{dx}{d\theta} \Delta\theta \qquad (6.13)$$

However, the mass of desiccant computed from the experimental data in comparison with the value obtained from the count of the desiccant volume during manufacturing, forms an important check on the accuracy of the analysis, and should thus be determined.

The distribution of the constant pattern waves is modeled by Eqs. (5.69). The model equations form a non-stiff system of ordinary differential equations which is easy to integrate numerically. There are two parameters that determine the shape of the wave in the dimensionless coordinate τ. These parameters are the passage Nusselt number and the overall Lewis number. By a curve fit method and the $\Delta\tau_{10-90}$ method, the Nusselt number and the overall Lewis number can be determined with acceptable accuracy.

This single blow technique is easy to perform. The step in inlet conditions does not need to be 'near' square. The computations involved are minimal, and can easily be implemented on a microcomputer for on-line performance evaluation.

CHAPTER 7

CONCLUSION AND RECOMMENDATIONS

This thesis forms a study of two related topics: the equilibrium sorption properties of water vapor on regular density silica gel, and the exchange performance of a prototype compact dehumidifier with dynamic sorption of water vapor on R.D. silica gel.

A literature review of experimental equilibrium sorption studies for water vapor on regular density silica gel indicates that there exist several theoretical expressions for the sorption isotherm which can fit the experimental data with equal accuracy. Previous studies have shown that the characteristic curve exists for R.D. silica gel and water, and that the Dubinin-Astakhov equation can be used for curve fitting the experimental data. However, these studies considered only one set of experimental data which were obtained for one specific grade of silica gel, and with one measuring technique.

This work retrieves experimental data for the equilibrium sorption of water on R.D. silica gel from the technical literature, and shows that the characteristic curve exists for seven data sets, obtained for several grades of silica gels and with various measuring techniques. The experimental data can be correlated with the Dubinin-Astakhov expression with good accuracy. The isotherm equation is written as

$$W_d = W_{o,1} \exp(-(A/E_{o,1})^2) + W_{o,2} \exp(-(A/E_{o,2})^2). \quad (7.1)$$

and the following parameters for the equilibrium sorption of water on R.D. silica gel are recommended based upon 110 experimental data points: $E_{o,1}$ = 7740 J/mol; $E_{o,2}$ = 2500 J/mol; $W_{o,1}$ = 0.117 kg/kgDD; $W_{o,2}$ = 0.237 kg/kgDD. The accuracy of Eq. (7.1) with these parameters is substantiated by an analysis of original dynamic sorption data presented in this work.

The analysis indicates that their exists two varieties of R.D. silica gel, each with a specific set of characteristic energies of adsorption, $E_{o,1}$ and $E_{o,2}$. This difference is not contributed to a specific fact or explained by a particular mechanism, because of lack of information about the reported experimental data.

In this first part, the phenomena of hysteresis is also discussed and found insignificant for the microporous desiccants, including R.D. silica gel.

The second part of this thesis presents the analysis of experimental dynamic sorption data for water vapor on regular density silica gel. Data are presented for single-blow experiments for the laminar flow of humid air through a parallel-plate matrix, in which the channel walls are coated with R.D. silica gel. A technique is used to analyze the adiabatic temperature and humidity response of the air stream which has

previously only been used for isothermal dynamic sorption responses. The results of the analysis shows that the dimensionless air-side and desiccant-side transfer coefficients are approximately constant with respect to time and direction in the flow direction. The actual transfer coefficients are proportional to the diffusivities of the air stream and the desiccant layer, respectively, and can vary with an order of magnitude for the desiccant during the course of a single sorption event.

The thermal diffusivity of silica gel is much larger than the air diffusivity, and the overall heat transfer coefficient can be assumed equal to the air-side heat transfer coefficient. If the mass transfer resistance of the air stream is dominant, established techniques to account for temperature dependent properties can be applied to compute the air-side and overall heat and mass transfer coefficients. If the mass transfer resistance of the desiccant is dominant, no such techniques exist and a conservative estimate of the overall mass transfer coefficient based upon the smallest value of the desiccant mass diffusivity is recommended.

The relative transfer resistance of the desiccant layer is reflected by the value of the effective Lewis number. A theoretical expression for the Lewis number contains the desiccant-particle conductive Sherwood number and mass diffusivity. A table is presented which shows the conductive

Sherwood number for crushed particles with one insulated surface, and indicates that this number can vary over a range of 2 to 10. A correlation for the diffusivity of water vapor in R.D. silica gel is established based upon a limited set of experimental data, and the uncertainty in the correlation may be large. An analysis technique is presented to compute the Lewis number directly from the single-blow experimental data. For fully developed laminar flow of humid air through parallel plates with D_h = 2 mm and crushed silica gel particles with D_p = 0.22 mm, the effective experimental Lewis number is 4.5 ± 1.5.

A single-blow technique for characterizing the exchange performance of compact dehumidifiers is developed. The technique is insensitive to the quality of the step change in inlet conditions. The experimental facility can have simpler control instrumentation than a similar single-blow facility for compact heat exchangers. The governing partial differential equations are reduced to a set of non-stiff ordinary differential equations by a coordinate transformation, and the mathematical model can be implemented on microcomputers for direct on-line performance evaluation.

Based upon the work performed to establish this manuscript, the author makes the following suggestions and recommendations for future study.

1. Activated alumina and molecular sieves 4A and 13X are currently considered or used for regenerative dehumidification of air. The characteristic curves for these desiccants and water vapor have been established; however, the parameters in the Dubinin-Astakhov isotherm expression have not yet been determined. A curve fit of experimental data retrieved from the technical literature can yield the values for these parameters.
2. Several simplified models for regenerative dehumidifiers have been developed. There does not yet exist a simple, generic model valid for any microporous desiccant. The Dubinin-Astakhov isotherm expression can form the basis for such a model. A simple dehumidifier model could be used for comparitive studies of microporous desiccants and for the optimization of microporous desiccant sorption properties, a topic which is currently under investigation.
3. The diffusivity of water vapor in R.D. silica gel is not known with acceptable accuracy. A more accurate correlation for this diffusivity can be used to predict the value of the dehumidifier Lewis number theoretically, rather than computing this value from experimental data. Such a diffusivity correlation could be established with specific existing diffusion techniques.

4. Actual commercial dehumidifiers use geometries different from the parallel plate configuration for reasons primarily answered by current manufacturing technologies. Single blow experiments on dehumidifier matrices with core geometries representative for actual dehumidifiers can provide valuable information on the heat and mass transfer characteristics of these matrices. Such experiments could establish a large data pool which can be used for modeling regenerative dehumidifiers similar to the situation that currently exists for compact heat exchangers.

REFERENCES

Allander, C.G., 1953, "Untersuchung des Adsorptionsvorganges in Adsorbentenschichten mit linearer Adsorptionsisotherme," *Kungl. Tekniska Hoegskolans handlingar*, Vol. 70, pp. 1-160.

Ahlberg, J.E., 1939, "Rates of Water Vapor Adsorption from Air by Silica Gel," *Ind. Eng. Chem.*, Vol. 31, No. 8, pp. 988-992.

Anzelius, A., 1926, "Uber Erwarmung vermittels durchstromender Medien," *Ztshr. f. angew. Math. und Mech.*, Vol. 6, No. 4, pp. 291-294.

ASHRAE, 1981, *ASHRAE Handbook, 1981 Fundamentals Volume*, American Society of Heating, Refrigeration and Air-Conditioning Engineers, Atlanta, GA, pp. 5.1-5.10.

Baclic, B.S., 1985, "The Application of the Galerkin Method to the Solution of the Symmetric and Balanced Counterflow Regenerator Problem," *J. Heat Transfer*, Vol. 107, pp. 214-221.

Baclic, B.S., P.J. Heggs and H.Z.Z. Abou Ziyan, 1986, "Differential Fluid Enthalpy Method for Predicting Heat Transfer Coefficients in Packed Beds," Proceedings, *8th International Heat Transfer Conference*, San Fransisco, pp. 2617-2622.

Banks, P.J., 1982, "Effect of Fluid Carryover on Regenerator Performance," *J. Heat Transfer*, Vol 104, pp. 215-217.

Banks, P.J., 1984, "The Representation of Regenerator Fluid Carryover by Bypass Flows," *J. Heat Transfer*, Vol. 106, pp. 216-220.

Banks, P.J., 1985a, "Prediction of Heat and Mass Regenerator Performance Using Nonlinear Analogy Method: Part 1 - Basis," *J. Heat Transfer*, Vol. 107, pp. 222-229.

Banks, P.J., 1985b, "Prediction of Heat and Mass Regenerator Performance Using Nonlinear Analogy Method: Part 2 - Comparison of Methods," *J. Heat Transfer*, Vol. 107, pp. 230-238.

Barlow, R.S, 1981, *Analysis of Adsorption Process and of Desiccant cooling Systems. A Pseudo-Steady-State Model for Coupled Heat and Mass Transfer*, SERI/TR-631-1330, Solar Energy Research Institute, Golden, CO.

Barrer, R.M., 1978, *Zeolites and Clay Minerals as Sorbents and Molecular Sieves*, Academemic Press, New York, NY.

Bateman, H., 1944, *Partial Differential Equations*, Dover Publications, New York, N.Y., pp. 123-125.

Benedict, R.P., 1984, *Fundamentals of Temperature, Pressure and Flow Rate Measurement*, John Wiley & Sons, New York, NY, pp. 101-107.

Bergles, A.E., 1981, "Principles of Heat Transfer Augmentation," in *Heat Exchangers, Thermal-Hydraulic Fundamentals and Design*, 1981, S. Kakac, A.E. Bergles and F. Mayinger, Eds., Hemisphere Publishing Corp. McGraw-Hill Book. Co., NY., pp. 819-842.

Bergles, A.E. and R.L. Webb, 1978, "Bibliography on Augmentation of Convective Heat and Mass Transfer - Part 2," *Prev. Heat Mass Transfer*, Vol. 4, No. 4, pp. 89-106.

Bird, R.B., C.F. Curtiss and J.O. Hirschfelder, 1955, "Fluid Mechanics and the Transport Phenomena," in *Mass Transfer - - Transport Properties*, F.J. Van Antwerpen, Ed., *Chem. Eng. Prog. Symp. Ser.*, Vol. 51, No. 16, pp. 69-85.

Bird, R.B., W.E. Stewart and E.N. Lightfoot, 1960, *Transport Phenomena*, , John Wiley & Sons, NY., pp. 1-780.

Biswas, P., S. Kim and A.F. Mills, 1984, "A Compact Low-Pressure Drop Desiccant Bed for Solar Air Conditioning Applications: Analysis and Design," *J. Solar Energy Engng.* Vol. 106, pp. 153-158.

Bjurstroem, H. and B. Carlsson, 1984, "The Importance of Heat Transfer in a Chemical Heat Pump Utilizing a Gas-Solid Sorption Reaction," *Proceedings, 3rd Multi-Phase Flow and Heat Transfer Symp. Workshop*, Miami Beach, Florida (1983), Elsevier, Amsterdam, Vol. III, Part B: Applications, pp. 711-726.

Bjurstroem, H., E. Karawacki and B. Carlsson, 1984, "Thermal Conductivity of a Microporous Particulate Medium: Moist Silica Gel," *Int. J. Heat Mass Transfer*, Vol. 27, No. 11, pp. 2025-2036.

Brakell, J.P. and T.A. Cowell, 1986, "An analysis of the Uniform Naphtalene Layer Mass Transfer Analogue Method applied to Laminar Flow over a flat Plate," *Proceedings, 8th International Heat Transfer Conference*, San Fransisco, pp. 495-499.

Brandemuehl, M.J., 1982, *Analysis of Heat and Mass Regenerators with Time Varying or Spatially Nonuniform Inlet Conditions*, Ph.D. Thesis, University of Wisconsin-Madison, Madison, WI.

Brandemuehl, M.J., and P.J. Banks, 1984, "Rotary Heat Exchangers With Time Varying or Nonuniform Inlet Temperatures," *J. Heat Transfer*, Vol. 106, pp. 750-758.

Brauer, H., 1961, "Stroemungswiderstand und Waermeubergang bei Ringspalten mit rauhen Kernrohren," *Atomkernenergie*, Vol. 6, No. 4, pp. 152-161, pp. 207-211.

Bullock and Threlkeld, 1966, "Dehumidification of Moist Air by Adiabatic Adsorption," *Trans. Am. Soc. Heat Refrig. Air-Condit. Engrs.*, Vol. 72, pp. 301-313.

Burns, P.R., J.W. Mitchell, and W.A. Beckman, 1985, "Hybrid Desiccant Cooling Systems in Supermarket Applications," *ASHRAE Trans.*, Vol. 91, Pt.1.

Carnot, N.L.S., 1824, *Reflections sur la Puissance Motrice du Feu et sur les Machines*, Bachelier, Paris.

Carslaw, H.S., and J.C. Jaeger, 1959, *Conduction of Heat in Solids*, Oxford University Press, Oxford.

Carter, J.W., 1960, "Adsorption Drying of Gases, Parts I, II and III," *British Chemical Engineering*, pp. 472-476, 552-555, 625-631.

Carter, J.W., 1966, "A Numerical Method for prediction of Adiabatic Adsorption in Fixed Beds," *Trans. Instn. Chem. Engrs.*, Vol. 44, pp. 253-259.

Carter, J.W., 1968, "Isothermal and Adiabatic Adsorption in Fixed Beds," *Trans. Instn. Chem. Engrs.*, Vol. 46, pp.213-221.

Chang, S.C., and J.A. Roux, 1985, "Thermodynamic Analysis of a Solar Zeolite Refrigeration System," *J. sol. Energy Engng.*, Vol. 107, pp. 189-195.

Chase, C.A., D. Gidaspow and R.E. Peck, 1969, "Adiabatic Adsorption in a Regenerator," *AIChE Symp. Ser.*, Vol. 65, No. 96, pp. 34-47.

Chi C.W. and D.T. Wasan, 1970, "Fixed Bed Adsorption Drying," *AIChE Journal*, Vol. 16, No. 1, pp. 23-31.

Chihara, K, and M. Suzuki, 1983, "Air Drying by Pressure Swing Adsorption," *J. Chem. Engng Japan*, Vol. 16, No. 4, pp. 293-299.

Chinery, G.T., and T.R. Penney, 1987, *Desiccant Newsletter*, Vol. 1, No. 1, Tennessee Valley Authority, Chattanooga, TN.

Clark, J.E., A.F. Mills, and H. Buchberg, 1981, "Design and Testing of Thin Adiabatic Desiccant Beds for Solar Air Conditioning Applications," *J. Solar Energy Engineering*, Vol. 103, pp. 89-91.

Close, D.J., and P.J. Banks, 1972, "Coupled Equilibrium Heat and Single Adsorbate TRansfer in Fluid Flow through a Porous Medium - II Predictions for a Silica-Gel Air-Drier using Characteristic Charts," *Chem. Engng Sci.*, Vol. 27, pp. 1157-1168.

Close, D.J., 1983, "Characteristic Potentials for Coupled Heat and Mass Transfer Processes," *Int. J. Heat Mass Transfer*, Vol. 26, No. 7, pp. 1098-1102.

Collier, R.K., R.S. Barrow and F.H. Arnold, 1982, "An Overview of Open-Cycle Desiccant-Cooling Systems and Materials," *J. sol. Energy Engng.*, Vol. 104, pp. 28-34.

Cornish, R. J., 1928, "Flow in a Pipe of Rectangular Cross Section," *Proc. Roy. Soc. A*, Vol. 120, pp. 691-700.

CRC, 1980, *Handbook of Chemistry and Physics*, R.C. Weast and M.J. Astle, Eds., CRC Press, Boca Raton, FL, p. F80, p. E6.

Davison, 1981, *Davison Silica Gels*, IC-15-1181, W.R. Grace & Co., Baltimore, MD.

de Boer, J.H., 1958, "The Shapes of Capillaries," in *The Structure and Properties of Porous Materials*, D.H. Everett and F.S. Stone, eds., Academic Press, NY., pp. 68-94.

Dubinin, M.M., 1972, "Fundamentals of the Theory of Physical Adsorption of Gases and Vapours in Micropores," in *Adsorption-Desorption Phenomena*, F. Ricca, ed., Academic Press, New York, NY, pp. 3-17.

Dubinin, M.M., 1975, "Physical Adsorption of Gases and Vapors in Micropores," *Prog. Surf. Membrane Sci.*, Vol. 9, pp. 1-70.

Eagleton, L.C., and H. Bliss, 1953, "Drying of Air in Fixed Beds," *Chem Eng. Progress*, Vol. 49, No. 10, pp. 543-548.

Eckert, E.R.G. and R.M. Drake, 1972, *Analysis of Heat and Mass Transfer*, McGraw-Hill Book Co., New York, NY., pp. 689-697.

Elliot M.P., C.W. Rapley and A.I.C. Webb, 1986, "Application of the Single Blow Experimental Method to Square Duct Heat Transfer," *Proceedings, 8th International Heat Transfer Conference*, San Fransisco, pp. 981-986.

Enderby, J.A., 1955, "The Domain Model of Hysteresis, Part 1: Independent Domains," *Trans. Far. Soc.*, Vol. 51, pp. 835-848.

Enderby, J.A., 1956, "The Domain Model of Hysteresis, Part 2: Interacting Domains," *Trans. Far. Soc.*, Vol. 52, pp. 106-120.

Epstein, M., M. Grolmes, K. Davidson and D. Kosar, 1985, "Desiccant Cooling System Performance: A Simple Approach," *J. sol. Energy Engng.*, Vol. 107, pp. 21-28.

Everett, D.H. and W.I. Whitton, 1952, "A General Approach to Hysteresis," *Trans. Far. Soc.*, Vol. 48, pp. 749-757.

Everett, D.H. and F.W. Smith, 1954, "A General Approach to Hysteresis - Part 2: Development of the Domain Theory," *Trans. Far. Soc.*, Vol. 50, pp. 187-197.

Everett, D.H., 1954a, "A General Approach to Hysteresis - Part 3: A Formal Treatment of the Independent Domain Model of Hysteresis," *Trans. Far. Soc.*, Vol. 50, pp. 1077-1096.

Everett, D.H., 1954b, "A General Approach to Hysteresis - Part 4: An Alternative Formulation of the Domain Model," *Trans. Far. Soc.*, Vol. 51, pp. 1551-1557.

Everett, D.H., 1958, "Adsorption Hysteresis," in *The Structure and Properties of Porous Materials*, D.H. Everett and F.S. Stone, eds., Butterworths, London, pp. 1055-1113.

Everett, D.H., and J.M. Haynes, 1972, "Model Studies of Capillary Condensation - Part I. Cylindrical Pore Model with Zero Contact Angle," *J. Colloid Interface Sci.*, Vol. 38, No. 1, pp. 125-137.

Fraioli, A.V., 1984, *Rates of Adsorption of Water on Manganese Oxides and Silica Gel*, Report ANL-84-98, Argonne National Laboratory, Argone, IL.

Garg, D.R., and D.M. Ruthven, 1975, "Performance of Molecular Sieve Adsorption Columns: Combined Effects of Mass Transfer

and Longitudinal Diffusion," *Chem. Engng Sci.*, Vol. 30, pp. 1192-1194.

Ghezelayagh H., and D. Gidaspow, 1982, "Micro-Macropore Model for Sorption Of Water On Silica Gel in a Dehumidifier," *Chem. Engng Sci.*, Vol 37, No. 8, pp 1181-1197.

Glueckauf, E., 1947, J. Chem. Soc. pp.1302-29.

Graber, H., 1970, "Der Warmeubergang in glatten Rohren zwischen parallelen Platten, in Ringspalten und langs Rohrbundeln bei exponentieller Warmeflussverteiling in erzwungener laminarer oder turbulenter Stromung," *Int. J. Heat Mass Transfer*, Vol. 13, pp. 1645-1703.

Gregg, S.J., and K.S.W. Sing, 1982, *Adsorption, Surface Area and Porosity*, Academic Press, New York, NY.

Grolmes, M.A., and M. Epstein, 1985, "Property and Composition Effects on the Cyclic Performance of Fixed Bed Desiccant Air Dehumidification," *ASME Paper 85-HT-69*, ASME/AIChE National Heat Transfer Conference, Denver, CO.

Guilleminot, J.J., F. Meunier and B. Mischler, 1980, "Etude de Cycles Intermittents a Adsorption Solide pour la Refrigeration Solaire," *Rev. Phys. Appl.*, Vol. 15, No. 3, pp. 441-452.

Haar, L., J.S. Gallagher and G.S. Kell, 1984, *NBS/NRC Steam Tables. Thermodynamic and Transport Properties and Computer Programs for Water Vapor and Liquid States of Water in SI Units*, Hemisphere Publishing Co., Washington.

Hasz, J.W., and C.A. Barrere, 1969, "Prediction of Equilibrium Adsorption Capacity and Heats of Adsorption by the Polanyi Potential Theory," *Chem. Engng Progr. Symp. Ser.*, Vol. 65, No. 96, pp.48-56.

Hart, R.C.G.C., I.L. Maclaine-cross and C.W. Ambrose, 1980, *The Reduction of Flow Non-uniformities in Regenerator Test Rigs using a Ribbon Screen*, Memorandum No. 1, Department of Mechanical Engineering, Monash University, Victoria, Australia.

Haul, R. and H. Stremming, 1984, "Nonisothermal Sorption Kinetics in Porous Adsorbents," *J. Colloid Interface Sci.*, Vol. 97, No. 2, pp. 348-355.

Hausen, 1929, "Ueber die Theory von Waermeaustauches in Regeneratoren," *Z. Angew. Math. Mech.*, Vol. 9, pp. 173-200.

Heggs, P.J., 1983, "Experimental Techniques and Correlations for Heat Exchanger Surfaces: Packed Beds", in *Low Reynolds Number Flow Heat Exchangers*, S. Kakac, R.K. Shah and A.E. Bergles, Eds., Hemisphere Publishing Corp., NY., pp. 341-368,

Hexcel TSB 102, 1973, *Honeycomb in Air Directionalizing Applications*, Hexcel Honeycomb Brochure TSB 102, Dublin, CA.

Holmberg, R.B., 1979, "Combined Heat and Mass Transfer in Regenerators with Hygroscopic Materials," *J. Heat Transfer*, Vol. 101, pp. 205-210.

Hougen, O.A., and W.R. Marshall, Jr., 1947, "Adsorption from a Fluid Stream Flowing through a Stationary Granular Bed," *Chemical Engineering Progress*, Vol. 43, No. 4, pp. 197-208.

Hubard, S.S, 1954, "Equilibrium Data for Silica Gel and Water Vapor," *Ind. Engng Chem.*, Vol. 46, pp. 356-358.

IMSL, 1982, *IMSL Library Reference Manual*, 9th ed., Vols. 1-4, International Mathematical & Statistical Libraries, Inc., Houston, TX.

Ingram J.B., and G.C. Vliet, 1982, "Solid Desiccant Rotary Dryer Performance Charts," *Progress Solar Energy*, Vol. 5, pp. 603-608.

ISO 5168, 1978, *Measurement of Fluid Flow - Estimation of Uncertainty of a Flow-Rate Measurement*, International Organization for Standardization, Ref. No. ISO-5168-1978(E), Switzerland.

ISO 5167, 1980, *Measurement of Fluid Flow by Means of Orifice Plates, Nozzles and Venturi Tubes Inserted in Circular Cross-Section Conduits Running Full*, International Organization for Standardization, Ref. No. ISO-5167-1980(E), Switzerland.

Jeffreson, C.P., 1968, "Dynamics of Packed Beds with Intraphase Heat and Mass Transfer," *Chemical Engineering Science*, Vol. 23, pp. 509-523.

Jeffreson, C.P., 1970, "Dynamic Testing - a Unification," *Chemical Engineering Science*, Vol. 25, pp.1319-1329.

Jeffreson, C.P., 1972, "Prediction of Breakthrough Curves in Packed Beds: I. Applicability of Single Parameter Models," *AIChE Journal*, Vol. 18, No. 2, pp. 409-420.

Jurinak, J.J., 1982, *Open Cycle Desiccant Cooling - Component Models and Systems Simulations*, PhD thesis, University of Wisconsin-Madison, Madison, WI.

Jurinak, J.J., and P.J. Banks, 1982, "A Numerical Evaluation of Two Analogy Solutions for a Rotary Silica Gel Dehumdifier," in *Heat Transfer in Porous Media*, J.V. Beck and L.S. Yao, eds., HTD-Vol. 22, The American Society of Mechanical Engineers, New York, NY.

Jurinak, J.J., and J.W. Mitchell, 1982, "Effect of Matrix Properties on the Performance of of a Counterflow Rotary Dehumidifier," in *Heat Transfer in Porous Media*, J.V. Beck and L.S. Yao, eds., HTD-Vol. 22, American Society of Mechanical Engineers, New York, NY.

Jurinak, J.J., and J.W. Mitchell, 1984a, "Recirculation of Purged Flow in an Adiabatic Counterflow Rotary Dehumidifier," *J. Heat Transfer*, Vol. 106, pp. 369-375.

Jurinak, J.J., J.W. Mitchell and W.A. Beckman, 1984b, "Open-Cycle Desiccant Air Conditioning as an Alternative to Vapor Compression Cooling in Residential Applications," *J. Solar Energy Engineering*, Vol. 106, pp. 252-260.

Jury, S.H., and H.R. Edwards, 1971, "The Silica Gel-Water Vapor Sorption Therm," *Can. J. Chem. Engng.*, Vol. 49, pp. 663-666.

Kays, W.M., 1950, "Loss Coefficients for Abrupt Changes in Flow Cross Section with Low Reynolds Number Flow in Single and Multiple-Tube Systems," *Trans. ASME*, Vol. 72, pp. 1067-1074.

Kays, W.M. and A.L. London, 1984, *Compact Heat Exchangers*, 3th ed. McGraw-Hill Book Company, New York, NY., pp. 79-101.

Keenan, J.H., J. Chao and J. Kaye, 1983, *Gas Tables, Thermodynamic Properties of Air Products and Component Gases Compressible Flow Functions*, 2nd Ed., John Wiley and Sons, New York.

Kester, F.L., and P.J. Lunde, 1973, "Chemisorption-B.E.T. Model for Adsorption of Water Vapor on Silica Gel," *A.I.Ch.E. Symp. Ser.*, Vol. 69, No. 134, pp. 87-94.

Kestin, J., 1976, "New Values for the Viscosity of Water Substance," *Mechanical Engineering*, Vol. 98, No. 7, p. 79.

Kestin, J., 1978. "Thermal Conductivity of Water and Steam," *Mechanical Engineering*, Vol. 100, No. 8, pp. 46-48.

Khelifa, N., E. Lavemann, R. Hallemayer and R. Sizmann, 1983, "Refrigeration et Climatisation Solaire au moyen du Gel de Silice et de la Vapeur d'Eau de l'Air," *Rev. Int. d'Heliotechnique*, pp. 45-49.

Kim, S., P. Biswas and A.F. Mills, 1985, "A Compact Low-Pressure Drop Desiccant Bed for Solar Air Conditioning Applications - II Bench Scale Tests," *J. Solar Energy Engng.*, Vol. 107, pp. 120-127.

Kulacki, F.A. and D. Gidaspow, 1967, "Convective Diffusion in a Parallel Plate Duct with One Catalytic Wall - Laminar Flow - First Order Reaction, Part II - Experimental," *Can. J. Chem. Engng.*, Vol. 45, pp. 72-78.

Lapidus, L. and G. F. Pinder, 1982, *Numerical Solution of Partial Differential Equations in Science and Engineering*, John Wiley & Sons, New York, NY.

Lavan, Z., and D. Gidaspow, 1979, "Development of a Solar Desiccant Dehumidifier," in *Proc. 3rd Annual sol. Heating Cooling R & D Branch Contr. Meeting*, Sept. 1978, U.S. Dept. of Energy, Washington, D.C.

Lavan, Z., J-B. Monnier, and W.M. Worek, 1982, "Second Law Analysis of Desiccant Cooling Systems," *J. sol. Energy Engng*, Vol. 104, pp. 229-236.

London, A.L., F.R. Biancardi and J.W. Mitchell, 1959, "The Transient Response of Gas-Turbine-Plant Heat Exchangers-Regenerators, Intercoolers, Precoolers, and Ducting," *ASME J. of Engineering for Power*, Vol. 81, pp. 433-448.

Lunde, P.J., and F.L. Kester, 1975, "Chemical and Physical Gas Adsorption in Finite Multimolecular Layers," *Chem. Engng Sci.*, Vol. 30, pp. 1497-1505.

Maclaine-cross, I.L., and P.J. Banks, 1972, "Coupled Heat and Mass Transfer in Regenerators-Prediction using an Analogy with Heat Transfer," *Int. J. Heat Mass Transfer*, Vol. 15, pp. 1225-1242.

Maclaine-cross, I.L., 1974, *A Theory of Combined Heat and Mass Transfer in Regenerators*, PhD thesis, Monash University, Australia

Maclaine-cross, I.L., 1974, *Thermocouple Radiation Error*, Personal Memorandum, University of New South Wales, Kensington, Australia.

Maclaine-cross, I.L., 1985, *Flow Uniformity Improvement and Turbulence Reduction in Single Blow Rig Test Section,* Internal Communication, Solar Energy Research Institute, Golden, CO.

Maclaine-cross, I.L. 1985, "High-Performance Adiabatic Desiccant Open-Cooling Cycles," *J. sol. Energy Engng,* Vol. 107, pp. 102-104

Mason, E.A. and L. Monschick, 1965, "Survey of the Equation of State and Transport Properties of Moist Gases," in *Humidity and Moisture Measurements and Control in Science and Industry,* Reinhold Publishing Corp. New York, NY, Vol. 3, pp. 257-272.

Mason, G., 1971, "A Model of the Pore Space in a Random Packing of Equal Spheres," *J. Colloid Interface Sci.,* Vol. 35, No. 2, pp. 279-287.

Mason, G., 1972, "Desaturation of Porous Media - I. Unconsolidated Materials," *J. Colloid Interface Sci.,* Vol. 41, No. 2, pp. 208-227.

Mason, G., 1982, "The Effect of Pore Space Connectivity on the Hysteresis of Capillary Condensation in Adsorption-Desorption Isotherms," *J. Colloid Interface Sci.,* Vol. 88, No. 1, pp. 36-46.

Mason, G., 1983, "A model of Adsorption-Desorption Hysteresis in which hysteresis is primarily developed by the interconnections in a network of pores," *Proc. R. Soc. Lond. A,* Vol. 390, pp. 47-72.

Mason, G., and G.D. Yadav, 1983, "Capillary Hysteresis in the Pore Space of a Packing of Spheres Measured by the Movement of Blobs," *J. Colloid Interface Sci.,* Vol. 95, No. 1, pp. 120-130.

Mathiprakasam, B., and Z. Lavan, 1980, "Performance Predictions for Adiabatic Desiccant Dehumdifiers Using Linear Solutions," *J. sol. Energy Engng,* Vol. 102, pp. 73-79.

Matsuki, K., M. Tatsuoka and T. Tonomora, 1983, "A Prototype Solar Desiccant Air-Conditioner," *Proc. 18th Intersoc. Energy Conversion Engng Conf.,* pp. 1927-1932.

Michaels, A.S., 1952, "Simplified Method of Interpreting Kinetic Data in Fixed-Bed Ion Exchange," *Ind. Eng. Chem.,* Vol. 44, No. 8, pp. 1922-1930.

Mikhail, R.Sh., and F.A. Shebl, 1970a, "Adsorption in Relation to Pore Structures of Silicas I. Organic Vapor Adsorption on Microporous Silica Gel," *J. Colloid Interface Sci.*, Vol. 32, No. 3, pp. 505-517.

Mikhail, R.Sh., and F.A. Shebl, 1970b, "Adsorption in Relation to Pore Structures of Silicas II. Water Vapor Adsorption on Wide-Pore and Microporous Silica Gels," *J. Colloid Interface Sci.*, Vol. 34, No. 1, pp. 65-75.

Mikhail, R.Sh., and F.A. Shebl, 1972, "Adsorption in Relation to Pore Structures of Silicas III. Persorption versus Specific Interactions," *J. Colloid Interface Sci.*, Vol. 38, No. 1, pp. 35-44.

Mitchell, J.W., 1983, *Energy Engineering*, John Wiley & Sons, New York, NY.

Molloy, J., 1967, *Rough Tube Friction Factors and Heat Transfer Coefficients in Laminar and Transition Flow*, Rep. AERE-R 5415, Atomic Energy Research Establishment, Harwell, U.K.

Neumann, E., 1973, "Molecular Hysteresis and Its Cybernetic Significance," *Angew. Chem. intern. Edit.*, Vol. 12, No. 5, pp. 356-369.

Ngoddy, P.O., and F.W. Bakker-Arkema, 1970, "A Generalized Theory of Sorption Phenomena in Biological Materials - Part I. The Isotherm Equation," *Trans. ASAE*, Vol. 13, No. 5, pp. 612-617.

Ngoddy, P.O. and F.W. Bakker-Arkema, 1975, "A Theory of Sorption Hysteresis in Biological Materials," *J. agric. Engng Res.*, Vol. 20, pp. 109-121.

Pashley, R.M., 1980, "Multilayer Adsorption of Water on Silica: An Analysis of Experimental Results," *J. Colloid Interface Sci.*, Vol. 78, No. 1, pp. 246-248.

Patankar, S.V., 1980, *Numerical Heat Transfer and Fluid Flow*, Hemisphere Publishing Corporation, Washington, DC.

Pendleton, P., and A.C. Zettlemoyer, 1984, "A Study of the Mechanism of Microporous Filling. II. Pore Filling of a Microporous Silica," *J. Colloid Interface Sci.*, Vol. 98, No. 2, pp. 439-446.

Penney, T.R., and I.L. Maclaine-cross, 1985, *Promising Advances in Desiccant Cooling*, presented at the D.O.E. Solar Buildings Conference, Washington, D.C.

Perry, R.H., and C.H. Chilton, *Chemical Engineers' Handbook*, 5th ed., McGraw-Hill Kogakusha, Ltd., Tokyo.

Pesaran, A.A., 1983, *Moisture Transport in Silica Gel Particle Beds*, PhD Thesis, University of California, Los Angeles, CA.

Pesaran, A.A., 1985, *Heat and Mass Transfer Analysis of Desiccant Dehumidifiers*, SERI Draft 252/6-5-12, Solar Energy Research Institute, Golden, CO.

Pesaran, A.A., and F. Zangrando, 1985, "Isothermal Dehumidification of Air in a Parallel Passage Configuration," *ASME Paper 85-HT-72*, 23rd ASME/AIChE National Heat Transfer Conference, Denver, CO.

Pesaran, A.A., I.L. Maclaine-cross and E. Van den Bulck, 1986, *Measurements on promising dehumifier materials and geometries*, Rep. SERI/TR-252-2898, Solar Energy Research Institute, Golden, CO.

Pla-Barby, F.E., G.C. Vliet and R.L. Panton, 1978, "Performance of Rotary Bed Silica Gel Solid Desiccant Dryers," *ASME Paper 78-HT-36*, AIAA-ASME Thermophysical and Heat Transfer Conference, Am. Soc. Mech. Engrs., New York, NY.

Polanyi, M., 1932, "Section III. - Theories of the Adsorption of Gases. A General Survey and some Additional Remarks," *Trans. Far. Soc.*, Vol. 28, pp. 316-333.

Rao, K.S., 1941, "Hysteresis in Sorption," *J. Chem. Phys.*, Vol. 45, pp. 500-539.

Rapley, C.W., and A.I.C. Webb, 1983, "Heat Transfer Performance of Ceramic Regenerator Matrices with Sine-Duct Shaped Passages", *Int. J. Heat Mass Transfer*, Vol. 26, pp. 805-814.

Reid, R.C., J.M. Prausnitz and T.K. Sherwood, 1977, *The Properties of Gases and Liquids*, 3th ed., McGraw-Hill Book Co., New York, NY.

Richards, D.R. and L.W. Florschuetz, 1986, "Forced Convection Heat Transfer to Air/Water Vapor Mixtures," *Proceedings, 8th Int. Heat Transfer Conf.*, pp. 1053-1058, also *ibid.*, 1984, *NASA Contractor Report 3769*, National Aeronautics and Space Administration, Washington, DC.

Rosas, F., 1980, *Pure Vapor Adsorption of Water on Silica Gels of Different Porosity*, MS thesis, Colorado School of Mines, Boulder, CO.

Rosen, J.R., 1952, "Kinetics of a Fixed Bed System for Solid Diffusion into Sperical Particles," *J. Chem. Physics*, Vol. 20, No. 3, pp. 387-394.

Rosen, J.B., 1954, "General Numerical Solution for Solid Diffusion in Fixed Beds," *Ind. Eng. Chem.*, Vol. 46, No. 8, pp. 1590-1594.

Roy, D., and D. Gidaspow, 1972, "A Cross Flow Regenerator - a Green's Matrix Representation," *Chem. Engng Sci.*, Vol. 27, pp. 779-793.

Ruckenstein, E., A.S. Vaidyanathan and G.R. Younquist, 1971, "Sorption by Solids with Bidisperse Pore Structure," *Chem. Engng Sci.*, Vol. 26, pp. 1305-1318.

Ruthven, D.M., 1984, *Principles of Adsorption & Adsorption Processes, pp. 124-166*, John Wiley & Sons, New York, NY.

Sakoda, A., and M. Suzuki, 1984, "Fundamental Study on Solar Powered Adsorption Cooling System," *J. Chem. Engng Japan*, Vol. 17, No. 1, pp. 52-57.

Scales, L.E., 1985, *Introduction to Non-Linear Optimization*, Springer-Verlag, New York, NY.

Schneider, P. and J.M. Smith, 1968a, "Adsorption Rate Constants from Chromatography," *AIChE Journal*, Vol. 14, No. 5, pp. 762-771.

Schneider, P. and J.M. Smith, 1968b, "Chromatographic Study of Surface Diffusion," *AIChE Journal*, Vol. 14, No. 6, pp. 886-895.

Schultz, K.J., J.W. Mitchell and W.A. Beckman, 1983, "The Performance of Desiccant Dehumidifier Air-Conditioning Systems using Cooled Dehumidifiers," *ASME Paper 83-WA/Sol-15*, ASME Winter Annual Meeting, Boston, MA.

Schultz, K.J., 1987, *Rotary Solid Desiccant Dehumdifiers, an Analysis of Models and Experimental Investigation*, PhD thesis, University of Wisconsin-Madison, Madison, WI.

Schumann, T.E.W., 1929, "Heat Transfer: A Liquid Flowing Through a Porous Prism," *J. Franklin Inst.*, Vol. 208, pp. 405-416.

Shah, R.K., 1981, "Thermal Design Theory for Regenerators," in *Heat Exchangers, Thermal-Hydraulic Fundamentals and Design*,

S. Kakac, A.E. Bergles and F. Mayinger, eds., Hemisphere Publishing Corp., Washington, DC.

Shah, R.K. and A.L. London, 1978, *Laminar Flow Forced Convection in Ducts*, in *Advances in Heat Transfer, Suppl. 1*, F.I. Thomas and J.P. Hartnett, Eds., Academic Press, New York, NY.

Schlichting, H., 1979, *Boundary Layer Theory*, 7th ed., Mc Graw-Hill Book Co., New York, NY.

Sing, K.S.W., 1982, "Reporting Physisorption Data for Gas/Solid Systems," *Pure & Appl. Chem.*, Vol. 54, No. 11, pp. 2201-2218.

Sizmann, R., D. Jung, and N. Khelifa, 1981, "Le Stockage de la Chaleur a Basse Temperature par Reactions ThermoChimiques," *Rev. Int. d'Heliotechnique*, pp. 42-51.

Stoeckli, H.F., 1977, "A Generalization of the Dubinin-Radushkevic Equation for the Filling of Heterogeneous Micropore Systems," *J. Colloid Interface Sci.*, Vol. 59, No. 1, pp. 184-185.

Solbrig, C.W. and D. Gidasbow, 1967, "Convective Diffusion in a Parallel Plate Duct with One Catalytic Wall - Laminar Flow - First Order Reaction, Part I - Analytical," *Can. J. Chem. Engng*, Vol. 45, pp. 35-39.

Taylor, R.K., 1945, "Water Adsorption Measurements on Silica Gel," *Ind. Engng Chem.*, Vol. 37, pp. 649-652.

Touloukian, Y.S., P.E. Liley and S.C. Saxena, 1970, *Thermal Conductivity, Nonmetallic Liquids and Gases, Thermophysical Properties of Matter*, Vol. 3, IFI/Plenum Data Corporation, New York, NY.

Touloukian, Y.S. and T. Makiti, 1970, *Specific Heat, Nonmetallic Liquids and Gases, Thermophysical Properties of Matter*, Vol. 6, IFI/Plenum Data Corporation, New York, NY.

Touloukian, Y.S., S.C. Saxena and P. Hestermans, 1975, *Viscosity, Thermophysical Properties of Matter*, Vol. 11, IFI/Plenum Data Corporation, New York, NY.

Van den Bulck, E., J.W. Mitchell and S.A. Klein, 1985a, "Design Theory for Rotary Heat and Mass Exchangers - I, Wave Analysis of Rotary Heat and Mass Exchangers with Infinite Transfer Coefficients," *Int. J. Heat Mass Transfer*, Vol. 28, No. 8, pp. 1575-1586.

Van den Bulck, E., J.W. Mitchell and S.A. Klein, 1985b, "Design Theory for Rotary Heat and Mass Exchangers - II, Effectiveness-Number-of-Transfer-Units Method for Rotary Heat and Mass Exchangers," *Int. J. Heat Mass Transfer*, Vol. 28, No. 8, pp. 1587-1595.

Van den Bulck, E., J.W. Mitchell and S.A. Klein, 1986, "The Use of Dehumidifiers in Desiccant Cooling and Dehumidification Systems," *J. Heat Transfer*, Vol. 108, No. 3, pp. 684-692.

Van den Bulck, E., S.A. Klein and J.W. Mitchell, 1987, "Second Law Analysis of Rotary Dehumidifiers," *J. sol. Energy Engng*, in press, also ASME Paper 85-HT-71, presented at the 23th ASME/AIChE Heat Transfer Conf., Denver. CO.

White, F.M., 1979, *Fluid Mechanics*, McGraw-Hill Book Co., New York, NY.

Zappa, R.F. and G.E. Geiger, 1971, "Effect of Artificial Surface Roughness on Heat Transfer and Pressure Drop for a High Prandtl Number Fluid in Laminar Flow," *ASME Paper No. 71-HT-36*, ASME/AIChE Heat Transfer Conf., Tulsa, OK.

APPENDIX A

HEAT AND MASS TRANSPORT IN GASES AND MICROPOROUS ADSORBENTS

The conservation equations describing the change of mass, momentum, and energy, for laminar flow of humid air through parallel plates, and for adiabatic, dynamic sorption of water vapor in regular density silica gel particles, are used for the analysis of the experimental data presented in this work. These conservation equations are supported by constitutive expressions for the transport fluxes. General expressions for the mass, momentum, and heat fluxes in gas mixtures and in porous media in terms of the transport properties of the respective media are reviewed in this appendix. These expressions also provide the unambiguous definitions of the thermal and mass diffusivity coefficients in the various media for which empirical correlations are presented in the next appendix.

A.1 The Transport Fluxes for Combined Heat and Mass Transfer in Binary Gas Mixtures in Terms of the Transport Coefficients

General expressions for the fluxes in terms of the transport coefficients are presented by Bird, Stewart and Lightfoot (1960) and this review is based upon their description.

The change of momentum of fluids is determined by the forces which act upon elementary volumes within the fluid. These forces include the internal shear stress or momentum flux, τ. For multicomponent Newtonian fluid mixtures, τ can be written in the same form as for single component fluids,

$$\tau = -\mu(\nabla \boldsymbol{V} + \nabla \boldsymbol{V}^t) + (2\mu/3 - \kappa)(\nabla \cdot \boldsymbol{V})\delta. \qquad (A.1)$$

τ is a second order tensor, $\nabla \boldsymbol{V}$ is the diadic product of the differential operator ∇ with the velocity vector $\boldsymbol{V}$, the superscript ^{t} denotes the transpose, and δ is the unit tensor. The viscosity μ is a mixture property and, at low pressure, dependent only upon temperature and mass fractions of the species. The bulk velocity κ is small and is usually neglected. For two dimensional flow with u- and v-velocity components in the x- and y-direction, respectively, τ_{yx} is the most important component of the stress tensor, representing the viscous flux of x-momentum in the y-direction,

$$\tau_{yx} = -\mu\left(\frac{\partial u}{\partial y} + \frac{\partial v}{\partial x}\right). \qquad (A.2)$$

With the boundary layer assumption for flow in the x-direction, the gradient of this flux can be expressed in the conventional form,

$$\frac{\partial \tau_{yx}}{\partial y} = -\frac{\partial}{\partial y}\left(\mu \frac{\partial u}{\partial y}\right) \qquad (A.3)$$

This form is used in the x-momentum equation for the air flow in the analysis of the present work.

The mass diffusion flux of a diffusing species w through a multicomponent fluid mixture is the sum of four separate fluxes:

$$\boldsymbol{j}_w = \boldsymbol{j}_w^{(x)} + \boldsymbol{j}_w^{(g)} + \boldsymbol{j}_w^{(P)} + \boldsymbol{j}_w^{(T)}. \tag{A.4}$$

$\boldsymbol{j}_w^{(x)}$ is the ordinary molecular diffusion flux due to gradients of the chemical potential of the species. For binary mixtures of species a and w, this flux is conventionally expressed proportional to the concentration gradient,

$$\boldsymbol{j}_w^{(x)} = -\rho D_{aw} \nabla \omega, \tag{A.5}$$

in which ω is the mass fraction of the diffusing species, ρ is the density of the mixture, and D_{aw} is the binary diffusion coefficient or mass diffusivity. For gas mixtures at low pressure, D_{aw} is inversely proportional to the pressure, increases with temperature, and is almost independent of the composition.

$\boldsymbol{j}_w^{(g)}$ is the forced diffusion flux generated by external forces other than gravity and which act on the individual species. This flux appears in ionic systems in the presence of an electrical field. If gravity is the only force, $\boldsymbol{j}_w^{(g)}$ is identically zero.

$j_w^{(P)}$ is the pressure diffusion term. It represents the migration of the species due to pressure gradients, and is proportional to the gradient of the total pressure. This flux is important only for systems in which large pressure gradients are created artificially, such as centrifugal separators.

$j_w^{(T)}$ is the thermal diffusion term and represents the diffusion of species due to temperature gradients. This effect, known as the Soret effect, is generally very small, although industrial applications exist in thermal diffusion columns. For binary gas mixtures the thermal diffusion flux is written in terms of an additional diffusion property,

$$j_w^{(T)} = -\rho D_{aw} \alpha_T \omega(1-\omega) \nabla \ln(T), \qquad (A.6)$$

in which α_T is the thermal diffusion factor. α_T is almost independent of the mixture composition and is usually very small, e.g. for air-water vapor mixtures ranges from 0.01 to 0.03.

For the present work, gravity is the only external force. Two dimensional flow in association with the boundary layer assumption is accepted for which the pressure gradient is directed in the x-direction. The gradient of the pressure diffusion flux is thus directed parallel with the flow, and is therefore neglected as part of the boundary layer assumption, in which axial diffusion terms are negligible compared to convective changes. The thermal diffusion flux is less than 1% of

the ordinary diffusion flux. The total mass flux can thus be modeled with good accuracy by the conventional form of Fick's first law of binary diffusion,

$$\boldsymbol{j}_w = -\rho D_{aw} \nabla \omega \ . \tag{A.7}$$

The divergence of this flux is the local rate of change of mass of the species w due to diffusion, and with the boundary layer approximation is, written as:

$$\nabla \cdot \boldsymbol{j}_w = -\frac{\partial}{\partial y}(\rho D_{aw} \frac{\partial \omega}{\partial y}) \ . \tag{A.8}$$

This form is used in the continuity equation for the water vapor in the analysis presented in this work.

For mixtures, the local heat flux $\boldsymbol{q}$ has to be interpreted as a total energy flux, consisting of contributions from heat conduction, enthalpy transport by the interdiffusion of the various species, and the Dufour effect. These terms are additive, i.e.,

$$\boldsymbol{q} = \boldsymbol{q}^{(T)} + \boldsymbol{q}^{(d)} + \boldsymbol{q}^{(x)} \ . \tag{A.9}$$

$\boldsymbol{q}^{(T)}$ is the energy flux due to conduction. For single component fluids, this is the only contribution. For fluid mixtures, the expression for the conductive heat flux is retained,

$$q^{(T)} = -k\nabla T, \tag{A.10}$$

in which k is the local thermal conductivity of the mixture. For gaseous mixtures at low pressure, k increases with temperature, and varies with the mixture composition.

$q^{(d)}$ is the enthalpy flux caused by the migration of species through a nonuniform temperature field. For a binary mixture of species a and w, an energy balance on an elementary control volume shows,

$$q^{(d)} = (i_w - i_a)\, j_w, \tag{A.11}$$

where i_w and i_a are the partial molal enthalpies of the two species, respectively.

$q^{(x)}$ is the Dufour energy flux, associated with the diffusion-thermo effect. The general expression for this flux is extremely complex; however, for dilute binary mixtures of ideal gases, Bird, Curtiss and Hirschfelder (1955) established the following expression,

$$q^{(x)} = P\left(\frac{1}{\rho_a} + \frac{1}{\rho_w}\right) k_T\, j_w \tag{A.12}$$

where P is the total pressure, ρ_a and ρ_w are the densities of the two species, j_w is the mass diffusion flux, and k_T is the thermal diffusion ratio. k_T is related to the thermal diffusion factor α_T,

$$k_T = \alpha_T x_w(1-x_w) \qquad \text{(A.13)}$$

where x_w is the molar concentration of species w. The Dufour energy flux and the thermal diffusion flux are related through Onsager's reciprocal principle.

In the present work, the Dufour energy flux is less than 1% of the conductive energy flux and is therefore neglected. The divergence of the local energy flux contributes to the rate of change of the local energy density. For two-dimensional flow with the boundary layer assumption, the divergence can be approximated by:

$$\nabla\cdot\boldsymbol{q} = -\frac{\partial}{\partial y}\left(k\frac{\partial T}{\partial y}\right) + (c_{p,w}-c_{p,a})\,\boldsymbol{j}_w\nabla T + (i_w-i_a)\nabla\cdot\boldsymbol{j}_w. \qquad \text{(A.14)}$$

The last term of this equation represents the local volumetric rate of energy increase due to the volumetric rate of change of mass, Eq.(A.8), and drops out in the complete form of the energy conservation equation used in the analysis presented in this work.

A.2 The Transport Fluxes for Combined Heat and Mass Transfer in Porous Media in Terms of the Transport Coefficients

The diffusion mechanisms within porous adsorbents are generally categorized in the groups of micropore and macropore diffusion and are described in the reference work by Ruthven

(1984). The review presented in this appendix follows his description.

In micropore diffusion, the transport of the individual adsorbate molecules is controlled by the force field of the adsorbent surface. Within the group of microporous diffusion mechanisms, surface diffusion is most frequently occurring. The molecules of the adsorbed phase move along the surface of the adsorbent pores by jumping between neighboring adsorption sites. The diffusion process thus describes the mass transport within the adsorbed liquid layer. The mass diffusion flux per unit internal particle area is conventionally expressed as proportional to the gradient of the local sorbate mass concentration W_d,

$$j_W = -(1-\varepsilon_p)\,\rho_s \frac{D_S}{\tau_S} \nabla W_d, \qquad \text{(A.15)}$$

where ε_p is the volumetric porosity of the adsorbent, ρ_s is the density of the dry solid phase, and W_d is the mass of the adsorbed phase per unit dry adsorbent mass. D_S is the surface diffusion coefficient and τ_S is the particle tortuosity depending only upon the geometry of the internal pores of the sorbent particle. τ_S is 1 for a straight, cylindrical pore; 3 for straight, randomly oriented, cylindrical pores; and ranges from 2 to 6 in general. Experimental dynamic sorption data yield only the effective surface diffusion coefficient which is defined as:

$$D_{S,e} = \frac{D_S}{\tau_S}. \tag{A.16}$$

The surface diffusion coefficient is often correlated as a function of the temperature in terms of an Arrhenius expression,

$$D_S = D_{S,o} \exp(-\beta \frac{Q_{st}}{RT}), \tag{A.17}$$

in which Q_{st} is the isosteric heat of adsorption. $D_{S,o}$ and β are constants depending upon the nature the sorptive and sorbent, and β is less than 1.

Macropore diffusion involves the molecular transport within the gas phase and includes molecular diffusion, Knudsen diffusion and Poiseuille flow. Molecular diffusion is ordinary diffusion of the adsorptive within the gas phase. The driving forces arise from gradients in concentration, or chemical potential, of the adsorptive. If the mean free path of the gas molecules is small compared to the diameter of the adsorbent pores, collisions between the individual molecules of the adsorptive are predominant. However, if the mean free path length is larger, collisions between the gas molecules and the pore walls occur more frequently and the process is then referred to as Knudsen diffusion. For Knudsen diffusion, the resistance to molecular transport is different from ordinary diffusion. Poiseuille flow is generated by gradients of total

pressure across the external surface of the adsorbent particles. The flow within the pores is viscous, low Reynolds number flow. The various fluxes within the gas phase occur independent from each other and are additive. Thus, the mass flux of the adsorptive *w* per unit particle area through the pores of the adsorbent can be written as:

$$j_w = j_w^{(x)} + j_w^{(K)} + j_w^{(P)} \tag{A.18}$$

where the superscripts refer to the three individual diffusion mechanisms in the gas phase. The ordinary molecular flux in macropore diffusion is proportional to the gradient of the sorbate concentration in the gas phase and the expression for the flux is identical to that of ordinary diffusion in the gas phase. For a binary gas mixture of species *a* and *w*, the expression is:

$$j_w^{(c)} = -\varepsilon_p \rho \frac{D_{aw}}{\tau} \nabla \omega. \tag{A.19}$$

The rate of Knudsen diffusion is determined by the collisions of the gas molecules with the pore walls, and can be estimated with the kinetic theory of gases. Knudsen's law of diffusion is written as:

$$j_w^{(K)} = -\varepsilon_p \rho \frac{D_K}{\tau_K} \nabla \omega, \tag{A.20}$$

where D_K is the Knudsen diffusion coefficient, given by the theoretical expression:

$$D_K = \frac{d_p}{3}\left[\frac{8RT}{\pi M}\right]^{0.5} \tag{A.21}$$

in which d_p is the pore diameter and M is the molecular weight of the diffusing species w.

Pouseuille flow is described by the classical theory of Hagen-Poiseuille for laminar, viscous flow through cylindrical channels. The mass flux is proportional to the gradient of the total pressure,

$$j_w^{(P)} = -\frac{\varepsilon_p \rho d_p^2}{32\mu\tau}\nabla P. \tag{A.22}$$

Ruthven (1984) has shown by an order of magnitude analysis that the contribution of Poisseuille flow to the total mass flux is negligible for pores with diameters less than 10^{-8} m. For microporous adsorbents such as regular density silica gel, the average pore diameter is 22×10^{-10} m and thus the Poisseuille flux can be neglected. The mean free path length of hard sphere molecules at atmospheric pressure can be estimated with the kinetic theory of gases and is about 10^{-7} m for water molecules at room temperatures. This length is much larger than the average pore diameter of microporous adsorbents. Thus Knudsen diffusion is the dominant transport mechanism and

molecular diffusion does not occur. The total flux of the adsorptive through a microporous adsorbent is then given by:

$$\boldsymbol{j}_w = -\varepsilon_p \rho D_{K,e} \nabla \omega, \tag{A.23}$$

where $D_{K,e}$ is the effective Knudsen diffusion coefficient,

$$D_{K,e} = \frac{D_K}{\tau_K}, \tag{A.24}$$

and D_K is given by Eq. (A.21)

The total mass flux per unit particle area is the sum of the mass fluxes of the adsorptive and the adsorbate,

$$\boldsymbol{j} = \boldsymbol{j}_w + \boldsymbol{j}_W. \tag{A.25}$$

The local change of mass of the water within the sorbent particle is determined by the divergence of the flux field $\boldsymbol{j}$. The continuity equation for an isothermal particle is analogous to the continuity equation of a stagnant binary gas mixture. The total effective diffusivity D_{sw},

$$D_{sw} = \frac{\dfrac{\varepsilon_p \rho D_{K,e}}{(1-\omega)} + (1-\varepsilon_p)\rho_s \left.\dfrac{\partial W}{\partial \omega}\right)_T D_{S,e}}{\dfrac{\varepsilon_p \rho}{(1-\omega)} + (1-\varepsilon_p)\rho_s \left.\dfrac{\partial W}{\partial \omega}\right)_T}, \tag{A.26}$$

is analogous to the binary diffusion coefficient D_{aw} in (Eq. A.7), and their values can be directly compared for estimating characteristic response times. Note, however, that this

effective diffusivity is a mass average diffusivity and should not be used to directly compare the relative magnitude of the diffusion fluxes in the particle and in the air stream.

The local energy flux within the adsorbent particle is the sum of the conductive energy flux and the transport of enthalpy by the diffusing species,

$$\boldsymbol{q} = \boldsymbol{q}^{(T)} + \boldsymbol{q}^{(d)}. \tag{A.27}$$

$\boldsymbol{q}^{(T)}$ is the conductive energy flux and is expressed in terms of the temperature field by Fourier's law,

$$\boldsymbol{q}^{(T)} = -k\nabla T \tag{A.28}$$

where k is the local thermal conductivity. k is determined by the material of the adsorbent, increases with the sorbate concentration, and varies slightly with temperature. The thermal conductivity of the solid adsorbent is generally an order of magnitude larger than the thermal conductivity of the gaseous adsorptive.

$\boldsymbol{q}^{(d)}$ represents the energy transported by the species migration through a nonuniform temperature field, and can be obtained from an energy balance on an elementary control volume within the adsorbent particle. For the adsorption of a species w within a binary gas mixture $a + w$, $\boldsymbol{q}^{(d)}$ is given by:

$$\mathbf{q}^{(d)} = i_w \mathbf{j}_w + I_W \mathbf{j}_W. \qquad \text{(A.29)}$$

where the mass fluxes are given by Eqs. (A.15) and (A.23). i_w and I_W are the partial molal enthalpy of the species w in the gas phase and adsorbed phase, respectively. This expression assumes that the species a is stagnant within the pores of the sorbent. The divergence of this vector expression is used in the equation of change of energy in the analysis of the present work.

APPENDIX B

THERMO-PHYSICAL PROPERTIES OF HUMID AIR AND REGULAR DENSITY SILICA GEL

Constitutive expressions for the transport fluxes in binary gas mixtures and microporous adsorbents in terms of the transport coefficients are presented in the previous appendix. Mass, momentum and thermal diffusivities are defined for the various fluxes. These coefficients are material properties and, for a given gas mixture or sorbent-sorptive pair, are dependent upon temperature, pressure and mass concentrations. Reliable data for the transport properties are usually derived from specific experiments. In this appendix, correlations for the thermo-physical transport properties of air-water vapor mixtures and regular density silica gel are retrieved from the literature and presented.

B.1 Thermo-Physical Properties of Air - Water Vapor Mixtures

The conservation and transport equations modeling the air flow incorporate the density, specific heat, viscosity, mass diffusivity, thermal diffusivity, and thermal conductivity of the humid air mixture and of the individual components. As usual, the bulk viscosity is not considered as an important property in conventional engineering applications. The mixture

properties are obtained from the pure component properties using standard mixing rules and standard relationships for estimating the component properties as functions of temperature and pressure.

Dry Air

The density of dry air ρ_a is computed with the ideal gas law as recommended for air at low pressures in the standard Gas Tables (Keenan, Chao and Kaye, 1983). The specific gas constant for standard dry air is 287.031 J/kg·K. The specific heat $c_{p,a}$ is calculated with the polynomial expression for specific heat as function of the temperature, given by Touloukian and Makita (1970),

$$c_{p,a}\ [\text{J/kg·K}] = 4184\,(0.249679 - 7.55179\text{x}10^{-5}\,T + 1.69194\text{x}10^{-7}\,T^2 - 6.46128\text{x}10^{-11}\,T^3)\,. \qquad \text{(B.1)}$$

The enthalpy of the air i_a is obtained from the integral of the specific heat with respect to the absolute temperature T, and referred to a zero value at 0°C. Values computed with this polynomial expression have been compared with numerical values listed in the Gas Tables (Keenan, Chao and Kaye, 1983) and indicate agreement well within the accuracy of the formula, ± 1%.

The thermal conductivity k_a and viscosity μ_a of dry air are calculated by linear interpolation between table values

published, respectively, by Touloukian, Liley and Saxena (1970) and Touloukian, Saxena and Hestermans (1975). Values are listed in these reference sources with 10 K intervals and have accuracies of ± 1% for conductivity and ± 2% for viscosity. Table B.1 lists computed or retrieved values for the specific heat, dynamic viscosity and thermal conductivity of dry air at low pressure as a function of temperature. The effect of pressure on these thermo-physical properties is neglected.

Dry Steam

The properties of dry steam are computed using the most recent relationships accepted as standards by the International Association for the Properties of Steam (IAPS). The density of

Table B.1 Selected thermo-physical properties of dry air at low pressures

T	$c_{p,a}$	μ_a	k_a	D_{aw}
K	J/kg·K	10^{-5} kg/m·s	10^{-3} W/m·K	10^{-5} m^2/s
270	1005.6	1.707	23.84	2.18
280	1005.8	1.757	24.61	2.32
290	1006.0	1.805	25.38	2.46
300	1006.3	1.853	26.14	2.60
310	1006.7	1.900	26.87	2.75
320	1007.2	1.946	27.59	2.90
330	1007.8	1.992	28.30	3.06
340	1008.4	2.037	29.00	3.22
350	1009.2	2.081	29.70	3.38
360	1010.0	2.125	30.39	3.54
370	1011.0	2.168	31.07	3.71
380	1012.0	2.211	31.37	3.88

water vapor ρ_w is computed with the ideal gas law as recommended in the NBS/NRC Steam Tables (Haar, Gallagher and Kell, 1984) for steam at low pressures. The specific gas constant for steam is 461.522 J/kg·K. The specific heat $c_{p,w}$ and enthalpy i_w are computed from the polynomial expression for the Gibb's free energy as a function of temperature for the ideal gas state (Steam Tables, 1984). Corrections for nonideal behavior with pressure are neglected because of the low vapor pressure of water at room temperatures. The accuracy of specific heat and enthalpy is estimated at ± 1%. The thermal conductivity k_w and viscosity μ_w are computed using the standard IAPS correlations presented by Kestin (1978, 1976). The claimed accuracy is ± 2% for conductivity and ± 1% for viscosity. The correlations presented in these reference sources are quite complicated and are therefore not repeated in this text. Table B.2 lists the specific heat, viscosity and thermal conductivity of dry steam at low pressure, and the specific heat of liquid water, c_w.

Air-Water Vapor

Density ρ, specific heat c_p, and enthalpy h of moist air are computed assuming a perfect mixture of standard dry air and water vapor, i.e., a mass-fraction weighted average of the pure component properties is used. The transport properties, thermal conductivity k and viscosity μ, are computed using the

Table B.2 Selected thermo-physical properties of dry steam at low pressures and liquid water

T	$c_{p,w}$	μ_w	k_w	c_w
K	J/kg·K	10^{-5} kg/m·s	10^{-3} W/m·K	J/kg·K
270	1858.4	0.914	16.26	4214
280	1860.3	0.938	16.98	4197
290	1862.4	0.964	17.70	4185
300	1864.8	0.992	18.44	4179
310	1867.4	1.022	19.20	4176
320	1870.3	1.053	19.96	4177
330	1873.5	1.085	20.74	4182
340	1876.9	1.118	21.53	4188
350	1880.5	1.152	22.33	4197
360	1884.4	1.187	23.15	4206
370	1888.5	1.223	23.98	4216
380	1892.7	1.260	24.82	4227

mixing principles of Saxena (Reid, Prausnitz and Sherwood, 1977) which are based upon the Chapman-Enskog kinetic theory of gases,

$$\mu = \frac{x_a}{x_a + \psi_w x_w}\mu_a + \frac{x_w}{x_w + \psi_a x_a}\mu_w,$$

$$k = \frac{x_a}{x_a + \phi_w x_w}k_a + \frac{x_w}{x_w + \phi_a x_a}k_w. \qquad \text{(B.2)}$$

Values for the mixing coefficients are $\psi_w = 0.8390$, $\psi_a = 0.7438$, $\phi_w = 0.8153$, and $\phi_a = 0.7257$, respectively. These values are taken from Richards and Florschuetz (1986), and are derived from available experimental values for the mixture viscosity and conductivity.

The binary diffusion coefficient D_{aw} and the thermal diffusion α_T of air-water vapor mixtures are taken from Mason and Monschick (1965). The accuracy of the transport properties is estimated at ± 2%. The diffusion coefficient retrieved from this reference is listed in Table B.1 for a range of temperatures and for atmospheric pressure. D_{aw} is inversely proportional to the absolute pressure. α_T ranges from 0.01 to 0.03 and increases with temperature and water vapor mass fraction.

For an engineering estimate of characteristic response times, the following diffusivities are defined at 25°C, atmospheric pressure and 0.015 kg-water/kg-dry-air: the kinematic viscosity is 1.57×10^{-5} m^2/s, the thermal diffusivity is 2.19×10^{-5} m^2/s, and the mass diffusivity is 2.58×10^{-5} m^2/s. These diffusivities yield a Prandl number of 1.57/2.19 = 0.72, a Schmidt number of 1.57/2.58 = 0.61 and a Lewis number of 2.19/2.58 = 0.85.

B.2 Thermo-Physical Properties of Regular Density Silica Gel

The mass and energy equations modeling adiabatic, dynamic sorption processes require expressions for the mass and energy fluxes in terms of the material properties. Definitions of the thermal and mass diffusivities are presented in the previous

appendix. Also, the density and specific heat of the sorbent are needed. These thermo-physical properties are presented in this section for regular density silica gel and water vapor.

The density of pure silica, i.e., clear fused quartz, is ρ_s = 2200 kg/m^3 (CRC Handbook of Chemistry and Physics, 1980). The density of a R.D. silica particle is reported by the manufacturer, ρ_p = 1200 kg/m^3. The porosity of a porous particle is defined as the ratio of the pore volume to total volume,

$$\varepsilon_p = \frac{V_p}{V_s + V_p} = 1 - \frac{\rho_p}{\rho_s}, \tag{B.3}$$

and is 0.45 for R.D. silica gel. This value yields a pore volume of 0.38×10^{-3} m^3/kg-dry-silica, which compares very well with the maximum sorption capacity for water, 0.36 kg-water/kg-dry-silica, obtained independently from the Dubinin-Polanyi sorption isotherm presented in Chapter 3 of this thesis.

The specific heat of R.D. silica gel c has been determined experimentally with a calorimeter (Bjurstroem and Carlson, 1983) and their data are represented with a polynomial expression in terms of the absolute temperature and the water content of the gel,

$$\begin{aligned} c\ [\mathrm{J/kg \cdot K}] = {} & 833 + 1.578(T-273.15) \\ & + W(3992 + 5.526(T-273.15) - 219W + 3303W^2) \end{aligned} \tag{B.4}$$

This equation agrees with an average value reported by Allander (1953), 1250 J/kg·K. The value of dry silica gel at room temperature is in between the value reported by the manufacturer, 920 J/kg·K, and the value for fused quartz, 750 J/kg·K. Bjurstroem and Carlson's equation (B.4) can be expressed in a linear form,

$$c\ [\mathrm{J/kg{\cdot}K}] = 917 + 1.578(T-273.15) + W(2177 + 0.091(T-273.15)) \qquad (B.5)$$

which correlates with Eq. (B.4) with $r^2 = 97\%$. In this linear form, the dry silica value does agree with the manufacturer's data, however, the coefficient of W does not match the specific heat of liquid water, $c_w \approx 4186$ J/kg·K. Equation (B.5) may reflect that the physical state of adsorbed water is different from that of liquid water in the bulk state. This explanation is reasonable, although not supported by existing data or theories within the author's knowledge. Equation (B.5) is accepted to express the specific heat of dry silica gel, c_s,

$$c_s\ [\mathrm{J/kg{\cdot}K}] = 917 + 1.578(T-273.15). \qquad (B.6)$$

The specific heat of liquid water, c_w, is retrieved from Touloukian and Makita (1970), and is written as a polynomial expression in T,

$$c_w = 4184(2.13974 - 9.68137\times10^{-3}T + 2.68536\times10^{-5}T^2 - 2.42139\times10^{-8}T^3 \qquad (B.7)$$

The specific heat of wet silica gel is the mass-fraction weighted sum of the specific heats of dry silica and liquid water, and is based upon a unit mass of dry desiccant:

$$c = c_s + W_d c_w \tag{B.8}$$

The integral of Eq. (B.6) with respect to temperature yields the specific enthalpy of dry silica gel, I_s. The integral of Eq. (B.7) gives the enthalpy of liquid water I_w with a constant added to refer to a zero value at 0°C. The enthalpy of wet silica gel is written as:

$$I = I_s + W_d I_w - I_{ads}. \tag{B.9}$$

The partial molal enthalpy of the adsorbed water is the derivative of I with respect to the desiccant water content,

$$I_W = \left.\frac{\partial I}{\partial W_d}\right|_T = I_w - A \tag{B.10}$$

I_{ads} is the net integral heat of adsorption which is the integral of the net differential heat of adsorption, A, with respect to the desiccant water content. A is the adsorption potential in the Dubinin-Polanyi isotherm expression. The total differential heat of adsorption, Q_{st}, is the difference between the enthalpies of the water in the gas phase and adsorbed phase,

$$Q_{st} = i_w - I_W \tag{B.11}$$

The theoretical expression for the Knudsen diffusion coefficient is given by:

$$D_K = \frac{d_p}{3}\left[\frac{8RT}{\pi M}\right]^{0.5}. \qquad \text{(B.12)}$$

The pore diameter of regular density silica gel is $22\text{x}10^{-10}$ m and the molecular weight of water is 18.015. The Knudsen diffusion coefficient for water vapor and regular density silica gel can thus be written as:

$$D_K\ [\text{m}^2/\text{s}] = 4.15\text{x}10^{-7}\sqrt{(T/273.15)}, \qquad \text{(B.13)}$$

where T is the absolute temperature. The tortuosity factor τ_K has been investigated by A. Pesaran (1983) based upon a literature review, and an average value of 2.8 was proposed. This value compares with the theoretical value of 3.0 for an assembly of straight, randomly oriented, cylindrical pores and is accepted for the analysis in this work. The effective Knudsen diffusivity is then:

$$D_{K,e}\ [\text{m}^2/\text{s}] = 1.50\text{x}10^{-7}\sqrt{(T/273.15)}. \qquad \text{(B.14)}$$

The theoretical expression for the surface diffusion coefficient is:

$$D_{S,e} = D_{S,o}\exp(-\beta\frac{Q_{st}}{RT}), \qquad \text{(B.15)}$$

in which Q_{st} is the isosteric heat of adsorption, Eq. (B.11). The parameter β was also investigated by A. Pesaran (1983) as part of a literature survey, and 0.45 was retrieved from an accepted theory. This value is also accepted for this analysis. The coefficient $D_{S,e}$ needs to be obtained from experimental data. Two publications (Allander, 1953; Chihara and Suzuki, 1983) exist in which experimental values for the effective surface diffusivity for water vapor and R.D. silica gel are presented. The mass diffusivity is obtained from an analytical solution of the sorbate-mass conservation equation,

$$\frac{\partial W}{\partial \theta} = D_{S,e} \nabla^2 W \qquad \text{(B.16)}$$

in comparison with a series of quasi-isothermal, dynamic sorption experiments on a siliga gel particle with a small step change in water vapor pressure as the driving potential. Figure B.1 shows the experimental values of ln $D_{S,e}$ vs. $-Q_{st}/RT$ for both publications. The experimental values can be curve fitted by Eq. (B.15) with a least squares procedure in $D_{S,o}$ and $\beta = 0.45$. The results are $D_{S,o} = 2.23 \times 10^{-6}$ m^2/s with $r^2 = 92\%$ for Allander's data, and $D_{S,o} = 1.95 \times 10^{-7}$ m^2/s with $r^2 = 44\%$ for Chihara's data. However, Chihara and Suzuki (1983) report that their values are at least a factor 2 to 3 too low to agree with an analysis of pressure swing sorption experiments. Furthermore, their dynamic sorption experiments did not carefully

approach quasi-isothermal conditions. Haul and Stremming (1984) showed both experimentally and analytically that for non-isothermal, dynamic sorption experiments, the effective diffusion coefficient computed from Eq. (B.16) may be too low by a factor of 5 to 10. The effect of non-isothermal conditions may explain the large scatter of Chihara's data in Fig. B.1 and the difference with Allander's data. Allander (1953) experimentally verified the assumption of isothermal sorption for his experiments and his data are used in the analysis of the present work. The effective surface diffusivity including tortuosity effects can then be written as:

$$D_{S,e}\ [m^2/s] = 2.23 \times 10^{-6} \exp(-0.45 \frac{Q_{st}}{RT}), \qquad (B.17)$$

The thermal conductivity of regular density silica gel was experimentally determined by Bjurstroem, Karawacki and Carlsson (1984). These authors carefully distinguished between the conductivity of a single desiccant particle and that of a packed bed assembly. They determined the effect of temperature and gel-water content, and their data can be represented with a linear equation in T and W,

$$k\ [W/m \cdot K] = 0.37 + 0.97\, W + 0.0014\, (T-273.15). \qquad (B.18)$$

This equation agrees with the average experimental value reported by Allander (1953), 0.81 W/m·K. Equation (B.18) is used in the analysis of this work.

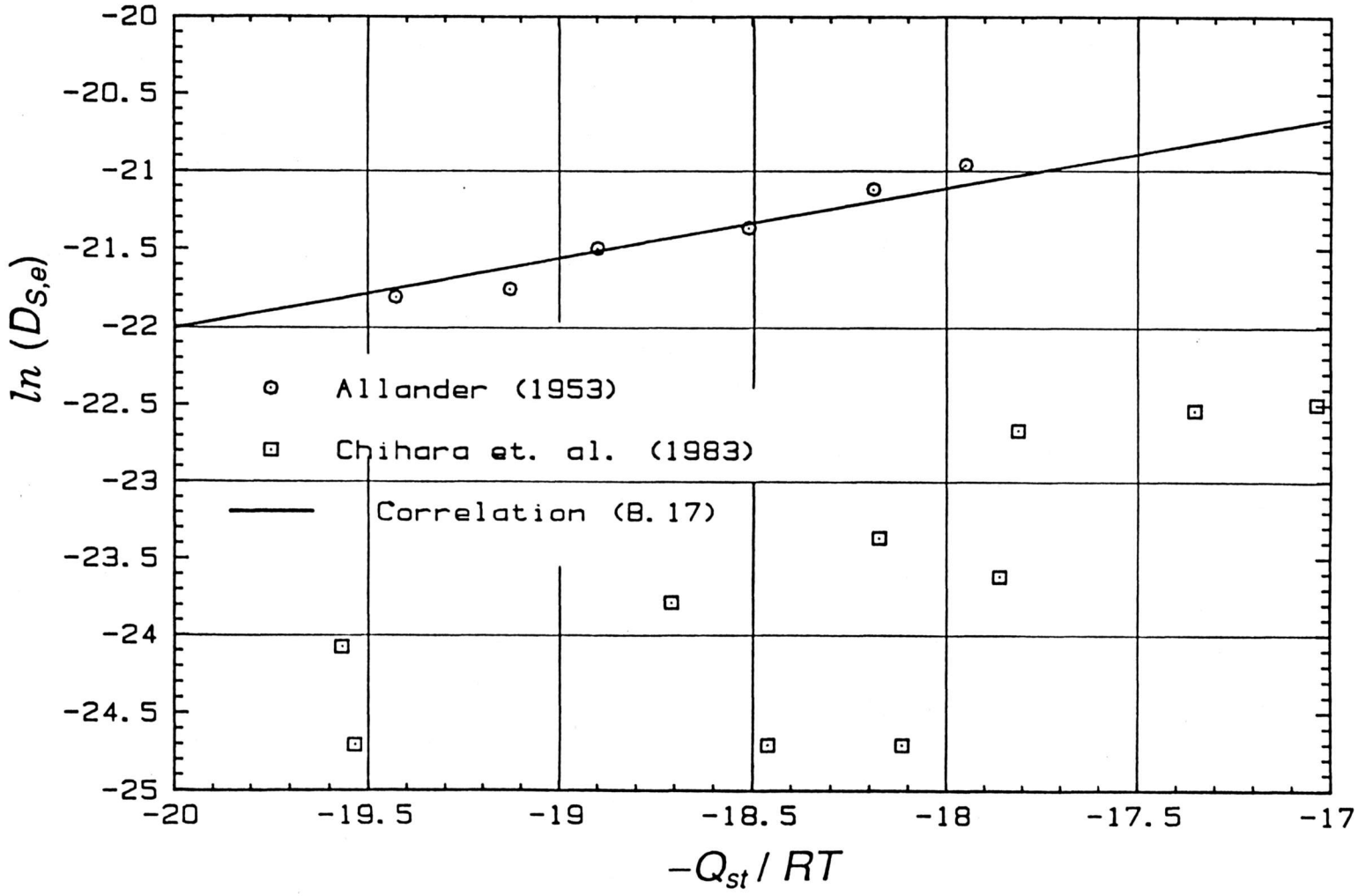

Figure B.1 Effective surface diffusivity of R.D. silica gel and water.

The thermal and mass diffusivities can be computed and, for 25°C, atmospheric pressure and 0.015 kg-water-vapor/kg-dry-air, are 2.8×10^{-7} m^2/s and 6.8×10^{-10} m^2/s, respectively. The Lewis number *Le* for the silica gel particle is 410! For typical sorption processes on R.D. silica gel, the internal temperature distribution develops about 500 to 1000 times faster than the water load distribution.

APPENDIX C

GRAPHICAL PRESENTATION OF EXPERIMENTAL RESULTS

C.1 Pressure Drop Experiments, Series P

Tables C.1.1 - C.1.4 list the pressure drop across the test matrix as a function of the process air mass flow rate for constant inlet and initial states.

Table C.1.1 Experimental results for Experiment P1-1. Data recorded on 12/23/1985 at 20:48:03.

#	t_f	w_f	P	ΔP	$\dot{m}_f$
	(°C)	(kg/kgDA)	(Pa)	(Pa)	(kgDA/s)
69	22.63	0.00335	83112	9.2	0.00199
72	22.54	0.00336	83117	19.1	0.00403
81	22.42	0.00331	83166	28.9	0.00601
72	22.23	0.00327	83162	39.6	0.00809
72	22.15	0.00330	83143	50.2	0.01009
85	22.05	0.00329	83142	60.8	0.01206
75	21.95	0.00325	83147	72.0	0.01408
76	21.82	0.00320	83144	83.1	0.01605
77	21.71	0.00315	83134	95.0	0.01813
92	21.66	0.00317	83140	106.5	0.02004
81	21.63	0.00319	83133	118.8	0.02207
82	21.63	0.00320	83120	131.4	0.02409
71	21.62	0.00316	83132	144.6	0.02615
81	21.63	0.00316	83139	157.8	0.02819
89	21.65	0.00314	83161	170.6	0.03007
75	21.75	0.00318	83151	184.8	0.03209
76	21.91	0.00321	83149	200.5	0.03413
83	22.07	0.00321	83154	216.2	0.03613
70	22.24	0.00320	83147	232.8	0.03824
95	22.40	0.00321	83138	248.7	0.04016
70	22.68	0.00323	83139	265.7	0.04218
73	22.99	0.00327	83102	283.9	0.04421
75	23.31	0.00327	83105	302.3	0.04628
71	23.62	0.00323	83090	315.1	0.04758

Table C.1.2 Experimental results for Experiment P1-2. Data recorded on 1/13/1986 at 19:44:49.

#	t_f	w_f	P	ΔP	$\dot{m}_f$
	(°C)	(kg/kgDA)	(Pa)	(Pa)	(kgDA/s)
91	24.89	0.00325	83002	28.7	0.00579
94	24.72	0.00325	83008	39.0	0.00782
81	24.51	0.00322	83002	48.9	0.00971
96	24.42	0.00315	83015	59.7	0.01170
88	24.38	0.00307	83019	70.8	0.01371
79	24.38	0.00299	82983	82.3	0.01570
76	24.41	0.00290	82991	93.7	0.01766
86	24.50	0.00282	82978	105.6	0.01963
77	24.62	0.00274	83002	117.5	0.02158
76	24.67	0.00266	82981	130.9	0.02370
82	24.64	0.00268	82958	143.3	0.02558
77	24.58	0.00268	82955	156.6	0.02759
91	24.51	0.00255	82980	170.6	0.02967
93	24.46	0.00248	82988	183.7	0.03156
72	24.43	0.00240	82989	199.1	0.03357
88	24.48	0.00233	82999	214.1	0.03548
92	24.54	0.00228	83015	229.8	0.03748
79	24.61	0.00222	82994	246.6	0.03955
99	24.69	0.00216	82953	262.5	0.04146
75	24.78	0.00212	82971	281.9	0.04371
76	24.90	0.00207	83002	297.5	0.04547
66	25.06	0.00203	83001	312.4	0.04708

Table C.1.3 Experimental results for Experiment P1-3. Data recorded on 1/13/1986 at 21:46:50.

#	t_f	w_f	P	ΔP	$\dot{m}_f$
	(°C)	(kg/kgDA)	(Pa)	(Pa)	(kgDA/s)
99	21.77	0.00155	82774	19.1	0.00385
68	22.45	0.00146	82777	24.1	0.00484
84	21.66	0.00154	82749	28.8	0.00581
87	22.53	0.00146	82780	34.0	0.00676
71	22.33	0.00146	82785	39.1	0.00777
82	21.50	0.00152	82758	38.9	0.00778
65	22.18	0.00144	82812	44.2	0.00876
99	22.68	0.00145	82794	44.5	0.00877
99	21.43	0.00151	82744	49.7	0.00980
85	22.84	0.00145	82776	55.0	0.01073
82	21.44	0.00149	82777	59.8	0.01172
92	23.01	0.00145	82783	66.0	0.01271
92	21.53	0.00147	82775	70.6	0.01368
87	23.15	0.00145	82783	77.5	0.01475
80	21.70	0.00147	82783	82.5	0.01573
72	23.27	0.00146	82743	89.0	0.01669
79	21.94	0.00146	82780	93.8	0.01763
99	23.29	0.00145	82790	101.0	0.01871
81	22.32	0.00145	82770	105.8	0.01963
86	23.15	0.00144	82769	112.8	0.02064
73	22.83	0.00145	82805	118.7	0.02164

Table C.1.4 Experimental results for Experiment P2-1. Data recorded on 1/14/1986 at 19:25:34.

#	t_f	w_f	P	ΔP	$\dot{m}_f$
	(°C)	(kg/kgDA)	(Pa)	(Pa)	(kgDA/s)
98	23.79	0.00221	82782	8.2	0.00596
79	23.83	0.00217	82767	11.0	0.00787
90	23.82	0.00215	82789	14.3	0.00994
80	23.76	0.00212	82791	17.1	0.01193
76	23.65	0.00211	82792	20.2	0.01392
82	23.56	0.00210	82780	23.2	0.01589
76	23.42	0.00209	82721	26.7	0.01792
89	23.31	0.00209	82718	30.2	0.01999
87	23.23	0.00209	82705	33.5	0.02187
80	23.23	0.00209	82678	36.7	0.02383
73	23.28	0.00209	82690	40.5	0.02589
80	23.34	0.00210	82704	44.3	0.02789
77	23.41	0.00210	82723	48.1	0.02986
81	23.50	0.00211	82740	51.7	0.03186
83	23.60	0.00211	82732	55.7	0.03394
75	23.71	0.00212	82720	59.8	0.03595
79	23.84	0.00213	82694	64.5	0.03788
85	24.00	0.00214	82724	68.3	0.03991
77	24.18	0.00215	82705	73.1	0.04190
75	24.36	0.00215	82656	76.8	0.04378
74	24.59	0.00215	82676	82.1	0.04595
86	24.85	0.00215	82708	87.5	0.04794
87	25.11	0.00215	82707	92.5	0.04977

C.2 Dynamic, Adiabatic Sorption Experiments with Varying Process Inlet and Initial States, Series I.

Figures C.2.1.a - C.2.8.b show the process air inlet and outlet temperature and humidity ratio as a function of time for constant mass flow rate and varying initial and inlet conditions.

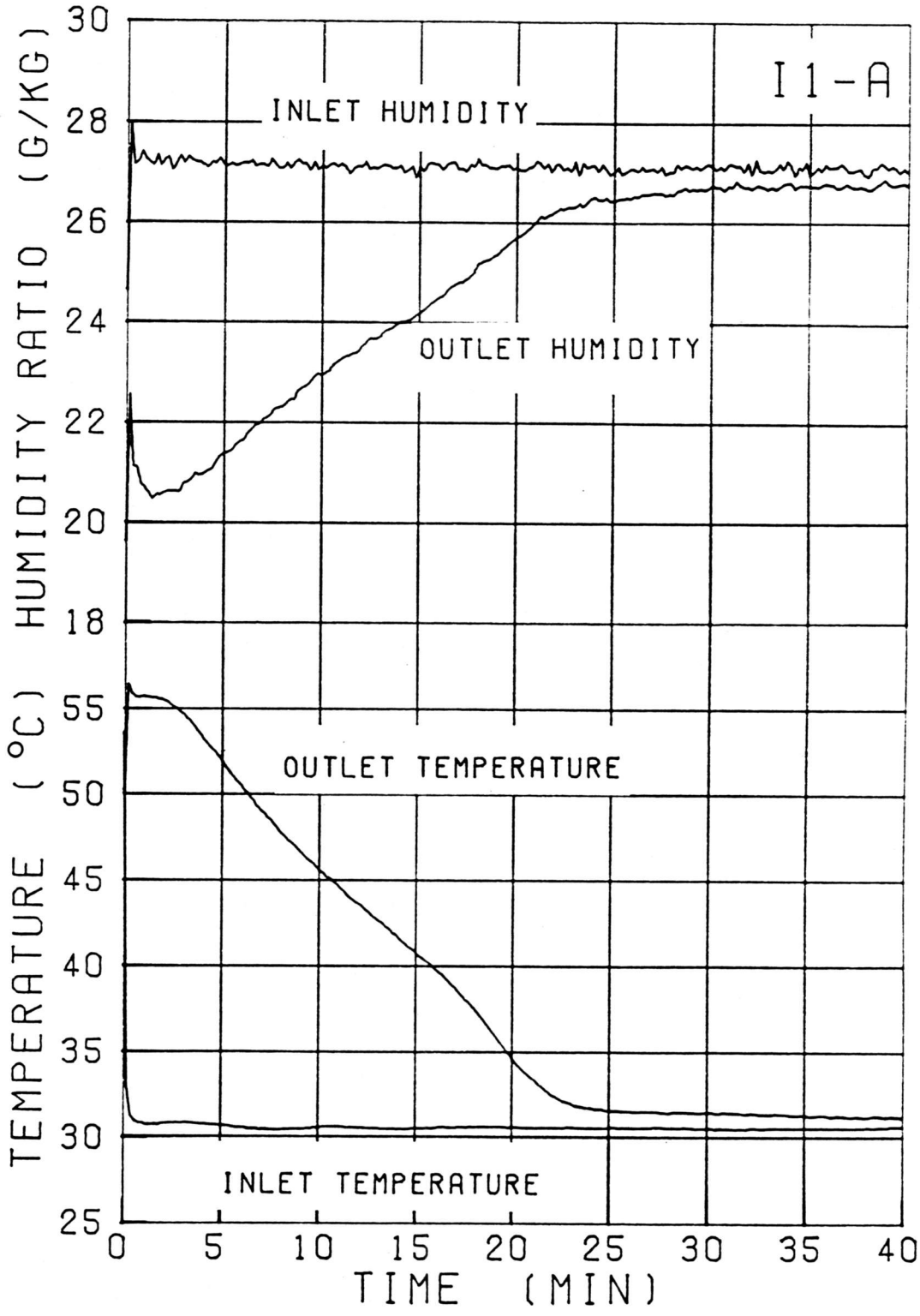

Figure C.2.1.a Temperature and humidity response of experiment I1-A

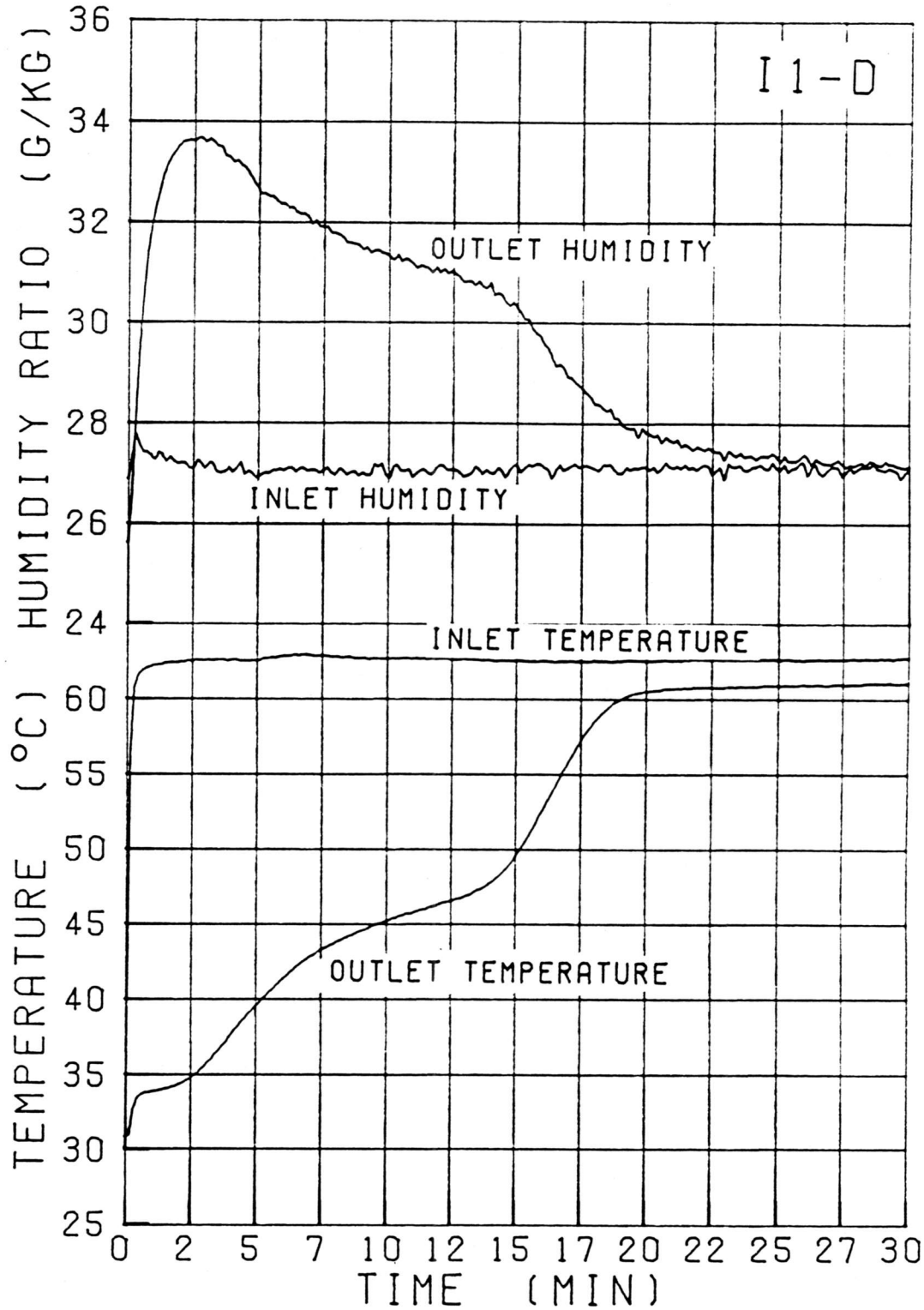

Figure C.2.1.b Temperature and humidity response of experiment I1-D

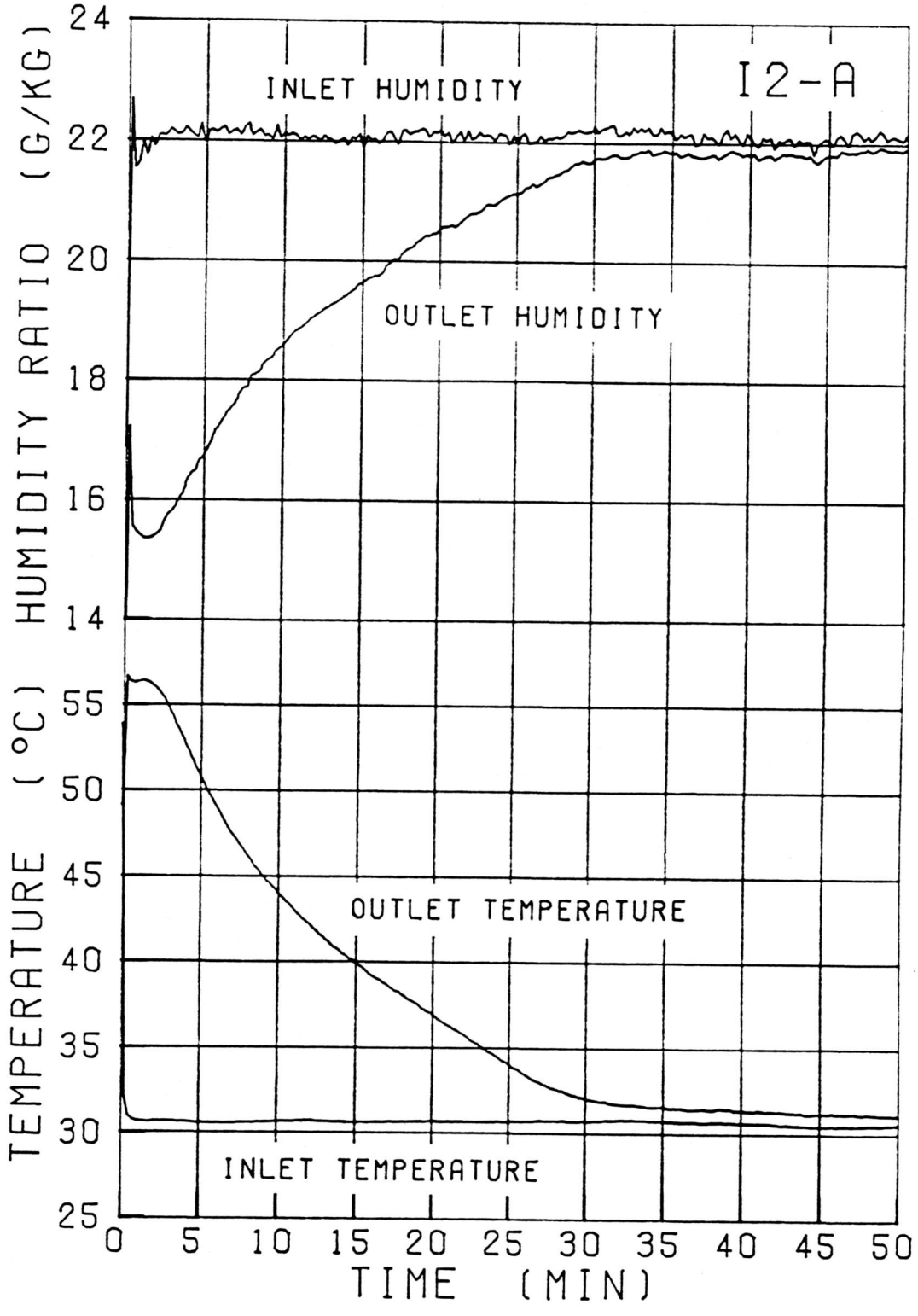

Figure C.2.2.a Temperature and humidity response of experiment I2-A

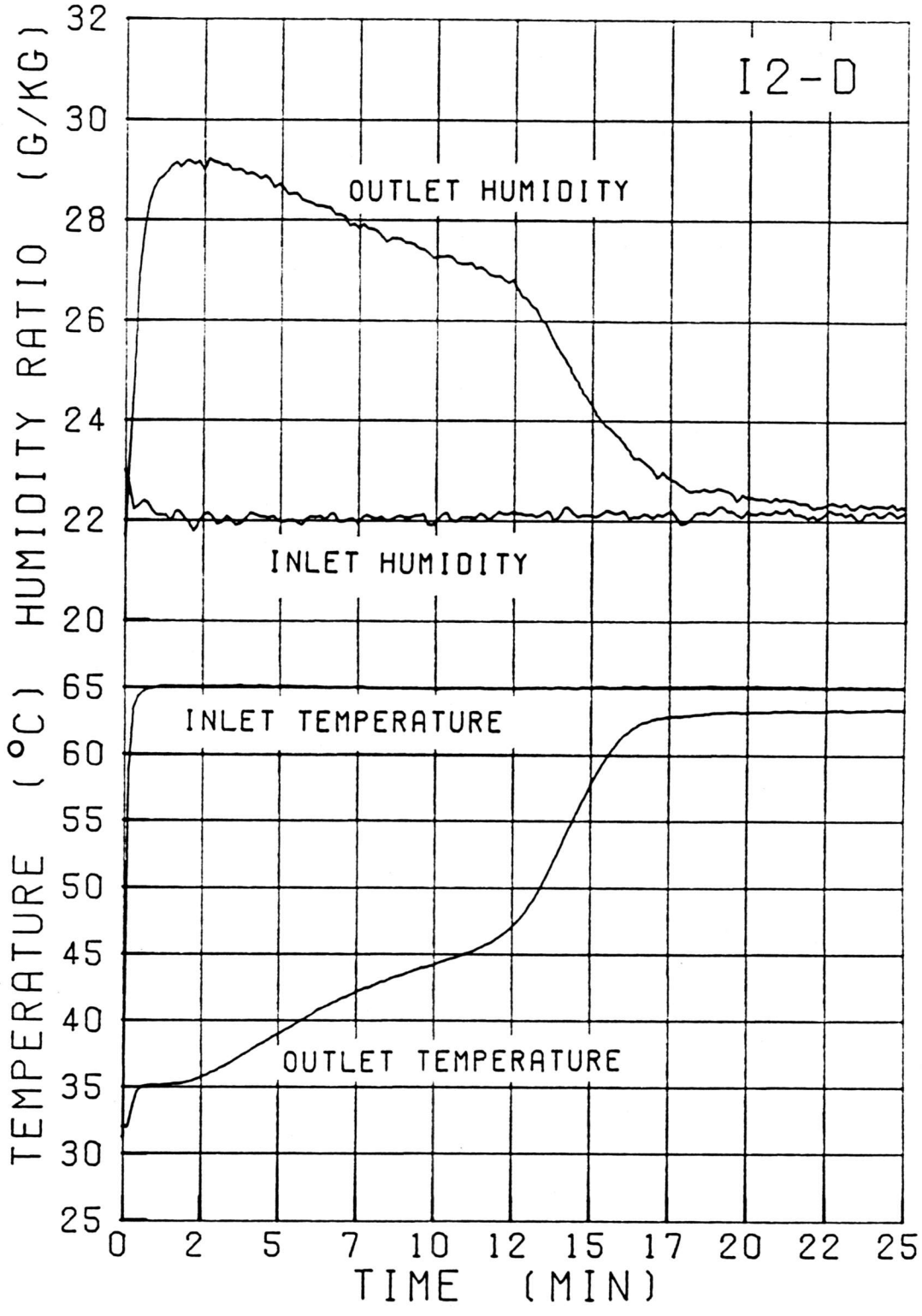

Figure C.2.2.b Temperature and humidity response of experiment I2-D

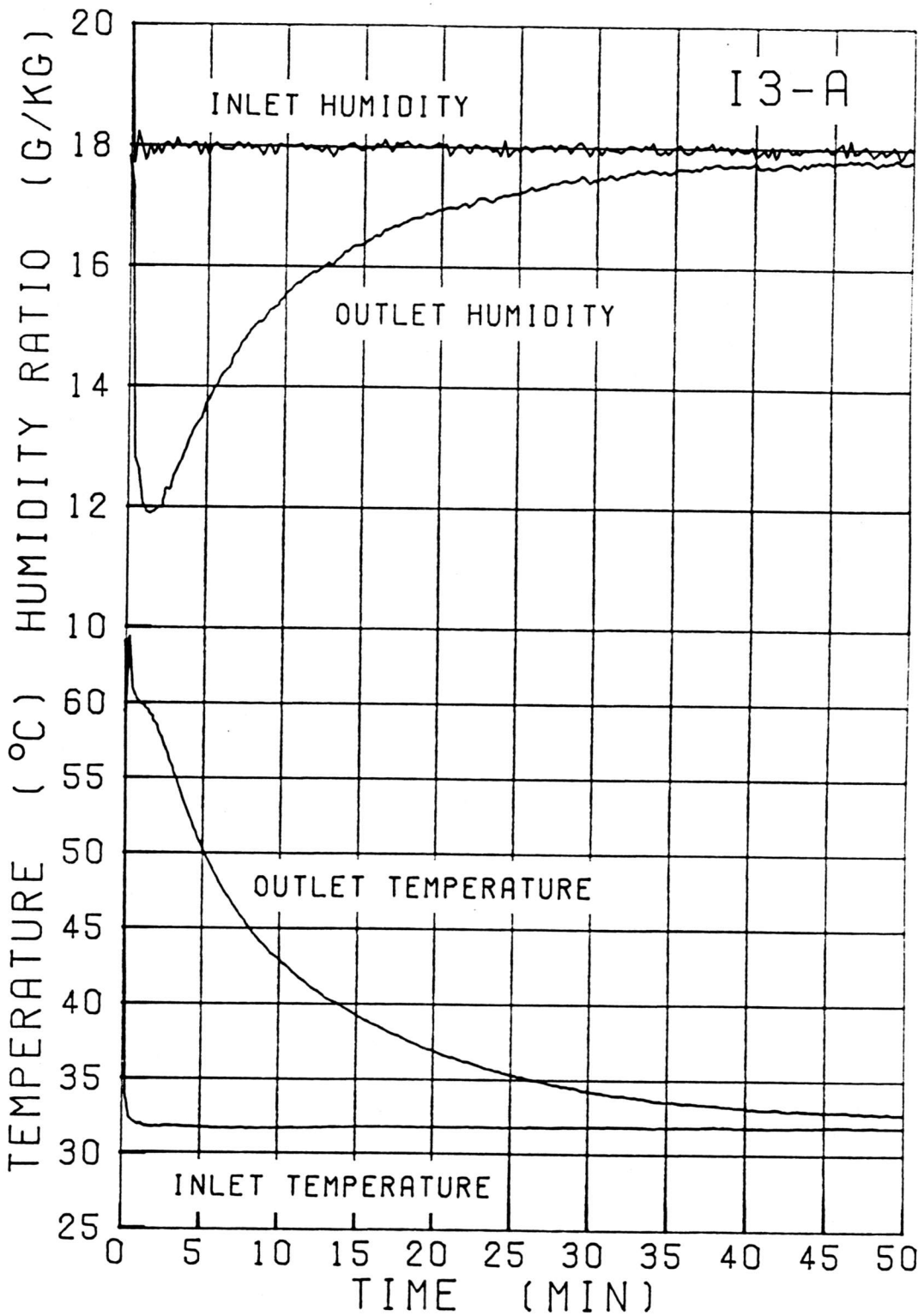

Figure C.2.3.a Temperature and humidity response of experiment I3-A

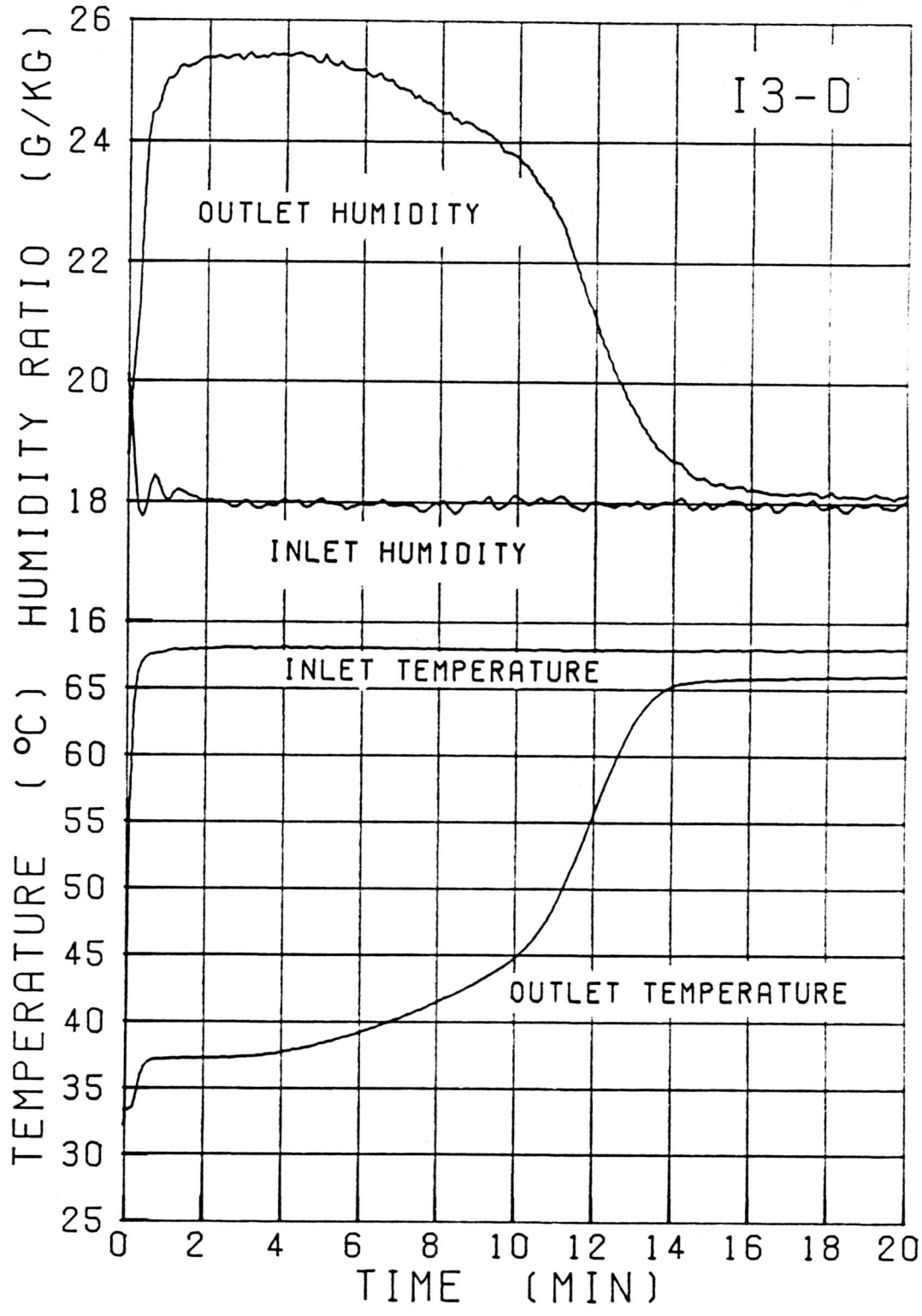

Figure C.2.3.b Temperature and humidity response of experiment I3-D

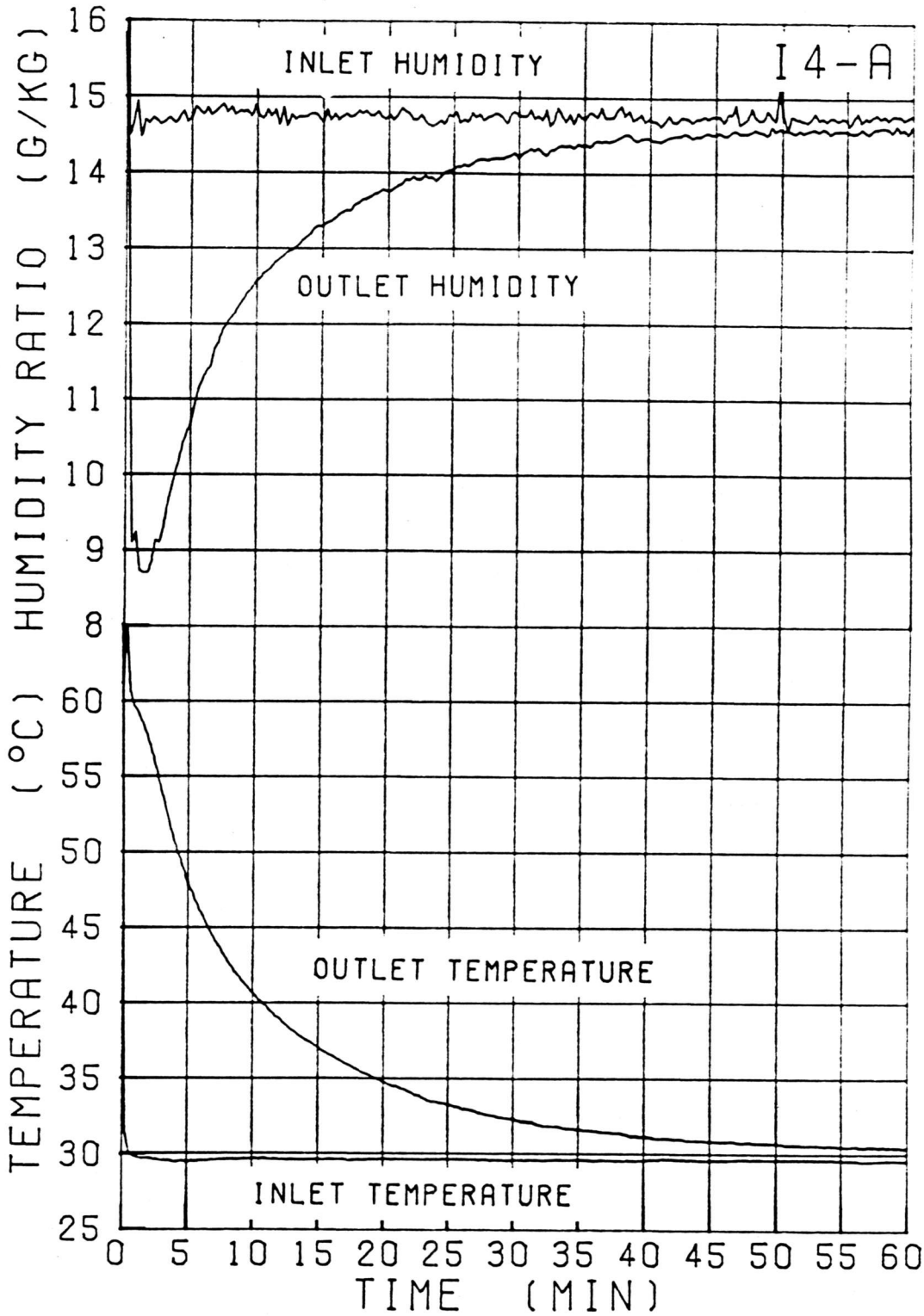

Figure C.2.4.a Temperature and humidity response of experiment I4-A

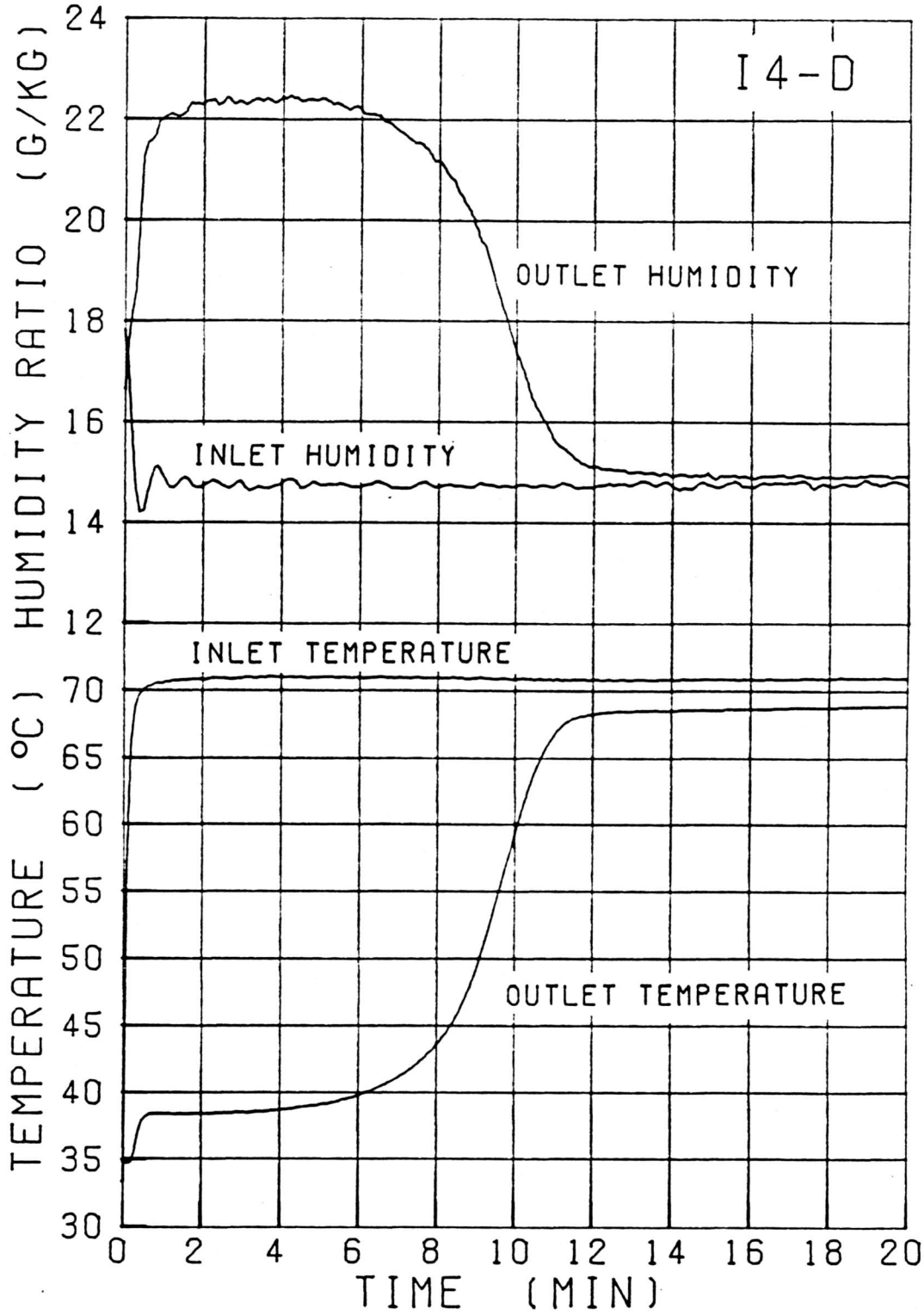

Figure C.2.4.b Temperature and humidity response of experiment I4-D

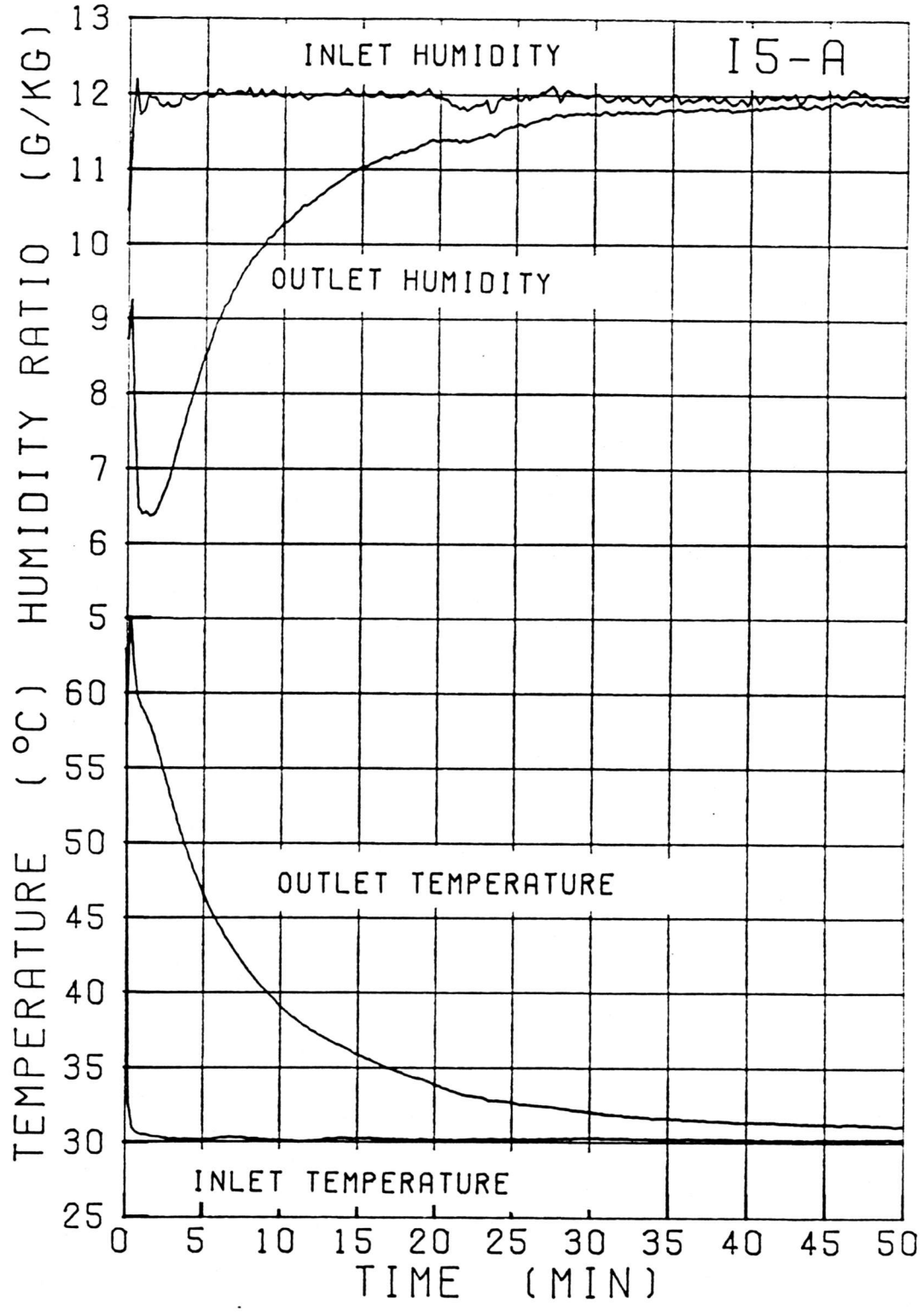

Figure C.2.5.a Temperature and humidity response of experiment I5-A

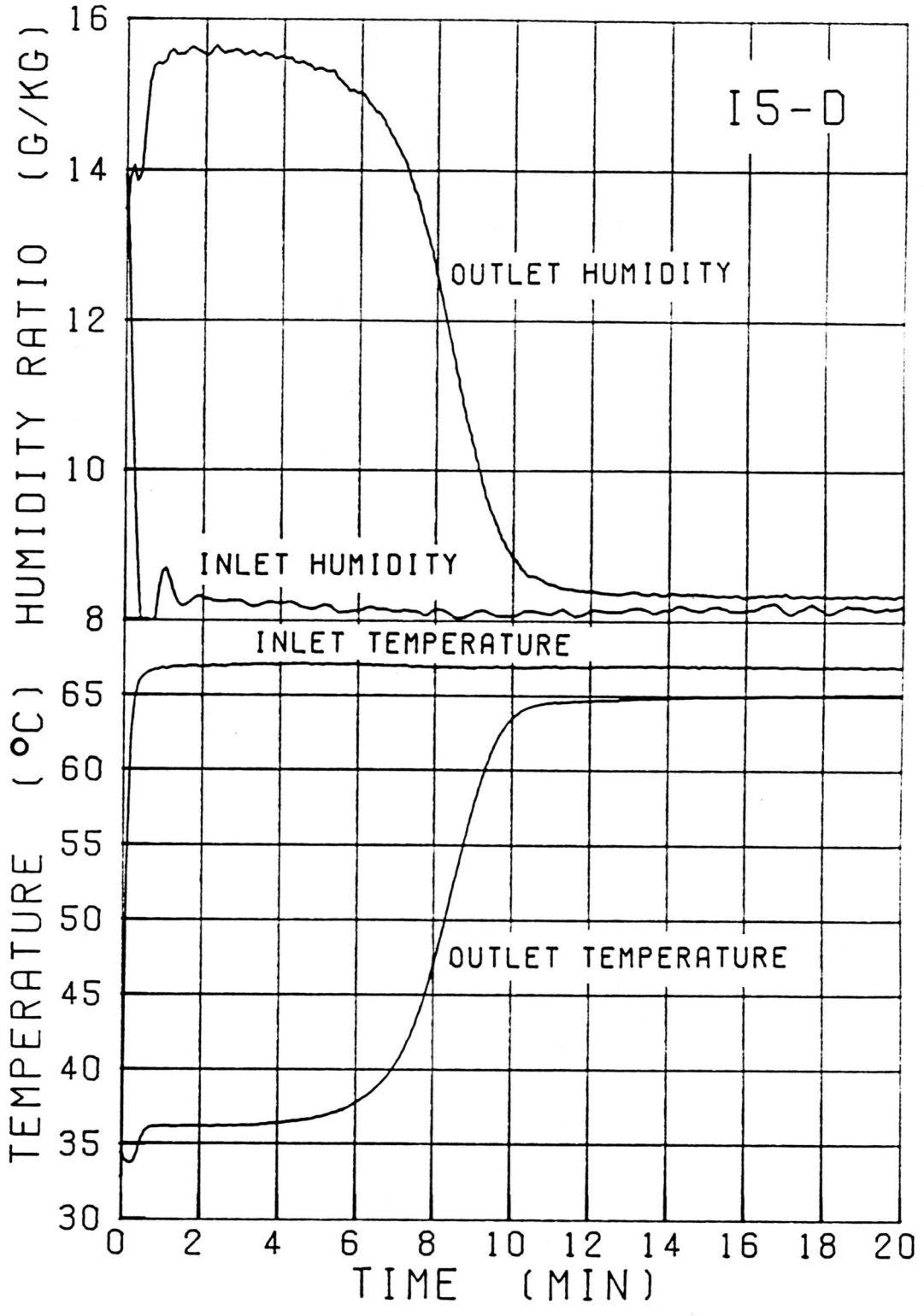

Figure C.2.5.b Temperature and humidity response of experiment I5-D

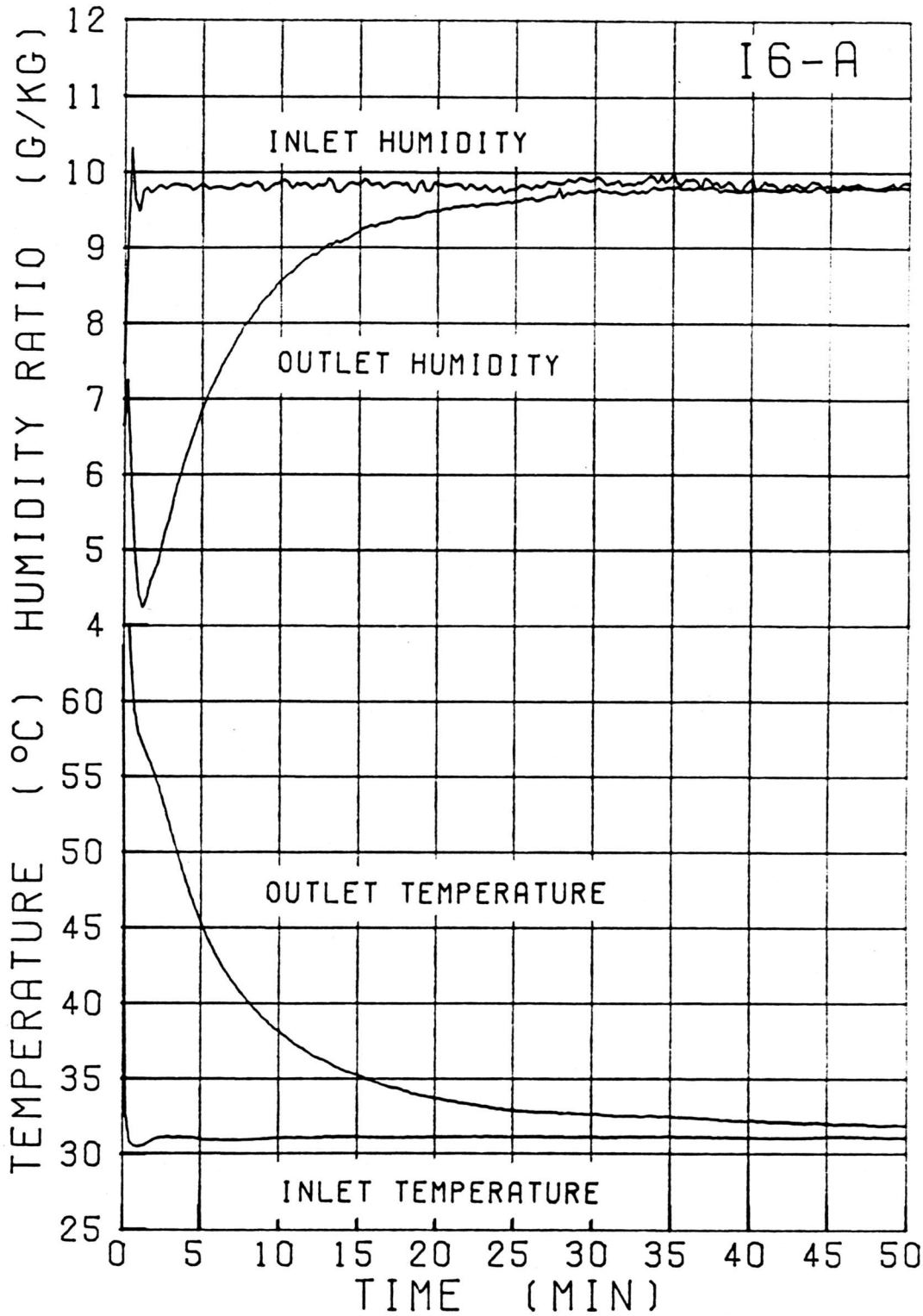

Figure C.2.6.a Temperature and humidity response of experiment I6-A

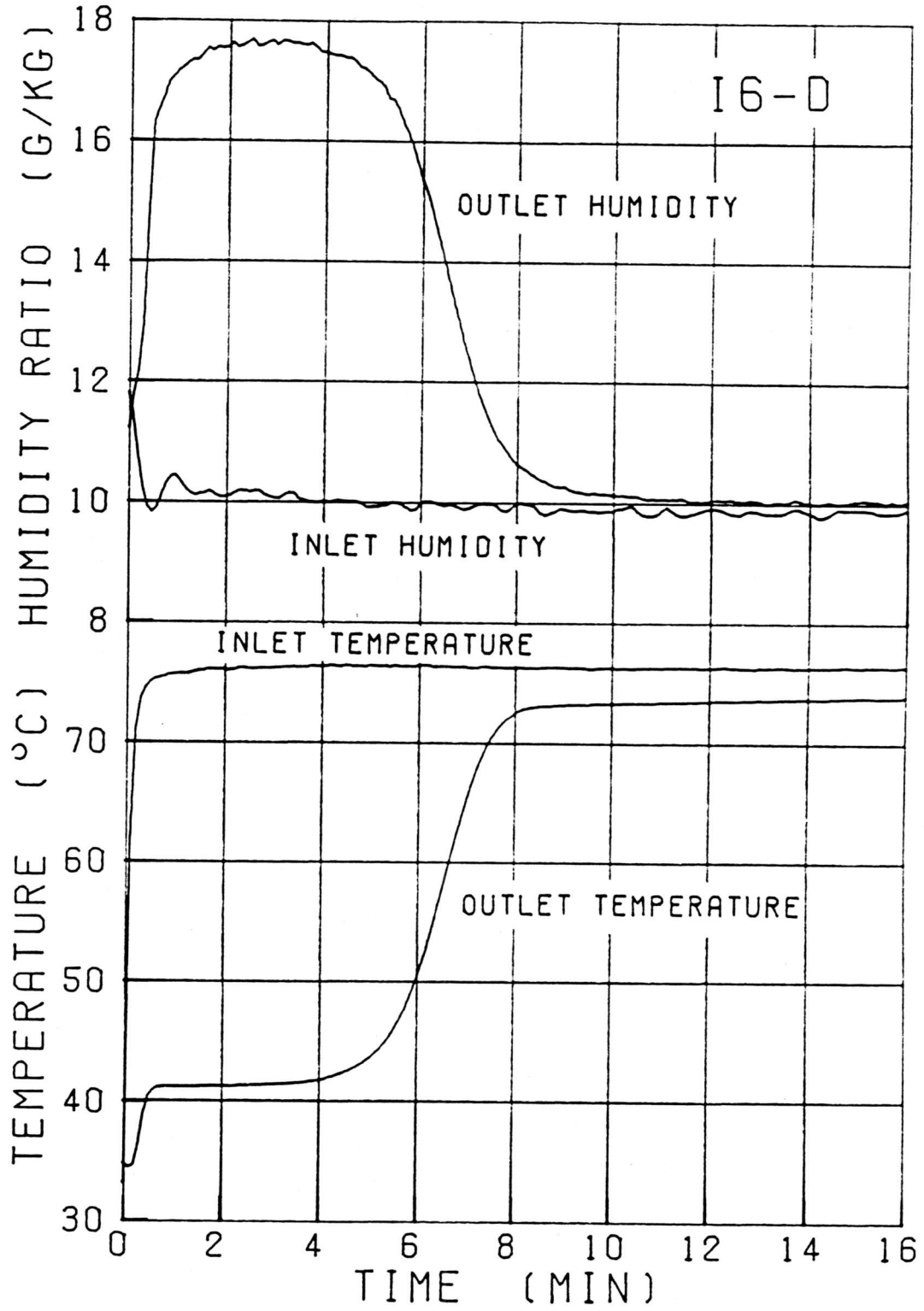

Figure C.2.6.b Temperature and humidity response of experiment I6-D

Figure C.2.7.a Temperature and humidity response of experiment I7-A

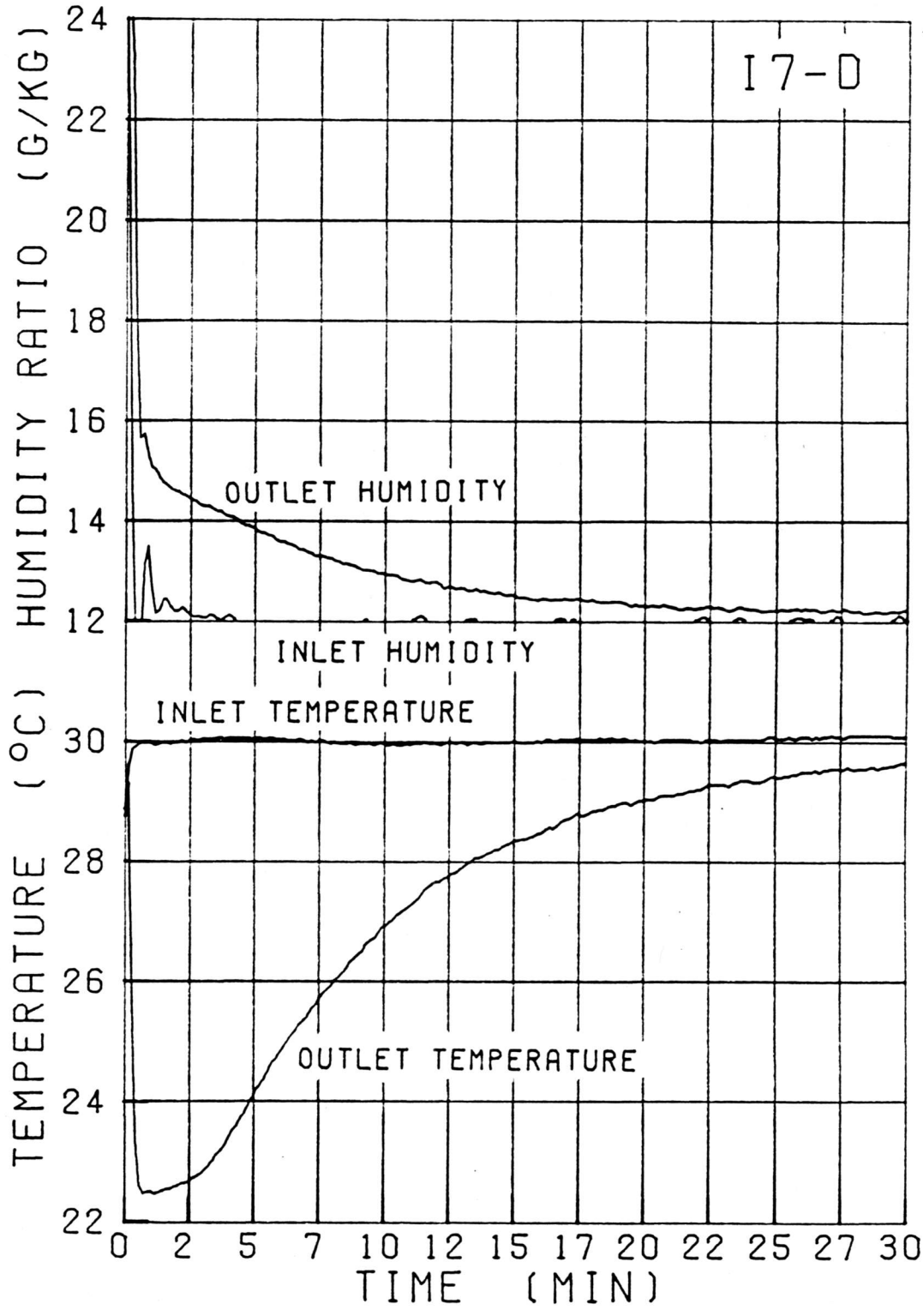

Figure C.2.7.b Temperature and humidity response of experiment I7-D

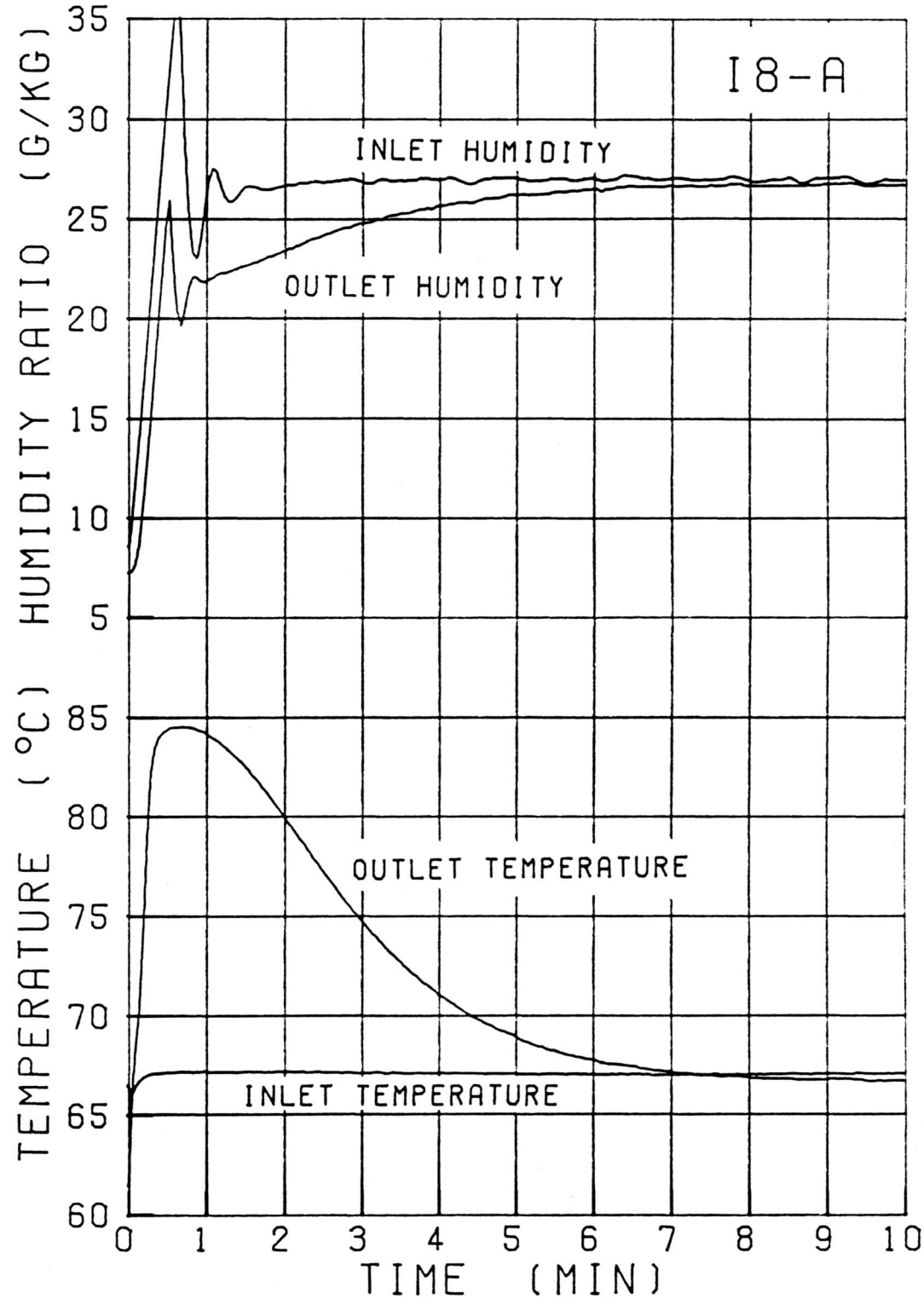

Figure C.2.8.a Temperature and humidity response of experiment I8-A

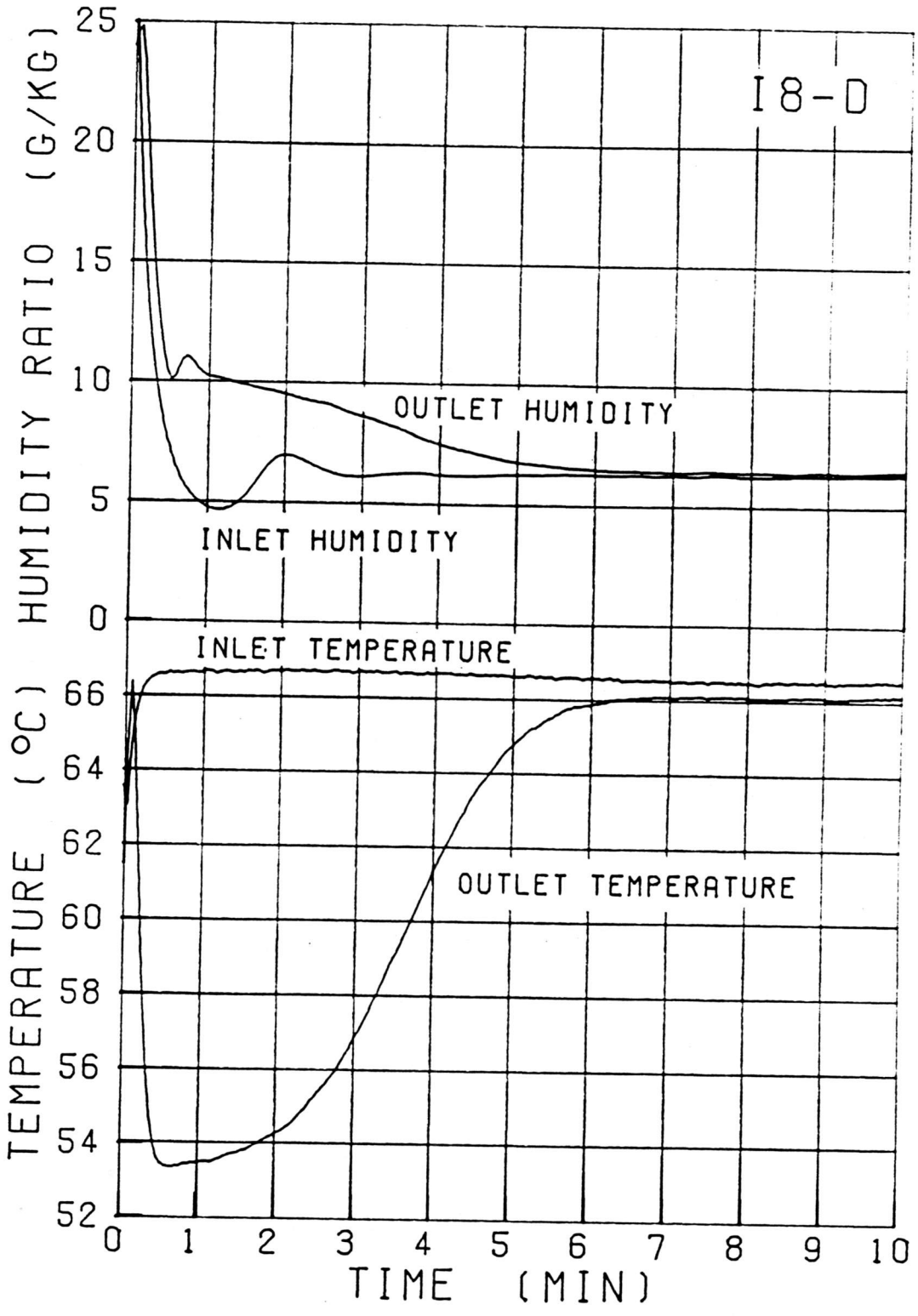

Figure C.2.8.b Temperature and humidity response of experiment I8-D

C.3 Dynamic, Adiabatic Sorption Experiments with Varying Process Air Mass Flow Rate, Series M.

Figures C.3.1.a - C.3.15.b show the process air inlet and outlet temperature and humidity ratio as a function of time for constant initial and inlet conditions and varying mass flow rate.

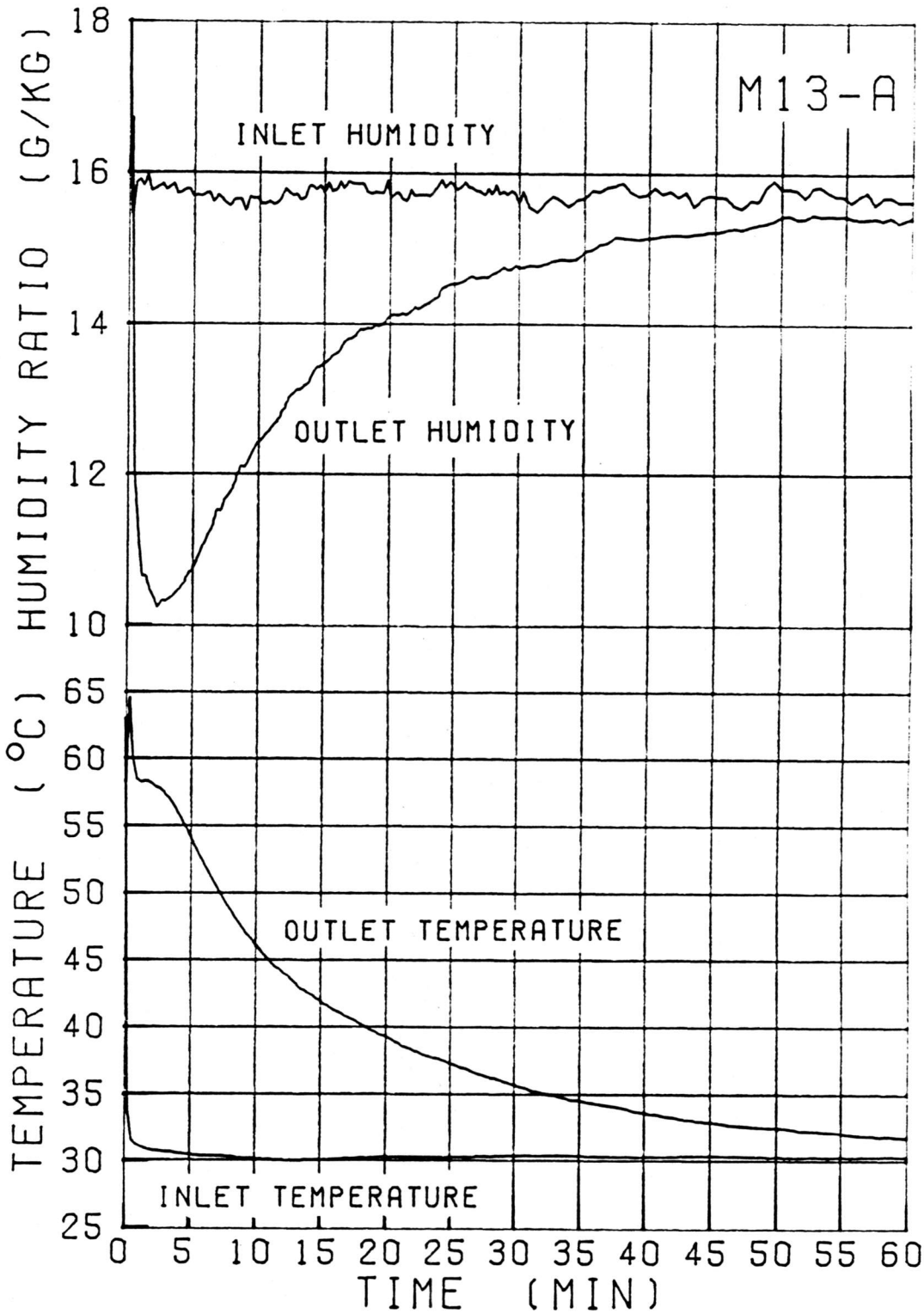

Figure C.3.1.a Temperature and humidity response of experiment M13-A

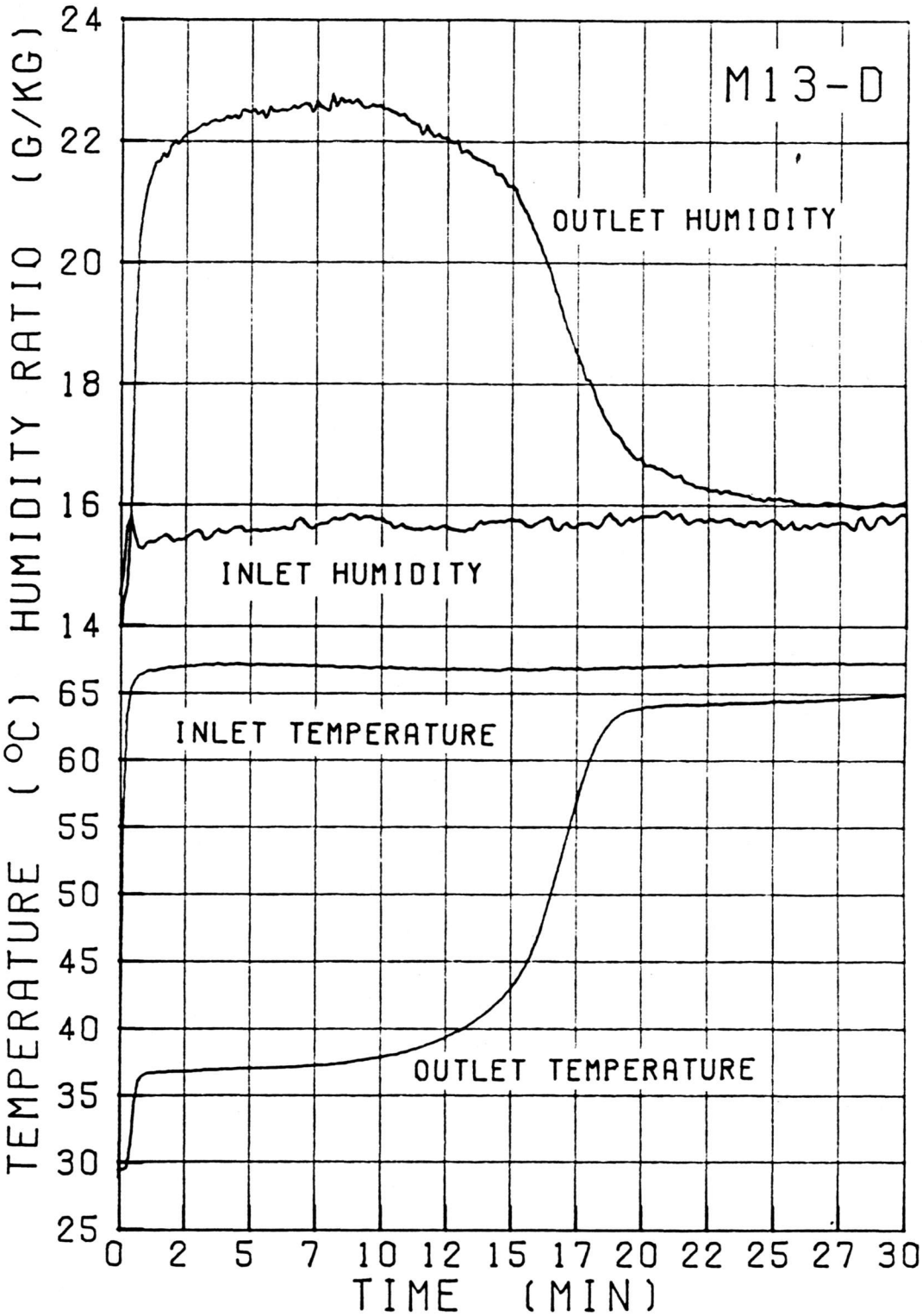

Figure C.3.1.b Temperature and humidity response of experiment M13-D

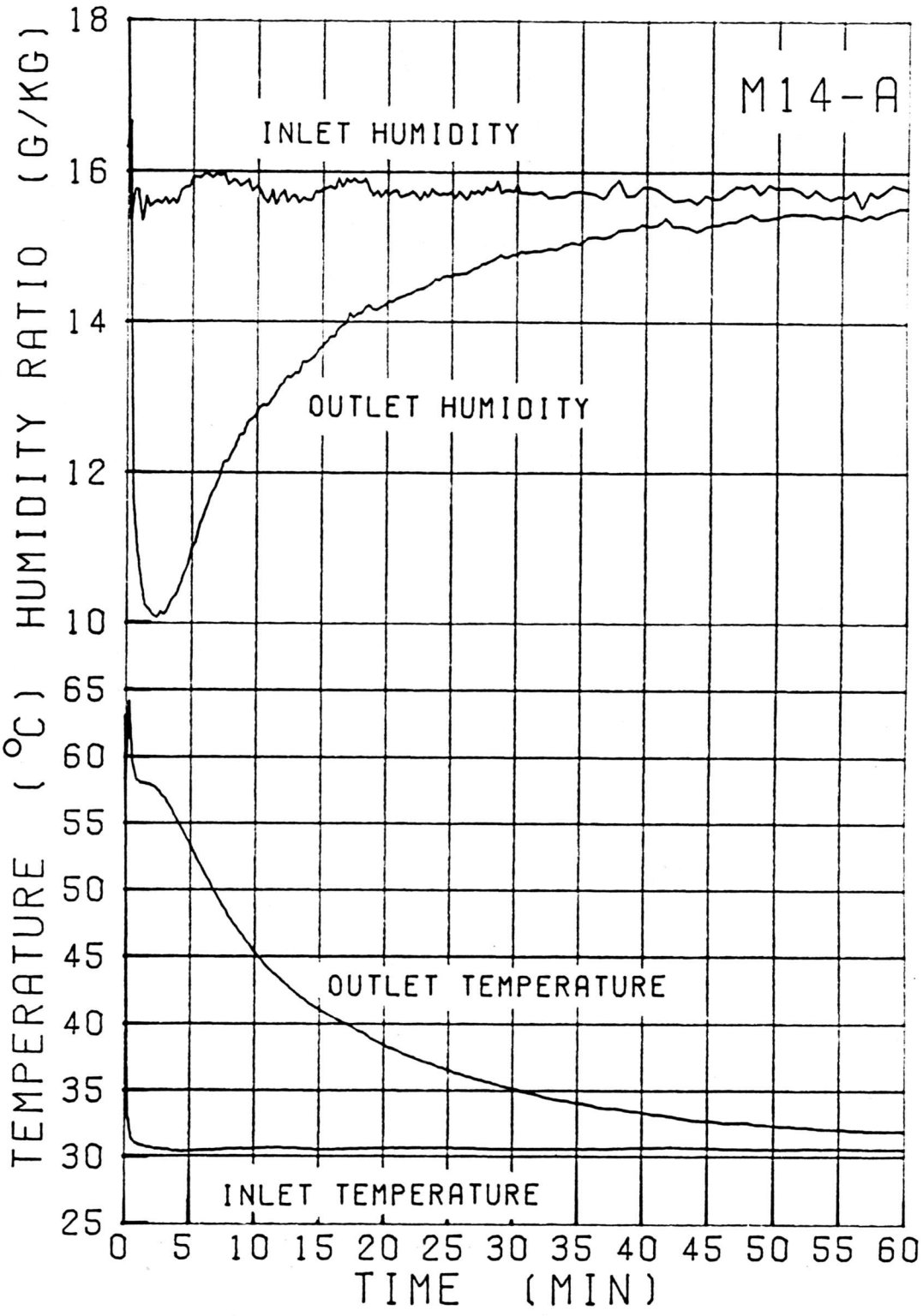

Figure C.3.2.a Temperature and humidity response of experiment M14-A

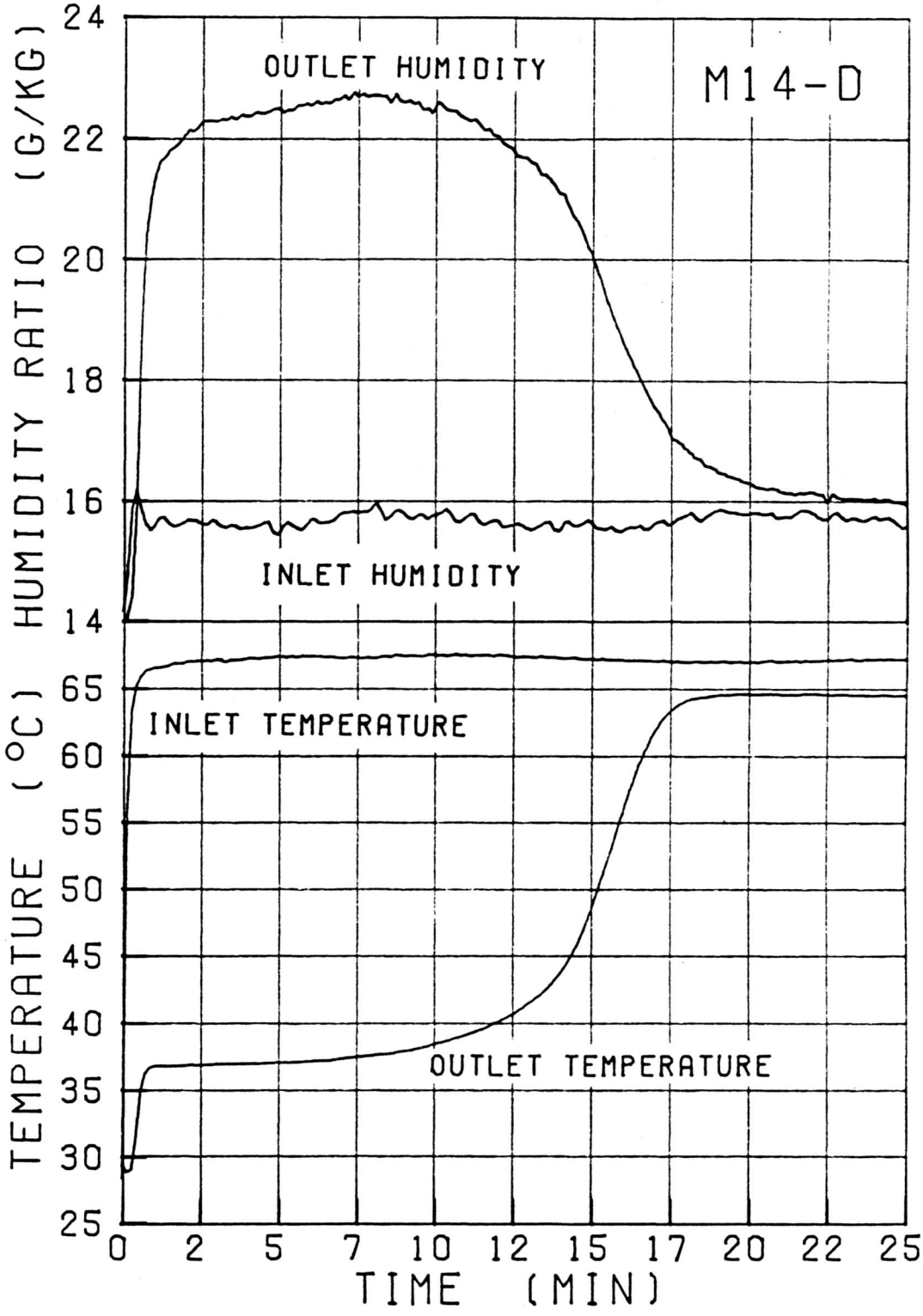

Figure C.3.2.b Temperature and humidity response of experiment M14-D

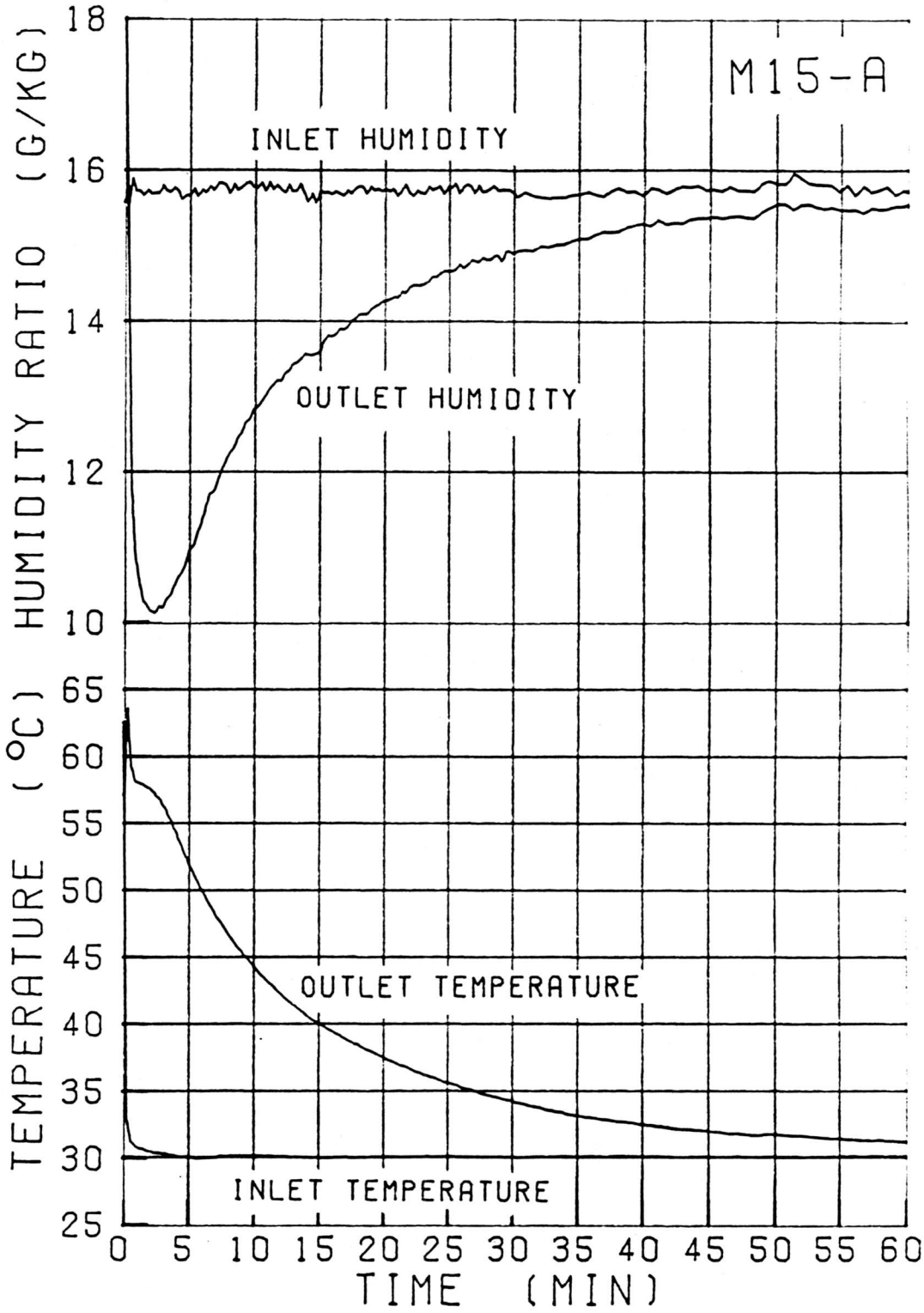

Figure C.3.3.a Temperature and humidity response of experiment M15-A

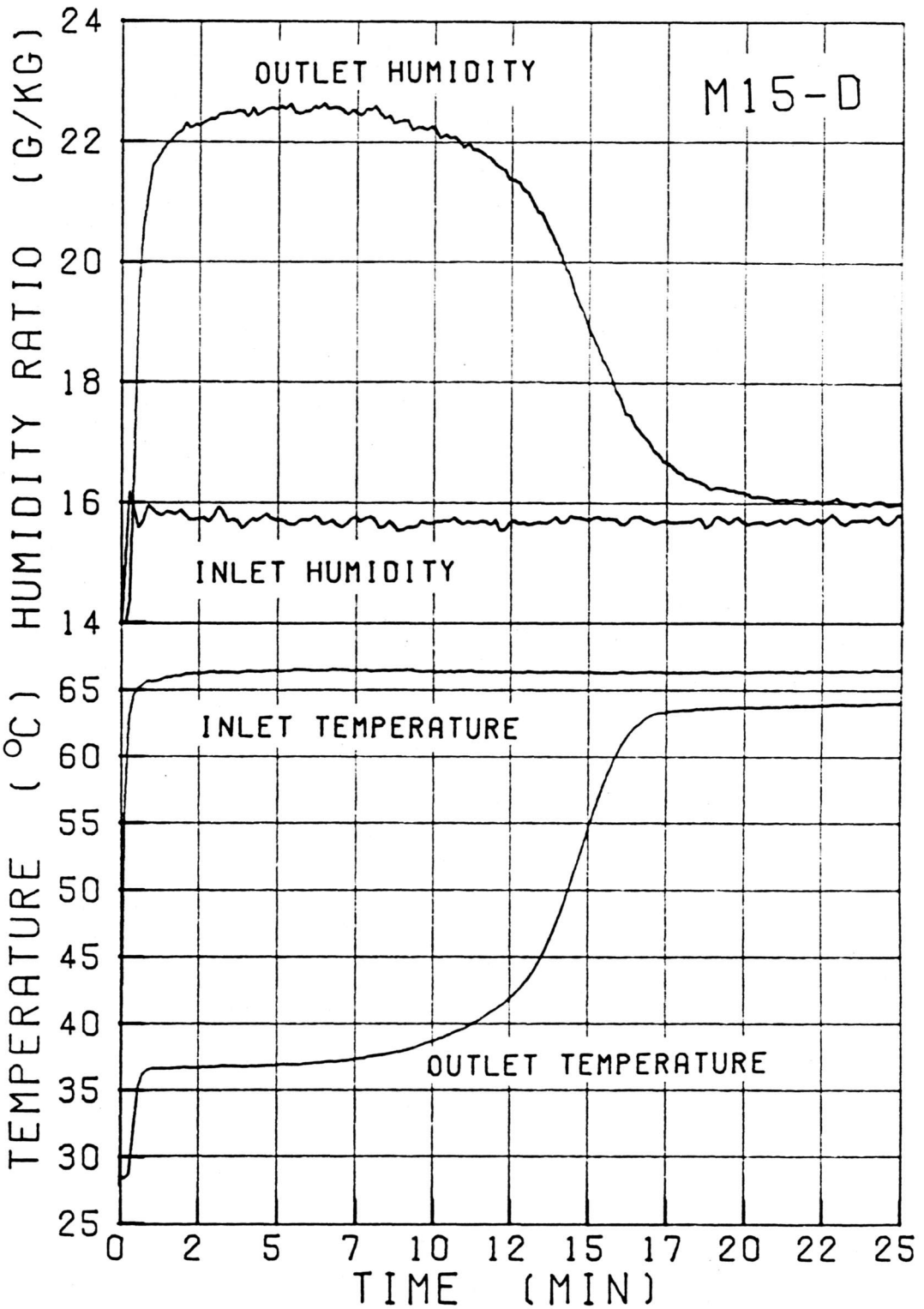

Figure C.3.3.b Temperature and humidity response of experiment M15-D

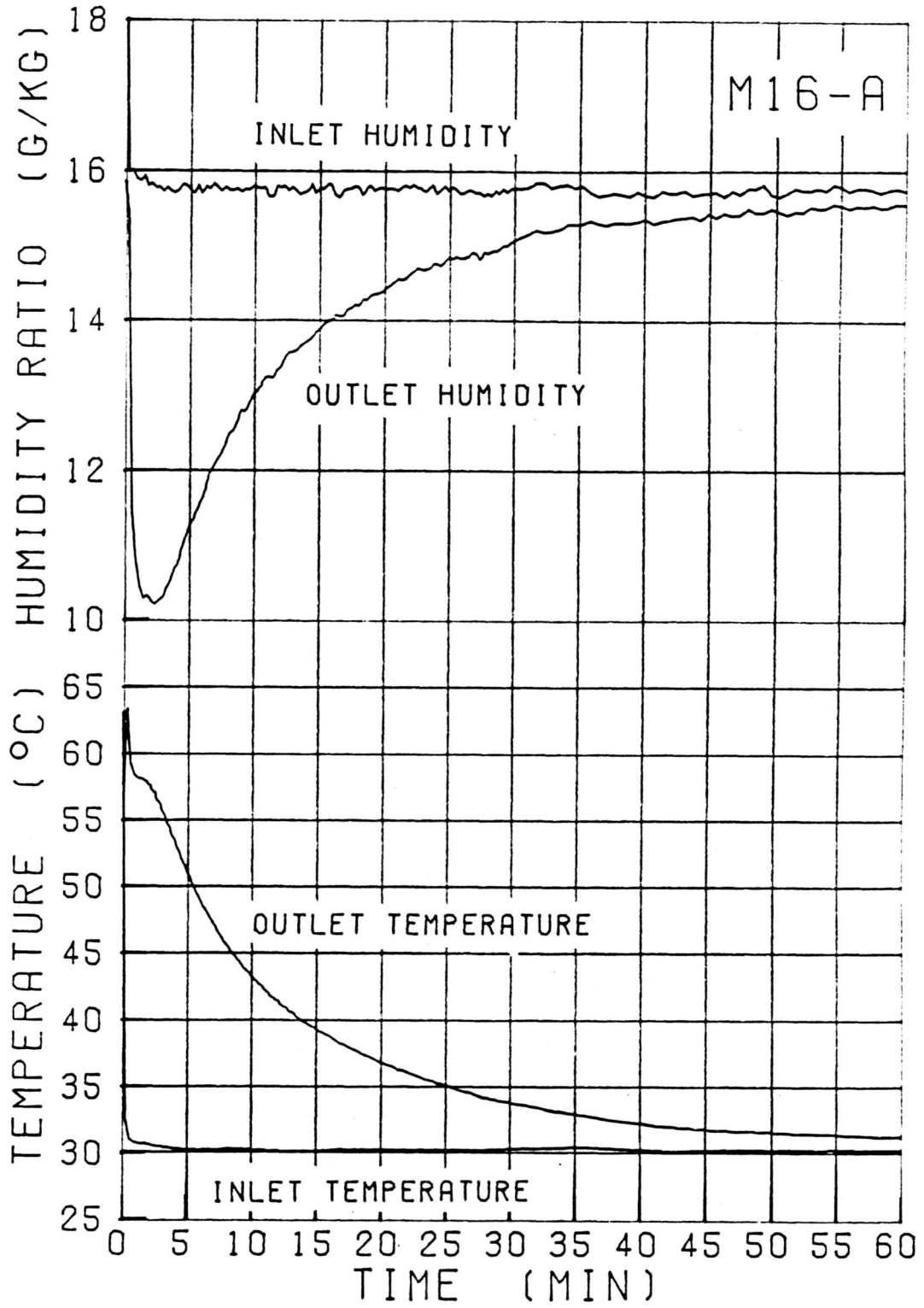

Figure C.3.4.a Temperature and humidity response of experiment M16-A

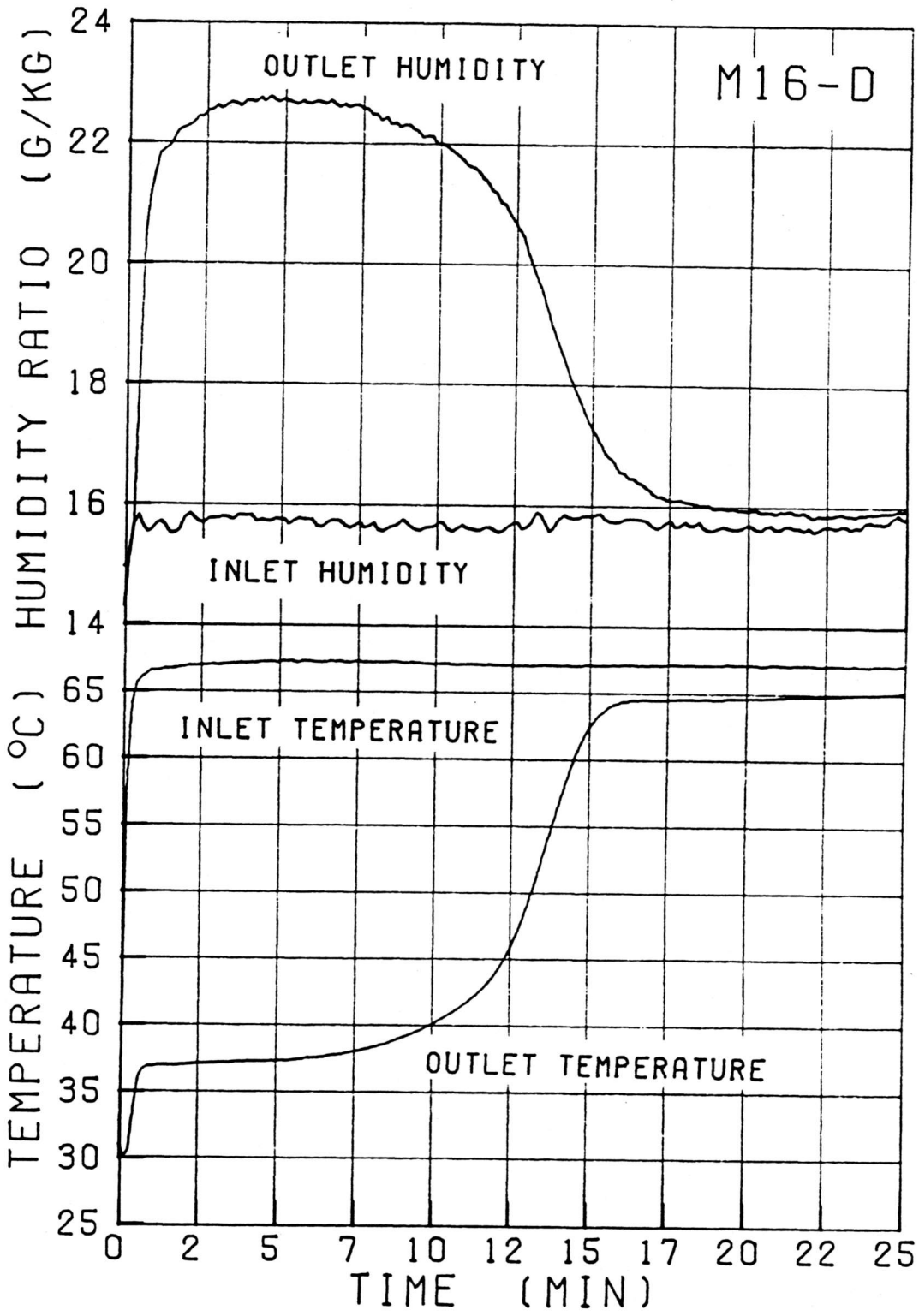

Figure C.3.4.b Temperature and humidity response of experiment M16-D

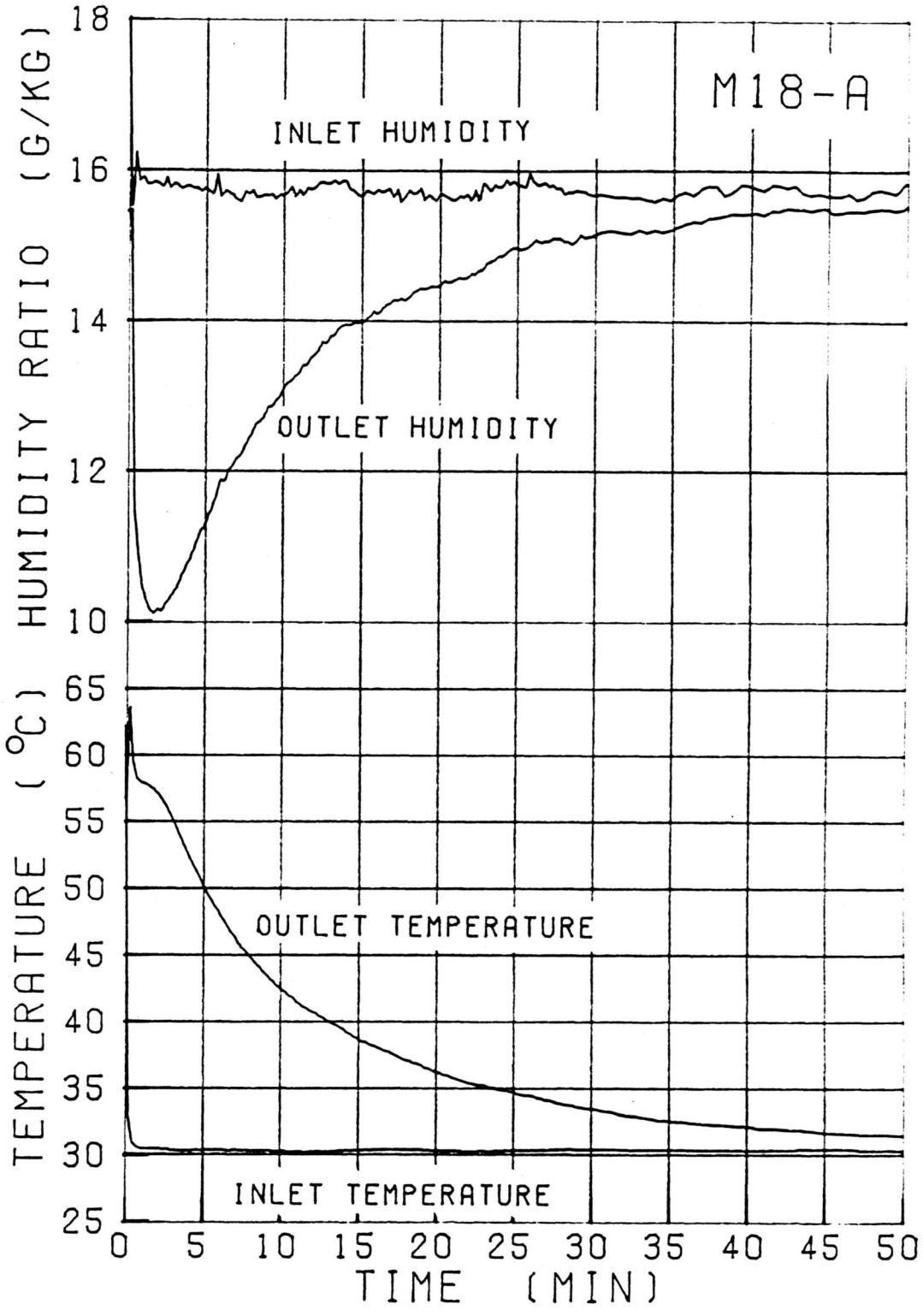

Figure C.3.5.a Temperature and humidity response of experiment M18-A

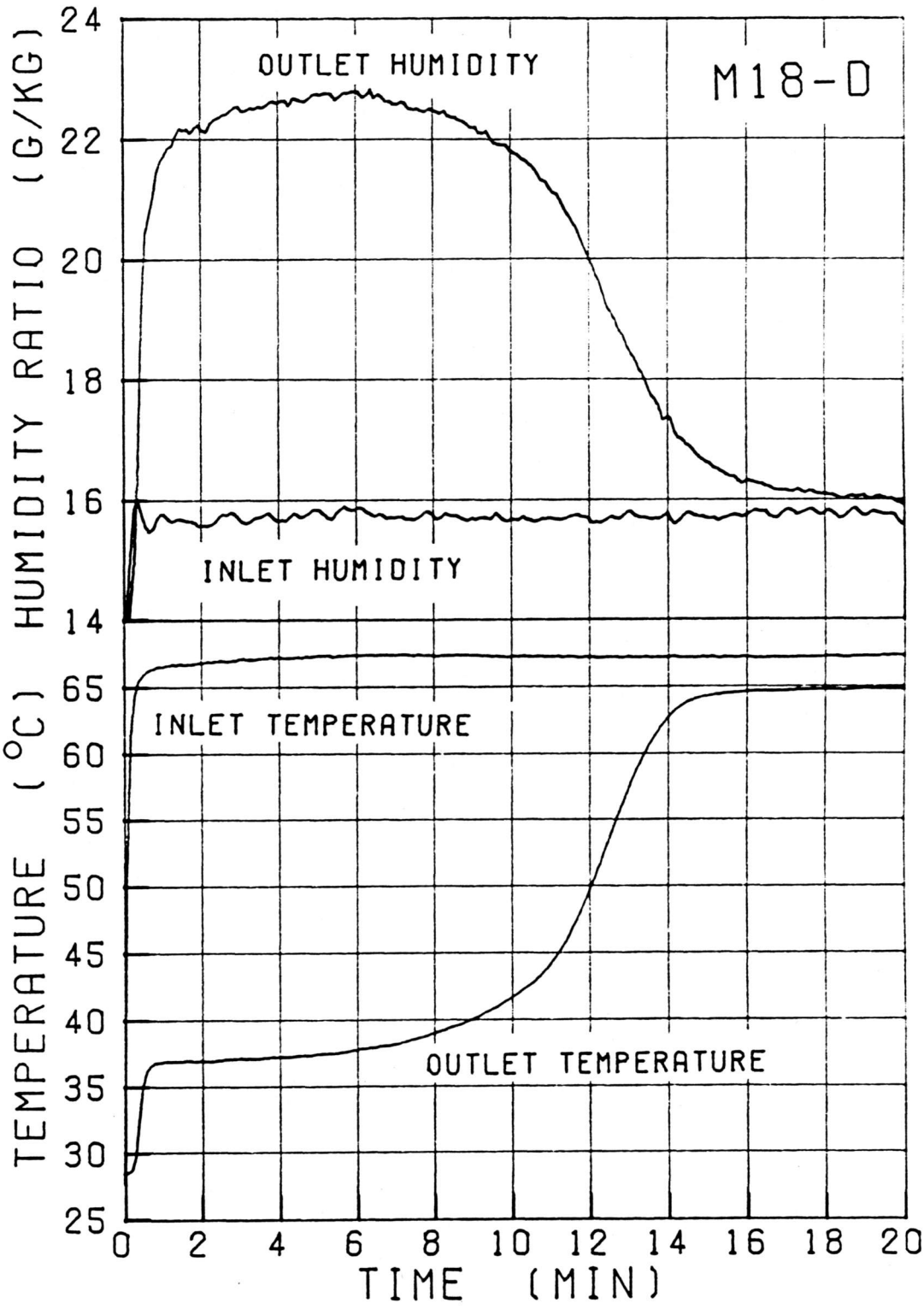

Figure C.3.5.b Temperature and humidity response of experiment M18-D

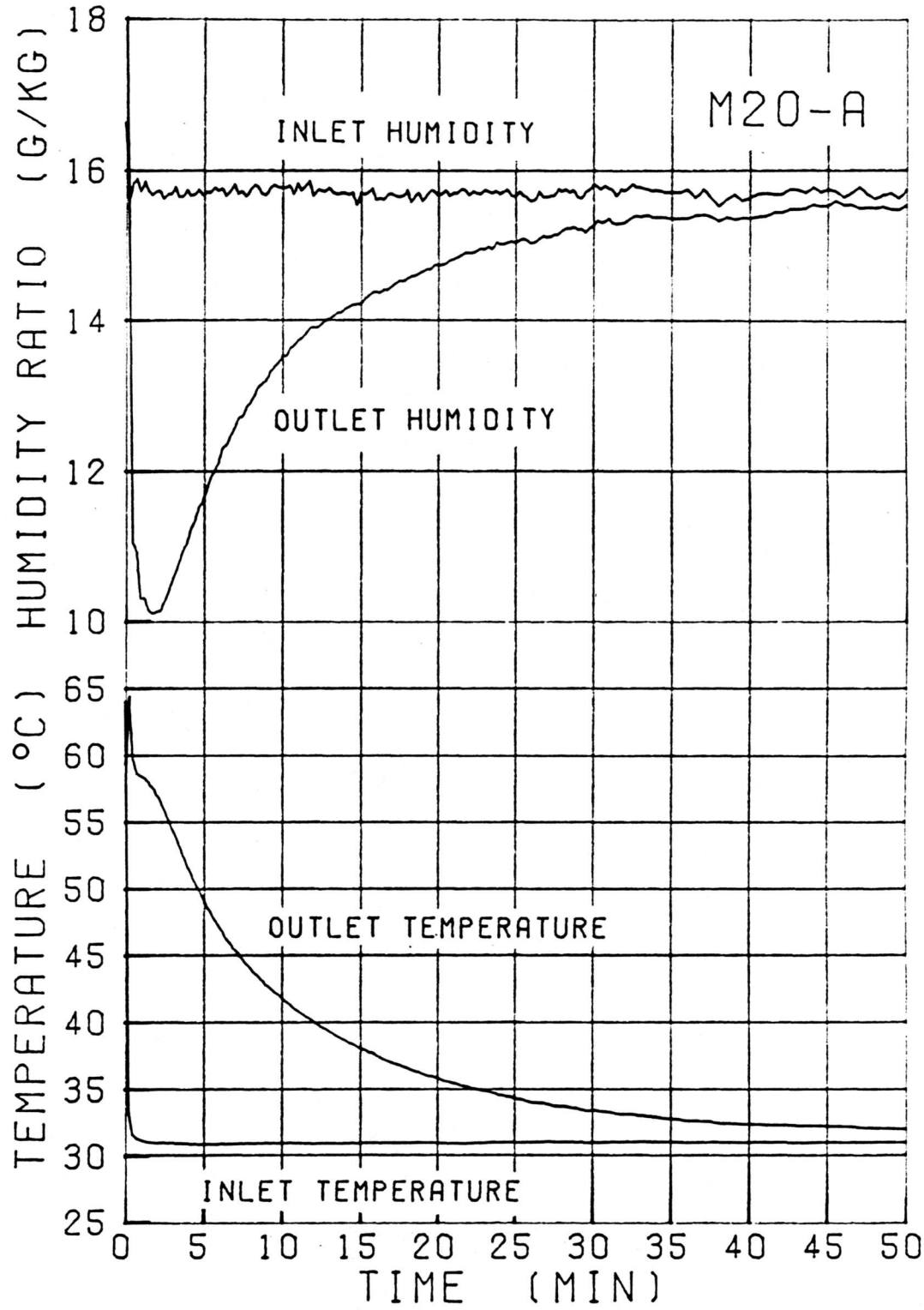

Figure C.3.6.a Temperature and humidity response of experiment M20-A

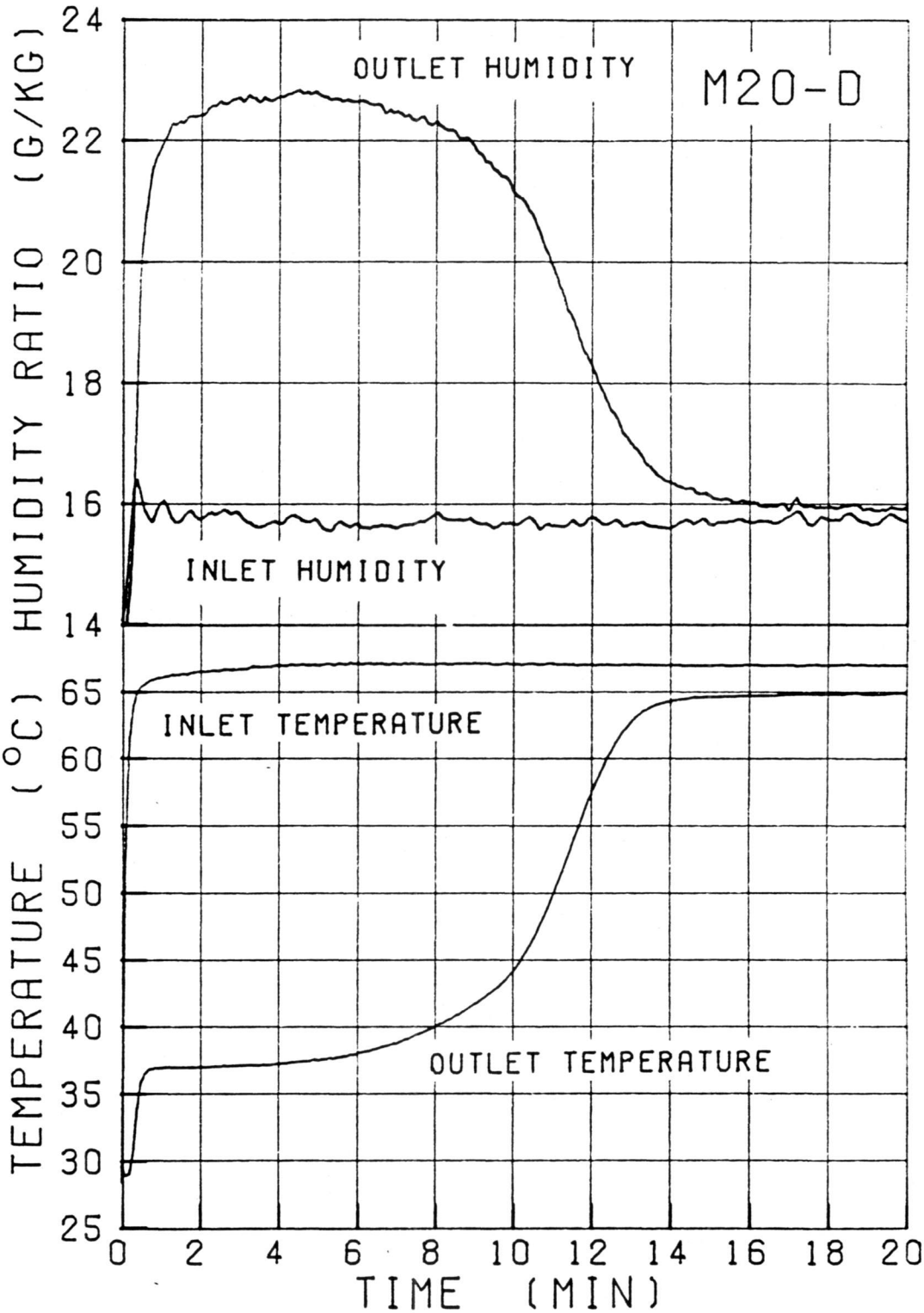

Figure C.3.6.b Temperature and humidity response of experiment M20-D

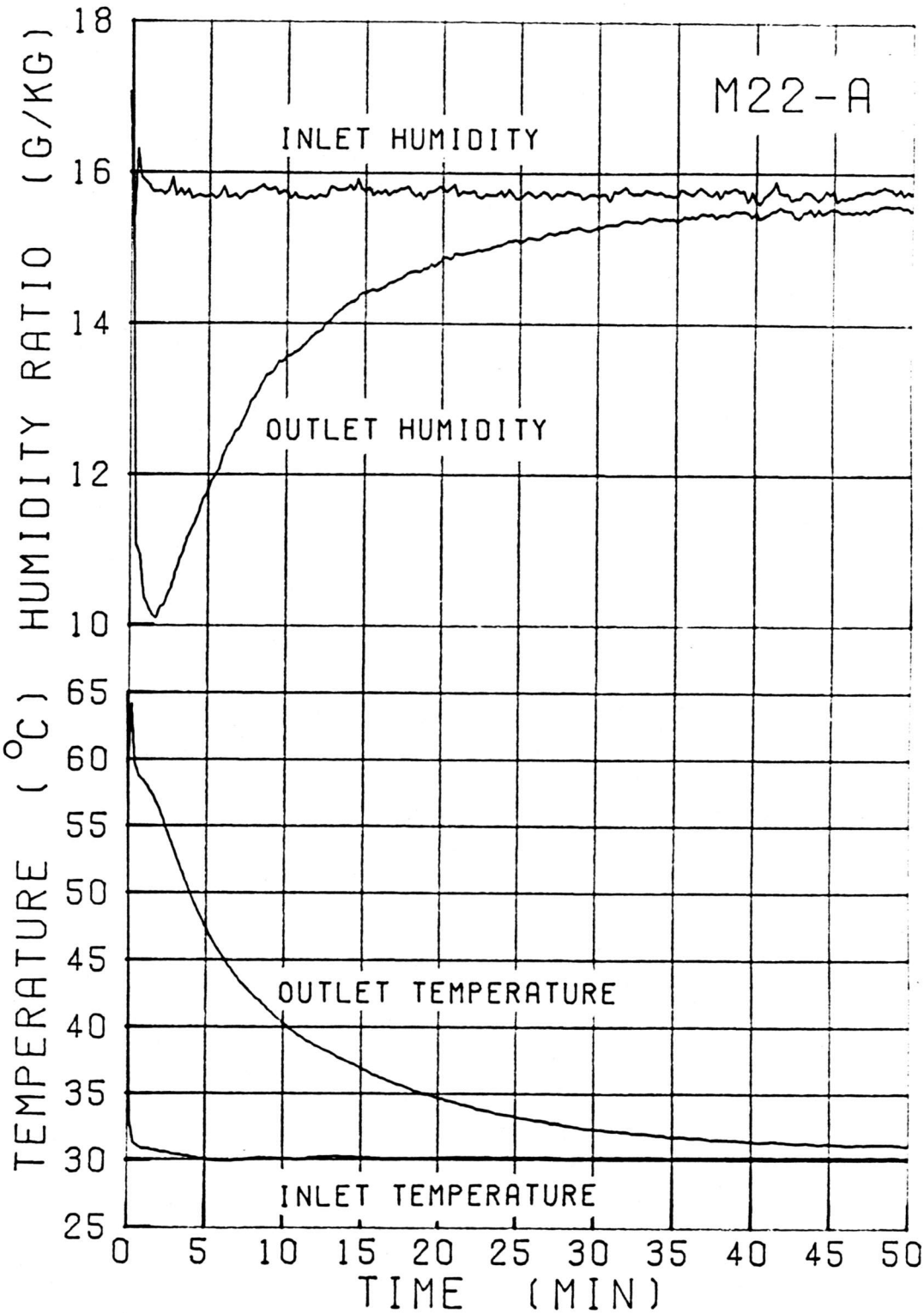

Figure C.3.7.a Temperature and humidity response of experiment M22-A

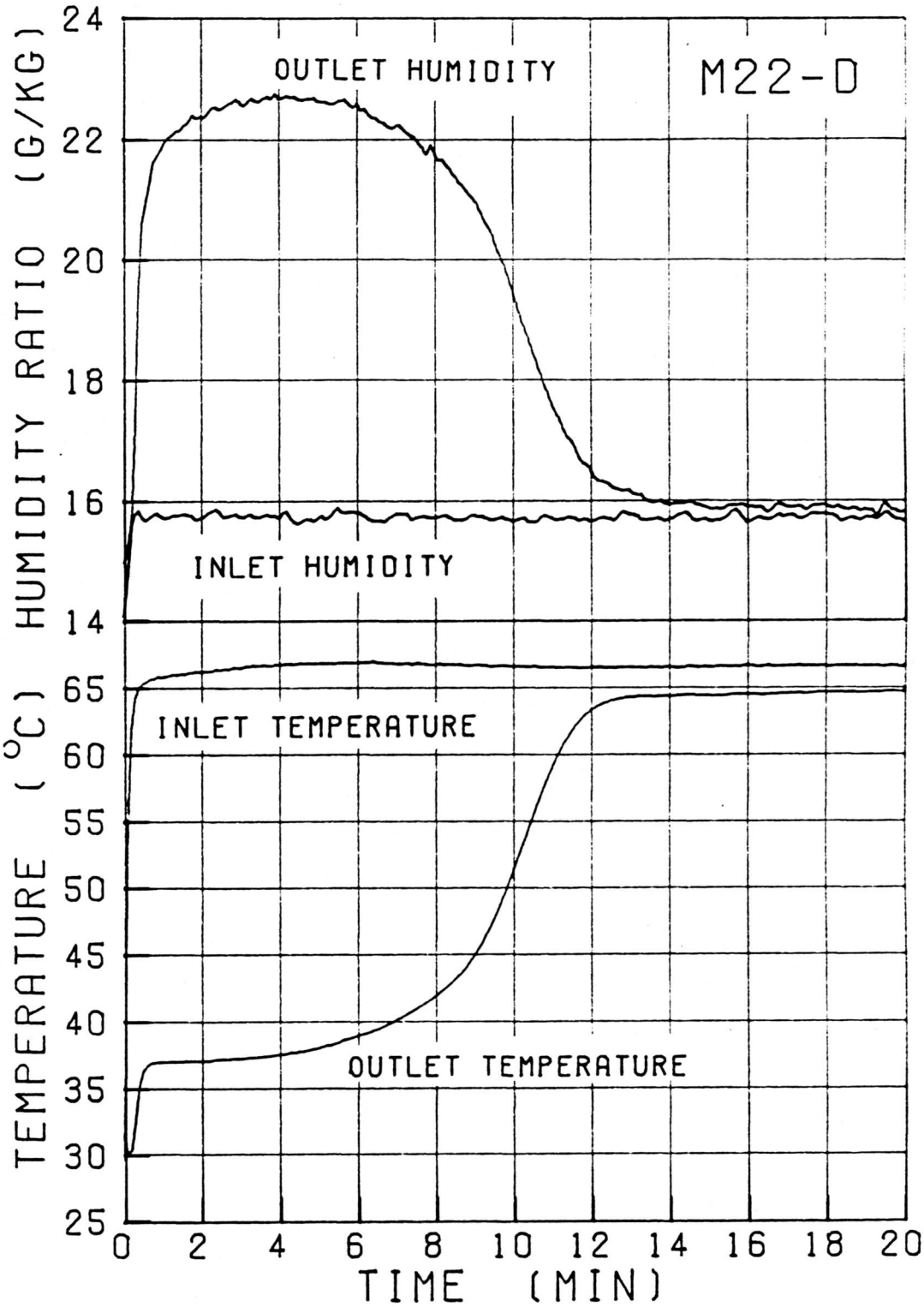

Figure C.3.7.b Temperature and humidity response of experiment M22-D

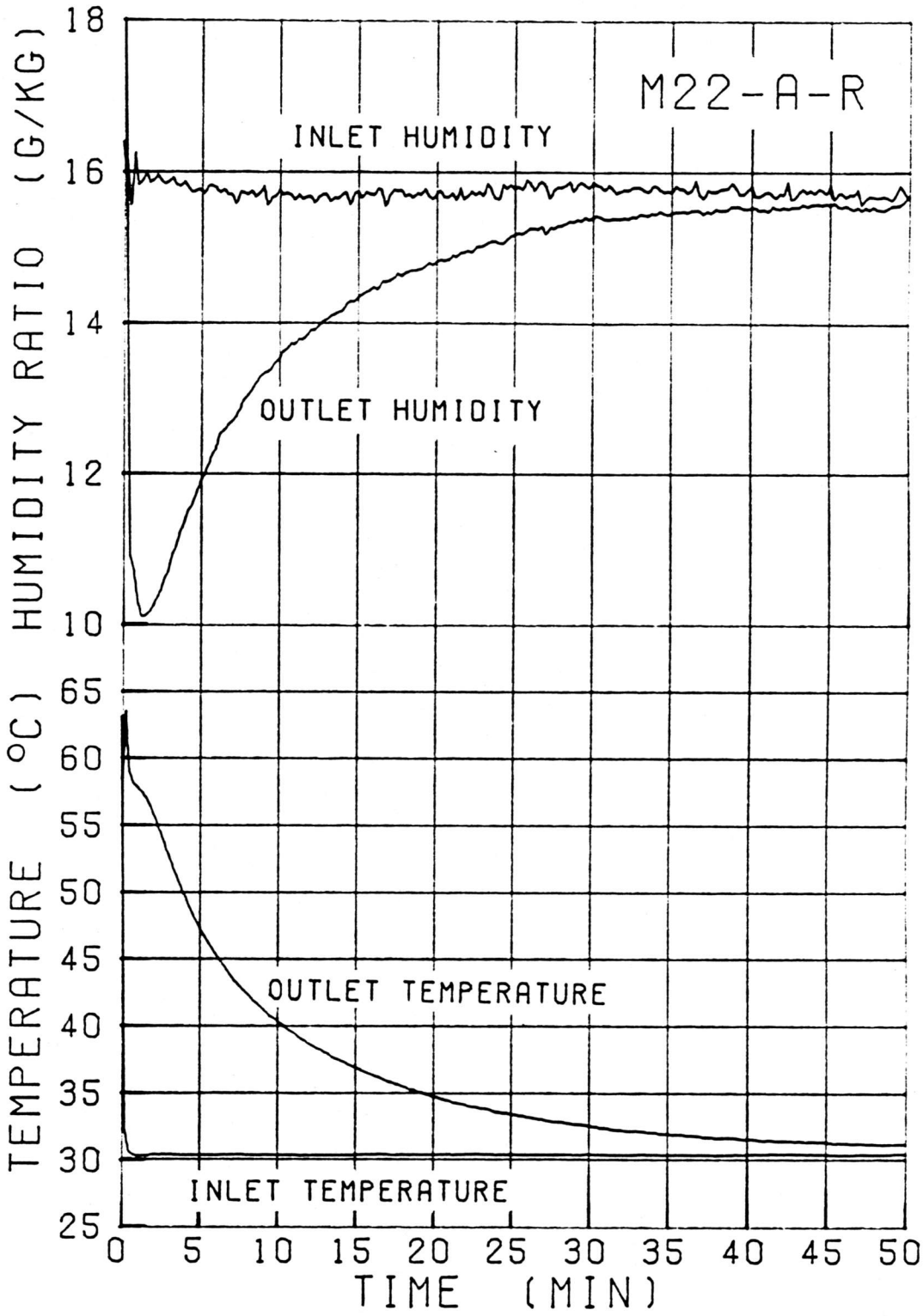

Figure C.3.8.a Temperature and humidity response of experiment M22-A-R

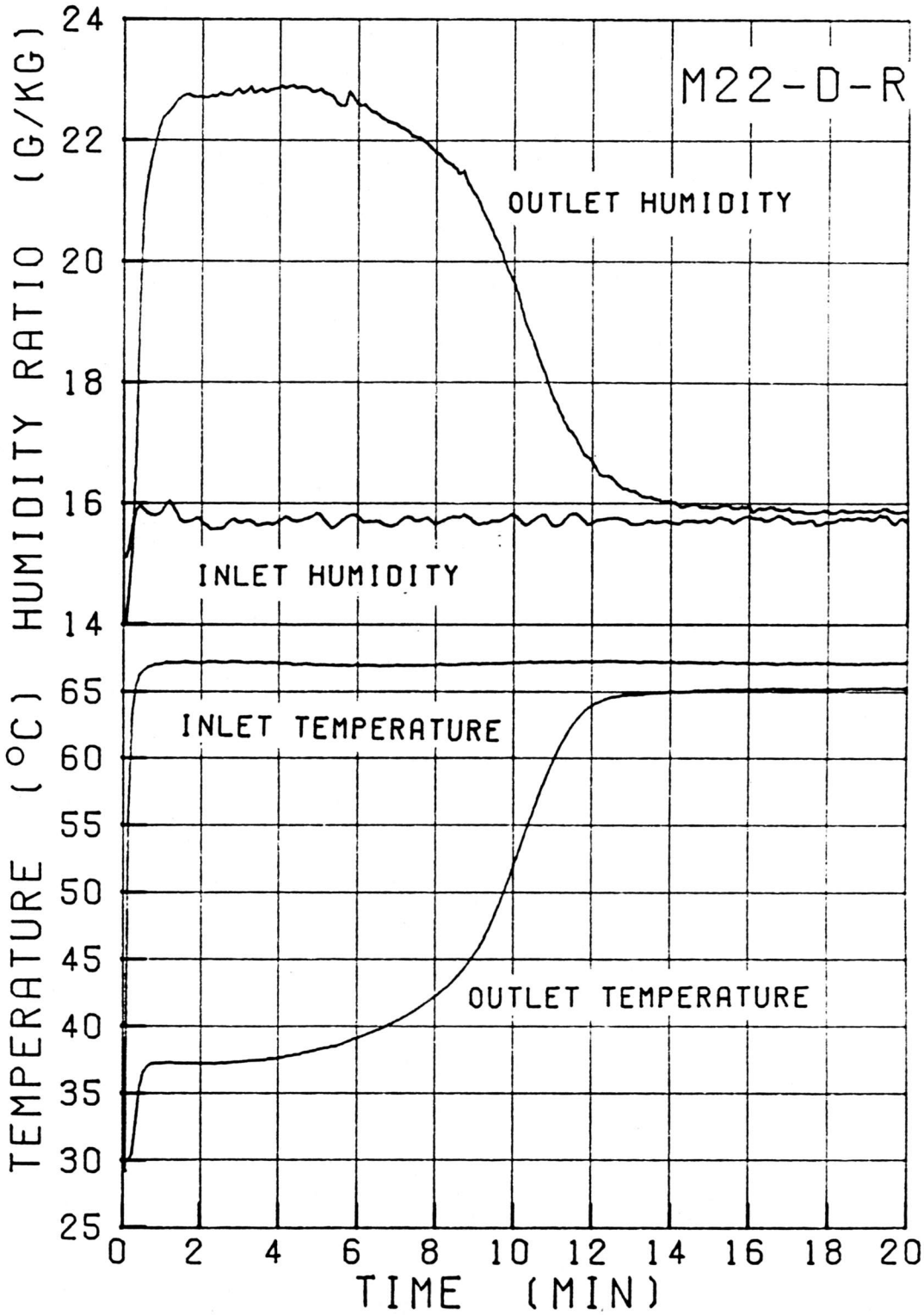

Figure C.3.8.b Temperature and humidity response of experiment M22-D-R

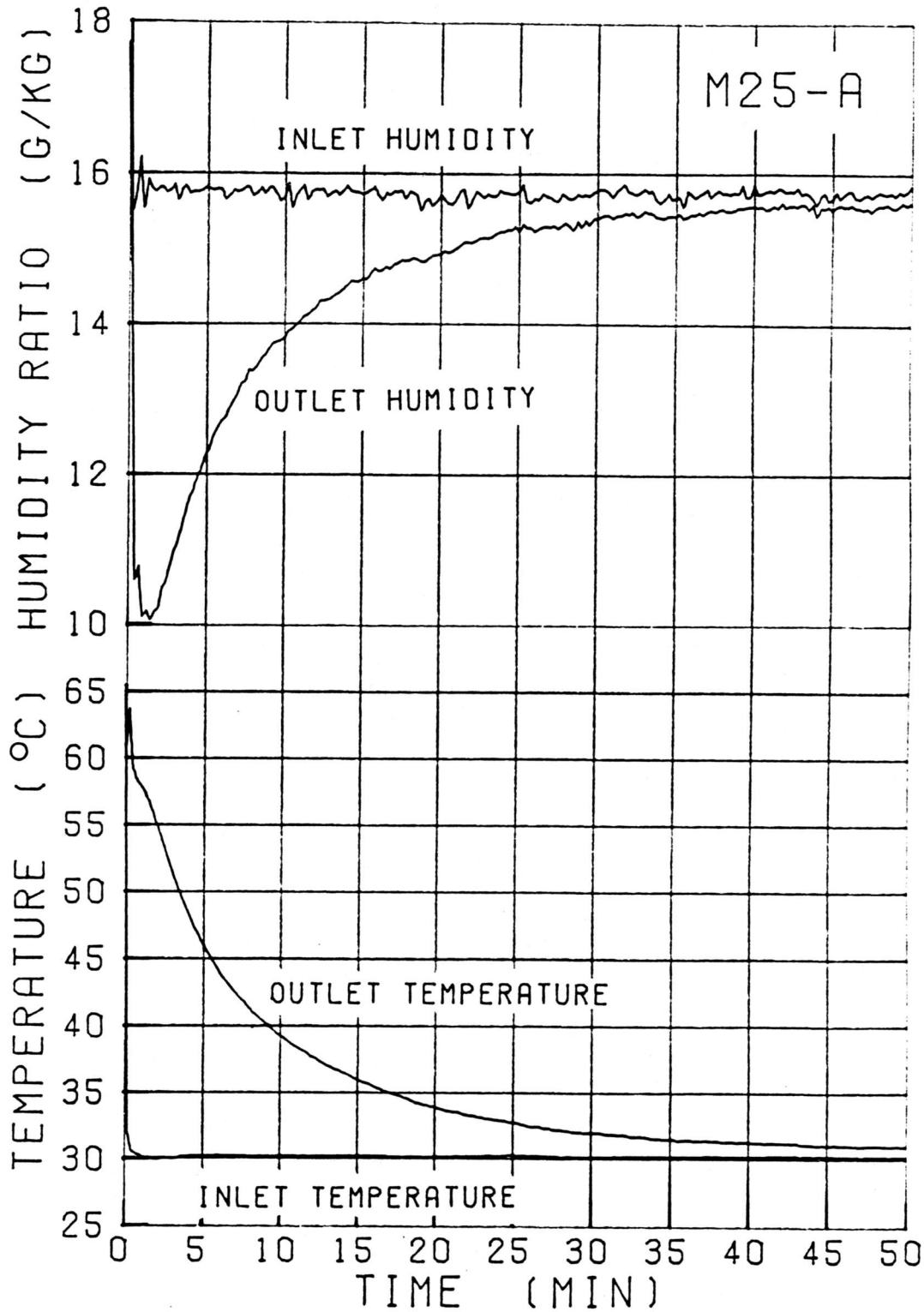

Figure C.3.9.a Temperature and humidity response of experiment M25-A

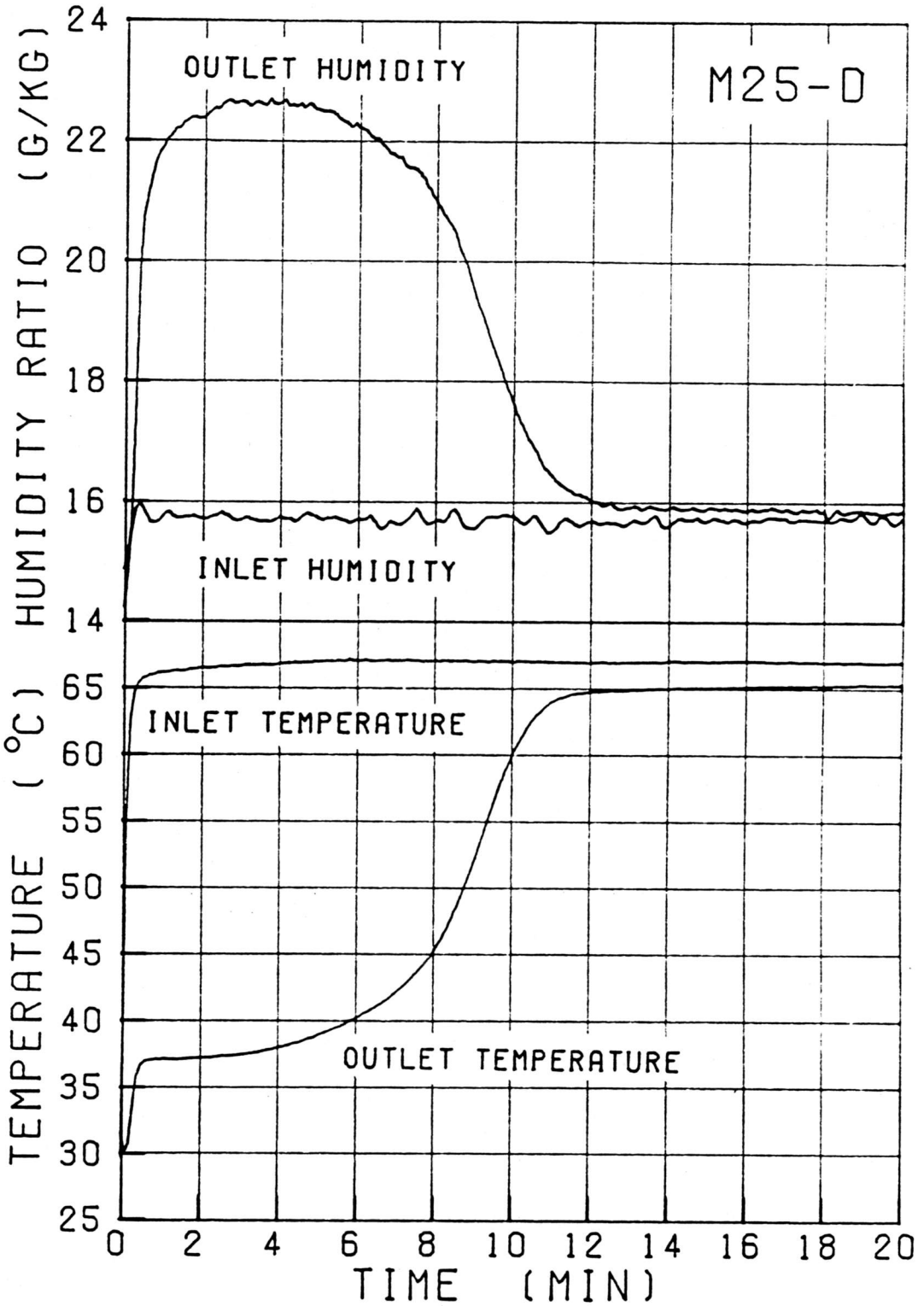

Figure C.3.9.b Temperature and humidity response of experiment M25-D

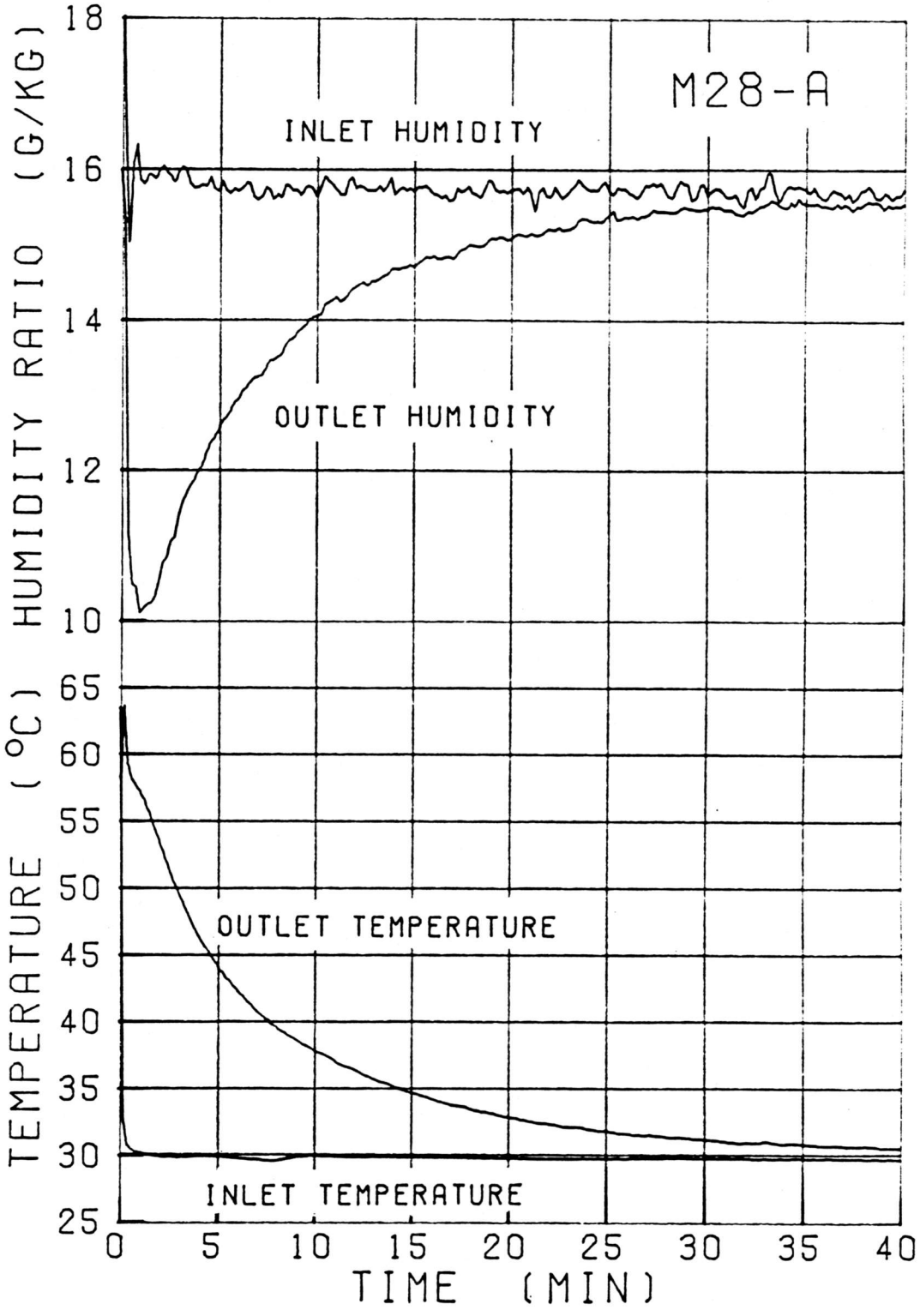

Figure C.3.10.a Temperature and humidity response of experiment M28-A

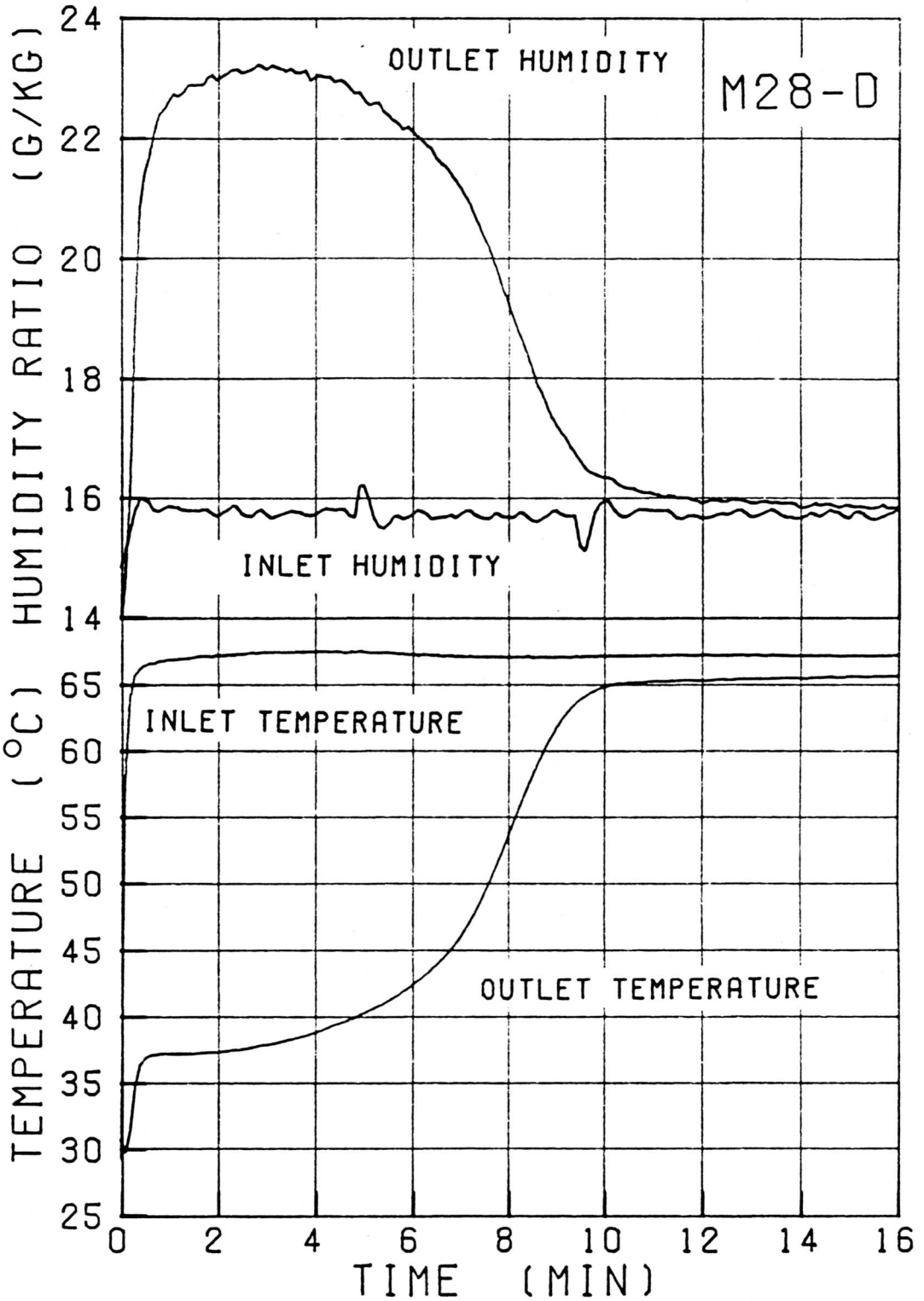

Figure C.3.10.b Temperature and humidity response of experiment M28-D

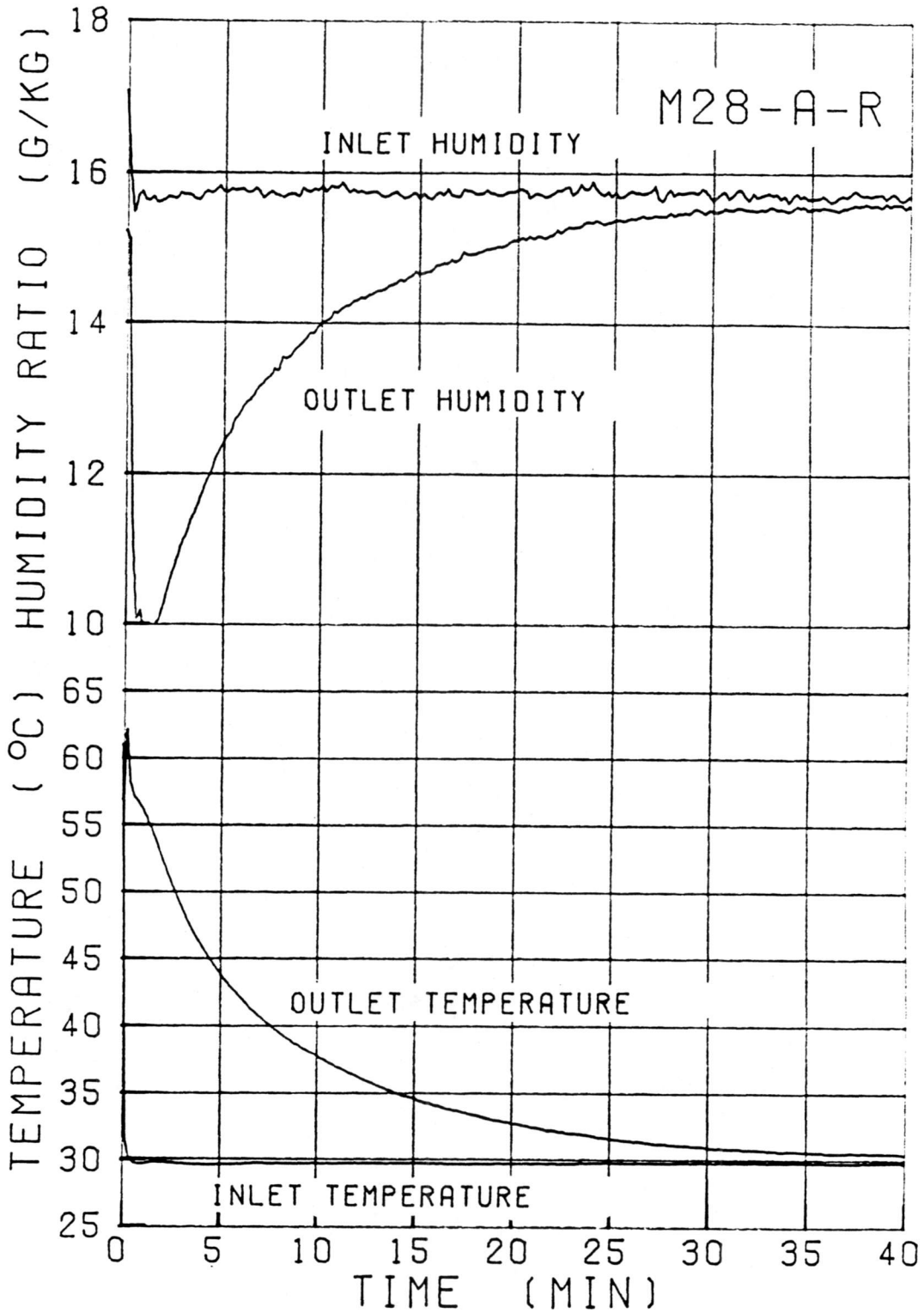

Figure C.3.11.a Temperature and humidity response of experiment M28-A-R

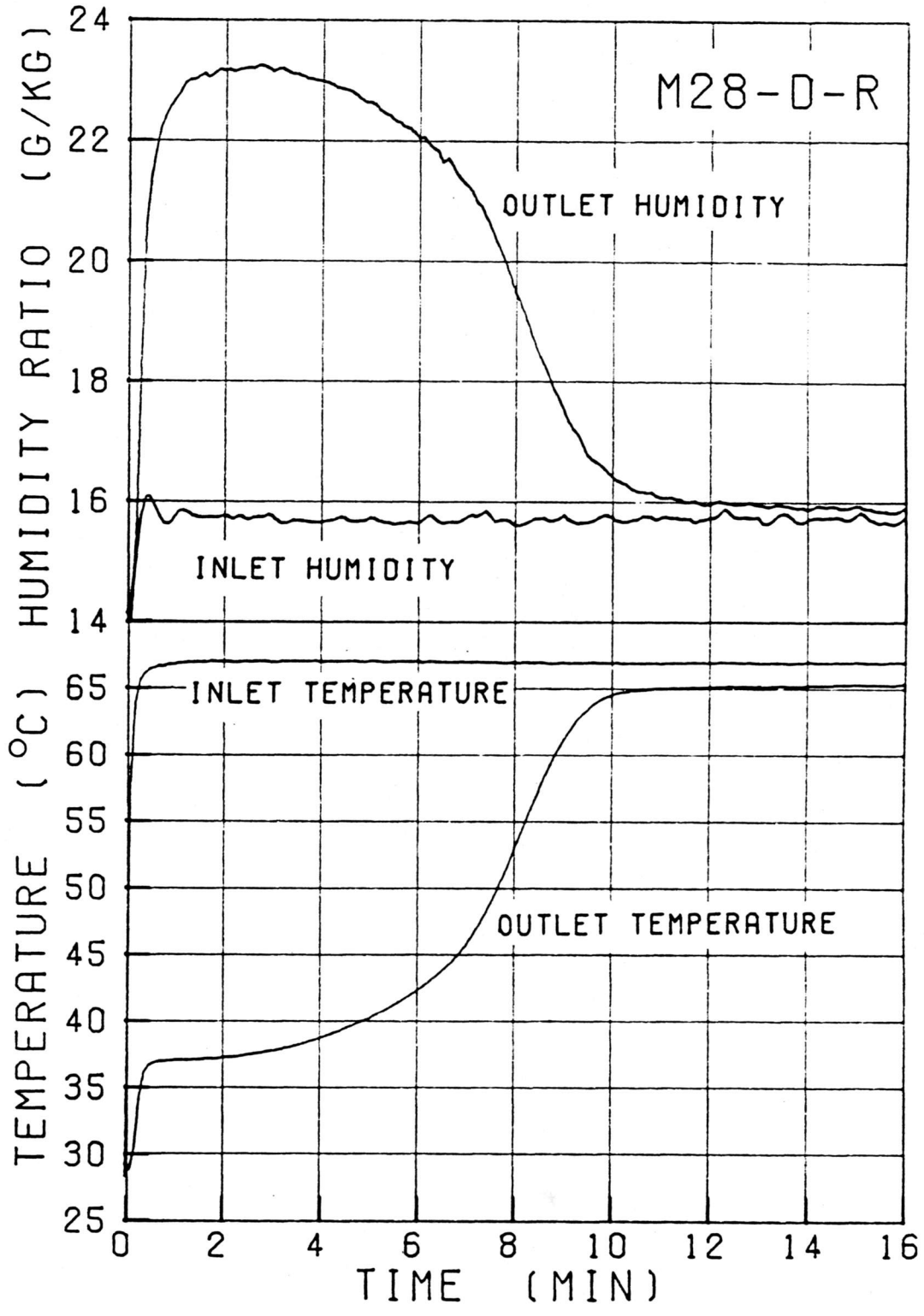

Figure C.3.11.b Temperature and humidity response of experiment M28-D-R

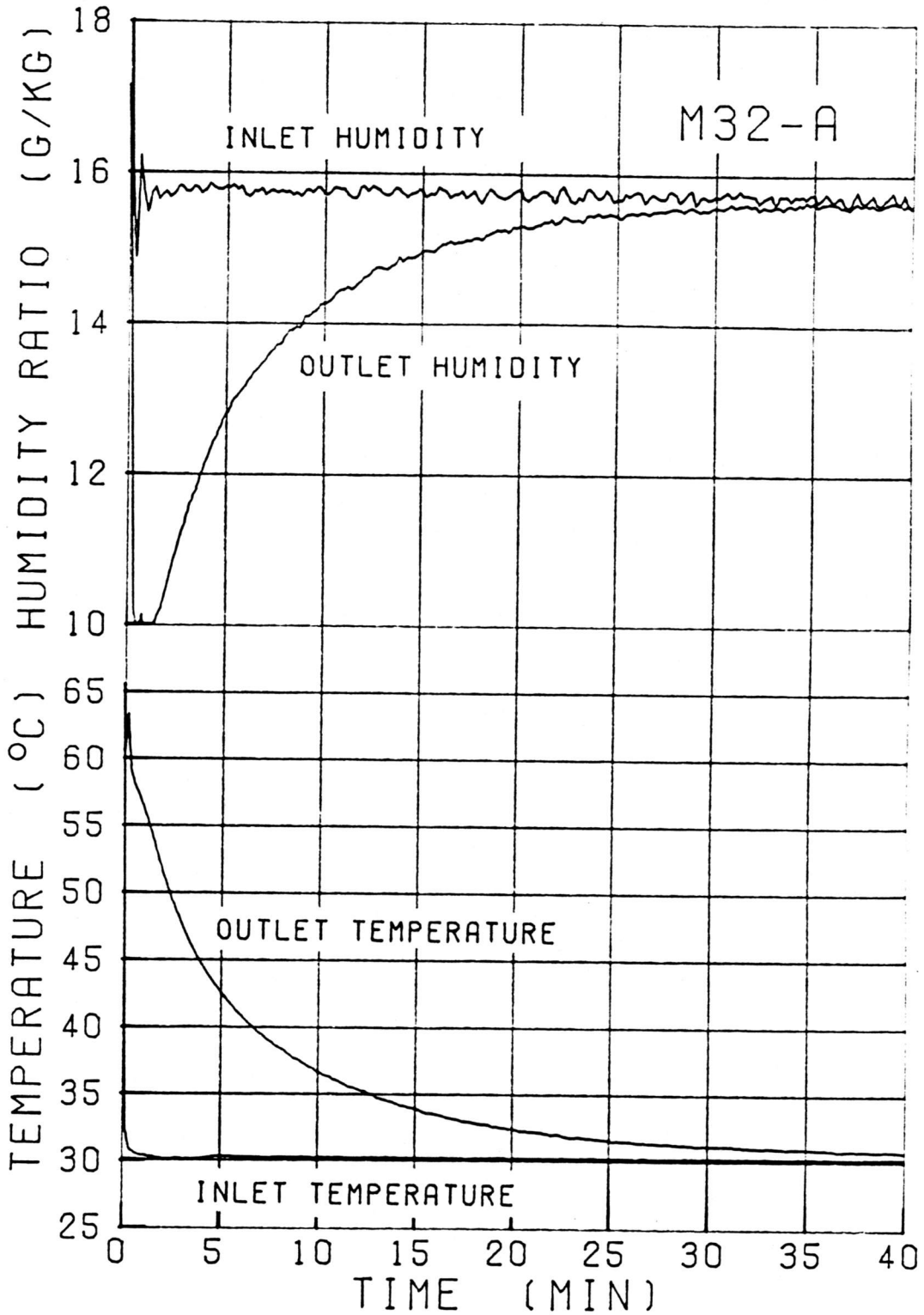

Figure C.3.12.a Temperature and humidity response of experiment M32-A

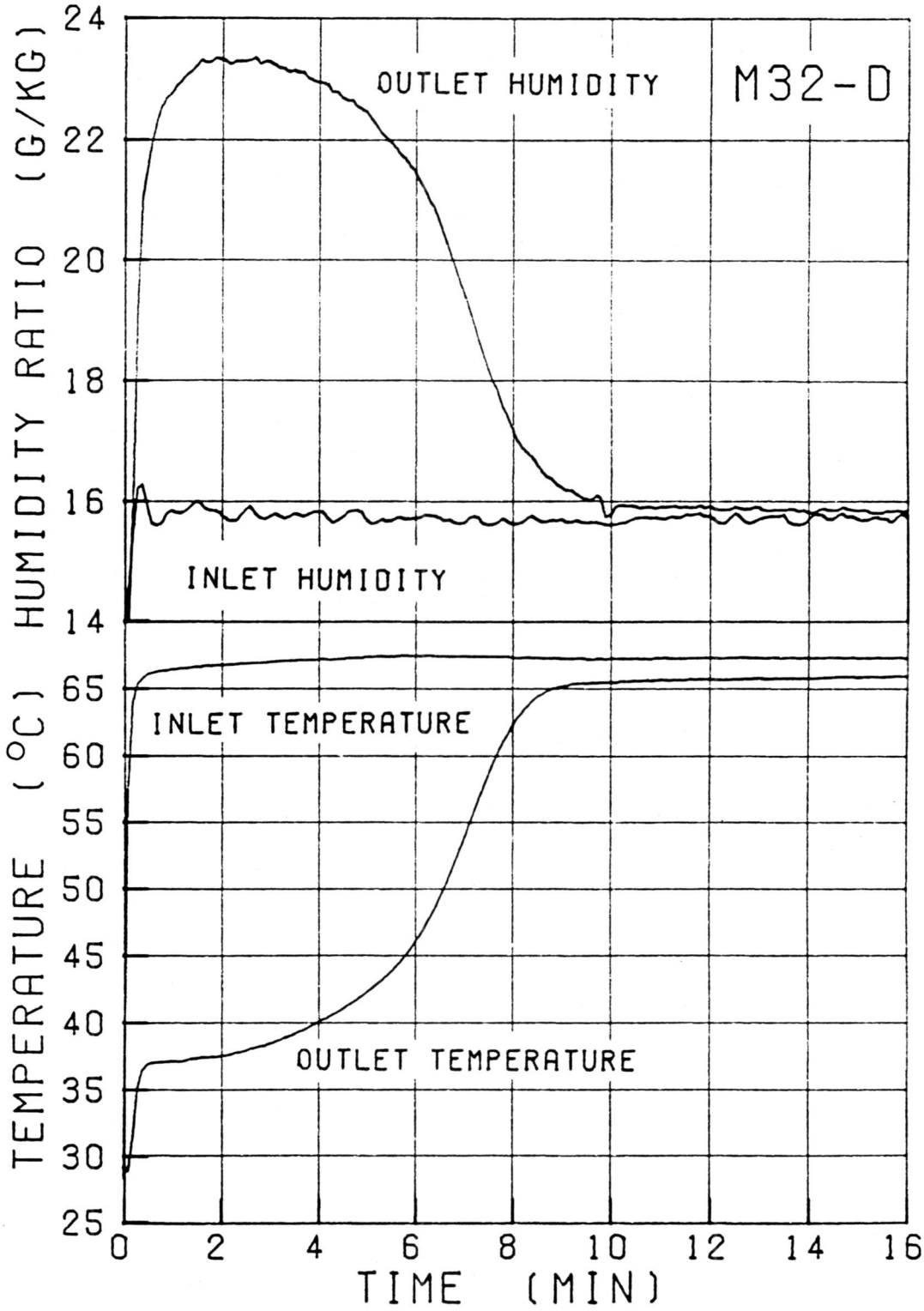

Figure C.3.12.b Temperature and humidity response of experiment M32-D

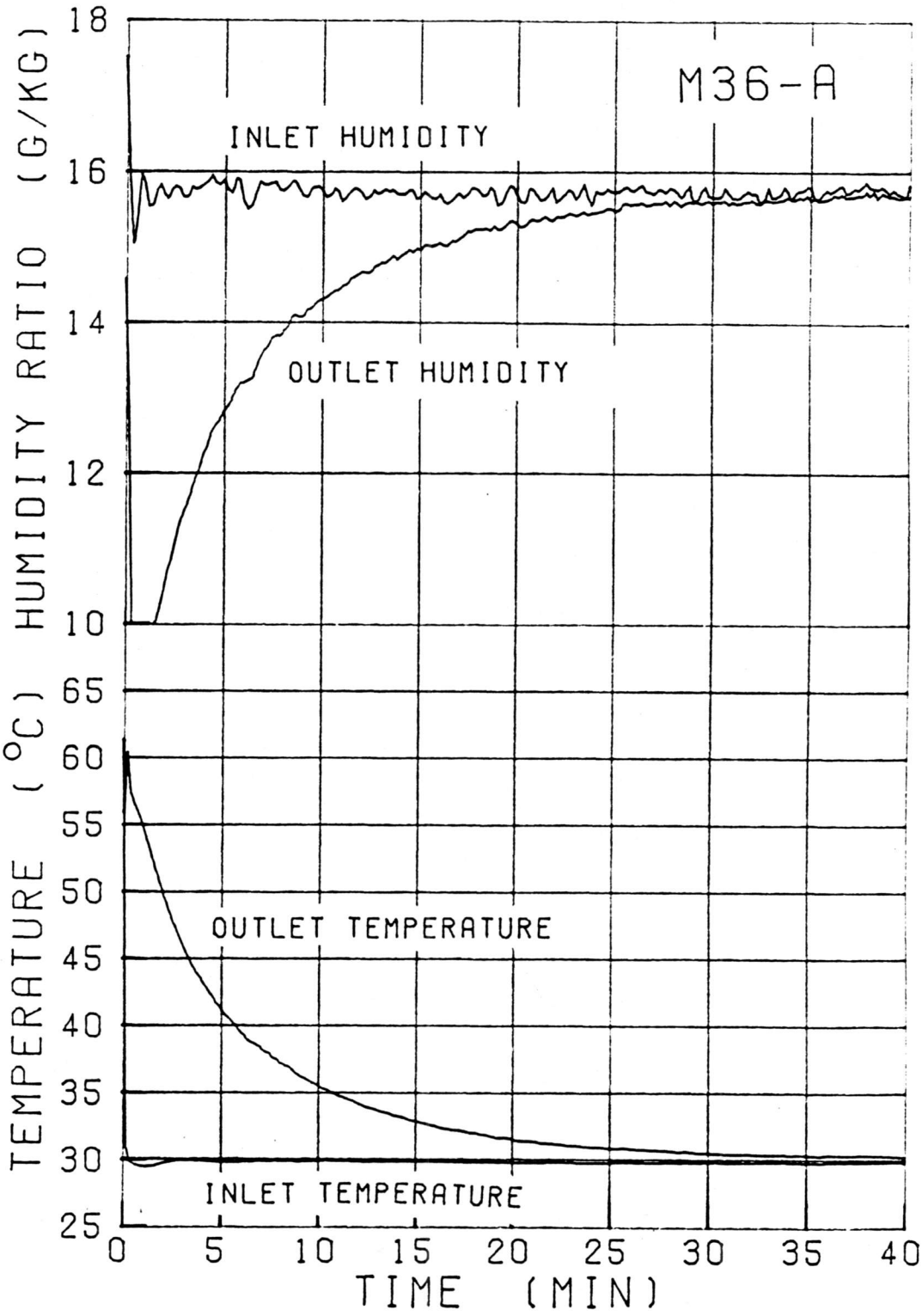

Figure C.3.13.a Temperature and humidity response of experiment M36-A

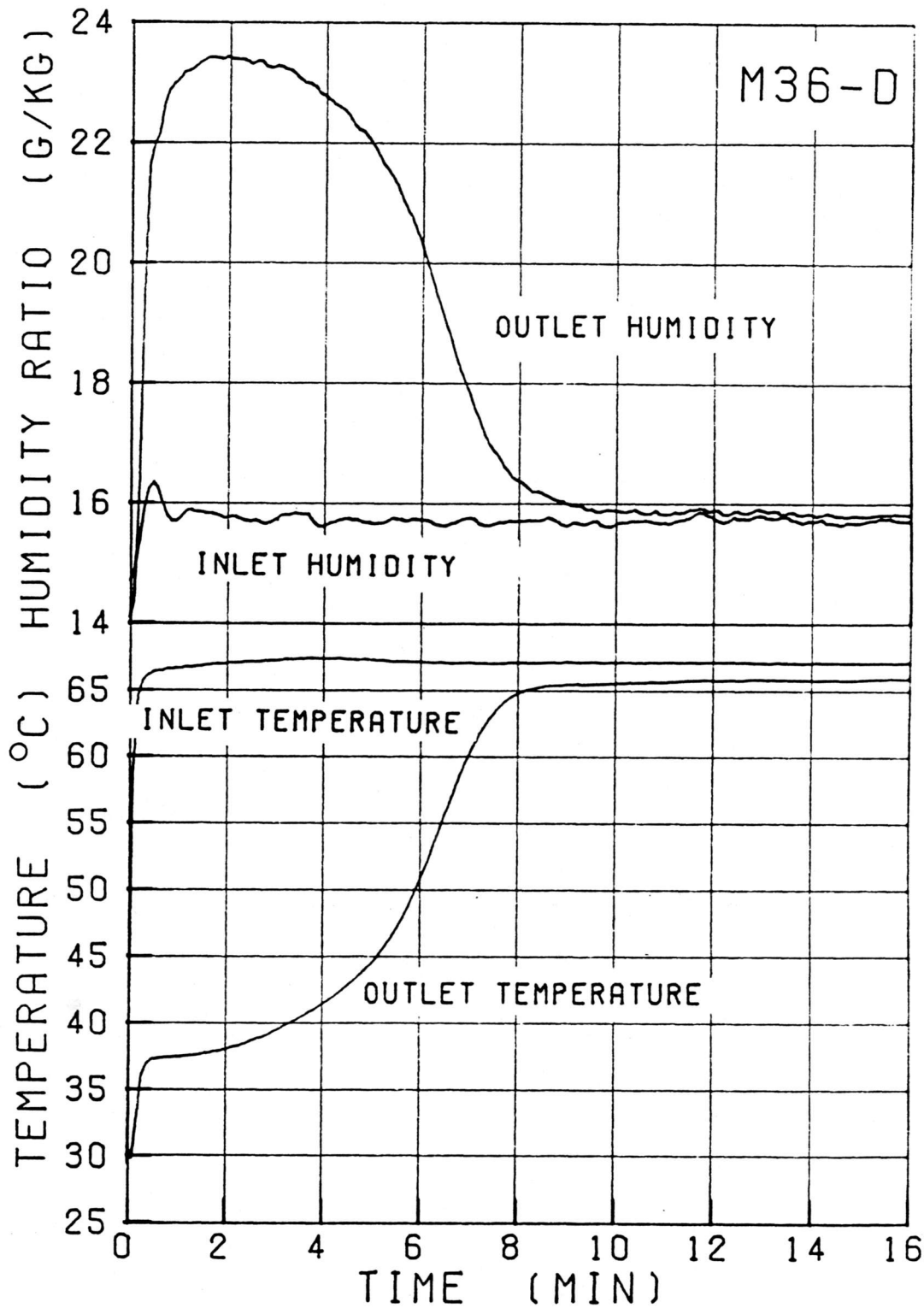

Figure C.3.13.b Temperature and humidity response of experiment M36-D

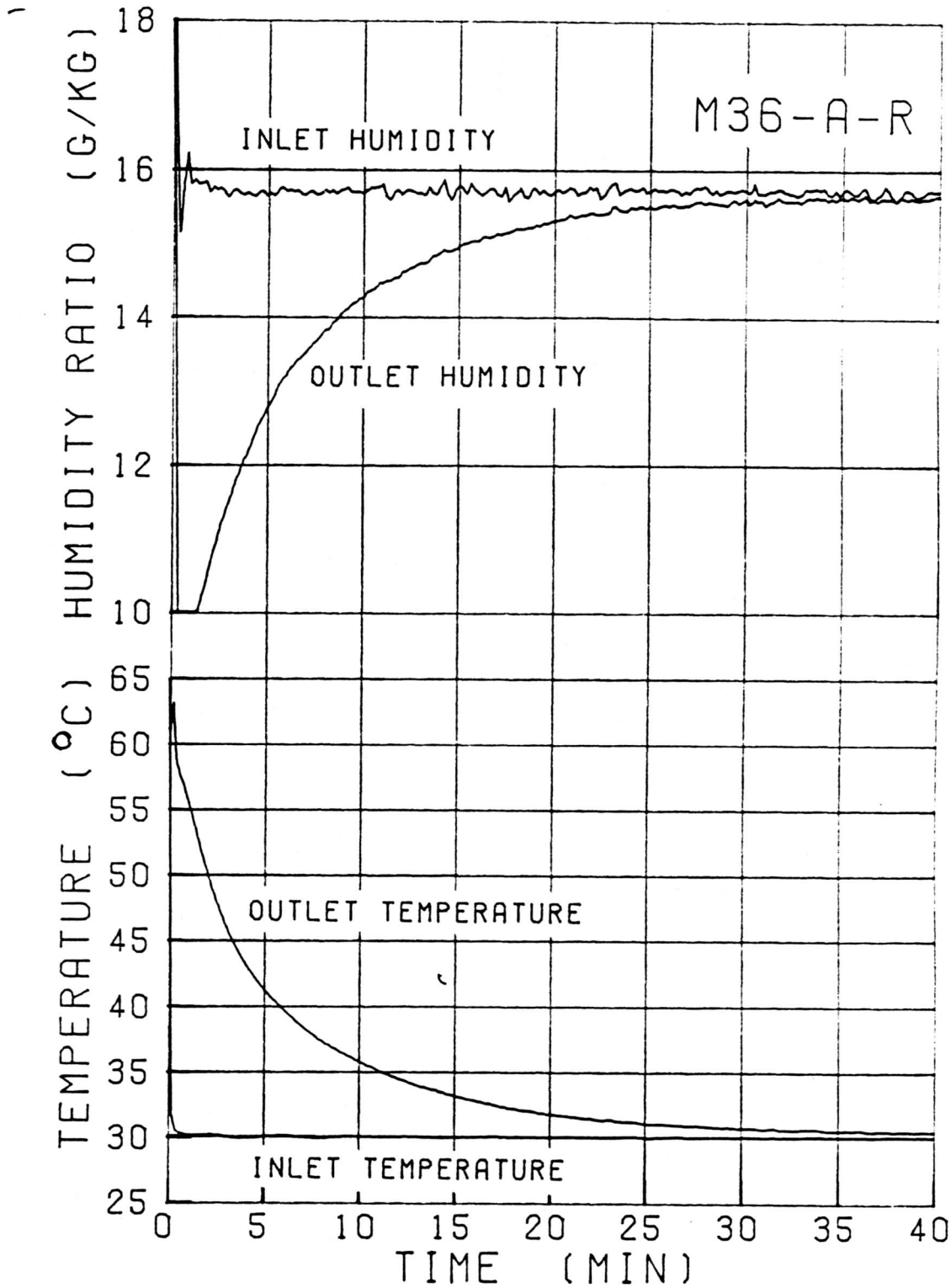

Figure C.3.14.a Temperature and humidity response of experiment M36-A-R

Figure C.3.14.b Temperature and humidity response of experiment M36-D-R

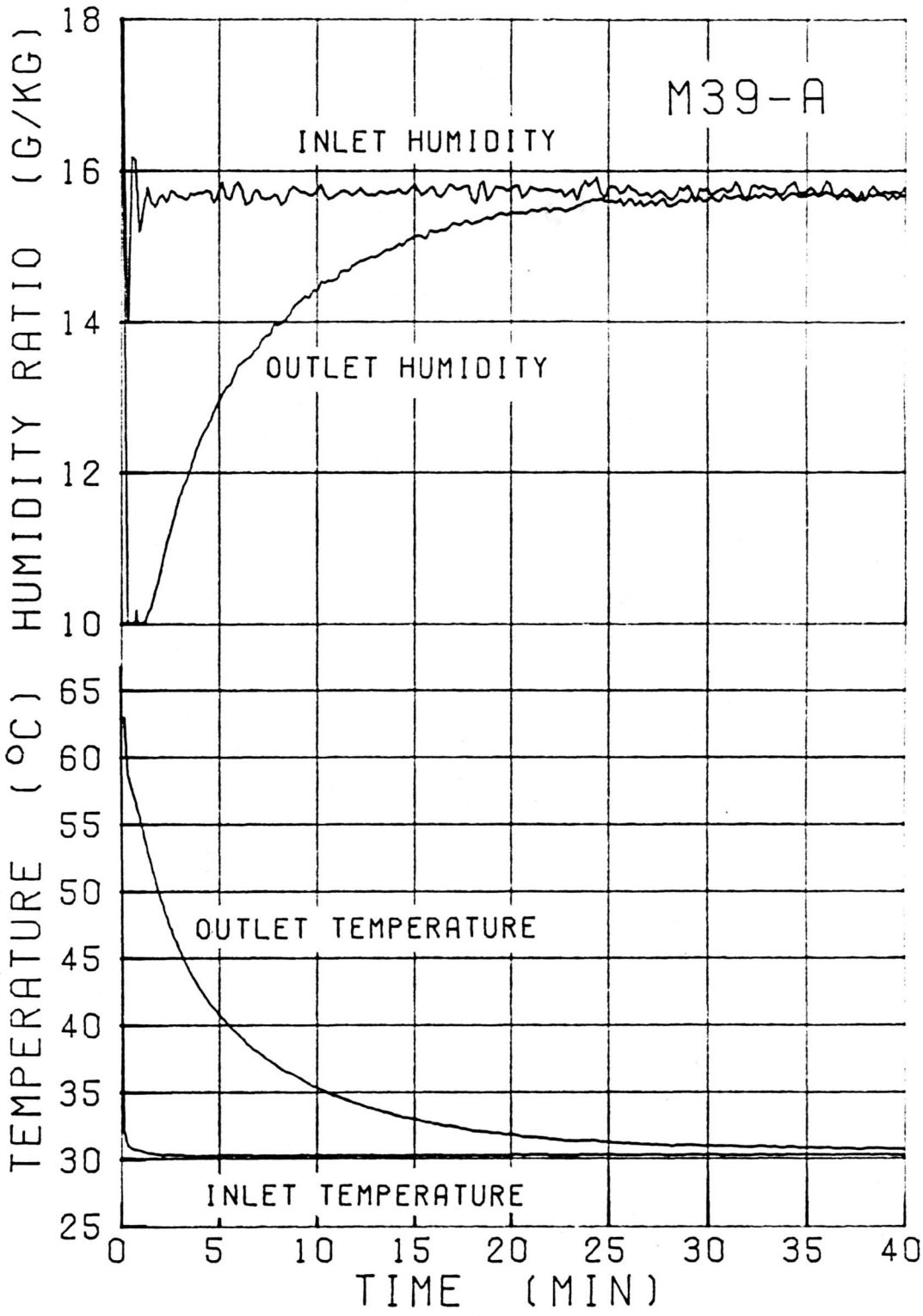

Figure C.3.15.a Temperature and humidity response of experiment M39-A

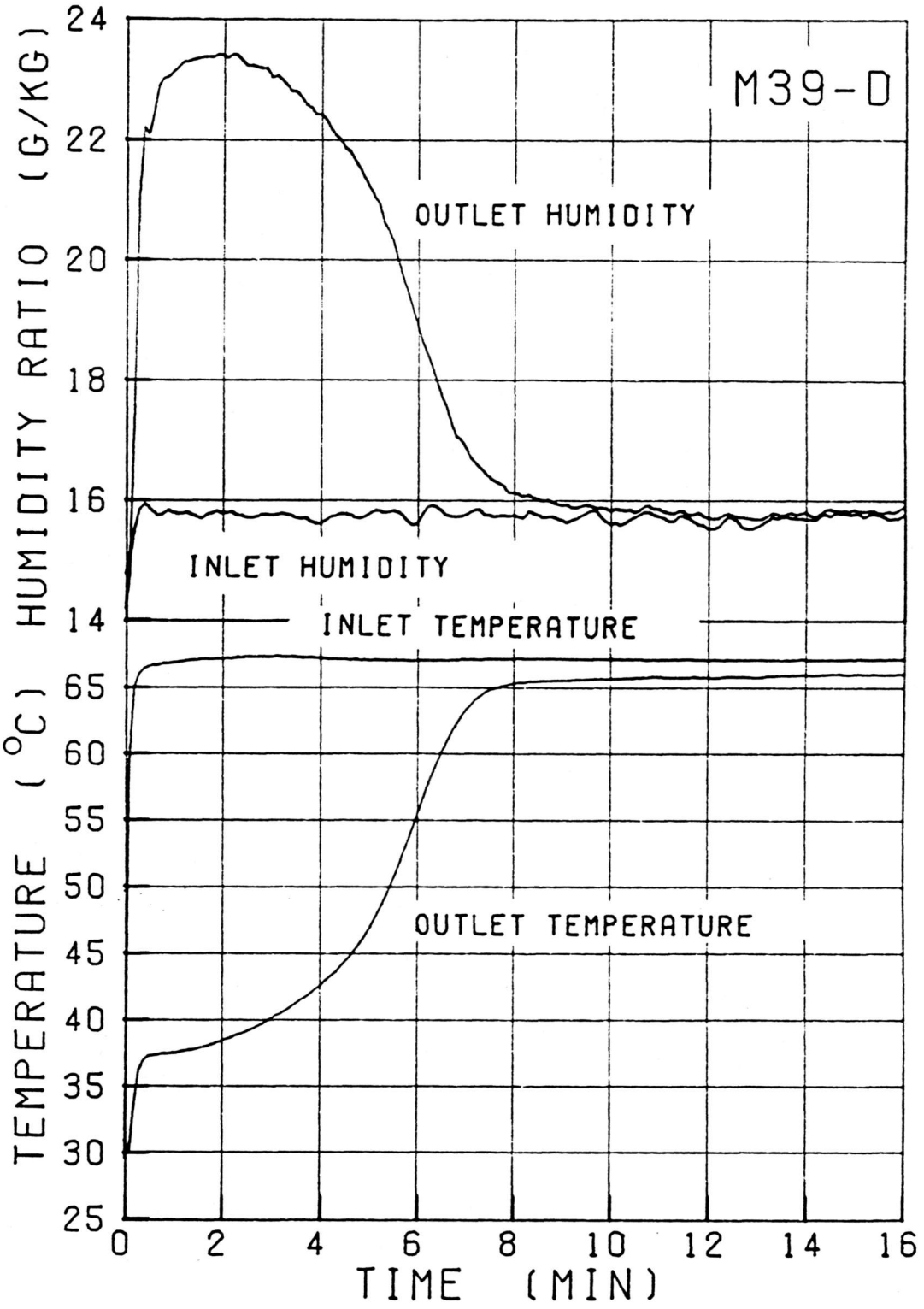

Figure C.3.15.b Temperature and humidity response of experiment M39-D